UNIVERSIDAD
DE MÁLAGA

TESIS DOCTORAL

Raúl González Núñez

Málaga, 2025

TESIS DOCTORAL 2025 Raúl González Núñez

Molecular and supramolecular strategies to tune charge transport in π-conjugated organic semiconductors based on naphthalimide and diketopyrrolopyrrole units

TESIS DOCTORAL 2025
Raúl González Núñez

DIRECTORAS: Rocío Ponce Ortiz y María del Carmen Ruiz Delgado
Doctorado en Química y Tecnologías Químicas. Materiales y Nanotecnología
Departamento de Química Física, Facultad de Ciencias, Universidad de Málaga

UNIVERSIDAD
DE MÁLAGA

AUTOR: Raúl González Núñez

https://orcid.org/0000-0003-0170-8492

EDITA: Publicaciones y Divulgación Científica.

Universidad de Málaga

UNIVERSIDAD DE MÁLAGA

ANDALUCÍA TECH
Campus de Excelencia Internacional

Escuela de Doctorado

DECLARACIÓN DE AUTORÍA Y ORIGINALIDAD DE LA TESIS PRESENTADA PARA OBTENER EL TÍTULO DE DOCTOR

D. **Raúl González Núñez**
Estudiante del programa de doctorado Química y Tecnologías Químicas, Materiales y Nanotecnología de la Universidad de Málaga, autor de la tesis, presentada para la obtención del título de doctor por la Universidad de Málaga, titulada: **“Molecular and supramolecular strategies to tune charge transport in π-conjugated organic semiconductors based on naphthalimide and diketopyrrolopyrrole units”.**

Realizada bajo la tutorización de Dña. **Rocío Ponce Ortiz** y dirección de Dña. **Rocío Ponce Ortiz** Y Dña. **María del Carmen Ruiz Delgado**.

Declaro que:

La tesis presentada es una obra original que no infringe los derechos de propiedad intelectual ni los derechos de propiedad industrial u otros, conforme al ordenamiento jurídico vigente (Real Decreto Legislativo 1/1996, de 12 de abril, por el que se aprueba el texto refundido de la Ley de Propiedad Intelectual, regularizando, aclarando y armonizando las disposiciones legales vigentes sobre la materia), modificado por la Ley 2/2019, de 1 de marzo.

Igualmente asumo, ante a la Universidad de Málaga y ante cualquier otra instancia, la responsabilidad que pudiera derivarse en caso de plagio de contenidos en la tesis presentada, conforme al ordenamiento jurídico vigente.

En Málaga, a 9 de septiembre de 2025

Fdo.: **Raúl González Núñez** Doctorando	Fdo.: **Rocío Ponce Ortiz** Tutora
Fdo.: **Rocío Ponce Ortiz** y **María del Carmen Ruiz Delgado** Directoras de tesis	

UNIVERSIDAD DE MÁLAGA

Dña. **Rocío Ponce Ortiz** y Dña. **María del Carmen Ruiz Delgado**, Profesora Titular y Catedrática Universitaria respectivamente, del Departamento de Química-Física de la Universidad de Málaga,

Certifican:

Que la memoria presentada por D. **Raúl González Núñez** bajo el título **“Molecular and supramolecular strategies to tune charge transport in π-conjugated organic semiconductors based on naphthalimide and diketopyrrolopyrrole units”** para optar al título de Doctor por la Universidad de Málaga, ha sido realizada bajo nuestra dirección en los laboratorios del Departamento de Química-Física de la Universidad de Málaga.

Considerando que constituye una investigación de alta calidad en el campo de la ciencia de materiales, se autoriza mediante este escrito su presentación y defensa como Tesis Doctoral en la Facultad de Ciencias de la Universidad de Málaga.

Y para que así conste, firman el presente certificado en Málaga a 9 de septiembre de 2025.

Fdo.: Dña. **Rocío Ponce Ortiz**

Fdo.: **María del Carmen Ruiz Delgado**

UNIVERSIDAD DE MÁLAGA

Dña. **Rocío Ponce Ortiz** y Dña. **María del Carmen Ruiz Delgado**, Profesora Titular y Catedrática Universitaria respectivamente, del Departamento de Química-Física de la Universidad de Málaga y directoras de la tesis doctoral de D. **Raúl González Núñez** bajo el título “***Molecular and supramolecular strategies to tune charge transport in π-conjugated organic semiconductors based on Naphthalimide and Diketopyrrolopyrrole units***” para optar al título de Doctor por la Universidad de Málaga,

Certifican:
Que los artículos que avalan la tesis doctoral de **Raúl González Núñez:**

1. **R. González-Núñez**, A. de la Peña, C. Valderrama-Callejón, J. L. Segura and R. Ponce Ortiz, Small asymmetric halogenated Phenylene–Naphthalimide molecules for organic field-effect transistors, *Dyes and Pigments*, 2025, **242**, 112984. **doi.org/10.1016/j.dyepig.2025.112984**

2. **R. González-Núñez**, G. Martinez, N. R. Avila-Rovelo, K. I. Hong, A. Ruiz-Carretero and R. Ponce Ortiz, The effect of hydrogen bond interactions on the electronic nature of DPP-based organic semiconductors: implications on charge transport, *J Mater Chem C*, 2024, **12**, 18264–18273. **doi.org/10.1039/D4TC02496F**

No han sido utilizados en tesis doctorales anteriores, ni serán utilizados en ocasiones venideras con el mismo fin.

Y para que así conste, firman el presente certificado en Málaga a 9 de septiembre de 2025.

Fdo.: Dña. **Rocío Ponce Ortiz**

Fdo.: Dña. **María del Carmen Ruiz Delgado**

UNIVERSIDAD DE MÁLAGA

D. **Juan Carlos Otero Fernández de Molina**, Catedrático de Universidad y Director del Departamento de Química Física de la Universidad de Málaga,

Certifica:

Que la Tesis Doctoral titulada **“Molecular and supramolecular strategies to tune charge transport in π-conjugated organic semiconductors based on naphthalimide and diketopyrrolopyrrole units”** constituye la memoria que presenta D. **Raúl González Núñez** para optar al título de Doctor por la Universidad de Málaga, y ha sido realizada bajo la dirección de las Doctoras Dña. **Rocío Ponce Ortiz** y Dña. **María del Carmen Ruiz Delgado**, en el Departamento de Química Física de la Universidad de Málaga.

Y para que así conste, firmo el presente certificado en Málaga a 9 de septiembre de 2025.

Fdo.: D. **Juan Carlos Otero Fernández de Molina**

Con estas líneas comienza el final de una etapa, una etapa que me ha enriquecido inmensamente y me ha hecho crecer no sólo en el mundo académico sino como persona. Llegado este punto, me gustaría agradecer a todas esas personas que han estado de una u otra forma implicadas en este camino, aun sabiendo que por mucho esfuerzo que ponga no encontraré palabras suficientes para agradecer todo lo que he recibido en estos años.

Estas primeras líneas me gustaría dedicárselas a mis directoras de Tesis, Rocío y Mari Carmen. Bendito aquel día que aparecí por la cuarta planta, creo que fue una de las mejores decisiones que he tomado en mi vida. Aquel día te conocí, Rocío, y desde ese momento me has guiado durante toda mi vida académica poniendo finalmente la guinda al pastel con esta Tesis. Tu pasión por la ciencia y tu forma de transmitirla a las nuevas generaciones es algo que admiro, gracias por inculcarme ese amor por la ciencia. En cuanto a ti, Mari Carmen, desde el primer momento me has tendido la mano, has estado al pie del cañón y me has enseñado que el esfuerzo siempre tiene su recompensa. Y por supuesto cómo no agradecerte que me introdujeses en ese mundo abstracto llamado "cálculos químico-cuánticos", un mundo del cual he descubierto el gran potencial que tiene, gracias a ti. A vosotras os debo ser el científico que soy a día de hoy, gracias por todo ese tiempo que me habéis dedicado aun cuando no lo teníais, no puedo estar más orgulloso de las directoras que he tenido.

Agradecer, cómo no, al resto de gente del grupo, por todos esos desayunos, cervezas y sobre todo por todas esas horas de trabajo juntos. Quiero agradecer a María y Sara por siempre tener buenas palabras y tenderme la mano siempre que lo he necesitado. Gracias a Iratxe y Alexandra, por ayudarme a despegar en mis inicios e introducirme en este maravilloso mundo de los transistores. Y cómo no agradecer al veterano del grupo, Víctor, por compartir tu sabiduría con todos nosotros en esas largas charlas. Gracias a Irene por tener siempre una buena palabra, por levantarme el ánimo en esas mañanas duras y por enseñarme a ser crítico conmigo mismo. Eres alegría por naturaleza y a veces esa "mamá" que todos hemos necesitado, poniendo cordura dentro de la locura. A las últimas incorporaciones del grupo, Juan, también conocido como "Juanito", gracias por tu disposición y por sacarme una sonrisa siempre con tus "cuñadismos". Sigue así, porque tu cultura del trabajo te llevará lejos, confía en ti. Fernando, o "F", mi fiel escudero de despacho, gracias por todas esas charlas científicas y no tan científicas sobre deporte, tu pensamiento crítico y rigor científico te llevarán donde tú quieras. ¡Y tranquilos muchachos, que algún día el Málaga y el Córdoba volverán a primera!

Por último, debo tener unas palabras especiales para mi fiel camarada, Sergio. Hemos compartido muchos momentos dentro y fuera de la ciencia. Mis primeros congresos, mis primeras charlas, hora de pádel y fútbol, junto con un sinfín de anécdotas de las cuales podría estar hablando días. Desde que vivíamos en “villa cuqui” me demostrarte que eres una persona en la que se puede confiar, trabajadora y con una ambición que pocas personas tienen. Gracias por guiarme en todo momento, nunca me cansaré de decírtelo, te debo mucho, y no sería quién soy a día de hoy si la ciencia no tu hubiese puesto en mi camino. ¡Eres muy grande!

Cómo no, agradecer al resto de personas que forman ese maravilloso grupo llamado “jóvenes quifiteros”. Gracias a Cristina y Zafra, por ser los mejores técnicos con los que me podría haber cruzado, por vuestra ayuda incondicional siempre que lo he necesitado, aunque a veces me queráis matar cuando se ha roto alguna que otra cubeta… Gracias por todo lo compartido dentro y fuera de la universidad a personas cómo Moles y Samara, por vuestras palabras siempre que lo he necesitado y alguna que otra fiestecilla. Gracias a Fran por todas esas conversaciones científicas y no tan científicas, que siempre de una manera u otra acababan en risas. A Fernando Gordillo por tu ayuda incondicional en toda esa maravillosa burocracia que teneos. A Marcos y Nacho, por no matarme cuando os pedía los equipos y os dejaba sin medir, siempre con una buena palabra, y lo más importante… “Furbo!!”. Gracias a Beloqui por ser un maquinaria en todos los sentidos, siempre estando ahí para el que necesite una mano, y no te preocupes que, aunque te llamemos persona mayor, en realidad…… bueno sí, lo pensamos, pero siempre con cariño máximo. Gracias a Abel o también conocido como “Eibol”, eres la locura que todos necesitamos a veces y eso se agradece, por todas esas cervezas juntos y todas esas horas de pádel.

También agradecer al resto de personas del departamento, que de una forma u otra han estado presentes en esta etapa. Gracias por acogerme desde el primer momento y hacer que sintiese que ese era mi sitio.

Me gustaría agradecer al grupo del profesor José Luis segura y al grupo de la profesora Amparo Ruiz Carretero por proporcionarme los compuestos que han hecho posible que esta tesis salga adelante. La ciencia requiere colaboración, y junto hemos sabido sacar lo mejor de cada uno en todo momento.

Mi agradecimiento también a todas esas personas que me hicieron sentir cómo en casa durante mi estancia en Cambridge. Al profesor George Malliaras por acogerme en su grupo sin poner trava alguna. Al resto de personas del grupo que me acogieron como uno más desde el primer día. Y en especial agradecer a Antonio por ser mi pilar durante toda mi estancia, cómo dijimos… ¡haremos cosas grandes!

Para finalizar, quiero agradecer con todo mi corazón a mi familia y amigos. En especial a mis padres y mis hermanos. Gracias por educarme en el camino del esfuerzo, la constancia y la perseverancia. Por estar siempre ahí en los momentos buenos y en los no tan buenos. Sin vosotros no sería la persona que soy hoy en día. Y como no, a ti, Rocío, mi compañera de vida. Hemos crecido juntos y siempre hemos ido de la mano en todo el camino recorrido, gracias por tu apoyo incondicional, por levantarme en mis peores momentos y por gritar de alegría en los mejores. Agradecerte tu comprensión en todo momento, esto de la ciencia no es fácil y has sabido ver que es lo que necesitaba en cada uno de mis pasos. Por todo ello, este trabajo hecho con tanto esfuerzo y dedicación tiene una parte de cada uno de vosotros.

Gracias a todos, de todo corazón.

"Nothing in life is to be feared, it is only to be understood. Now is the time to understand more, so that we may fear less."

(*Marie Curie)*

Table of contents

CONTENTS

1. Introduction

2. Methodology

3. Results and Conclusions

Chapter I

Chapter II

Chapter III

Chapter IV

5. Resumen

6. Appendices

1

Introduction

Table of contents

CONTENTS

Looking around us, in a society as advanced and technological as the one we live in, in which most of our daily activities involve the use of electronic devices, different aspects such as economy, health or social relationships are mainly related to technological advancement, see Figure 1.1.[1–4] This increasingly dependent relationship is growing at a vertiginous pace, and electronic systems are taking up an ever-larger part of our lives.

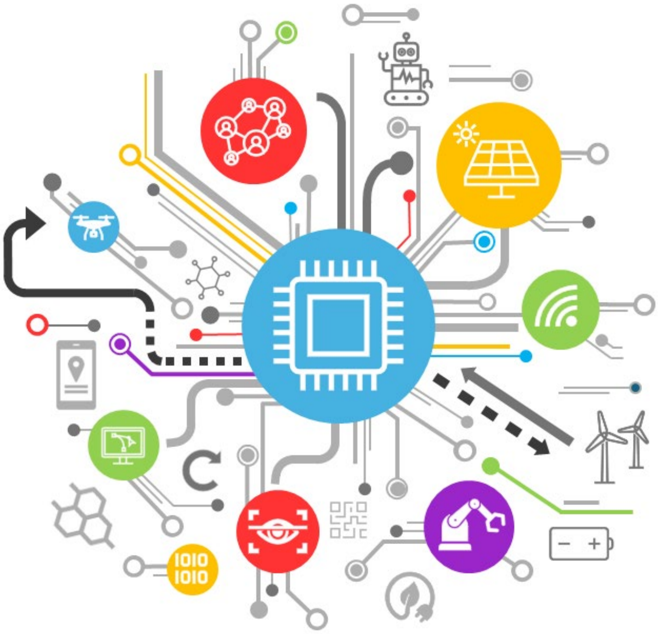

Figure 1.1 Scheme representing the use of technology in society.

So far, this need has been met using silicon and other inorganic materials. However, limited resources and mass manufacturing of devices raise urgent issues to be resolved, with special attention to the environmental aspects associated with the manufacture, use and subsequent disposal of these electronic devices. In this sense, carbon-based electronics, organic electronics, with more sustainable manufacturing and disposal processes, open up a new field. This, together with the use of small organic molecules, polymers and other organic materials that offer electronic structures with unique properties, positions organic electronics as an alternative in the electronics of the future.[5,6]

Organic electronics arose as a result of a mistake in the 1970s, when a student of Hideki Shirakawa, following the traditional Ziegler-Natta polyacetylene synthesis route, mistakenly added a thousand times more catalyst than necessary. Instead of obtaining a dark and opaque solid, he obtained a shiny and sticky film similar to aluminium.[7] This film was flexible like plastic and had surprisingly high conductivity. From this discovery, Shirakawa, Heeger, and MacDiarmind made great advances in the study of conducting polymers. These three scientists discovered that the conductivity of polyacetylene could be modulated from an insulating character to a conducting character by oxidative doping with I_2, Br_2, or Cl_2 vapors.[8] In the case of exposure to iodine, conductivity increased up to seven orders of magnitude. The discovery and development of conducting polymers by these three researchers led them to receive the Nobel Prize in Chemistry in 2000.[9] From this point on, efforts in this field of research have focused on the development of conjugated organic semiconductors, doped or not, for use in electronic devices.

Today, we already are surrounded by electronic devices made from organic materials: mobile phone screens, portable solar cells, television, screens, etc.[10] This is possible thanks to the enormous development that organic electronics has undergone and the improvement in the miniaturization of organic semiconductors.[11,12] However, there is still a long way to go for these electronics to become an industrial and commercial reality. To do so, it will be necessary to overcome different challenges by making a great effort in research. In fact, technology companies invest in the manufacture of low-cost, high-performance organic devices, a market worth billions of dollars that is growing rapidly. The key to the development of organic electronics is associated with the intrinsic characteristics of the organic materials themselves, with advantages such as: reduction in production costs, versatility in synthesis processes or compatibility with transparent, flexible and deformable substrates.[13] Cooperation between researchers from all disciplines is vital for this electronic to become an industrial and social reality.

1.1 Semiconductor materials in electronics

Depending on their conductivity, materials can be divided into three different categories: conductors, semiconductors and insulators (Figure 1.2). Semiconductors form an intermediate group between conductors and insulators, presenting relatively small conductivity values at low temperatures that increase with temperature or doping. To explain the conductivity phenomenon, it is necessary to consider the band theory.[14] This is based on the fact that the atoms in a solid are so closely packed that their electronic levels form a continuum of energy states called a band. The valence band (of lower energy) is the one that contains the valence electrons, and the conduction band (of higher energy) is the band formed by the immediately higher unoccupied energy levels.

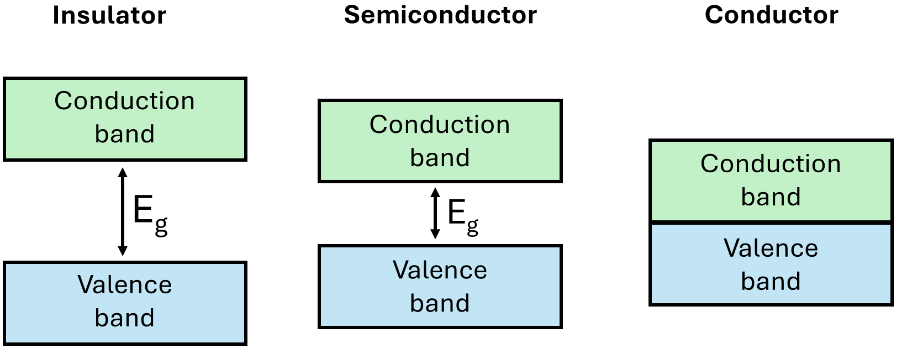

Figure 1.2 Representation of energy bands for solids.

In conducting materials (metals), these two bands are partially overlapped. In contrast, in insulating materials, the bands are separated by a large energy interval (bandgap), preventing the promotion of electrons from the valence band to the conduction band.[15,16] In semiconductors, the valence band is completely filled and the conduction band empty, with a small bandgap energy, so that a small energy input can lead to electron transit between both bands.

1.1.1 Transistors

Semiconductor materials are the basic components of all modern electronics, with the transistor being the device of excellence where these materials are used. A transistor consists of a semiconductor device that is used to obtain an output signal based on an input signal. It can be used as an amplifier, switch, signal modulator, voltage stabilizer, among other functions. The transistor is the main device that gave rise to integrated circuits and is considered one of the greatest discoveries of recent centuries.

The transistor was born out of the need of the replacement of the vacuum tubes to make long-distance calls. Vacuum tubes were large, produced a lot of heat, consumed a lot of energy and had to be replaced frequently. For this reason, the American Telephone and Telegraph Corporation, formerly known as the Bell Telephone Company, established a research centre in 1926 called the Bell Telephone Laboratories. After World War II, laboratory director Mervin Kelly hired scientists William Shockley, Walter Brattain and John Bardeen to develop his idea based on the use of semiconductors to solve the problems caused by vacuum tubes. Thus, in 1947, the first point-contact transistor was born made of two gold contacts pressed onto germanium very close to each other.[17] The impact of this discovery was such that Shockley, Bardeen and Brattain were jointly awarded the 1956 Nobel Prize in Physics.[18,19]

From the very beginning, the huge difference in size between transistors and vacuum tubes was striking. In 1965, Gordon Moore predicted that the number of transistors per unit area on a microchip could double every 12 months, an axiom known as Moore's Law. In 1975, he modified his own law, changing it from 12 months to 24 months.[20] It can be said that this law has been precisely fulfilled for decades, going from having chips with hundreds of transistors to having chips with millions of transistors. The challenge is to make devices even smaller.

1.1.2 Future of electronics

According to Nature magazine, Moore's Law no longer applies in 2016. Today, there are microprocessors with a technology with a distance between transistors of 5 nm. From this point on, at this scale, the behaviour of electrons will be governed by quantum uncertainties, which will make transistors unreliable. Technology that reduces the size of the transistor is reaching its limit. This means that reducing the size of a transistor no longer increases speed or decreases power consumption. Therefore, new technologies must be developed to overcome the Moore's Law limit.[21] In order to address the limitations of Moore's Law, a range of approaches may be considered in future research, including:

- **Three-Dimensional System-in-package integration:** 3D System-in-package (SiP) technologies allow silicon dies to be stacked and connected in a three-dimensional space, thereby improving circuit efficiency and transistor density. Rather than relying solely on transistor density, SiP technologies, and especially 3D SiP, go beyond Moore's law in a way that has been termed "More than Moore."[22] 3D SiP packaging optimizes space use with designs such as package-on-package, improving circuit efficiency and reducing costs by producing smaller chips with higher yields.[23] However, it presents technical challenges, such as thermal mismatch between materials, cooling issues, and environmental vulnerability.

- **Chiplets:** Chiplets are multi-chip modules made up of small, individual integrated circuits (ICs) that act as building blocks for larger systems, such as CPUs.[24,25] They were developed to improve the transmission of information from smaller nodes, optimizing performance in devices such as computers and smartphones.[26] These modules have advantages such as: better signal transmission, advanced designs, cost reduction or ease of producing more powerful chips. However, they also offer some disadvantages, such as problems with interfaces or greater complexity.

- **Non-volatile memory (NVM):** Moore's Law addresses challenges such as power consumption, heat dissipation, and data storage as transistors are miniaturized and their density increases. Non-volatile memory (NVM) is a type of computer memory that can retain stored information even after the power is removed[27,28]. It emerges as a promising solution to address problems such as i) Power consumption: as it reduces power and sometimes endurance. ii) Heat dissipation: emerging NVMs reduce the heat generated, thereby improving system reliability and lifetime. iii) Data storage: NVM offers solutions through high density to store large amounts of information in a small space, thereby increasing capacity without increasing size or power consumption, iv) Integration: NVM can be integrated into existing systems, improving their performance and extending their lifetime without significant redesigns.

- **Photon-based computing:** The heat generated by high transistor density limits chip performance, a significant challenge to Moore's Law. One proposed solution is photon-based computing, which uses light (photons) instead of electricity to transmit and process information, significantly reducing heat and improving speed and efficiency.[29] Data is transmitted via light instead of electricity, using lasers, waveguides and detectors, allowing for greater speed and lower power consumption compared to electrical interconnects.[30] They are also capable of performing calculations using light, being faster and more efficient than electronic processors. They are useful for complex tasks such as Fourier transforms, signal processing and image recognition. Photon-based computing has advantages such as reducing the heat generated by chips, increasing data transmission speed and improving energy efficiency. However, they have certain disadvantages such as requiring the development of practical and cost-effective photonic components, as well as effective integration with traditional electronics.

- **Biocomputing:** Computing based on biological molecules, such as DNA, RNA, and proteins, offers a potential solution to overcome the limits of Moore's Law. These molecules possess unique properties that make them ideal for certain tasks, such as data storage and complex calculations, with high precision and low heat generation.

An option is DNA computing, which uses DNA to both store and process information.[31,32] A prominent example is the storage of 200 MB of data in DNA sequences, achieving extreme compactness and efficient addressing, similar to storage on hard drives. On the other hand, protein-based computing, uses protein molecules as computing components.[33] Proteins offer high storage capacity, low energy consumption, and can perform complex calculations quickly, in addition to mitigating the problem of heat dissipation. This type of computing has certain advantages such as high storage density, energy efficiency, capacity for complex calculations and reduction of heat generated. Instead, it must improve in aspects such as the speed and precision of biological calculations and overcome technical barriers for wider adoption.

- **Quantum computer:** Quantum computers, based on principles of quantum mechanics and using qubits, offer solutions to overcome the challenges of Moore's Law. Qubits, which can exist in multiple states simultaneously, allow certain calculations to be performed much faster than classical computers.[34–36] These computers enable the simulation of complex systems, facilitating the efficient and accurate simulation of the behaviour of atoms and molecules, crucial for areas such as materials science, overcoming the limitations of classical computers. Quantum computers also have the ability to solve optimization problems, using quantum algorithms, such as quantum annealing. These computers can identify optimal solutions to problems with a large number of possibilities, relevant to sectors such as finance, logistics and transportation. These types of computers are capable of solving problems in a faster and more efficient way, ideal for complex scientific and industrial applications. Although they are in an early stage of development and are not in widespread use, they represent a promising advance against the limitations imposed by Moore's Law.

- **Polymers and organic molecules:** Polymers and organic molecules offer promising potential to overcome certain challenges of Moore's Law, thanks to their versatility and unique electronic properties. They offer a simpler and less expensive alternative to traditional methods such as photolithography and are easy to meld into complex shapes ideal for small and intricate devices.[37] Some of these materials possess high electron mobility, allowing their use in devices such as organic field-effect transistors (OFETs), applicable in displays and sensors.[38–40] Combined with conductive materials such as metals or carbon nanotubes, they allow the creation of flexible and stretchable devices, useful in sectors such as robotics and wearable technology.

Although they still face challenges such as improving stability, polymers offer a cost-effective and adaptable way to advance the miniaturization and functionality of electronic devices, helping to mitigate the limitations of Moore's Law.

1.2 Organic semiconductors

Organic semiconductors stand out over inorganic semiconductors due to their flexibility, environmental friendliness, ease of large-scale production, and ability to be processed at low temperatures using simple methods such as inkjet or laser printing.[41] The weak intermolecular bonds in organic semiconductors (Van der Waals and electrostatic interactions), in contrast to inorganic semiconductors (Se, Ge) which are characterized by covalent bonds,[42–45] allow their processing at room temperature and ambient pressure, unlike inorganic semiconductors that require extreme conditions such as high temperature and vacuum. On the other hand, these types of materials can be integrated into unconventional substrates such as glass, polymers, fabrics and paper, expanding their potential applications.[46–48] Due to their ability to be produced on a large scale with flexible chemical methods, they are more environmentally friendly and compatible with design innovations. This combination of properties and ease of manufacturing positions organic semiconductors as a promising alternative to traditional inorganic semiconductors, opening new opportunities in the electronics industry.

Organic semiconductors are characterized by being based on structures formed by carbon atoms, an element belonging to group IV of the periodic table, whose electronic configuration ends in s^2p^2. The most relevant property of these materials lies in the electronic delocalization along a π-conjugated structure, where each carbon atom presents sp^2 hybridization. The three sp^2 orbitals of each atom are arranged in the same plane, while one p_z orbital remains perpendicular to these planes. The overlap of the p_z orbitals by π bonds generates the formation of π molecular orbitals. This phenomenon is illustrated in Figure 1.3a, using the benzene molecule (C_6H_6) as an example. The main structure of this conjugated skeleton is composed of σ bonds (bonding and antibonding) between carbon atoms, originating from the overlap of the sp^2 orbitals, and π bonds (bonding and antibonding) resulting from the overlap of the p_z orbitals. Because π bonds are notably weaker than σ bonds and are delocalized, facilitate charge mobility.[49] As seen in Figure 1.3b for the case of benzene, the bonding π orbitals constitute the highest energy occupied molecular orbital (HOMO), while the antibonding π* orbitals form the lowest energy unoccupied molecular orbital (LUMO). The energy difference between these two orbitals is called the HOMO-LUMO gap.

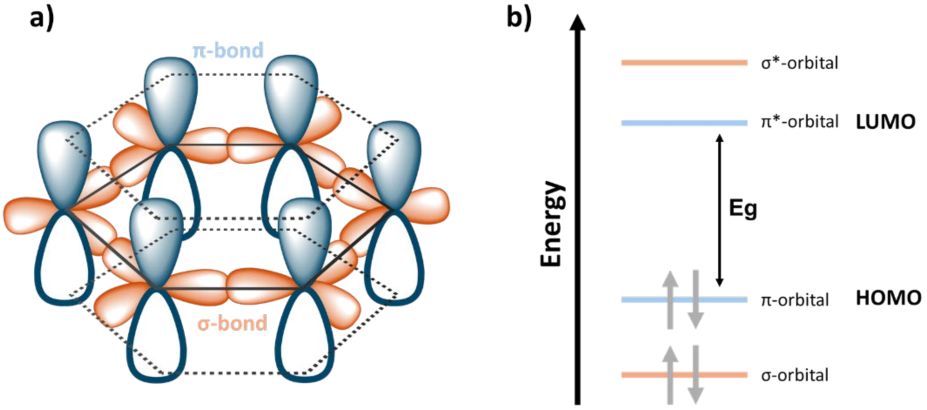

Figure 1.3 Note that sp^2 orbitals lie on the same plane and form σ-bonds while p_z orbitals are orthogonal to the plane and form π-bonds. a) Formation of σ and π-bonds in benzene. b) Energy level diagrams of molecular orbitals in benzene.

In linear π-conjugated systems, the value of the gap depends on several structural factors, such as chain length and degree of planarity.[50,51] In addition, there are multiple synthetic strategies to modulate or optimize the HOMO-LUMO gap. Among the most common are the incorporation of aromatic rings and functionalization with groups that act as electron donors and/or acceptors. One of the key properties of organic semiconductors is charge transport, which is directly linked to electron or hole mobility, one of the most relevant parameters in OFETs. The modulation of the gap energy in these materials to achieve high charge mobilities is the basis of numerous research studies.[52,53]

Throughout this Doctoral Thesis, continuous reference will be made to π-electronic conjugation, the HOMO and LUMO orbitals, as well as the HOMO-LUMO gap (Eg) that separates them, since these parameters are fundamental for the analysis of the electronic properties of the materials studied in this Thesis.

1.3 Applications of organic semiconductors: organic field-effect transistors

Organic semiconductors play a key role in various applications of organic electronics, such as lasers, molecular wires, and chemical and biological sensors, among others.[54,55] In addition, they are used as active components in a variety of electronic devices, such as solar cells (OPVs),[56–58] organic light-emitting diodes (OLEDs),[59–62] and organic-based field-effect transistors (OFETs)[63–65]. This PhD Thesis focuses on the analysis of organic semiconductor materials applied to OFETs.

A field-effect transistor (FET) is a device in which an electric field induces a net spatial charge in the semiconductor. This charge is polarized by applying a potential difference between the electrodes. FETs are essential elements in electronic circuits, where they perform functions such as switches or signal amplifiers, among others.[66,67] In the specific case of OFETs, the active layer is composed of organic materials, either polymers or conjugated molecules.[68–70]

Although the first transistors based on organic materials were described in 1970,[71] the development of OFETs took off in 1986 with the fabrication of the first device of this type, based on electrochemically polymerized polythiophene.[72] Three years later, in 1989, the first OFET based on a conjugated molecule, sexithiophene, was developed. Today, OFETs are capable of greatly exceeding charge mobilities higher than the mobility of amorphous silicon (0.1–1 $cm^2/V\,s$)[73]. Among the advantages of these devices compared to inorganic FETs are those of organic semiconductors: they can be deposited at low temperatures, which makes them compatible with flexible and deformable plastic substrates, and they are suitable for large-scale production processes, such as printing, reducing costs.[74]

In the latest generation of optoelectronic devices, charge transport efficiency within the organic layer is crucial. For example, in solar cells, charges generated by photoexcitation of the active material must efficiently travel to the metal contacts to be harvested as electrical energy. In light-emitting diodes, it is important that holes and electrons injected from the electrodes exhibit balanced and efficient transport characteristics, favouring volumetric recombination rather than recombination quenching near a metal interface. Another key challenge is the design of materials that exhibit high charge transport properties for both holes and electrons in field-effect architectures, in order to facilitate the development of complex organic circuits.

1.3.1 Components and configurations of an OFET

As mentioned above, an OFET is a three-terminal device in which a voltage applied to the gate electrode controls the current flow between the source and drain electrodes by an imposed voltage. The basic schematic of an OFET is presented in Figure 1.4.

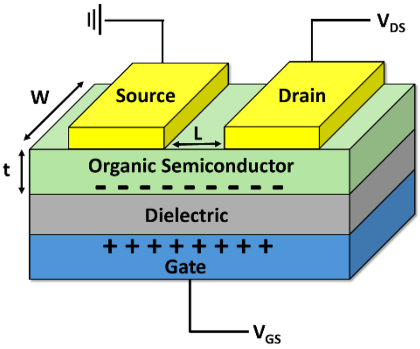

Figure 1.4 Illustration of top contact–bottom gate organic field effect transistor. L is the channel length; W is the channel width and t is the thickness of the semiconductor layer.

An organic-based field-effect transistor is composed of three main elements:[75]

- **Contacts:** also known as gate, source and drain electrodes. Typically, the source and drain electrodes are made of gold, while the gate electrode is made of doped silicon.

- **Dielectric material layer:** this is usually a metal oxide, with silicon dioxide (SiO_2) being the most used material. Polymers are also a potential alternative due to their intrinsic insulating properties and are widely used as dielectrics.

- **Thin film of organic semiconductor:** this material connects the source and drain electrodes, forming the channel through which the current flows. If the device transports holes, it is classified as p-type; if it transports electrons, it is n-type. Semiconductors capable of transporting both holes and electrons are called ambipolar.

Depending on the different situations of these layers, OFETs can be categorized in four device architectures: bottom contact-bottom gate (BC-BG, Figure 1.5a), top contact -bottom gate (TC-BG, Figure 1.5b), bottom contact -top gate (BC-TG, Figure 1.5c), and top contact-top gate (TC-TG, Figure 1.5d). Each of these architectures shows different advantages and disadvantages, making the choice of design dependent on the specific application requirements.[76,77]

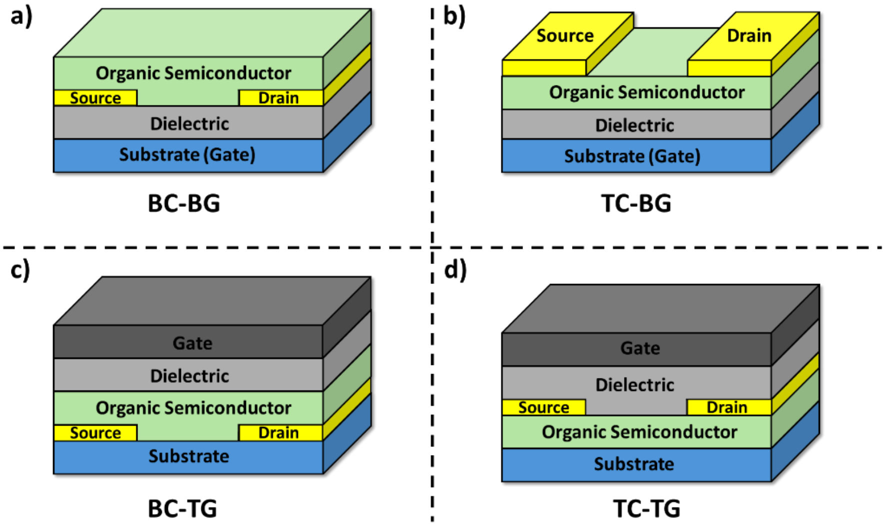

Figure 1.5 Representation of the four OFET configurations: (a) bottom contact–bottom gate (BC-BG), (b) top contact–bottom gate (TC-BG), (c) bottom contact–top gate (BC-TG) and (d) top contact–top gate (TC-TG).

BC-BG and TC-BG devices allow for rapid testing of new semiconductors because the insulating layer and terminal electrodes can be prefabricated. However, these configurations leave the semiconductor partially or fully exposed to environmental conditions that favour accelerated degradation. In contrast, BC-TG and TC-TG architectures mitigate the environmental degradation of the semiconductor by using the dielectric layer as a barrier. However, these designs require careful selection and deposition of the dielectric to maintain the integrity of the semiconductor layer. Among these configurations, the TC mode is often better for obtaining high-quality semiconducting layers, as the prefabricated electrodes in the BC configuration can serve as nucleation sites, negatively impacting the contact quality between the semiconductor and the source and drain electrodes.[78] Considering these factors, in all devices of this thesis we use a TC-BG configuration.

1.3.2 OFET operation

As shown in Figure 1.4, to understand the operation of an OFET, it is essential to define several parameters. We designate V_{GS} as the voltage applied between the gate electrode and the source electrode, and V_{DS} as the voltage applied between the source and drain electrodes.

To explain the field effect, we will take as a reference the diagram illustrated in Figure 1.6.[79] This diagram describes how the field effect induces charges in the semiconductor layer, based on the energy levels of the HOMO and LUMO orbitals of the organic material in relation to the Fermi level of the source and drain electrodes.

When the voltage applied between the gate electrode and the source electrode is zero (V_{GS} =0), the current flowing between the source and drain electrodes is practically zero, indicating that the transistor is in the off state (Figure 1.6a). When a positive voltage is applied (V_{GS}>0), the transistor is activated, generating a shift towards lower energy levels in the HOMO and LUMO orbitals. If the voltage is high enough, the LUMO reaches resonance with the Fermi levels of the electrodes, thus allowing the injection of electrons from the electrodes to the LUMO (Figure 1.6b). When a voltage is also applied between the source and drain electrodes (V_{DS}>0), a current flow is established between them, characterizing the semiconductor as n-type (Figure 1.6d). In contrast, if V_{GS}<0, the HOMO and LUMO orbitals shift to higher energy levels, becoming destabilized (Figure 1.6c). In this case, if the HOMO of the semiconductor meets the Fermi level of the electrodes, the injection of charges from the electrodes to the HOMO is made possible. By applying a negative voltage (V_{DS}<0), a flow of charges is generated between the source and drain electrodes, which defines the material as a p-type semiconductor (Figure 1.6e).

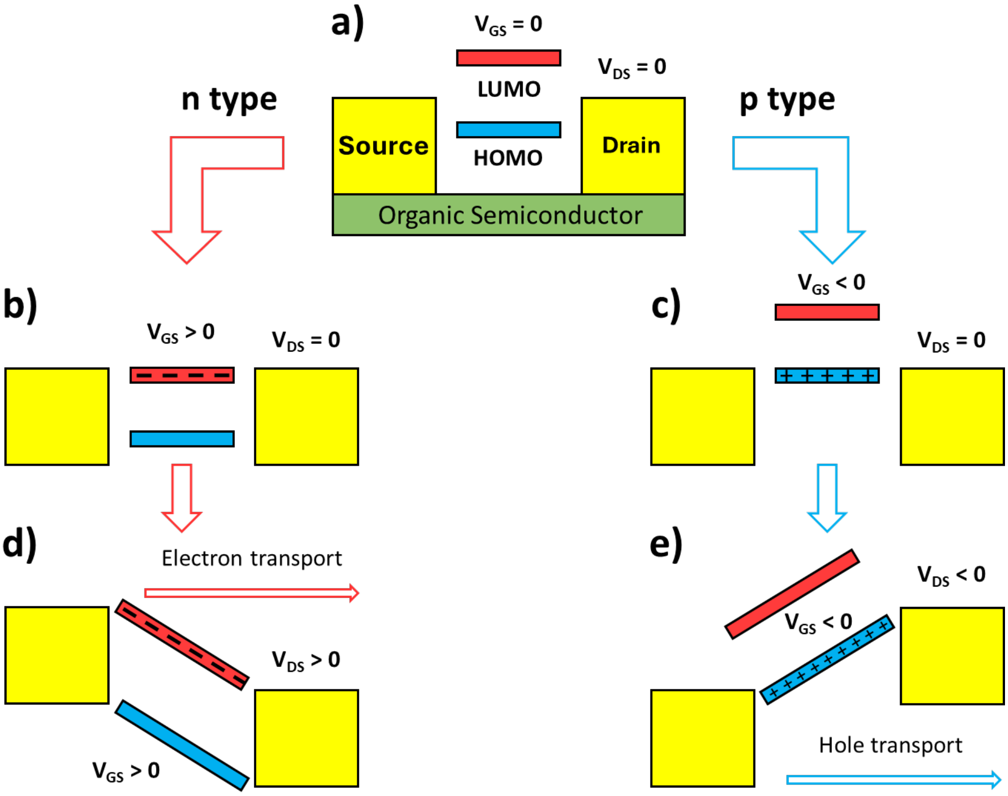

Figure 1.6 (a) Idealized diagram of the energy levels of an OFET with respect to the Fermi levels of the source and drain electrodes for V_{GS}=0 and V_{DS}=0. (b-e) Schematic representation of the field effect, (b) and (d) electron accumulation and transport, (c) and (e) hole accumulation and transport.

The diagram in Figure 1.6 presents an idealized version of the field effect. However, it is important to consider several factors, such as mismatches between the Fermi level and the HOMO or LUMO orbitals, impurities or charge trapping, which cause mobile charges not to be introduced into the semiconductor exactly at $V_{GS} = 0$. Therefore, a threshold voltage (V_T) is defined, which corresponds to the minimum voltage value necessary to induce mobile charges in the semiconductor. The induced charge density (q_{ind}) (C/cm^2) in the channel for a position x is expressed as:

$$q_{ind}(x) = n(x) \cdot e \cdot t \qquad [1.1]$$

$$n(x) \cdot e \cdot t = C_{ox}\big(V_{GS} - V_T - V(x)\big) \qquad [1.2]$$

where C_{ox} is the capacitance of the dielectric per unit area ($nFcm^2$), n(x) is the charge density in the channel, e is the fundamental unit of charge and t is the thickness of the semiconductor film.

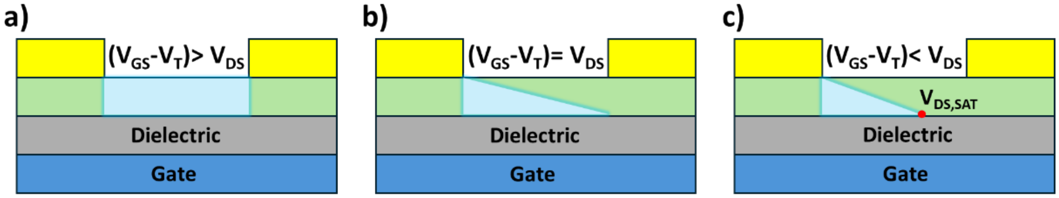

Figure 1.7 Schematic representation of the charge density distribution during the operation of an OFET: (a) in linear regime, (b) for $V_{GS}-V_T = V_{DS}$, (c) in saturation regime $V_{GS}-V_T < V_{DS}$.

In the case of n-type conduction, the application of a positive voltage at the gate electrode ($V_{GS}>0$) generates positive charges at the gate/dielectric interface and an equivalent number of negative charges at the semiconductor/dielectric interface. If no voltage is applied between the source and drain electrodes ($V_{DS}=0$), the induced charge density remains uniform along the entire channel. Assuming in an idealized way that V_T is not a function of x, and when $V_{DS}=0$, also $V(x)=0$ (see Figure 1.7a). However, if V_{DS} takes a value different than zero but smaller than V_{GS}, a linear gradient in the charge concentration is generated along the channel. Under these conditions, for a small value of V_{DS}, the average value of q_{ind} is:

$$q_{ind} = C_{ox}(V_{GS} - V_T - \frac{V_{DS}}{2}) \qquad [1.3]$$

On the left side of the channel, the charge density will be higher, while on the right side it will be lower (Figure 1.7b). As an approximation, it can be considered that:

$$V(x) = \frac{V_{DS}}{2} \qquad [1.4]$$

By applying Ohm's Law, it is possible to establish a simplified relationship between current and voltage in an OFET:[80]

$$\frac{I_{DS}}{t \cdot W} = \sigma \frac{V_{DS}}{L} \rightarrow I_{DS} = \frac{W}{L}(n_{x,av} \cdot e \cdot t)\mu \cdot V_D \qquad [1.5]$$

Here, I_D represents the current flowing between the source and the drain, while t, W, and L correspond to the thickness, width, and length of the channel, respectively. Furthermore, σ denotes the conductivity ($\sigma = n_{x,av} \cdot e \cdot \mu$), μ the mobility of the charges, and $n_{x,av}$ the average concentration of charges in the channel.

Substituting equation [1.2] in [1.5] and rearranging terms, we obtain:

$$I_{DS} = \frac{W}{L} C_{ox} \cdot \mu[(V_{GS} - V_T) \cdot V_{DS} - \frac{V_{DS}^2}{2}] \qquad [1.6]$$

This equation describes the transport of charges in a linear regime, case of Figure 1.7b, when $V_{DS} < V_{GS}$-V_T.

As V_{DS} increases, a point is reached where V_{DS}=V_{GS}−V_T. At this instant, there is no potential difference between the gate electrode and the channel region close to the drain electrode, which generates an area devoid of charge carriers (Figure 1.7b). If V_{DS} continues to increase, this effect is intensified (Figure 1.7c), but no further increase in current is achieved. In this state, the transistor enters in the saturation regime. By substituting V_{DS}=V_{GS}−V_T in equation [1.5], the relationship I−V that characterizes the behaviour of the transistor in the saturation regime, described by equation [1.6], is obtained.

$$I_{DS,saturation} = \frac{W}{2L} C_{ox} \cdot \mu_{sat} (V_{GS} - V_T)^2$$

$$|V_{DS}| > |V_{GS} - V_T| > 0 \qquad [1.7]$$

1.3.3 OFET characterization

OFETs are characterized by two types of representations, see Figure 1.8:

- **Output curves:** In this case, the current I_{DS} is measured by keeping V_{GS} constant while performing an incremental sweep of V_{DS}. These curves allow to identify the two main regimes of an OFET: the linear regime, where the current follows a parabolic trajectory, and the saturation regime,[81,82] in which the current between the source and the drain is independent of V_{DS} (Figure 1.8a).

- **Transfer curves:** Here, the current I_{DS} is measured by keeping V_{DS} constant while varying V_{GS} (Figure 1.8b).

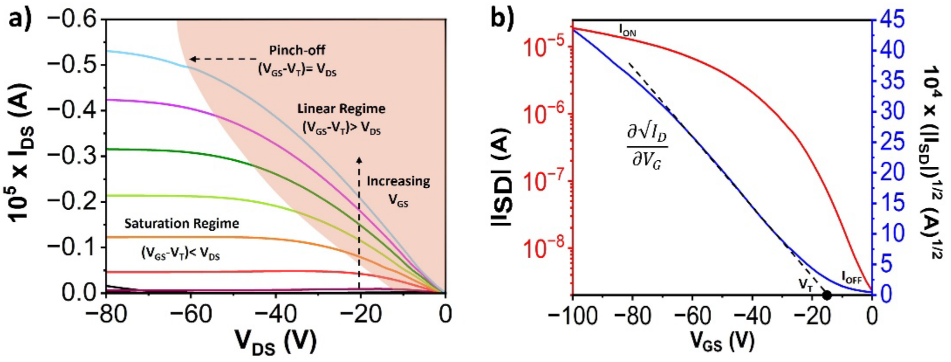

Figure 1.8 Representative a) output and b) transfer plots of a p-type OFET.

Using the saturation transfer curves ($V_{DS} \gg V_{GS} - V_T$) and applying the previously mentioned equation [1.6], it is possible to determine the characteristic parameters of an OFET in a simple way (Figure 1.8b):

- **Mobility (μ):** It represents the speed of the charge carriers per unit of electric field ($cm^2V^{-1}s^{-1}$). It is calculated from the slope of the linear section in the graph of $I_{DS}^{1/2}$ versus V_{GS}.

- **On/off current ratio (Ion/Ioff):** It is the ratio between the current in the on and off states of the transistor.

- **Threshold voltage (V_T):** It is the minimum potential necessary to induce mobile charges at the dielectric/semiconductor interface. It is determined from the intersection of the linear interpolation of the square root of the intensity obtained in the transfer curve with the abscissa axis.

1.4 Understanding charge transport in organic semiconductor materials

Unlike inorganic semiconductors, whose atoms are covalently bonded to form a highly crystalline three-dimensional solid with a strong overlap of atomic orbitals that facilitates charge transport through delocalized bands, order in molecular solids depends on non-covalent intermolecular interactions.[83,84] Due to the weakness of these interactions, the solid structure of an organic semiconductor can vary depending on the distances and orientations between molecules (positional disorder), generating a diverse molecular environment that gives rise to different energy levels.[85,86] It is possible to clearly distinguish between disordered organic semiconductors, such as amorphous polymers, and organic semiconductors with highly ordered or crystalline structures.[87] Charge transport in disordered semiconductors is mainly described by a hopping mechanism, which occurs by thermal activation through a distribution of localized states (Figure 1.9).[88,89] This mechanism, proposed by Marcus[90] for chemical reactions and biological electron transfer processes, requires that for a charge to jump between neighbouring molecules, the molecular configuration of the initial site (occupied) and the final molecular configuration site (empty) must be distorted towards a common configuration, which is made possible by thermal activation.

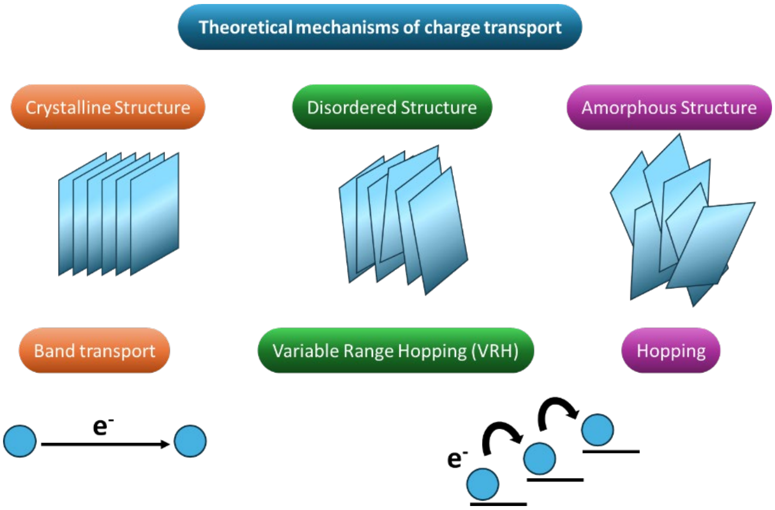

Figure 1.9 Theoretical methods proposed for explaining charge transport in materials with different supramolecular agreements.

However, in experimental charge transport processes, these mechanisms can be influenced by other factors. Vissenberg and Matters[91] developed a model to analyze the dependence of temperature and voltage applied to the gate electrode in organic semiconductors, especially in amorphous polymers. This model introduces the concept of variable hopping range (VRH), where a charge carrier can perform a short hop with a high activation energy or a long hop with a low activation energy. In this system, the temperature dependence of charge transport is closely related to the density of localized states. In an organic field-effect transistor (OFET), the voltage applied to the gate electrode causes the accumulation of charges at the semiconductor/dielectric interface, filling the lower energy states of the organic semiconductor. As a result, additional charges will occupy higher energy states, which reduces the energy required to jump between neighbouring molecules. This means that an increase in the gate voltage increases mobility. Also, since this mechanism is thermally activated, an increase in temperature also increases mobility. On the other hand, for ordered molecules, experimental data show that mobility increases as the temperature decreases, suggesting a delocalized state band mechanism rather than a hopping mechanism, similar to that of inorganic semiconductors.

In organic semiconductor materials we have two types of charge carriers: i) negatively charged particles or electrons, that are generated and transported through the LUMO energy levels of the semiconductor. ii) positively charged effective particles or holes, that are interpreted as electron vacancies in the HOMO energy levels. These holes are generated by the excitation of an electron or by electron transfer processes with an electrode.[92,93] Depending on the predominant type of charge carrier, semiconductors are classified as: p-type, when the charge comes as holes or n-type, when the transport is dominated by electrons. Additionally, there are ambipolar semiconductors, which have the ability to transport both electrons and holes thanks to the capability of simultaneous injection of both types of charge from the electrodes,[94,95] see Figure 1.10.

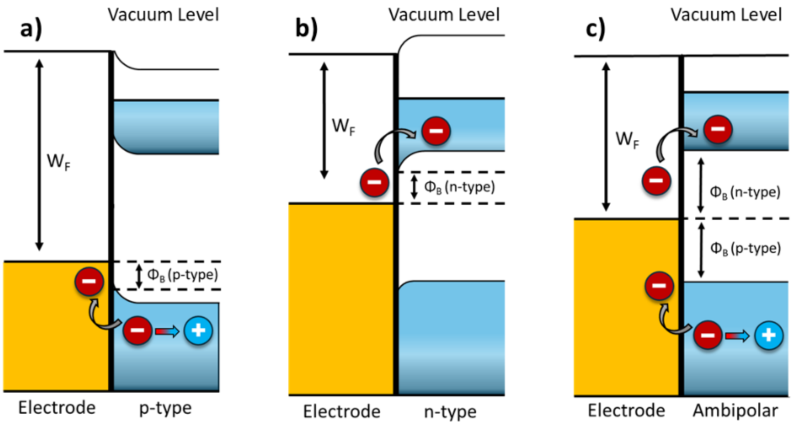

Figure 1.10 Scheme of (a) holes and (b) electrons injection into the HOMO and LUMO orbitals of p-type and n-type semiconductors, respectively. (c) Electrodes with work function (WF) in between the HOMO and LUMO levels can facilitate ambipolar transport. The ϕ_B denotes the difference between WF and the corresponding semiconductor energy.

On the other hand, the interface between the organic layer and the electrodes is key to the charge injection process, while the interface between the organic layer and the dielectric directly affects charge transport and device stability. To improve charge injection, various strategies have been developed, one of the most common being the introduction of an intermediate layer between the source or drain electrode and the organic layer. This intermediate layer reduces the energy barrier and prevents the penetration of metal atoms into the organic layer. On the other hand, the interface between the organic layer and the dielectric controls charges transport and device stability in three main ways:[96,97]

- **Trap density:** the trap density on the dielectric surface considerably impacts performance, especially in n-type OFETs.

- **Morphology:** the dielectric layer influences the morphology of the organic semiconductor, which affects both device performance and stability.

- **Crystalline grain aggregation:** This interface also influences crystalline grain aggregation, where highly ordered and continuous thin films with lamellar packing are essential to achieve high mobility and stability.

Efficient molecular packing improves orbital overlap between adjacent molecules, which facilitates charge transfer. Optimizing both the electrode/organic semiconductor and dielectric/organic semiconductor interfaces is an effective strategy to obtain high-performance devices.

1.5 Characteristics of molecular materials influencing charge transport

The charge transport mechanism in OFETs is complex and not fully understood, so continued efforts are needed to develop design rules for new materials to elucidate the mechanisms involved in the device's operation.

From a molecular perspective, a π-conjugated system is composed of four main structural elements: the conjugated backbone, heteroatoms, substituents (electron-donating or electron-withdrawing groups or atoms), and side chains (such as solubilizing groups)[98]. Of these components, the conjugated backbone is the predominant factor determining most of the material's optoelectronic properties. In addition, this backbone significantly influences molecular packing.

However, heteroatoms, substituents, and side chains also play a crucial role in the optoelectronic properties of conjugated systems, especially in the solid state where morphological features such as aggregation and molecular packing are strongly influenced by the choice of these structural elements. The impact of these features on charge transport properties will be discussed in detail in the following sections.

1.5.1 π-conjugation extension

As mentioned above, the π orbitals are energetically accessible for charge transport. This allows the charge, once it enters the conjugated molecule, to be rapidly delocalized along the conjugated π system. To achieve efficient charge injection in p-type materials from metallic electrodes, such as gold, towards the HOMO, it is necessary that the ionization potential is around 5 eV.[99,100] On the other hand, in n-type materials, the electron affinity must be high enough to guarantee an efficient injection of electrons towards the LUMO of the semiconductor. This value should not exceed 3 eV,[101] since a lower electron affinity can compromise the environmental stability of the material.

A key strategy to increase charge mobility is to extend the molecular skeleton. This extension increases π-conjugation, which favours charge transport. In this context, naphthalene-based compounds are a point of reference among π-conjugated semiconductors.[102–104] However, when focusing on semiconductors formed by fused rings, linear acenes become the protagonists,[105–107] see Figure 1.11. These systems are composed of aromatic hydrocarbons with fused benzene rings in a ladder-like fashion. Thanks to their high aromaticity, acenes have been widely used in the design of organic semiconductors with improved charge transport properties.

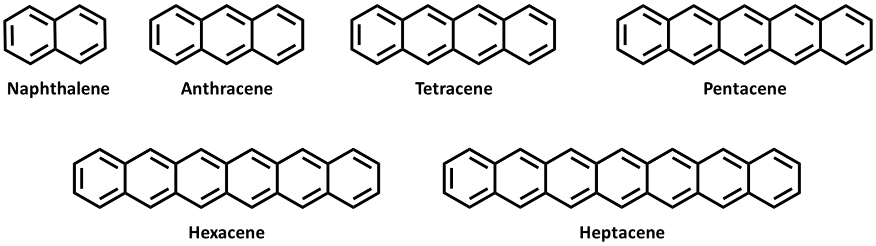

Figure 1.11 Chemical structures of some representative acenes.

Theoretical studies have shown that charge mobility in these systems increases with increasing number of benzene rings, due to lower reorganization energy, which indicate the structural changes of the molecules needed to accommodate a positive or negative charge, and higher charge transfer integrals, which shows the efficiency of the frontier molecular orbital coupling between neighbouring pairs of molecules. On the other hand, in practical applications, the length of the acene core limits chemical stability. Among the existing acenes, pentacene has received considerable attention as an active semiconductor for use in organic field-effect transistors due to its high charge carrier mobility.[108] However, poor environmental stability is one of the problems limiting its practical application. The longer acenes are difficult to characterize due to their chemical instability and lower solubility.[109,110]

1.5.2 Substitution with heteroatoms

The incorporation of heteroatoms represents an effective strategy to tune the electronic properties, solubility, and molecular packing of materials.[111] Replacing benzene rings with aromatic thiophene rings, for example, decreases HOMO levels and widens the HOMO-LUMO energy range. Furthermore, conjugated systems containing sulfur atoms have been shown to be robust and stable under ambient conditions.[112–114] This type of materials also exhibits a remarkable ability to enhance intermolecular π-π overlap in the solid state, thanks to the multiple S···S contacts between adjacent molecules.[115,116]

In this context, Takimiya and his team demonstrated that incorporating fused thiophenes into oligoacene frameworks is an efficient strategy to develop promising new organic semiconductors.[117] A prominent example is the C8-BTBT-C8 compound (Figure1.12), which exhibits charge mobility higher than that of pentacene, reaching over 31 $cm^2V^{-1}s^{-1}$ in single-crystal thin films. Furthermore, this material offers significant advantages such as improved solution processability and higher stability against oxidation, retaining its electrical properties for over 200 days without significant changes in the devices. From a supramolecular perspective, the excellent electrical properties of C8-BTBT-C8-based OFET devices are attributed to the formation of two-dimensional semiconductor channels with strong intermolecular overlap.[118] Therefore, C8-BTBT-C8 has become a reference model for the design of new organic semiconductors.[119–122]

Depending on the type of heteroatom used, it is possible to obtain materials with n-type (electrons), p-type (holes), or ambipolar charge transport. For example, substitution of sp_2 carbon atoms by N in the conjugated backbone of TIPS-pentacene (see TIPS-TAP in

Figure 1.12) leads to charge transport properties with p-type mobilities of 13 $cm^2V^{-1}s^{-1}$ for semicrystalline thin films.[123–126]

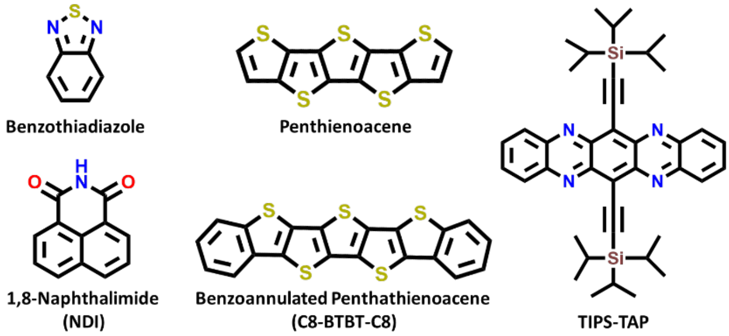

Figure 1.12 Representative heteroatom substituted compounds in organic semiconductors.

1.5.3 Substitution with donor or acceptor groups

Electron-withdrawing groups, such as F, Cl, Br, and CN, can decrease the electron density of a π-conjugated system through resonance and inductive effects. Incorporation of these groups into the conjugated backbone often confers increased molecular stability against oxidation,[127–130] resulting in ambipolar or electron charge transport behaviour. Energetically, replacing the π-conjugated system with electron-withdrawing groups is an effective strategy to reduce the LUMO energy.[131,132] In contrast, electron-rich groups, such as alkoxy or alkyl thioethers, increase the HOMO energy, with a minor impact on the LUMO, thereby reducing semiconductor stability in the presence of air.[133,134]

A notable example of this effect is the substitution of dicarboximide acceptor groups at the peri positions of a naphthalene molecule. This generates an extended oligoarylene system known as naphthalene diimide (NDI), which exhibits good electron mobilities.[135–137] Furthermore, additional functionalization on the nitrogen atoms of the imide groups and on the naphthalene core with acceptor units, such as cyano or nitro, shifts the electron density away from the π system by mesomeric effects.[138,139] This shift reduces the energy of the LUMO and facilitates electron injection. Another approach to making a conjugated system more electron-deficient is to introduce groups with inductive electron-withdrawing effects, such as halides. This substitution directly affects the polarization of the σ orbitals, decreasing the electron density on the atoms of the π system and stabilizing both the HOMO and the LUMO orbitals.[140]

The concept of donor-acceptor (D-A) systems was introduced by Wynberg in 1992 as an efficient approach to design polymers composed of alternating electron-rich (donor) and electron-deficient (acceptor) groups.[141] In these compounds, the HOMO is mainly associated with the donor moiety, while the LUMO is mostly located in the acceptor group. This design allows modulating the HOMO-LUMO gap by adjusting the choice of donor and acceptor blocks, as well as by appropriate functionalization of the conjugated main chain, including the insertion of peripheral substituents.

1.5.4 Molecular packing

Effective overlap between the molecular orbitals of adjacent molecules is a fundamental requirement for efficient charge transport in a semiconductor. This phenomenon depends largely on the degree of molecular order in the material. Depending on the molecular order in the solid state, three types of packing can be identified: crystalline, polycrystalline and amorphous.[142]

In crystalline solids, molecules are arranged in an orderly fashion in a periodic network, influenced by intermolecular interactions such as hydrogen bonds or Van der Waals forces. Due to these interactions, different molecular environments can coexist, forming polycrystalline solids with multiple differently oriented crystalline domains. Although within each crystalline domain the molecules maintain an order, the overall periodicity breaks down at the limit between domains, known as grain boundaries. In contrast, when molecules are randomly distributed without any periodic pattern, the solid is considered amorphous.[143–145]

The degree of molecular order decisively influences the macroscopic properties of the material. Structural defects and grain boundaries in amorphous and polycrystalline structures often complicate charge transport, making dense and ordered molecular packing with minimal defects desirable.[146] For example, in pentacene films, charge carrier mobilities vary significantly depending on the molecular order, from values in the range of 10^{-5} $cm^2V^{-1}s^{-1}$ in amorphous solids, to $10^{-3}cm^2V^{-1}s^{-1}$ in polycrystalline solids, with these values being greatly exceeded in crystalline solids, where they can reach around 30 $cm^2V^{-1}s^{-1}$.[147]

Molecular packing in organic semiconductor thin films also plays a crucial role in the operation of OFETs. Factors such as reorganization energy and charge transfer integrals, which depend on molecular packing, are determinants for good charge transport between molecules. Dense molecular packing facilitates this transport. There are four main types of crystalline molecular packing:[148] (i) Herringbone packing with no π-π overlap between adjacent molecules (Figure 1.13a). (ii) Herringbone packing with π-π overlap between adjacent molecules (Figure 1.13b). (iii) Lamellar packing with one-dimensional π stacking (Figure 1.13c). (iv) Lamellar packing with two-dimensional (2D) π stacking (Figure 1.13d). This last type of packing, 2D π stacking, is the most efficient for charge transport, as it maximizes charge transfer integrals by allowing charge carriers to travel along a nearly straight path.[149]

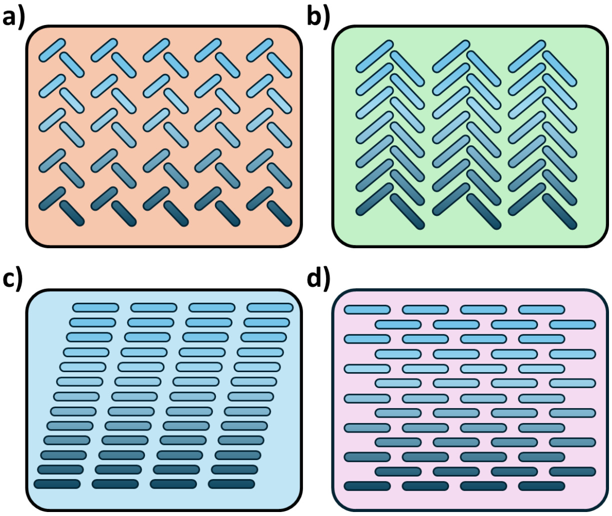

Figure 1.13 Most important crystalline molecular packing in organic semiconductors: a) herringbone packing without π-π overlap, b) herringbone packing with π–π overlap, c) 1D π-stacking, d) 2D π-stacking.

1.5.5 Incorporation of solubilizing functional groups

To ensure good solubility of the material and thus improve the processability of organic semiconductors in solution, solubilizing side substituents, such as alkyl chains, are introduced into the π-conjugated backbone. These groups are considered insulating materials and do not contribute to charge transport directly. However, over the years it has been shown that these alkyl side chains have a substantial impact on charge transport properties due to their influence on molecular packing and thin film morphology in the solid state.[150–152] A clear example of this is the case of acenes, in which alkyl chains have been introduced into the molecular structure to improve oxidative stability and prevent dimerization of the molecules. These substitutions also changed the herringbone packing to face-to-face π stacking by decreasing the C-H····π interactions.[153,154] On the other hand, it is known that the size of the alkyl chains also plays a significant role in the formation of 2D and 3D polycrystalline solids, which directly affects the charge mobility.[155–157]

In this regard, the search for solution-processable pentacene derivatives has led to the discovery of various materials. For example, the introduction of TIPS groups into pentacene has led to materials such as TIPS-pentacene[158–160] (see Figure 1.14), in which solution deposition yielded devices with good hole mobilities,[161–163] suggesting that the material can form highly crystalline films, with the side chains giving rise to soluble materials without disturbing the conjugated system. Even more remarkable is the case of rubrene in which arylation at tetracene peri-positions resulted in single-crystal-based OFETs with mobilities around 15 cm^{2}V^{-1}s^{-1}.[164,165] However, in many cases low mobility thin film OFETs were reported as a consequence of poor film quality, which was attributed to inefficient molecular packing caused by distortion of phenylene units.[166,167] Therefore, based on the above considerations, it is of crucial importance that the incorporation of side groups helps to solubilize the conjugated material without disturbing the molecular planarity and hence the delocalization of the π orbitals.

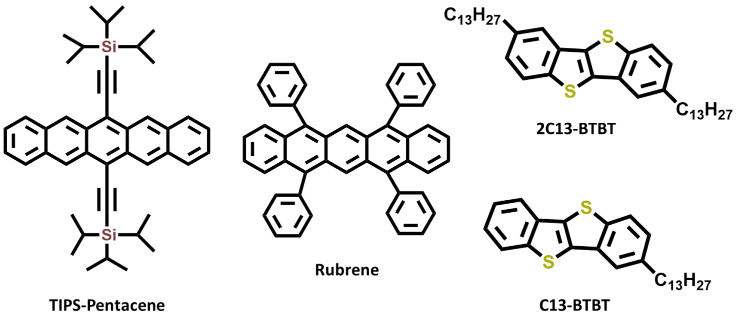

Figure 1.14 Chemical structure of some representative molecules which incorporate solubilizing groups.

1.6 Organic materials in the development of OFETs

The challenge to replace traditional inorganic semiconductors has resulted in the exploration of new materials, such as organic semiconductors, with the objective of enhancing mobility in these materials in comparison to conventional inorganic semiconductors. Following the initial reports on the subject of organic semiconductor-based transistors in the late 1980s, significant advancements have been made in the development of what has been termed "the perfect system". This has been accompanied by a steady improvement in the performance records of OFET devices on an annual basis (Figure 1.15). Indeed, in the 1980s, the mobility of the first reported organic semiconductor was approximately 10^{-5} $cm^2V^{-1}s^{-1}$. By contrast, in 2020, the values of single-crystal small molecules increased to 48 and 28 $cm^2V^{-1}s^{-1}$ for hole and electron transport, respectively.[168,169]

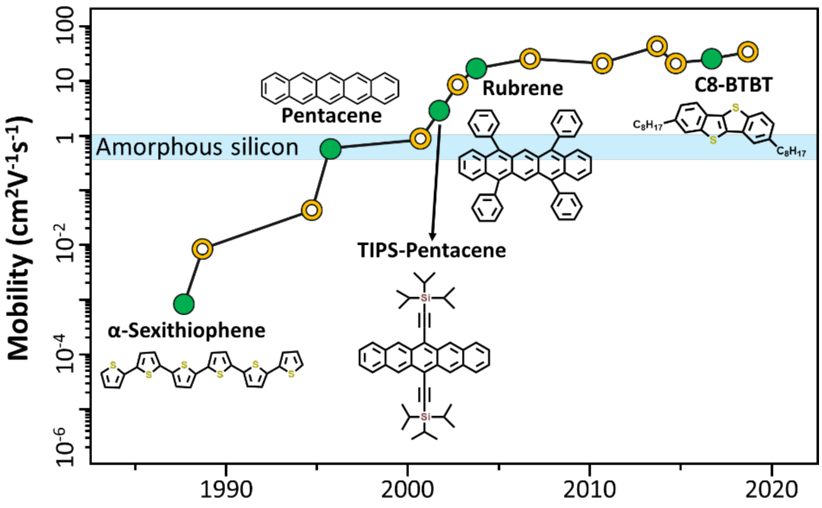

Figure 1.15 Charge carrier mobilities of organic semiconductors reported in the last few decades.

In organic electronics, one of the most widely used materials is ladder-type heteroarenes.[170,171] These molecules, composed of aromatic rings fused by sharing two or more adjacent atoms, represent a prominent class of high-performance small molecule semiconductors and building blocks for the fabrication of polymeric semiconductors.

Key advantages offered by the fusion of heteroaromatic rings into ladder-type heteroarenes include: i) Extended π-conjugation and increased electron delocalization thanks to their highly planar structures, which reduces HOMO-LUMO energy gaps.[172] ii) Reduced reorganization energies due to the suppression of rotation in the fused aromatic rings, enhancing intramolecular charge transport.[173] iii) More efficient π-stacking between neighbouring molecules, facilitated by the amplified π-conjugation systems, which strengthens intermolecular electron couplings.[174]

Most ladder-type molecules are electron-rich (p-type semiconductors), since the synthesis of electron-deficient n-type semiconductors is more complex due to the high density of π electrons in the aromatic skeleton. However, developing these systems is essential to obtain donor-acceptor semiconductors that support low-energy complementary organic circuits.

Among the most prominent p-type ladder-type organic semiconductors are large acenes, such as rubrene, pentacene, and TIPS-pentacene. However, larger acenes, such as hexacenes and heptacenes, show low environmental stability due to their high HOMO energy levels, limiting their application in electronics. In contrast, [n]-thienoacenes, formed by fused thiophenes, show better environmental stability thanks to the incorporation of heteroatoms in the aromatic rings, which stabilizes the molecular orbitals and improves charge transport.[175–177] However, their hole mobility is lower compared to that of acenes.

The lower availability of n-type semiconductors is mainly due to their limited stability under ambient conditions and the difficulty of synthesizing compounds with low LUMO energy levels. An efficient strategy to overcome this challenge is to replace p-type semiconductors with electron-withdrawing groups, such as F, Cl, Br, and CN. Examples such as perfluorinated pentacene have shown n-type behaviour with electron mobilities up to 0.1 $cm^2V^{-1}s^{-1}$.[178,179] Likewise, the addition of cyano groups to fluorene oligomers has generated n-type semiconductors.[180–183] Despite these advances, chemical modifications in p-type semiconductors to incorporate electron-withdrawing groups remain a challenge due to reduced chemical reactivity and unfavourable steric hindrance.

Among the most promising n-type organic semiconductors are perylene diimide[184,185] and naphthalene diimide derivatives.[186–188] Their electron transport capabilities are due to i) The strong electron withdrawing ability of the imide/amide groups that reduce LUMO levels, facilitating electron injection. ii) The planarity of the core, which improves π-conjugation and intramolecular charge transport. iii) The improved solubility due to alkyl substitutions in N-imide, allowing solution processability and controlled film morphology.

iv) The N-alkyl chains far from the aromatic core, which minimize steric hindrance. v) The ease of synthetic modifications, including the addition of electron-withdrawing groups such as CN and F, which improves electron mobility and environmental stability.[189–191]

On the other hand, the diketopyrrolopyrrole (DPP) unit has proven to be a key building block for developing high-performance functional semiconductors in OFET devices.[192,193] This conjugated and planar bicyclic unit facilitates strong π-π interactions, optimizing device performance. Hole mobilities in p-type DPP polymers can exceed 10 $cm^2V^{-1}s^{-1}$, whereas in n-type polymers they can reach values above 7 $cm^2V^{-1}s^{-1}$.[194] Furthermore, DPP-based ambipolar transistors have recorded hole and electron mobilities more than 3 $cm^2V^{-1}s^{-1}$.[195] Side chain engineering in DPP polymers has proven to be crucial, as they affect solubility and molecular packing. For example, the use of urea groups, which form hydrogen bonds, favours long-range order structures, which has led to higher field-effect mobilities, reaching 13 $cm^2V^{-1}s^{-1}$ compared to 3 $cm^2V^{-1}s^{-1}$ observed in non-urea polymers.[196] Figure 1.16 shows some examples of the molecule's building block described above.

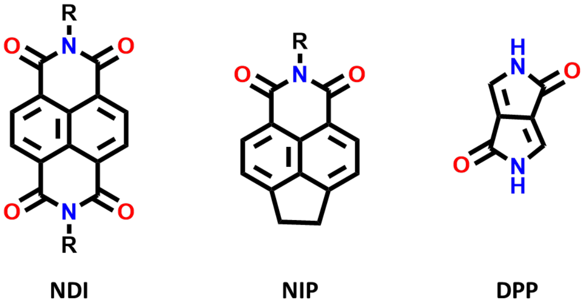

Figure 1.16 Chemical structure of some representative molecule's building block used in organic electronic devices.

1.6.1 Materials under study

In this doctoral thesis, various π-conjugated organic semiconductors are investigated for their application in organic field-effect transistors (OFETs), with the main objective of deepening the understanding of charge transport in organic materials. Charge transport is a complex phenomenon influenced by multiple factors, as previously discussed. This thesis studies several of these factors: (i) The effect of conjugated chain length and heteroatom substitution (Chapter I). (ii) Insertion of electronegative atoms (Chapter II). (iii) Insertion of electrodeficient groups (Chapter III). (iv) Intermolecular interaction and molecular packing (Chapter IV).

Therefore, the design and synthesis of new organic semiconductors in recent decades have been driven not only by the improvement of their optoelectronic characteristics and the introduction of new functionalities, but also by the need to better understand the complex relationships between structure and property.

In this context, the present PhD thesis focuses on a comprehensive physical-chemical analysis of imide-functionalized ladder-type organic semiconductors and diketopyrrolopyrrole-based semiconductors. The aim is, on the one hand, to gain a detailed understanding of the impact of different structural modifications on the intramolecular delocalization of π electrons, and on the other, to examine the implications of these modifications on the supramolecular organization, a key factor for the charge transport properties of the final materials.

To address these objectives, spectroscopic, electrochemical, spectroelectrochemical and quantum-chemical methods have been employed, providing detailed information on the structure and electronic properties. These analyses are essential to understand the electronic and optical characteristics of the conjugated materials, and to rationally guide synthetic efforts aimed at developing compounds with improved properties for application in OFETs.

The materials studied in this Doctoral Thesis have been divided into four chapters, according to the π-conjugated systems under study:

Chapter I: Tuning charge stabilization and transport in naphthalimides-based semiconductors: the role of fused-ring and core modifications.

In this first chapter, we present the design and characterization of a new family of compounds based on the combination of electron-withdrawing naphthalimides units with potent thiophene-derived donor moieties, connected by rigid and conjugated nitrogen connectivity units.[197] Also, we extended the length of the thiophene units and evaluated different isomers. Furthermore, we demonstrated that the implementation of a fused-ring-based strategy in the donor moiety can significantly modify the charge transport properties of organic semiconductors. The group of Prof. José Luis Segura from the Complutense

University of Madrid synthesized these semiconductors, and their chemical structures are depicted in Figure 1.17.

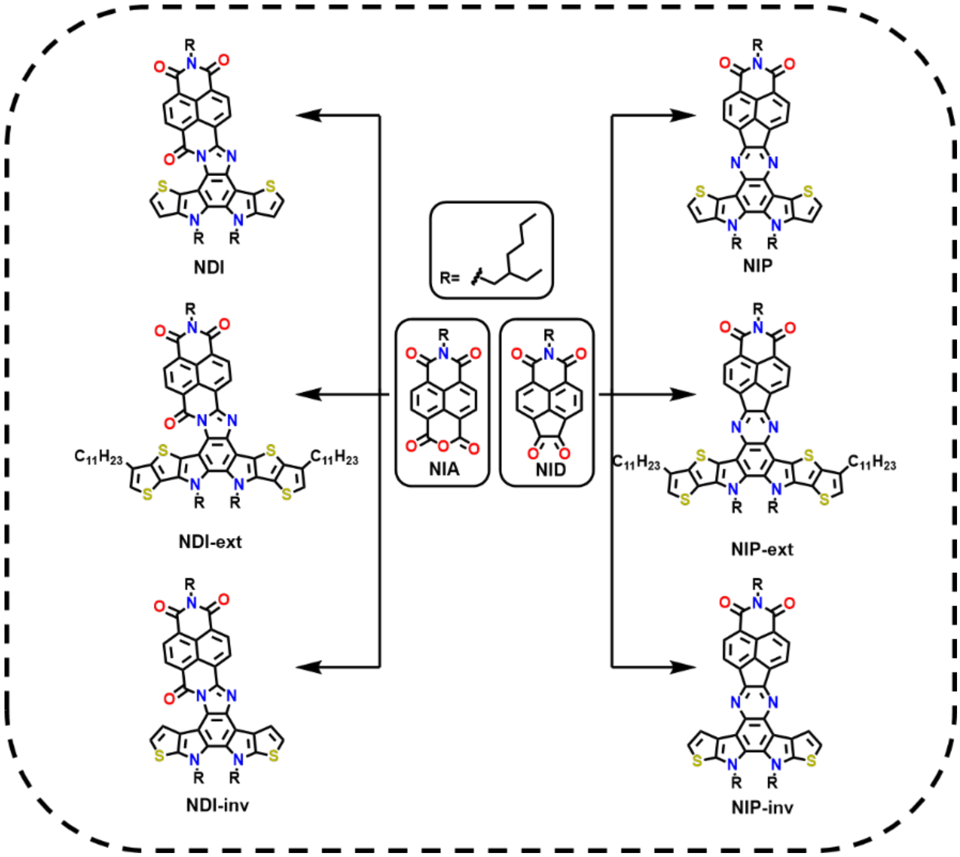

Figure 1.17 Schematic representation of the compounds studied in chapter I, based on naphthalimides as electron-withdrawing units together with donor moieties derived from thiophene, connected by rigid and conjugated nitrogen connectivity units.

Chapter II: Tuning charge stabilization and transport in naphthalimides-based semiconductors: effect of insertion of halogen atoms into the molecular structure.

In this chapter we have studied a series of compounds based on phenylene-naphthalimide assemblies (**NAI-Ph**, **NAI-Ph-F** and **NAI-Ph-Cl**), where both the phenylene units and the electron-withdrawing moieties of the naphthalimide are directly conjugated through rigid inverted amidine (NAI) units. In order to modify the electron-accepting and charge-transport properties of these new systems, different halogen atoms (F and Cl) were incorporated into the phenylene unit (Figure 1.18). The effect of the incorporation of these halogens (F and Cl) into the phenylene unit on the optical, electrochemical and charge-transport properties was studied.[198] These compounds also have been synthesized by the group of Prof. José Luis Segura from the Complutense University of Madrid.

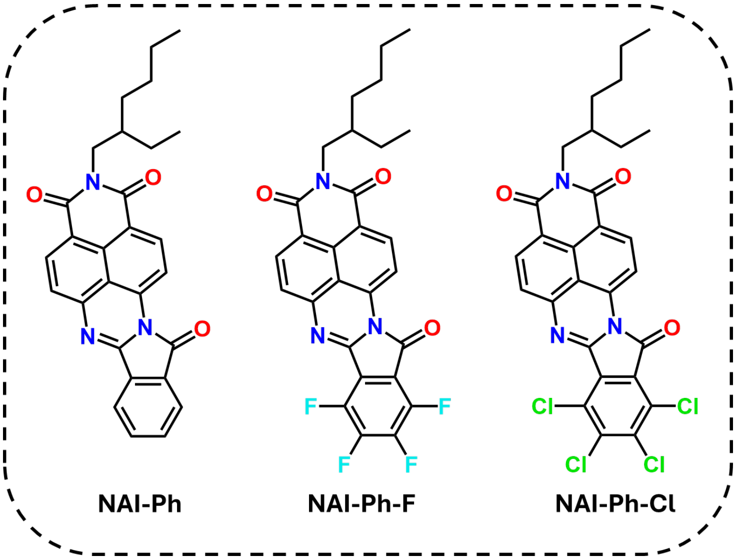

Figure 1.18 Molecular structures of naphthalimides derivatives studied in chapter II.

Chapter III: Tuning charge stabilization and transport in naphthalimides-based semiconductors: effect of introduction of electroactive units.

In this chapter, we studied a new family of processable terthiophene-naphthalimide assemblies (see Figure 1.19).[199] In this family of compounds, three end-capped units with strong electron-withdrawing capacity yield new organic semiconductors with tuneable optoelectrochemical properties. Comparison with the end-capped thienopyrazine derivatives reported in literature will allow to understand the effect of different linker units between the naphthalimide cores and the terthiophene units on the optical and electronic properties of these materials. The synthesis of these semiconductors was performed by the group of Prof. José Luis Segura from the Complutense University of Madrid.

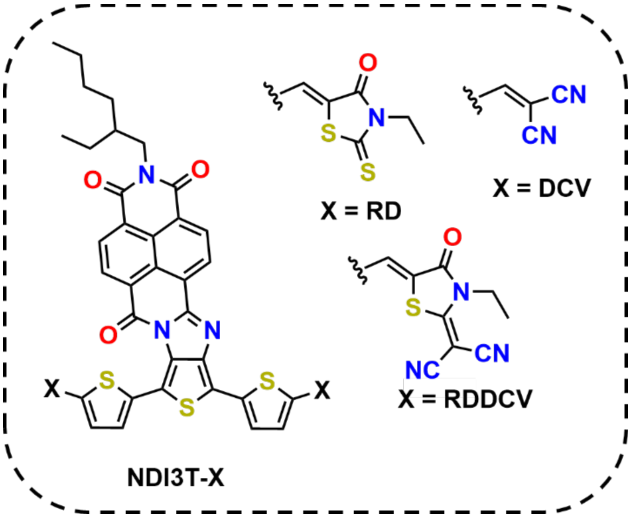

Figure 1.19 Representation of end-capped oligothiophene-naphthalimide assemblies connected via imidazole linkers reported in chapter III.

Chapter IV: Impact of supramolecular interactions by hydrogen bonding on the electronic properties and charge transport of DPP-based organic semiconductors.

In this chapter, the role of hydrogen bonds in the supramolecular order of DPP derivatives has been studied, as well as their effect on their molecular and electronic properties, favouring solid-state redox processes. Consequently, the generation of charge carriers in devices can be optimised, enhancing the electrical performance of several exceptionally small-sized molecular semiconductors. These are based on a thiophene-protected DPP-core as the electroactive component and amide groups as hydrogen-bonding units. Three different positions of amide groups, **DPP2C**, **DPP4C** and **DPP6C,** were investigated and the results were compared with a **Control** molecule, a molecule without amide groups.[200] Spectroelectrochemical experiments, complemented by vibrational spectroscopies and DFT calculations, revealed that hydrogen bond formation induces not only modifications in supramolecular level but also on the effective conjugation length of semiconductors, which can facilitate the generation of free charge carriers in organic field-effect transistors (OFETs). These findings propose a new strategy for the simplified design of organic semiconductors, allowing control of their morphological and electrical properties through the strategic incorporation of hydrogen-bonding units. The group of Prof. Amparo Ruiz Carretero from Instituto de Ciencia de Materiales de Madrid (ICMM) and University of

Strasbourg synthesized these semiconductors, and their chemical structures are shown in Figure 1.20.

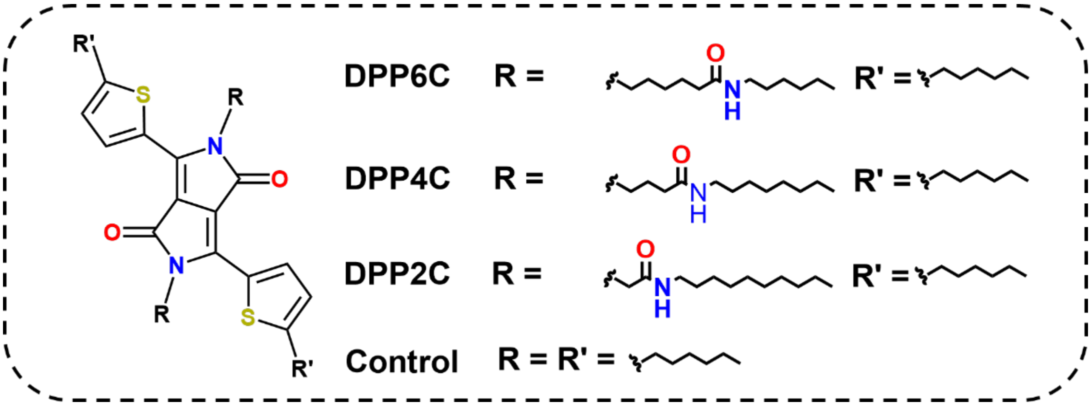

Figure 1.20 Structures of the diketopyrrolopyrrole (DPP) based compounds studied in chapter IV.

1.7 References

1 R. Lin, H. J. Kim, S. Achavananthadith, Z. Xiong, J. K. W. Lee, Y. L. Kong and J. S. Ho, Digitally-embroidered liquid metal electronic textiles for wearable wireless systems, *Nature Communications 2022 13:1*, 2022, **13**, 1–10.

2 Y. Lu, G. Yang, Y. Shen, H. Yang and K. Xu, Multifunctional Flexible Humidity Sensor Systems Towards Noncontact Wearable Electronics, *Nano-Micro Letters 2022 14:1*, 2022, **14**, 1–34.

3 T. Aichner, M. Grünfelder, O. Maurer and D. Jegeni, Twenty-Five Years of Social Media: A Review of Social Media Applications and Definitions from 1994 to 2019, *Cyberpsychol Behav Soc Netw*, 2021, **24**, 215–222.

4 S.-H. Sunwoo, S. I. Han, C. S. Park, J. H. Kim, J. S. Georgiou, S.-P. Lee, D.-H. Kim and T. Hyeon, Soft bioelectronics for the management of cardiovascular diseases, *Nature Reviews Bioengineering 2023 2:1*, 2023, **2**, 8–24.

5 K. Liu, B. Ouyang, X. Guo, Y. Guo and Y. Liu, Advances in flexible organic field-effect transistors and their applications for flexible electronics, *npj Flexible Electronics 2022 6:1*, 2022, **6**, 1–19.

6 B. King and B. H. Lessard, Review of recent advances and sensing mechanisms in solid-state organic thin-film transistor (OTFT) sensors, *J Mater Chem C*, 2024, **12**, 5654–5683.

7 H. Shirakawa and S. Ikeda, Preparation and morphology of as-prepared and highly stretch-aligned polyacetylene, *Synth Met*, 1980, **1**, 175–184.

8 H. Shirakawa, E. J. Louis, A. G. MacDiarmid, C. K. Chiang and A. J. Heeger, Synthesis of electrically conducting organic polymers: halogen derivatives of polyacetylene, (CH) x, *J Chem Soc Chem Commun*, 1977, **0**, 578–580.

9 Nobelprize.org, The Nobel Prize in Chemistry 2000 - NobelPrize.org, https://www.nobelprize.org/prizes/chemistry/2000/8961-the-nobel-prize-in-chemistry-2000/.

10 X. Wei, W. Zhang and G. Yu, Semiconducting Polymers Based on Isoindigo and Its Derivatives: Synthetic Tactics, Structural Modifications, and Applications, *Adv Funct Mater*, 2021, **31**, 2010979.

11 L. Xia, Y. Liu, R. T. Chen, B. Weng and Y. Zou, Advancements in miniaturized infrared spectroscopic-based volatile organic compound sensors: A systematic review, *Appl Phys Rev*, DOI:10.1063/5.0197236/3302955.

12 L. R. Gomez Palacios and A. G. Bracamonte, Development of nano- and microdevices for the next generation of biotechnology, wearables and miniaturized instrumentation, *RSC Adv*, 2022, **12**, 12806–12822.

13 Y. Bonnassieux, C. J. Brabec, Y. Cao, T. B. Carmichael, M. L. Chabinyc, K. T. Cheng, G. Cho, A. Chung, C. L. Cobb, A. Distler, H. J. Egelhaaf, G. Grau, X. Guo, G. Haghiashtiani, T. C. Huang, M. M. Hussain, B. Iniguez, T. M. Lee, L. Li, Y. Ma, D. Ma, M. C. McAlpine, T. N. Ng, R. Österbacka, S. N. Patel, J. Peng, H. Peng, J. Rivnay, L. Shao, D. Steingart, R. A. Street, V. Subramanian, L. Torsi and Y. Wu, The 2021 flexible and printed electronics roadmap, *Flexible and Printed Electronics*, 2021, **6**, 023001.

14 D. Adler and H. Brooks, Theory of Semiconductor-To-Metal Transitions, *Physical Review*, 1967, **155**, 826–840.

15 J. C. Woolley, *Introduction to solid state physics*, 1957, vol. 6.

16 Charles. Kittel and Paul. McEuen, Kittel's introduction to solid state physics, 2018, 609.

17 W. F. Brinkman, D. E. Haggan and W. W. Troutman, A history of the invention of the transistor and where it will lead us, *IEEE J Solid-State Circuits*, 1997, **32**, 1858–1864.

18 The Nobel Prize in Physics 1956 - NobelPrize.org, https://www.nobelprize.org/prizes/physics/1956/summary/.

19 J. Bardeen and W. H. Brattain, The transistor, a semi-conductor triode [14], *Physical Review*, 1948, **74**, 230–231.

20 A. Guerrero, S. Loser, G. Garcia-Belmonte, C. J. Bruns, J. Smith, H. Miyauchi, S. I. Stupp, J. Bisquert and T. J. Marks, Solution-processed small molecule: fullerene bulk-heterojunction solar cells: impedance spectroscopy deduced bulk and interfacial limits to fill-factors, *Physical Chemistry Chemical Physics*, 2013, **15**, 16456–16462.

21 F. Zhu, P. Xu and J. Zong, Moore's Law: The potential, limits, and breakthroughs, *Applied and Computational Engineering*, 2023, **10**, 307–315.

22 T. Li, J. Hou, J. Yan, R. Liu, H. Yang and Z. Sun, Chiplet Heterogeneous Integration Technology—Status and Challenges, *Electronics 2020, Vol. 9, Page 670*, 2020, **9**, 670.

23 W. Tian, B. Li, Z. Li, H. Cui, J. Shi, Y. Wang and J. Zhao, Using Chiplet Encapsulation Technology to Achieve Processing-in-Memory Functions, *Micromachines 2022, Vol. 13, Page 1790*, 2022, **13**, 1790.

24 J. Frazelle, Chipping Away at Moore's Law, *Queue*, 2020, **18**, 5–15.

25 X. Ma, Y. Wang, Y. Wang, X. Cai and Y. Han, Survey on chiplets: interface, interconnect and integration methodology, *CCF Transactions on High Performance Computing*, 2022, **4**, 43–52.

26 T. Wang, F. Feng, S. Xiang, Q. Li and J. Xia, Application Defined On-chip Networks for Heterogeneous Chiplets: An Implementation Perspective, *Proceedings - International Symposium on High-Performance Computer Architecture*, 2022, **2022-April**, 1198–1210.

27 L. Wu, A. Wang, J. Shi, J. Yan, Z. Zhou, C. Bian, J. Ma, R. Ma, H. Liu, J. Chen, Y. Huang, W. Zhou, L. Bao, M. Ouyang, S. J. Pennycook, S. T. Pantelides and H. J. Gao, Atomically sharp interface enabled ultrahigh-speed non-volatile memory devices, *Nature Nanotechnology 2021 16:8*, 2021, **16**, 882–887.

28 D. Bittman, P. Alvaro, U. Santa Cruz, U. Pankaj Mehra, I. Member, U. D. Darrell E Long, U. L. Ethan Miller, P. Mehra and D. D. E Long, Twizzler: A Data-centric OS for Non-volatile Memory, *ACM Transactions on Storage (TOS)*, 2021, **17**, 31.

29 N. Maring, A. Fyrillas, M. Pont, E. Ivanov, P. Stepanov, N. Margaria, W. Hease, A. Pishchagin, A. Lemaître, I. Sagnes, T. H. Au, S. Boissier, E. Bertasi, A. Baert, M. Valdivia, M. Billard, O. Acar, A. Brieussel, R. Mezher, S. C. Wein, A. Salavrakos, P. Sinnott, D. A. Fioretto, P. E. Emeriau, N. Belabas, S. Mansfield, P. Senellart, J. Senellart and N. Somaschi, A versatile single-photon-based quantum computing platform, *Nature Photonics 2024 18:6*, 2024, **18**, 603–609.

30 R. B. Liu, W. Yao and L. J. Sham, Quantum computing by optical control of electron spins, *Adv Phys*, 2010, **59**, 703–802.

31 F. Deng, J. Pan, Z. Liu, L. Zeng and J. Chen, Programmable DNA biocomputing circuits for rapid and intelligent screening of SARS-CoV-2 variants, *Biosens Bioelectron*, 2023, **223**, 115025.

32 H. Lv, Q. Li, J. Shi, C. Fan and F. Wang, Biocomputing Based on DNA Strand Displacement Reactions, *ChemPhysChem*, 2021, **22**, 1151–1166.

33 J. Wang, F. Qian, S. Huang, Z. Lv, Y. Wang, X. Xing, M. Chen, S.-T. Han and Y. Zhou, Recent Progress of Protein-Based Data Storage and Neuromorphic Devices, *Advanced Intelligent Systems*, 2021, **3**, 2000180.

34 A. SB, Quantum Computation and Quantum Information by Nielsen and Chuang, preprint, https://www.academia.edu/41154803/Quantum_Computation_and_Quantum_Information_by_Nielsen_and_Chuang.

35 A. Steane, Quantum computing, *Reports on Progress in Physics*, 1998, **61**, 117–173.

36 R. Rietsche, C. Dremel, S. Bosch, L. Steinacker, M. Meckel and J. M. Leimeister, Quantum computing, *Electronic Markets*, 2022, **32**, 2525–2536.

37 Q. Lin, Polymeric electronic materials for microelectronics manufacturing: A review, *Polymer (Guildf)*, 2023, **286**, 126395.

38 Y. Wu, Y. Zhao and Y. Liu, Toward Efficient Charge Transport of Polymer-Based Organic Field-Effect Transistors: Molecular Design, Processing, and Functional Utilization, *Acc Mater Res*, 2021, **2**, 1047–1058.

39 B. Raj, P. Kaur, P. Kumar and S. S. Gill, Comparative Analysis of OFETs Materials and Devices for Sensor Applications, *Silicon*, 2022, **14**, 4463–4471.

40 S. G. Surya, H. N. Raval, R. Ahmad, P. Sonar, K. N. Salama and V. R. Rao, Organic field effect transistors (OFETs) in environmental sensing and health monitoring: A review, *TrAC Trends in Analytical Chemistry*, 2019, **111**, 27–36.

41 A. D. Scaccabarozzi, A. Basu, F. Aniés, J. Liu, O. Zapata-Arteaga, R. Warren, Y. Firdaus, M. I. Nugraha, Y. Lin, M. Campoy-Quiles, N. Koch, C. Müller, L. Tsetseris, M. Heeney and T. D. Anthopoulos, Doping Approaches for Organic Semiconductors, *Chem Rev*, 2022, **122**, 4420–4492.

42 Z. A. Lamport, H. F. Haneef, S. Anand, M. Waldrip and O. D. Jurchescu, Tutorial: Organic field-effect transistors: Materials, structure and operation, *J Appl Phys*, 2018, **124**, 71101.

43 I. G. Lezama, M. Nakano, N. A. Minder, Z. Chen, F. V. Di Girolamo, A. Facchetti, A. F. Morpurgo and ., Single-Crystal Organic Charge-Transfer Interfaces probed using Schottky-Gated Heterostructures, *Nat Mater*, 2013, **11**, 788–794.

44 J. Krumland, A. M. Valencia and C. Cocchi, Exploring organic semiconductors in solution: The effects of solvation, alkylization, and doping, *Physical Chemistry Chemical Physics*, 2021, **23**, 4841–4855.

45 S. V. Kesava and M. K. Riede, Direct observation and evolution of electronic coupling between organic semiconductors, *Phys Rev Mater*, DOI:10.1103/PhysRevMaterials.5.015601.

46 C. Zhao, M. U. Ali, J. Ning and H. Meng, Organic single crystal phototransistors: Recent approaches and achievements.

47 V. Lapalikar, P. Dacha, M. Hambsch, Y. J. Hofstetter, Y. Vaynzof, S. C. B. Mannsfeld and M. Ruck, Influence of chemical interactions on the electronic properties of BiOI/organic semiconductor heterojunctions for application in solution-processed electronics.

48 D. Yang and D. Ma, Development of Organic Semiconductor Photodetectors: From Mechanism to Applications, *Adv Opt Mater*, DOI:10.1002/ADOM.201800522.

49 H. Wang, W. Wang and W. J. Jin, σ-Hole Bond vs π-Hole Bond: A Comparison Based on Halogen Bond, *Chem Rev*, 2016, **116**, 5072–5104.

50 T. Haclefendioğlu and E. Yildirim, Design Principles for the Acceptor Units in Donor–Acceptor Conjugated Polymers, *ACS Omega*, 2022, **7**, 38969–38978.

51 S. Oshima, M. Toyoda and S. Saito, Geometrical and electronic properties of unstrained and strained transition metal dichalcogenide nanotubes, *Phys Rev Mater*, DOI:10.1103/PHYSREVMATERIALS.4.026004.

52 J. Kou, G. Wang, H. Guo, L. Li, J. Fang, J. Ma and Z. Dong, Photocatalytic benzylamine coupling dominated by modulation of linkers in donor-acceptor covalent organic frameworks, *Applied Catalysis B: Environment and Energy*, 2024, **352**, 124020.

53 F. Abid, S. Sharma and B. K. Rajbongshi, Modulating the structural framework with electron-withdrawing groups and studying their effects on charge mobility in a new series of D-A-D based organic semiconductors, *Mater Sci Semicond Process*, 2025, **195**, 109534.

54 H. Yuan, N. Li, W. Fan, H. Cai, D. Zhao, H. Yuan, W. Fan, D. Zhao, N. Li and H. Cai, Metal-Organic Framework Based Gas Sensors, *Advanced Science*, 2022, **9**, 2104374.

55 W. Zhang, R. Li, H. Zheng, J. Bao, Y. Tang and K. Zhou, Laser-Assisted Printing of Electrodes Using Metal–Organic Frameworks for Micro-Supercapacitors, *Adv Funct Mater*, 2021, **31**, 2009057.

56 A. Sharma, S. Masoumi, D. Gedefaw, S. O'Shaughnessy, D. Baran and A. Pakdel, Flexible solar and thermal energy conversion devices: Organic photovoltaics (OPVs), organic thermoelectric generators (OTEGs) and hybrid PV-TEG systems, *Appl Mater Today*, 2022, **29**, 101614.

57 J. Liu, L. Qiu and S. Shao, Emerging electronic applications of fullerene derivatives: an era beyond OPV, *J Mater Chem C*, 2021, **9**, 16143–16163.

58 G. L. Ong, T. S. Ong, S. L. Yap, D. J. Liaw, T. Y. Tou, S. S. Yap and C. H. Nee, A brief review of nanoparticles-doped PEDOT:PSS nanocomposite for OLED and OPV, *Nanotechnol Rev*, 2022, **11**, 1870–1889.

59 G. Hong, X. Gan, C. Leonhardt, Z. Zhang, J. Seibert, J. M. Busch, S. Bräse, G. Hong, X. Gan, C. Leonhardt, Z. Zhang, J. Seibert, J. M. Busch and S. Bräse, A Brief History of OLEDs—Emitter Development and Industry Milestones, *Advanced Materials*, 2021, **33**, 2005630.

60 M. Sarma, L. M. Chen, Y. S. Chen and K. T. Wong, Exciplexes in OLEDs: Principles and promises, *Materials Science and Engineering: R: Reports*, 2022, **150**, 100689.

61 J. Y. Woo, M. H. Park, S. H. Jeong, Y. H. Kim, B. Kim, T. W. Lee and T. H. Han, Advances in Solution-Processed OLEDs and their Prospects for Use in Displays, *Advanced Materials*, 2023, **35**, 2207454.

62 Y. X. Hu, J. Miao, T. Hua, Z. Huang, Y. Qi, Y. Zou, Y. Qiu, H. Xia, H. Liu, X. Cao and C. Yang, Efficient selenium-integrated TADF OLEDs with reduced roll-off, *Nature Photonics 2022 16:11*, 2022, **16**, 803–810.

63 Y. Zhou, K. Zhang, Z. Chen and H. Zhang, Molecular Design Concept for Enhancement Charge Carrier Mobility in OFETs: A Review, *Materials 2023, Vol. 16, Page 6645*, 2023, **16**, 6645.

64 J. Tao, W. Sun and L. Lu, Organic small molecule semiconductor materials for OFET-based biosensors, *Biosens Bioelectron*, 2022, **216**, 114667.

65 H. J. Cheon, T. K. An and Y. H. Kim, Diketopyrrolopyrrole (DPP)-Based Polymers and Their Organic Field-Effect Transistor Applications: A Review, *Macromolecular Research 2022 30:2*, 2022, **30**, 71–84.

66 S. Das, A. Sebastian, E. Pop, C. J. McClellan, A. D. Franklin, T. Grasser, T. Knobloch, Y. Illarionov, A. V. Penumatcha, J. Appenzeller, Z. Chen, W. Zhu, I. Asselberghs, L. J. Li, U. E. Avci, N. Bhat, T. D. Anthopoulos and R. Singh, Transistors based on two-dimensional materials for future integrated circuits, *Nature Electronics 2021 4:11*, 2021, **4**, 786–799.

67 M. Waltl, T. Knobloch, K. Tselios, L. Filipovic, B. Stampfer, Y. Hernandez, D. Waldhör, Y. Illarionov, B. Kaczer and T. Grasser, Perspective of 2D Integrated Electronic Circuits: Scientific Pipe Dream or Disruptive Technology?, *Advanced Materials*, 2022, **34**, 2201082.

68 M. M. Torrent and C. Rovira, Novel small molecules for organic field-effect transistors: towards processability and high performance, *Chem Soc Rev*, 2008, **37**, 827–838.

69 G. Horowitz, Organic Field-Effect Transistors, DOI:10.1002/(SICI)1521-4095(199803)10:5.

70 Q. Zhang, T. Jin, X. Ye, D. Geng, W. Chen and W. Hu, Organic Field Effect Transistor-Based Photonic Synapses: Materials, Devices, and Applications, *Adv Funct Mater*, 2021, **31**, 2106151.

71 D. F. Barbe and C. R. Westgate, Surface state parameters of metal-free phthalocyanine single crystals, *Journal of Physics and Chemistry of Solids*, 1970, **31**, 2679–2687.

72 A. Tsumura, H. Koezuka and T. Ando, Macromolecular electronic device: Field-effect transistor with a polythiophene thin film, *Appl Phys Lett*, 1986, **49**, 1210–1212.

73 F. Wu, Y. Liu, J. Zhang, S. Duan, D. Ji, H. Yang, F. M. Wu, Y. X. Liu, J. Zhang, S. M. Duan, H. Yang and D. Y. Ji, Recent Advances in High-Mobility and High-Stretchability Organic Field-Effect Transistors: From Materials, Devices to Applications, *Small Methods*, 2021, **5**, 2100676.

74 A. Nawaz, L. Merces, L. M. M. Ferro, P. Sonar and C. C. B. Bufon, Impact of Planar and Vertical Organic Field-Effect Transistors on Flexible Electronics, *Advanced Materials*, 2023, **35**, 2204804.

75 C. R. Newman, C. D. Frisbie, D. A. Da Silva Filho, J. L. Brédas, P. C. Ewbank and K. R. Mann, Introduction to organic thin film transistors and design of n-channel organic semiconductors, *Chemistry of Materials*, 2004, **16**, 4436–4451.

76 M. Mas-Torrent and C. Rovira, Role of molecular order and solid-state structure in organic field-effect transistors, *Chem Rev*, 2011, **111**, 4833–4856.

77 L. Luo and Z. Liu, Recent progress in organic field-effect transistor-based chem/bio-sensors, *View*, 2022, **3**, 20200115.

78 Z. A. Lamport, H. F. Haneef, S. Anand, M. Waldrip and O. D. Jurchescu, Tutorial: Organic field-effect transistors: Materials, structure and operation, *J Appl Phys*, 2018, **124**, 71101.

79 S. Yuvaraja, A. Nawaz, Q. Liu, D. Dubal, S. G. Surya, K. N. Salama and P. Sonar, Organic field-effect transistor-based flexible sensors., *Chem Soc Rev*, 2020, **49**, 3423–3460.

80 G. Horowitz, Field-effect transistors based on short organic molecules, *J Mater Chem*, 1999, **9**, 2021–2026.

81 M. Chen, B. Peng, R. A. Sporea, V. Podzorov and P. K. L. Chan, The Origin of Low Contact Resistance in Monolayer Organic Field-Effect Transistors with van der Waals Electrodes, *Small Science*, 2022, **2**, 2100115.

82 B. Amna, R. Isci, H. M. Siddiqi, L. A. Majewski, S. Faraji and T. Ozturk, High-performance, low-voltage organic field-effect transistors using thieno[3,2- b]thiophene and benzothiadiazole co-polymers, *J Mater Chem C Mater*, 2022, **10**, 8254–8265.

83 S. Fratini, M. Nikolka, A. Salleo, G. Schweicher and H. Sirringhaus, Charge transport in high-mobility conjugated polymers and molecular semiconductors, *Nature Materials 2020 19:5*, 2020, **19**, 491–502.

84 C. Sutton, C. Risko and J. L. Brédas, Noncovalent Intermolecular Interactions in Organic Electronic Materials: Implications for the Molecular Packing vs Electronic Properties of Acenes, *Chemistry of Materials*, 2016, **28**, 3–16.

85 W. Kaiser, T. Albes and A. Gagliardi, Charge carrier mobility of disordered organic semiconductors with correlated energetic and spatial disorder, *Physical Chemistry Chemical Physics*, 2018, **20**, 8897–8908.

86 T. Okamoto, C. P. Yu, C. Mitsui, M. Yamagishi, H. Ishii, J. Takeya, J. Takeya and J. Takeya, Bent-Shaped p-Type Small-Molecule Organic Semiconductors: A Molecular Design Strategy for Next-Generation Practical Applications, *J Am Chem Soc*, 2020, **142**, 9083–9096.

87 D. Schwarz, A. Acharjya, A. Ichangi, Y. S. Kochergin, P. Lyu, M. V. Opanasenko, J. Tarábek, J. Vacek Chocholoušová, J. Vacek, J. Schmidt, J. Čejka, P. Nachtigall, A. Thomas and M. J. Bojdys, Tuning the Porosity and Photocatalytic Performance of

Triazine-Based Graphdiyne Polymers through Polymorphism, *ChemSusChem*, 2019, **12**, 194–199.

88 C. Zhao, M. U. Ali, J. Ning and H. Meng, Organic single crystal phototransistors: Recent approaches and achievements.

89 D. Schwarz, A. Acharjya, A. Ichangi, Y. S. Kochergin, P. Lyu, M. V. Opanasenko, J. Tarábek, J. Vacek Chocholoušová, J. Vacek, J. Schmidt, J. Čejka, P. Nachtigall, A. Thomas and M. J. Bojdys, Tuning the Porosity and Photocatalytic Performance of Triazine-Based Graphdiyne Polymers through Polymorphism., *ChemSusChem*, 2019, **121**, 194–199.

90 R. A. Marcus, Exchange reactions and electron transfer reactions including isotopic exchange. Theory of oxidation-reduction reactions involving electron transfer. Part 4.—A statistical-mechanical basis for treating contributions from solvent, ligands, and inert salt, *Discuss Faraday Soc*, 1960, **29**, 21–31.

91 M. C. J. M. Vissenberg and M. Matters, Theory of the field-effect mobility in amorphous organic transistors, *Phys Rev B*, 1998, **57**, 12964–12967.

92 R. Jiang, R. Zhu and Z. S. Li, Designing Hole Transport Materials with High Hole Mobility and Outstanding Interface Properties for Perovskite Solar Cells, *ChemPhysChem*, 2020, **21**, 1866–1872.

93 A. E. Jailaubekov, A. P. Willard, J. R. Tritsch, W. L. Chan, N. Sai, R. Gearba, L. G. Kaake, K. J. Williams, K. Leung, P. J. Rossky and X. Y. Zhu, Hot charge-transfer excitons set the time limit for charge separation at donor/acceptor interfaces in organic photovoltaics, *Nature Materials 2012 12:1*, 2012, **12**, 66–73.

94 Y. Zhang, Y. Wang, C. Gao, Z. Ni, X. Zhang, W. Hu and H. Dong, Recent advances in n-type and ambipolar organic semiconductors and their multi-functional applications, *Chem Soc Rev*, 2023, **52**, 1331–1381.

95 X. Xu, T. Xiao, X. Gu, X. Yang, S. V. Kershaw, N. Zhao, J. Xu and Q. Miao, Solution-Processed Ambipolar Organic Thin-Film Transistors by Blending p- and n-Type Semiconductors: Solid Solution versus Microphase Separation, *ACS Appl Mater Interfaces*, 2015, **7**, 28019–28026.

96 D. Ji, L. Li, H. Fuchs and W. Hu, Engineering the Interfacial Materials of Organic Field-Effect Transistors for Efficient Charge Transport, *Acc Mater Res*, 2021, **2**, 159–169.

97 M. Pei, J. Guo, B. Zhang, S. Jiang, Z. Hao, X. Xu and Y. Li, Semiconductor/dielectric interface in organic field-effect transistors: charge transport, interfacial effects, and perspectives with 2D molecular crystals, *Adv Phys X*, 2020, **5**, 1747945.

98 J. Mei, Y. Diao, A. L. Appleton, L. Fang and Z. Bao, Integrated materials design of organic semiconductors for field-effect transistors, *J Am Chem Soc*, 2013, **135**, 6724–6746.

99 J. D. Huang, S. H. Wen, W. Q. Deng and K. L. Han, Simulation of hole mobility in α-oligofuran crystals, *Journal of Physical Chemistry B*, 2011, **115**, 2140–2147.

100 R. Khatua, S. R. Sahoo, S. Sharma and S. Sahu, Anisotropic charge transport and optoelectronic properties of wide band gap organic semiconductors based on biphenyl derivatives: A computational study, *Synth Met*, 2020, **267**, 116474.

101 X. Lin, B. Wegner, K. M. Lee, M. A. Fusella, F. Zhang, K. Moudgil, B. P. Rand, S. Barlow, S. R. Marder, N. Koch and A. Kahn, Beating the thermodynamic limit with photo-activation of n-doping in organic semiconductors, *Nature Materials 2017 16:12*, 2017, **16**, 1209–1215.

102 R. Kim, P. S. K. Amegadze, I. Kang, H. J. Yun, Y. Y. Noh, S. K. Kwon and Y. H. Kim, High-Mobility Air-Stable Naphthalene Diimide-Based Copolymer Containing Extended π-Conjugation for n-Channel Organic Field Effect Transistors, *Adv Funct Mater*, 2013, **23**, 5719–5727.

103 R. Li, Z. Dai, M. Zheng, C. Wang, Z. Deng, T. Zhuang, K. Feng, W. Yang, K. Yang and H. Zhang, Benzo/Naphthodifuranone-Based Polymers: Effect of Perpendicular-Extended Main Chain π-Conjugation on Organic Field-Effect Transistor Performances, *Macromol Rapid Commun*, 2021, **42**, 2000703.

104 M. Sommer, Conjugated polymers based on naphthalene diimide for organic electronics, *J Mater Chem C*, 2014, **2**, 3088–3098.

105 M. L. Tang, A. D. Reichardt, N. Miyaki, R. M. Stoltenberg and Z. Bao, Ambipolar, high performance, acene-based organic thin film transistors, *J Am Chem Soc*, 2008, **130**, 6064–6065.

106 J. Freudenberg and U. H. F. Bunz, How to Stabilize Large Soluble (Hetero-)Acenes, *J Am Chem Soc*, 2024, **146**, 16937–16949.

107 A. Ong, T. Tao, Q. Jiang, Y. Han, Y. Ou, K.-W. Huang and C. Chi, Azulene-Fused Acenes, *Angewandte Chemie*, 2022, **134**, e202209286.

108 A. Naibi Lakshminarayana, A. Ong and C. Chi, Modification of acenes for n-channel OFET materials, *J Mater Chem C*, 2018, **6**, 3551–3563.

109 S. Sardar, Silicon-containing heteroacenes (SCHs) for organic electronic applications, *Mol Phys*, DOI:10.1080/00268976.2025.2486697.

110 R. Einholz, T. Fang, R. Berger, P. Grüninger, A. Früh, T. Chassé, R. F. Fink and H. F. Bettinger, Heptacene: Characterization in Solution, in the Solid State, and in Films, *J Am Chem Soc*, 2017, **139**, 4435–4442.

111 X. Feng, Y. Bai, M. Liu, Y. Li, H. Yang, X. Wang and C. Wu, Untangling the respective effects of heteroatom-doped carbon materials in batteries, supercapacitors and the ORR to design high performance materials, *Energy Environ Sci*, 2021, **14**, 2036–2089.

112 E. K. Lee, M. Y. Lee, C. H. Park, H. R. Lee and J. H. Oh, Toward Environmentally Robust Organic Electronics: Approaches and Applications, *Advanced Materials*, 2017, **29**, 1703638.

113 Z. Zhao, Z. Yin, H. Chen, L. Zheng, C. Zhu, L. Zhang, S. T.-Adv. Mater and undefined 2017, High-performance, air-stable field-effect transistors based on heteroatom-substituted naphthalenediimide-benzothiadiazole copolymers exhibiting ultrahigh, *academia.eduZ Zhao, Z Yin, H Chen, L Zheng, C Zhu, L Zhang, S Tan, H Wang, Y Guo, Q Tang, Y LiuAdv. Mater, 2017•academia.edu*.

114 S. E. Root, S. Savagatrup, A. D. Printz, D. Rodriquez and D. J. Lipomi, Mechanical Properties of Organic Semiconductors for Stretchable, Highly Flexible, and Mechanically Robust Electronics, *Chem Rev*, 2017, **117**, 6467–6499.

115 Y. Sun, L. Tan, S. Jiang, H. Qian, Z. Wang, D. Yan, C. Di, Y. Wang, W. Wu, G. Yu, S. Yan, C. Wang, W. Hu, Y. Liu and D. Zhu, High-performance transistor based on individual single-crystalline micrometer wire of perylo[1,12-6,c,d]thiophene, *J Am Chem Soc*, 2007, **129**, 1882–1883.

116 S. Wood, J. H. Kim, J. Wade, J. B. Park, D. H. Hwang and J. S. Kim, Systematic control of heteroatoms in donor–acceptor copolymers and its effects on molecular conformation and photovoltaic performance, *J Mater Chem C*, 2016, **4**, 7966–7978.

117 H. Ebata, T. Izawa, E. Miyazaki, K. Takimiya, M. Ikeda, H. Kuwabara and T. Yui, Highly soluble [1]benzothieno[3,2-b]benzothiophene (BTBT) derivatives for high-performance, solution-processed organic field-effect transistors, *J Am Chem Soc*, 2007, **129**, 15732–15733.

118 H. Minemawari, T. Yamada, H. Matsui, J. Y. Tsutsumi, S. Haas, R. Chiba, R. Kumai and T. Hasegawa, Inkjet printing of single-crystal films, *Nature 2011 475:7356*, 2011, **475**, 364–367.

119 K. Nakayama, Y. Hirose, J. Soeda, M. Yoshizumi, T. Uemura, M. Uno, W. Li, M. Jin Kang, M. Yamagishi, Y. Okada, E. Miyazaki, Y. Nakazawa, A. Nakao, K. Takimiya, J. Takeya, K. Nakayama, Y. Hirose, T. Uemura, M. Uno, W. Li, J. Takeya, M. Kang, E. Miyazaki, K. Takimiya, J. Soeda, M. Yoshizumi, M. Yamagishi, Y. Okada, Y. Nakazawa and A. Nakao, Patternable Solution-Crystallized Organic Transistors with High Charge Carrier Mobility, *Advanced Materials*, 2011, **23**, 1626–1629.

120 K. Gubanov, M. Johnson, M. Akay, B. C. Wolz, D. Shen, X. Cheng, S. Christiansen and R. H. Fink, C8-BTBT-C8 Thin-Film Transistors Based on Micro-Contact Printed PEDOT:PSS/MWCNT Electrodes, *Adv Electron Mater*, 2023, **9**, 2201233.

121 J. Li, A. Babuji, I. Temiño, T. Salzillo, F. D'Amico, R. Pfattner, C. Ocal, E. Barrena and M. Mas-Torrent, Chemical Doping of the Organic Semiconductor C8-BTBT-C8 Using an Aqueous Iodine Solution for Device Mobility Enhancement, *Adv Mater Technol*, 2022, **7**, 2101535.

122 T. Hawly, M. Johnson, A. Späth, H. Nickles Jäkel, M. Wu, E. Spiecker, B. Watts, A. Nefedov and R. H. Fink, Exploring the Preparation Dependence of Crystalline 2D-Extended Ultrathin C8-BTBT-C8 Films, *ACS Appl Mater Interfaces*, 2022, **14**, 16830–16838.

123 C. Wang, Z. Liang, Y. Liu, X. Wang, N. Zhao, Q. Miao, W. Hu and J. Xu, Single crystal n-channel field effect transistors from solution-processed silylethynylated tetraazapentacene, *J Mater Chem*, 2011, **21**, 15201–15204.

124 G. Xue, J. Wu, C. Fan, S. Liu, Z. Huang, Y. Liu, B. Shan, H. L. Xin, Q. Miao, H. Chen and H. Li, Boosting the electron mobility of solution-grown organic single crystals via reducing the amount of polar solvent residues, *Mater Horiz*, 2016, **3**, 119–123.

125 H. Jiang, B. Peng, S. Liu, J. Ren, W. Yang, C. Lin, R. Wu, H. Chen and H. Li, Bending TIPS-pentacene single crystals: from morphology to transistor performance, *J Mater Chem C*, 2021, **9**, 5621–5627.

126 N. Lago, M. Buonomo, F. Prescimone, S. Toffanin, M. Muccini and A. Cester, Direct Comparison of the Effect of Processing Conditions in Electrolyte-Gated and Bottom-Gated TIPS-Pentacene Transistors, *Electronic Materials*, 2022, **3**, 281–290.

127 L. Feriancová, M. Cigáň, J. Kožíšek, K. Gmucová, V. Nádaždy, T. Dubaj, M. Sobota, M. Novota, M. Weis and M. Putala, Dithienylnaphthalenes and quaterthiophenes substituted with electron-withdrawing groups as n-type organic semiconductors for organic field-effect transistors, *J Mater Chem C*, 2022, **10**, 10058–10074.

128 L. Feriancová, M. Cigáň, K. Gmucová, J. Kožíšek, V. Nádaždy and M. Putala, Effect of electron-withdrawing groups on molecular properties of naphthyl and anthryl bithiophenes as potential n-type semiconductors, *New Journal of Chemistry*, 2021, **45**, 9794–9804.

129 W. Qiu and S. Zheng, Effects of functionalization of Y6 end-groups with electron-withdrawing groups on the photovoltaic properties at the donor-acceptor interfaces of PM6/Y6 OSCs: A theoretical insight, *Org Electron*, 2021, **96**, 106235.

130 S. Liu, L. Zheng, M. Chen, Y. Sun, P. Wang, S. Li, H. Wu, X. Zhang and W. Hu, The effect of electron-withdrawing substituents in asymmetric anthracene derivative semiconductors, *J Mater Chem C*, 2021, **9**, 4217–4222.

131 N. K. Kalinichenko, D. O. Balakirev, P. S. Savchenko, A. L. Mannanov, S. M. Peregudova, D. Y. Paraschuk, S. A. Ponomarenko and Y. N. Luponosov, Effects of electron-withdrawing group and π-conjugation length in donor-acceptor oligothiophenes on their properties and performance in non-fullerene organic solar cells, *Dyes and Pigments*, 2021, **194**, 109592.

132 D. F. Nugraha, D. Kim, E. Yang, S. W. Lee, D. R. Whang, S. A. Lee, S. H. Park and D. W. Chang, Substituent Effects of Electron-Withdrawing and Electron-Donating Groups on Photovoltaic Properties of Quinoxaline-Based Polymers, *ACS Appl Electron Mater*, 2023, **5**, 1174–1182.

133 R. S. Ghadwal, Tuning the Electronic Properties of Main-Group Species by N-Heterocyclic Vinyl (NHV) Scaffolds, *Acc Chem Res*, 2022, **55**, 457–470.

134 C. L. Anderson, T. Zhang, M. Qi, Z. Chen, C. Yang, S. J. Teat, N. S. Settineri, E. A. Dailing, A. Garzón-Ruiz, A. Navarro, Y. Lv and Y. Liu, Exceptional Electron-Rich Heteroaromatic Pentacycle for Ultralow Band Gap Conjugated Polymers and Photothermal Therapy, *J Am Chem Soc*, 2023, **145**, 5474–5485.

135 D. Shukla, S. F. Nelson, D. C. Freeman, M. Rajeswaran, W. G. Ahearn, D. M. Meyer and J. T. Carey, Thin-film morphology control in naphthalene-diimide-based semiconductors: high mobility n-type semiconductor for organic thin-film transistors, *Chemistry of Materials*, 2008, **20**, 7486–7491.

136 X. Wang, S. Liu, C. Ren, L. Cao, W. Zhang and T. Wu, Synthesis, Characterization, and Field-Effect Transistor Properties of Naphthalene Diimide-Based Conjugated Polymers with Fluorine-Containing Branched Side Chains, *Macromolecules*, 2022, **55**, 6415–6425.

137 G. S. Lee, J. G. Oh, E. H. Suh, K. Lee, E. A. Yu, T. K. An, J. Jang and Y. H. Kim, Naphthalene-Diimide-Based Small Molecule Containing a Thienothiophene Linker for n-Type Organic Field-Effect Transistors, *Macromol Res*, 2022, **30**, 470–476.

138 S. V. Bhosale, M. Al Kobaisi, R. W. Jadhav, P. P. Morajkar, L. A. Jones and S. George, Naphthalene diimides: perspectives and promise, *Chem Soc Rev*, 2021, **50**, 9845–9998.

139 Z. Wang, Q. Peng, X. Huang, Q. Ma, J. Shao and Q. Shen, Recent progress of Acenaphthylene-imide-fused polycyclic aromatic hydrocarbons: Synthesis and application, *Dyes and Pigments*, 2021, **185**, 108877.

140 S. Zhao, Z. Ma, H. Wang and J. Shi, Organic Heterojunction Transistors Based on DEP-DTT Isomers and PTCDI-CH2C3F7, *Adv Mater Interfaces*, 2022, **9**, 2200259.

141 E. E. Havinga, W. ten Hoeve and H. Wynberg, A new class of small band gap organic polymer conductors, *Polymer Bulletin*, 1992, **29**, 119–126.

142 Z. Peng, L. Ye and H. Ade, Understanding, quantifying, and controlling the molecular ordering of semiconducting polymers: from novices to experts and amorphous to perfect crystals, *Mater Horiz*, 2022, **9**, 577–606.

143 J. E. Medvedeva, D. B. Buchholz and R. P. H. Chang, Recent Advances in Understanding the Structure and Properties of Amorphous Oxide Semiconductors, *Adv Electron Mater*, DOI:10.1002/AELM.201700082.

144 D. Schwarz, A. Acharjya, A. Ichangi, Y. ochergin, P. Lyu, M. V Opanasenko, J. arµbek, J. Vacek Chocholoušovµ, J. Vacek, J. Schmidt, J. C. ˇ ejka, P. Nachtigall, A. Thomas, M. J. Bojdys, A. Ichangi, Y. S. Kochergin, D. ojdys, A. Acharjya, J. Schmidt, D. arµbek, D. acek Chocholoušovµ, D. J. Vacek, P. Lyu, D. Opanasenko, D. ˇ ejka and D. Nachtigall, Tuning the Porosity and Photocatalytic Performance of Triazine-Based Graphdiyne Polymers through Polymorphism, *ChemSusChem*, 2019, **12**, 194–199.

145 G. R. Desiraju, Cryptic crystallography, *Nature Materials 2002 1:2*, 2002, **1**, 77–79.

146 Z. F. Yao, J. Y. Wang and J. Pei, Control of π-π Stacking via Crystal Engineering in Organic Conjugated Small Molecule Crystals, *Cryst Growth Des*, 2018, **18**, 7–15.

147 Z. Chen, S. Duan, W. Hu, Z. Chen, S. Duan, W. Hu, S. Duan, W. Hu and X. Zhang, Novel solution-processed 2D organic semiconductor crystals for high-performance OFETs, *Mater Chem Front*, 2024, **8**, 2227–2272.

148 D. K. Jones and N. Gavvalapalli, Controlling the π-Stack Growth Direction in Organic π-Conjugated Microcrystals, *Cryst Growth Des*, 2022, **22**, 1–19.

149 S. Bellani, A. Bartolotta, A. Agresti, G. Calogero, G. Grancini, A. Di Carlo, E. Kymakis and F. Bonaccorso, Solution-processed two-dimensional materials for next-generation photovoltaics, *Chem Soc Rev*, 2021, **50**, 11870–11965.

150 D. Zhang, L. Zhou, P. K. J. Wong and W. Zhang, Insight into the effect of alkyl chain length and substituent bulkiness on the mobility anisotropy of benzothieno[3,2- b][1]benzothiophenes, *J Mater Chem C*, 2022, **10**, 18423–18432.

151 H. Zhu, G. Wen, W. Zheng, N. H. Rees, W. Stawski, H. I. Wang, M. Bonn and H. L. Anderson, High Charge Carrier Mobility in Porphyrin Nanoribbons, *Angewandte Chemie*, 2024, e202417429.

152 Y. Pan, J. Huang, D. Gao, Z. Chen, W. Zhang and G. Yu, An insight into the role of side chains in the microstructure and carrier mobility of high-performance conjugated polymers, *Polym Chem*, 2021, **12**, 2471–2480.

153 L. L. Miller and K. R. Mann, π-Dimers and π-Stacks in Solution and in Conducting Polymers, *Acc Chem Res*, 1996, **29**, 417–423.

154 E. Y. Shin, S. Park, H. Ahn, H. Jin, I. S. Kim, J. H. Noh and H. J. Son, Effects of stretching on the molecular packing structure of conjugated polymers with hydrogen bonding, *J Mater Chem C*, 2021, **9**, 15132–15140.

155 Y. Hu, K. Miao, L. Xu, B. Zha, X. Miao and W. Deng, Effects of alkyl chain number and position on 2D self-assemblies, *RSC Adv*, 2017, **7**, 32391–32398.

156 E. Frederick, J. D. Cojal González, J. P. Rabe and S. L. Bernasek, Two-Dimensional versus Three-Dimensional Self-Assembly of a Series of 5-Alkoxyisophthalic Acids, *Langmuir*, 2018, **34**, 10739–10747.

157 A. Caiazzo, K. Datta, L. Bellini, M. M. Wienk and R. A. J. Janssen, Impact of Alkyl Chain Length on the Formation of Regular- and Reverse-Graded Quasi-2D Perovskite Thin Films, *ACS Mater Lett*, 2024, **6**, 267–274.

158 M. Bok, J. H. Lee, K. Won and E. Lim, Carrier behavior of a carbon material assisted TIPS-pentacene composite film for improvement of electrical conductivity, *RSC Adv*, 2024, **14**, 36308–36313.

159 B. Breeman, A. T. Tiglias, J. Mancuso, E. Zurek, D. P. Miller and L. Velarde, Insight into the Adsorption Structure of TIPS-Pentacene on Noble Metal Surfaces, *Journal of Physical Chemistry C*, 2022, **126**, 2689–2698.

160 H. Bai, Y. Yang, R. M. Voyles and R. A. Nawrocki, A no-hysteresis TIPS–pentacene:polystyrene blend-based organic field effect transistor by extruded direct ink writing and the application in a resistive load inverter circuit, *J Mater Chem C*, 2022, **10**, 10973–10980.

161 S. K. Park, T. N. Jackson, J. E. Anthony and D. A. Mourey, High mobility solution processed 6,13-bis(triisopropyl-silylethynyl) pentacene organic thin film transistors, *Appl Phys Lett*, DOI:10.1063/1.2768934/326270.

162 H. Bai, Y. Yang, R. M. Voyles and R. A. Nawrocki, A no-hysteresis TIPS–pentacene:polystyrene blend-based organic field effect transistor by extruded direct ink writing and the application in a resistive load inverter circuit, *J Mater Chem C*, 2022, **10**, 10973–10980.

163 N. Lago, M. Buonomo, F. Prescimone, S. Toffanin, M. Muccini and A. Cester, Direct Comparison of the Effect of Processing Conditions in Electrolyte-Gated and Bottom-Gated TIPS-Pentacene Transistors, *Electronic Materials*, 2022, **3**, 281–290.

164 V. Podzorov, E. Menard, A. Borissov, V. Kiryukhin, J. A. Rogers and M. E. Gershenson, Intrinsic charge transport on the surface of organic semiconductors, *Phys Rev Lett*, DOI:10.1103/PHYSREVLETT.93.086602/FIGURES/4/MEDIUM.

165 A. A. Al-Muntaser, M. M. El-Nahass, E. Alzahrani, F. A. Al-Marhaby, Z. M. Alharbi, S. A. Alghamdi and A. Saeed, Insight into electronic structure and the impact of annealing temperature on the optical properties of rubrene thin films for optoelectronic devices, *Opt Mater (Amst)*, 2024, **156**, 115947.

166 T. Takahashi, T. Takenobu, J. Takeya and Y. Iwasa, Ambipolar organic field-effect transistors based on rubrene single crystals, *Appl Phys Lett*, 2006, **88**, 1–3.

167 M. Moret and A. Gavezzotti, The crystalline state of rubrene materials: intermolecular recognition, isomorphism, polymorphism, and periodic bond-chain analysis of morphologies, *New Journal of Chemistry*, 2022, **46**, 7626–7637.

168 T. Hamai, S. Arai and T. Hasegawa, Effects of tunneling-based access resistance in layered single-crystalline organic transistors, *J Mater Res*, 2018, **33**, 2350–2363.

169 M. Chu, J.-X. Fan, S. Yang, D. Liu, C. Fai Ng, H. Dong, A.-M. Ren, Q. Miao, M. Chu, S. Yang, C. F. Ng, Q. Miao, J. Fan, A. Ren, D. Liu and H. Dong, Halogenated Tetraazapentacenes with Electron Mobility as High as 27.8 cm2 V−1 s−1 in Solution-Processed n-Channel Organic Thin-Film Transistors, *Advanced Materials*, 2018, **30**, 1803467.

170 H. Sun, New push–pull ladder-type chromophores with large hyperpolarizability for nonlinear optical application, *Struct Chem*, 2024, **36**, 39–48.

171 A. Harbuzaru, I. Arrechea-Marcos, A. D. Scaccabarozzi, Y. Wang, X. Guo, M. Caironi, J. T. López Navarrete, M. C. Ruiz Delgado and R. Ponce Ortiz, Ladder-type bithiophene imide-based organic semiconductors: understanding charge transport mechanisms in organic field effect transistors, *J Mater Chem C*, 2020, **8**, 15759–15770.

172 T. Haciefendioglu and E. Yildirim, The role of donor units in band gap engineering of donor–acceptor conjugated polymers, *J Mol Graph Model*, 2025, **138**, 109033.

173 W. Wang, Y. He, L. Tu and H. Liu, Electric-Field Effects on the Internal Charge Reorganization Energies of Crystalline Organic Semiconductors, *Journal of Physical Chemistry Letters*, 2023, **14**, 10233–10241.

174 A. Khasbaatar, Z. Xu, J. H. Lee, G. Campillo-Alvarado, C. Hwang, B. N. Onusaitis and Y. Diao, From Solution to Thin Film: Molecular Assembly of π-Conjugated Systems and Impact on (Opto)electronic Properties, *Chem Rev*, 2023, **123**, 8395–8487.

175 C. Zhang, Y. Liu, Z. Ma, G. Wang, C. Li, F. Yang, J. Shi, R. Li and H. Wang, Dragon-Boat-Type Heptathienoacenes: Synthesis, Structures, and Their Applications in OFETs, *Org Lett*, 2022, **24**, 8741–8746.

176 S. Liu, D. Xia, J. Wang, C. Ge, S. Hao, J. Zhang, P. Wang, K. Lin, S. Dong, E. Tretyakov, Y. Yang and X. Gao, Syntheses and properties of 11-ring-fused linear thienoacenes, *J Mater Chem C*, 2023, **11**, 6089–6094.

177 K. Takimiya, S. Shinamura, I. Osaka and E. Miyazaki, Thienoacene-Based Organic Semiconductors, *Advanced Materials*, 2011, **23**, 4347–4370.

178 Y. Sakamoto, T. Suzuki, M. Kobayashi, Y. Gao, Y. Fukai, Y. Inoue, F. Sato and S. Tokito, Perfluoropentacene: High-performance p-n junctions and complementary circuits with pentacene, *J Am Chem Soc*, 2004, **126**, 8138–8140.

179 Y. Sakamoto, T. Suzuki, M. Kobayashi, Y. Gao, Y. Inoue and S. Tokito, Perfluoropentacene and Perfluorotetracene: Syntheses, Crystal Structures, and FET Characteristics, *Molecular Crystals and Liquid Crystals*, 2006, **444**, 225–232.

180 Y. Li, E. Huang, X. Guo and K. Feng, Cyano-functionalized organic and polymeric semiconductors for high-performance n-type organic electronic devices, *Mater Chem Front*, 2023, **7**, 3803–3819.

181 J. Li, Z. Chen, J. Wang, S. Young Jeong, K. Yang, K. Feng, J. Yang, B. Liu, H. Y. Woo and X. Guo, Semiconducting Polymers Based on Simple Electron-Deficient Cyanated trans-1,3-Butadienes for Organic Field-Effect Transistors, *Angewandte Chemie International Edition*, 2023, **62**, e202307647.

182 X. Cao, Y. Min, H. Tian and J. Liu, Incorporating Cyano Groups to a Conjugated Polymer Based on Double B←N-Bridged Bipyridine Units for Unipolar n-Type Organic Field-Effect Transistors, *Organic Materials*, 2021, **3**, 469–476.

183 D. Wang, J. Li, K. Yang, Y. Wang, S. Y. Jeong, Z. Chen, Q. Liao, B. Li, H. Y. Woo, X. Deng and X. Guo, Terminal Cyano-Functionalized Fused Bithiophene Imide Dimer-Based n-Type Small Molecular Semiconductors: Synthesis, Structure-Property Correlations, and Thermoelectric Performances, *ACS Appl Mater Interfaces*, 2022, **15**, 16.

184 P. Cheng, X. Zhao and X. Zhan, Perylene Diimide-Based Oligomers and Polymers for Organic Optoelectronics, *Acc Mater Res*, 2022, **3**, 309–318.

185 B. A. Jones, A. Facchetti, M. R. Wasielewski and T. J. Marks, Effects of Arylene Diimide Thin Film Growth Conditions on n-Channel OFET Performance, *Adv Funct Mater*, 2008, **18**, 1329–1339.

186 L. Chen, Y. Hu, H. Huang, C. Liu, D. Wu and J. Xia, Direct laser patterning of organic semiconductors for high performance OFET-based gas sensors, *J Mater Chem C*, 2023, **11**, 7088–7097.

187 D. Kyung Hwang, R. R. Dasari, M. Fenoll, V. Alain-Rizzo, A. Dindar, J. Won Shim, N. Deb, C. Fuentes-Hernandez, S. Barlow, D. G. Bucknall, P. Audebert, S. R. Marder, B. Kippelen, D. K. Hwang, M. Fenoll, A. Dindar, J. W. Shim, C. Fuentes-Hernandez, B. Kippelen, R. R. Dasari, S. Barlow, S. R. Marder, N. Deb, D. G. Bucknall, V. Alain-Rizzo and P. Audebert, Stable Solution-Processed Molecular n-Channel Organic Field-Effect Transistors, *Advanced Materials*, 2012, **24**, 4445–4450.

188 Y. H. Ha, J. G. Oh, S. Park, S. K. Kwon, T. K. An, J. Jang and Y. H. Kim, Novel naphthalene-diimide-based small molecule with a bithiophene linker for use in organic field-effect transistors, *Org Electron*, 2018, **63**, 250–256.

189 Z. Cao, X. Huo, Q. Ma, J. Song, Q. Pan, L. Chen, J. Lai, X. Shan and J. Gao, TFT-CN/P3HT blending active layer based two-component organic field-effect transistor for improved H2S gas detection, *Sens Actuators B Chem*, 2023, **385**, 133685.

190 J. Li, Z. Chen, J. Wang, S. Young Jeong, K. Yang, K. Feng, J. Yang, B. Liu, H. Y. Woo and X. Guo, Semiconducting Polymers Based on Simple Electron-Deficient Cyanated trans-1,3-Butadienes for Organic Field-Effect Transistors, *Angewandte Chemie International Edition*, 2023, **62**, e202307647.

191 J. Li, E. Colantoni, I. Temiño, P. Branchini, L. Tortora and M. Mas-Torrent, Dopant Diffusion Inhibition in Organic Field-Effect Transistors Using Organic Semiconductor/High-Molecular-Weight Polymer Blends, *Chemistry of Materials*, 2023, **35**, 1527–1536.

192 S. Fusco, M. Barra, L. Gontrani, M. Bonomo, F. Chianese, S. Galliano, R. Centore, A. Cassinese, M. Carbone and A. Carella, Novel Thienyl DPP derivatives Functionalized with Terminal Electron-Acceptor Groups: Synthesis, Optical Properties and OFET Performance, *Chemistry – A European Journal*, 2022, **28**, e202104552.

193 T. Takaya, M. D. Mamo, M. Karakawa and Y. Y. Noh, Donor unit effect on DPP based organic field-effect transistor performance, *Dyes and Pigments*, 2018, **158**, 306–311.

194 H. J. Cheon, T. K. An and Y. H. Kim, Diketopyrrolopyrrole (DPP)-Based Polymers and Their Organic Field-Effect Transistor Applications: A Review, *Macromol Res*, 2022, **30**, 71–84.

195 S. Fusco, M. Barra, L. Gontrani, M. Bonomo, F. Chianese, S. Galliano, R. Centore, A. Cassinese, M. Carbone and A. Carella, Novel Thienyl DPP derivatives Functionalized with Terminal Electron-Acceptor Groups: Synthesis, Optical Properties and OFET Performance, *Chemistry – A European Journal*, 2022, **28**, e202104552.

196 H. J. Cheon, T. K. An and Y. H. Kim, Diketopyrrolopyrrole (DPP)-Based Polymers and Their Organic Field-Effect Transistor Applications: A Review, *Macromolecular Research 2022 30:2*, 2022, **30**, 71–84.

197 R. González-Núñez, M. J. Alonso-Navarro, F. Suárez-Blas, E. Gala, M. M. Ramos, J. L. Segura and R. Ponce Ortiz, Tuning the charge stabilization and transport in

naphthalimide-based semiconductors via a fused-ring and core-engineering strategy, *Volume 8, Issue 8, Pages 1981 - 1992*, 2024, **8**, 1981–1992.

198 R. González-Núñez, A. de la Peña, C. Valderrama-Callejón, J. L. Segura and R. Ponce Ortiz, Small asymmetric halogenated Phenylene–Naphthalimide molecules for organic field-effect transistors, *Dyes and Pigments*, 2025, **242**, 112984.

199 M. J. Alonso-Navarro, A. Harbuzaru, R. González-Núñez, M. M. Ramos, J. L. Segura and R. Ponce Ortiz, Tunable electroactive oligothiophene-naphthalimide semiconductors via end-capped engineering: cumulative effects beyond the linker, *J Mater Chem C*, 2023, **11**, 10852–10863.

200 R. González-Núñez, G. Martinez, N. R. Avila-Rovelo, K. I. Hong, A. Ruiz-Carretero and R. Ponce Ortiz, The effect of hydrogen bond interactions on the electronic nature of DPP-based organic semiconductors: implications on charge transport, *J Mater Chem C*, 2024, **12**, 18264–18273.

2

Methodology

Table of contents

CONTENTS

2.1 Spectroscopic techniques

Spectroscopy is defined as the study of the interaction between electromagnetic radiation and matter. As a result of this interaction, it becomes possible to obtain detailed information regarding the structure and other chemical properties of materials[1–3]. Based on the nature of the electromagnetic radiation, we obtained different kinds of information about the chemical systems, resulting in different types of spectroscopies (see Figure 2.1).

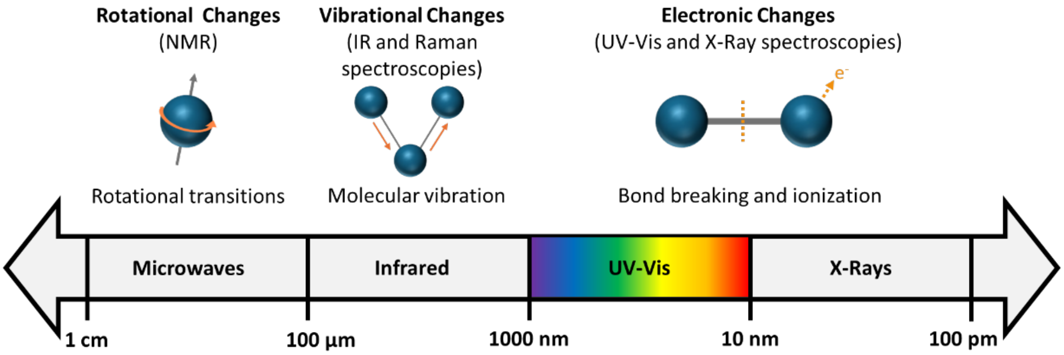

Figure 2.1. Representation of the different spectroscopies associated with the different electromagnetic radiation regions.

The basic spectroscopy phenomenon involves the absorption (or emission) of quantized radiation that moves a system from an initial energy state (E_0) to a final energy state (E_1). In compliance with Einstein's equation ($\Delta E = h\upsilon$), the energy of the absorbed radiation must match the energy difference between these two states. As Figure 2.2 illustrates, various possible energy transitions can occur between the energy levels within a molecular system.

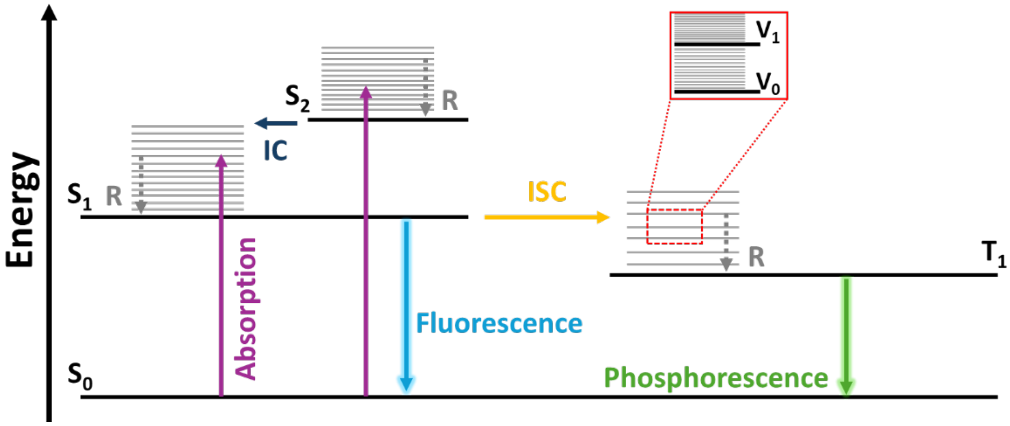

Figure 2.2. Representation of Jablonski diagram. S_n: singlet electronic state; T_n: triplet electronic states; R: thermal relaxation; IC: internal conversion; ISC: intersystem crossing; Vn: vibrational states.

2.1.1 Electronic absorption spectroscopy

Electronic absorption spectroscopy is a process that utilises electromagnetic radiation within the ultraviolet (UV), visible (Vis) and near-infrared (NIR) spectrum as a source of excitation, thereby inducing a transition from the ground electronic state (S_0) to a singlet excited state (S_n). This electronic transition gives rise to the formation of an absorption band. In contrast to atoms, the electronic transitions in molecular systems are associated with rotational and vibrational transitions of similar, albeit not identical, energies. Consequently, a number of these spectral lines form a band that possesses a vibronic structure. The analysis of these bands provides valuable information about the degree of delocalisation of electrons in π-conjugated systems.

The optical properties of the conjugated materials studied in this thesis were analysed by electronic absorption spectroscopy in solution and solid state[4] (as thin films).

For the absorption spectra in solution, different solvents such as dichloromethane (CH_2Cl_2), chloroform ($CHCl_3$), toluene, 1,2-dichlorobenzene (1,2-diClBz), chlorobenzene (ClBz), tetrahydrofuran (THF) and 2-methyltetrahydrofuran (2Me- THF) were used. For room temperature measurements, CH_2Cl_2 and $CHCl_3$ have been used due to the good solubility of the compounds under study. However, 2-MeTHF was used for low temperature absorption spectra, because this solvent generates a transparent matrix in the solid state, allowing the registration of UV-Vis measurements at 80 K. 2Me-THF along with ClBz were used for the measurements at high temperature, up to 380 K. The absorption spectra at variable temperature were recorded using an optical cryostat OPTISTAD®DN from Oxford Instrument (Figure 2.3), adding liquid nitrogen for low temperature measurements.

Figure 2.3. Optical cryostat OPTISTAD®DN.

On the other hand, for the absorption spectra in solid state, solutions of 2 mg/ml in $CHCl_3$ or toluene were prepared and deposited onto quartz substrates by drop-casting.

The following spectrophotometers were employed for electronic absorption:

- Agilent 8453 UV-Vis spectrophotometer (Figure 2.4a): multidiode spectrophotometer that use a deuterium lamp, with a spectral range from 190 nm to 1100 nm. It consists of 910 photodiodes, one for each nanometre, which allows very short registration times.

- Cary 5000 UV-Vis-NIR spectrophotometer (Figure 2.4b): multidiode spectrophotometer with a wavelength range from 175 nm to 3300 nm and a spectral resolution of 0.01 nm. The equipment uses a light tungsten halogen for the Vis-NIR region and a light source of deuterium for the UV spectral region, together with a PbSmart NIR detector.

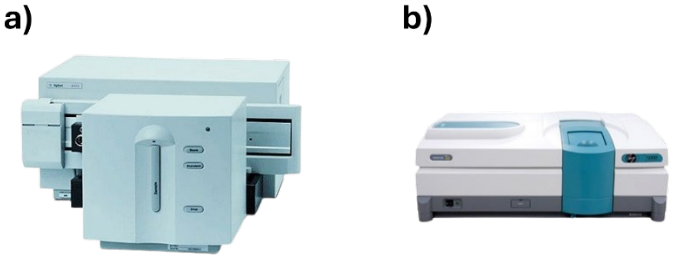

Figure 2.4. a) Agilent 8453 UV-Vis spectrophotometer and b) Cary 5000 UV-Vis-NIR spectrophotometer.

2.1.2 Fluorescence emission spectroscopy

As Figure 2.2 shows, the excited state is unstable and will return to the fundamental electronic state by releasing excess energy through either non-radiative or radiative processes. In non-radiative processes, energy is dissipated without emitting electromagnetic radiation, occurring through mechanisms such as vibrational relaxation, internal conversion, and intersystem crossing. In contrast, radiative processes release energy as electromagnetic radiation, emitting either fluorescence (from a singlet excited state) or phosphorescence (from a triplet excited state)[5]

The fluorescence spectra were recorded for 10^{-5} M solutions in $CHCl_3$ on an Edinburgh FLS920 fluorometer (Figure 2.5). This equipment has a 450W Xe lamp as excitation source and a R2658P detector.

Figure 2.5. Edinburgh FLS920 fluorometer.

2.1.3 Raman spectroscopy

As explained in the previous sections, the interaction between light and matter can be studied by absorption and emission processes. However, photons can also interact with the materials and then be re-emitted from them. This light scattering is the main phenomenon on which Raman spectroscopy is based.

In this technique, a molecular system is excited by laser radiation at a specific frequency, temporarily distorting the electron cloud around the nuclei (that is the molecular polarizability) and creating a short-lived virtual state. The energy of this virtual state depends on the energy of the light source, and due to its instability, the excited photon is quickly re-emitted either without energy exchange (phenomenon called Rayleigh scattering) or with energy transfer between the photons and the molecule, which is known as Stokes Raman scattering or anti-Stokes Raman scattering. Notably, Raman scattering is an unusual phenomenon, with only about one in 10^6 to 10^8 photons undergoing scattering.[6,7]

Due to the high polarizability of π-conjugated systems, originating from alternating C-C double and single bonds, Raman spectra exhibit two prominent features. The first of these is a remarkable selectivity at certain transitions, resulting in simple spectra, and the second feature refers to an increase in intensity along with a shift towards lower wavenumbers in some Raman signals as the π-conjugation is extended.[8,9]

An additional consideration in selecting laser excitation energy is the resonant Raman effect, which occurs when the excitation energy closely matches an electronic transition energy. This resonance enhances Raman scattering and selectively intensifies the Raman activity of chromophores involved in the electronic transition, allowing for the targeted detection of specific molecules within complex chemical systems.

The vibrational Raman spectra in the following chapters were recorded both as bulk materials and as thin films, using different laser excitation wavelengths:

- FT-Raman spectra were recorded by Jasco RFT-6000 (Figure 2.6a). It allows mapping thanks to the fact that it integrates a microscope and a motorized platform AXY-3000 Automatic X-Y stage (30 mm travel with 1 µ steps). This equipment incorporates 10x, 20x and 50x Olympus objectives, suitable for measuring FT-Raman spectra on a microscopic scale. The detection system is through an InGaAs detector, which can work at room temperature or cooled by a peltier system. The minimum guaranteed measurement range is 3600-50 cm^{-1} at 298 K. The excitation source is a Nd-YAG laser with a wavelength of 1064 nm and a power of 1 W.

- Raman spectra at 785, 633 and 582 nm laser excitations were recorded both bulk and thin films samples by using a Bruker Senterra (Figure 2.6b) dispersive Raman microscope equipped with a CCD detector thermoelectrically cooled to -65ºC, a confocal microscope with a x40 objetive and a neon lamp used for laser (Nd:YAG) calibration. The Raman scattering radiation was collected in a back-scattering set up with a resolution of 3-5 cm^{-1}. The power laser operation was between 0.2 and 10 mW. The spectra were recorded by using acquisition times of 10 co-additions of 10 s.

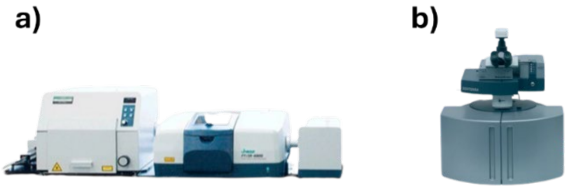

Figure 2.6. a) FT-Raman Jasco RFT-6000 and b) Bruker Micro-Raman Senterra.

2.1.4 Infrared spectroscopy

In this vibrational technique, the electronic dipole moment must change with the relative displacement of the atoms for an IR-active vibration to occur. This method is commonly used to study π-conjugated molecules with strongly polar groups, such as carbonyl or cyano groups, which exhibit characteristic vibrational wavenumbers in spectral regions where other groups do not absorb.[10–12]

The IR absorption spectra in Chapter IV, were recorded in thin film by drop casting solutions of 2 mg/ml and as bulk materials using a Specac ATR (Attenuated Total Reflectance). The following IR spectrometers were used for the Infrared absorption measurements:

- Bruker Vertex FT-IR 70 spectrometer (Figure 2.7a): the main module consists of a Michelson interferometer, coupled to a source and a Deuterated Triglycine Sulfate (DTGS) system for detecting infrared radiation, and a He-Ne laser as an internal reference. It allows the recording of FT-IR spectra in the mid- and near-infrared range (7500-400 cm^{-1}), with very short recording times. For the measurements of the ATR spectra, a Specac Golden Gate Single Reflection Diamond ATR System accessory is used (Figure 2.7b).

Figure 2.7. a) Bruker Vertex FT-IR 70 spectrometer and b) Specac Golden Gate Single Reflection Diamond ATR System accessory.

- Jasco FT-IR-6800FV (Figure 2.8): this spectrometer employed a Fourier transform infrared module that allows measurements in a range from 15000 cm^{-1} to 30 cm^{-1}. For this purpose, it uses a Mercury Cadmium Telluride (MCT) Mid Band detector (12000-650 cm^{-1}) and a Broad-Band Triglycine Sulfate (BBTGS-6000) detector, to ensure the effective measuring range of 15000-30 cm^{-1}.

Figure 2.8. Jasco FT-IR-6800FV spectrometer.

2.2 Electrochemical characterization

An efficient hole/electron injection from the electrodes into the semiconducting active layer is a crucial requirement to ensure the effective operation of electronic devices. Therefore, the charge injection ability of the studied materials was evaluated by analysing their charged species. For this, the work presented in this Thesis employed two different electrochemical techniques: cyclic voltammetry and spectroelectrochemistry.

2.2.1 Cyclic voltammetry

Cyclic voltammetry allows the study of the redox processes by measuring the current intensity generated between the working electrode with respect to reference electrode.

Cyclic voltammetry measurements of naphthalimide derivatives shown in Chapter I, Chapter II and Chapter III were performed by using a potentiostat together with a three-electrode single-compartment cell (5 mL). The working electrode consisted of a platinum wire with a surface of A = 0.785 mm^2, which was polished down to 0.5 µm in order to obtain reproducible surfaces. The counter electrode consisted of a platinum wire, and the reference electrode was an Ag/AgCl secondary electrode. An electrolyte solution of 0.1 M Tetrabutylammonium hexafluorophosphate ($TBAPF_6$) in freshly distilled and degassed CH_2Cl_2 (HPLC grade) was used in all experiments.

In all cases, the approximate HOMO and LUMO energy levels were obtained from the onsets of the first oxidation and reduction potentials respect Fc/Fc^+ potential according to the equations:[13–16]

$$E_{HOMO} = -[E_{onset}(ox) + E_{F_c/F_c^+}\ eV] \qquad [2.1]$$

$$E_{LUMO} = -[E_{onset}(red) + E_{F_c/F_c^+}\ eV] \qquad [2.2]$$

2.2.2 *In situ* spectroelectrochemistry

It is well known that spectroelectrochemistry is a useful tool for the study of charged species in π-conjugated systems since it provides an evolution of the UV-Vis/NIR spectra by progressive spectrochemical oxidation or reduction of diluted solutions (10^{-5} M). The oxidation and reduction processes were recorded using CH_2Cl_2 solutions in the presence of a high excess of supporting electrolyte, 0.1M of $TBAPF_6$, Sigma-Aldrich/Merck, 98%. The solutions were introduced in an Optically Transparent Thin-Layer Electrochemical (OTTLE) (Figure 2.9) cell situated in the sample section of the Cary 5000 spectrophotometer. This spectroelectrochemical cell is based on a transparent thin-layer of quartz and three electrodes: a Pt gauze as the working electrode (32 wires per cm), a Pt wire as the counter electrode and an Ag wire used as the pseudo-reference electrode. The cell is connected to an EC Epsilon potentiostat and a BASi C3 Cell Stand accessory, providing the voltage to oxidaze or reduce the samples.[17]

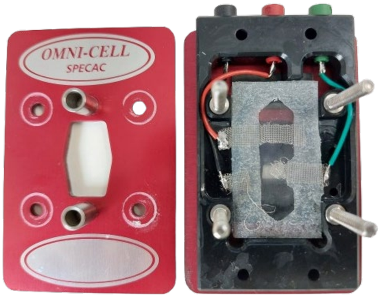

Figure 2.9. Optically Transparent Thin-Layer Electrochemical (OTTLE) cell.

2.3 DFT calculations

Theoretical calculations were conducted within the framework of Density Functional Theory (DFT)[18–20], using Gaussian 09[21] and Gaussian 16[22] software packages. For each family of compounds under study, the following functionals have been used:

- B3LYP utilises the non-local correlation provided by the LYP expression, and VWN functional III for local correlation.[23,24]

- CAM-B3LYP is the long-range-corrected version of B3LYP developed by Handy and coworkers, which employs the Coulomb-attenuating method.[25]

- ωB97 functional employs a long-range corrected (LC), which partitions the electron–electron Coulomb interaction into short-range and long-range components. In this approach, the short-range exchange is treated with a generalized gradient approximation (GGA) functional, while the long-range exchange is computed using exact Hartree–Fock exchange.[26]

- ωB97X-D is the latest functional from Head-Gordon and co-workers, which includes a version of Grimme's D2 empirical dispersion.[27]

- M06-2X is a functional, which is a hybrid meta-GGA functional of Truhlar and Zhao. This functional provides reliable ground electronic state polarization when compared to X-ray structures and accurate excited states dipole moments for a large variety of push-pull systems.[28]

These functionals were used in combination with 6-31G**[29,30] basis set. Theoretical calculations were performed either in gas phase or in solution, the latter simulated by a polarizable continuum model (PCM)[31,32] using dichloromethane or chloroform as solvent. On the other hand, all calculations of radical charged species were performed in the spin unrestricted regime.

To reduce the computational costs the large alkyl chains have been substituted by methyl groups in all compounds under study. All geometrical parameters were optimized independently, unless otherwise stated. The absence of imaginary frequencies confirmed that the global minimum energy configuration was achieved in all cases. An ultrafine integration grid and tight convergence criteria were applied during the optimization process. Molecular orbital topologies were obtained from the optimized geometries and visualized using ChemCraft 1.8 molecular modelling software.[33]

2.3.1 Time-dependent density functional theory

DFT has proven to be a powerful tool for investigating several properties in the ground state. In 1984, Runge and Gross expanded the DFT framework to address time-dependent phenomena, including the formulation and description of excited states. This extension is known as Time-Dependent DFT (TD-DFT).[34–36] Using this approach, we calculated the properties of the excited states for all systems under study and determined the electronic vertical transitions, enabling the prediction of their electronic absorption spectra. Absorption spectra were generated through convolution of the vertical transition energies and oscillator strengths using GaussSum 3.0.[37]

2.3.2 Frequency calculations

The theoretical analysis of molecular vibrations is considered an excellent demonstration of how theoretical chemistry can support the interpretation of experimental data. Calculated normal modes and their corresponding intensities are particularly valuable for assigning experimental Raman and Infrared peaks. Furthermore, analysing these normal modes provides insights into frequency shifts observed in certain vibrational peaks across a family of molecules. This, in turn, offers important information about the degree of effective π-conjugation.

The scientific literature has extensively detailed theoretical methods for calculating vibrational frequencies. Double harmonic approximation is one of the most commonly employed approximations for studying vibrational spectroscopy.[38] In this approach, molecular vibrations are modelled as harmonic oscillators, with spectroscopic intensities determined by the first-order geometric derivative of the dipole moment for infrared spectroscopy and the polarizability for Raman spectroscopy. Note that the calculation frequencies have been executed at the same level of theory used for geometry optimizations. All positive vibrational frequencies confirm the minimum energy of the optimized systems exposed in this thesis.

DFT has been demonstrated to be an effective method for calculating harmonic frequencies and simulating the vibrational spectra of complex molecules. However, DFT-calculated harmonic frequencies are typically scaled by a constant to be compared with experimental data. Comparing theoretical harmonic frequencies with the experimental data enables the determination of a specific scaling factor for each functional. Finally, the theoretical spectra were obtained from scaled frequencies and the Raman scattering activities with Gaussian functions (10 cm^{-1} width at the half-height). Vibrational eigenvectors were obtained using the ChemCraft 1.8[39] molecular modelling software.

2.3.3 Charge transport parameters

In order to study the charge transport process, two key theoretical parameters are predicted, the internal reorganization energy and the transfer integral, although the latter not been calculated in this thesis. Large transfer integrals and lower internal reorganization energies are sought to promote better intermolecular charge hopping.[40]

The internal reorganization energy (λ) reveals the structural changes of the molecules needed to accommodate a positive or negative charge. The reorganization energy for holes (λ_h) and the reorganization energy for electrons (λ_e) transport were computed directly from the relevant points on the potential surfaces by a standard procedure previously reported.[41,42] The λ_h and λ_e values need the calculations of four states, as shown in Figure 2.10 and equations [2.3] and [2.4].

$$\lambda_h = (E_0^* - E_{+1}) + (E_{+1}^* - E_0) \qquad [2.3]$$

$$\lambda_e = (E_0^* - E_{-1}) + (E_{-1}^* - E_0) \qquad [2.4]$$

Where E_0 is the optimized ground state energy of the neutral molecule, E_{-1} and E_{+1} are the optimized energy of the anion and cation state, E^*_{-1} and E^*_{+1} are the energy of the neutral molecule at the optimized anion or cation state geometry respectively, and finally E^*_0 is the energy of the anion or cation state at the optimized neutral state.

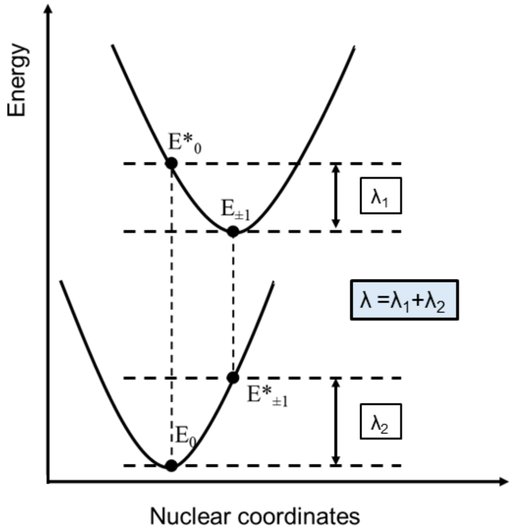

Figure 2.10. Energy diagram used for the prediction of reorganization energies.

2.4 OFET fabrication

As mentioned in the introduction chapter, OFETs serve as a base for directly assessing the electrical mobility of emerging semiconductors, a critical property for next-generation optoelectronic devices. Accordingly, all the materials examined in this thesis have been incorporated as semiconducting layers into OFETs for investigation.

2.4.1 Top Contact-Bottom Gate (TC-BG) configuration

Figure 2.11 shows the process of the fabrication of Top Contact-Bottom gate OFETs. We used commercially highly doped silicon wafers covered with a 300 nm thick thermally grown SiO_2 layer acting as gate electrode and dielectric layer, respectively. One of the advantages of these commercial wafers is that they can be directly used as substrates obtaining efficient reproducibility. First, Si/SiO_2 substrates were cut with dimensions of 2.5 x 1 cm^2 and cleaned twice with ethanol in an ultrasonic bath for 10 minutes. After that, the substrates were dried with a stream of N_2 and finally processed with UV-ozone, using a UVO CLEANER 342-220, for 10 minutes to eliminate any organic contamination of the surface.

Generally, the dielectric surfaces based on inorganic oxides are basically hydrophilic, while the majority of organic materials are mostly hydrophobic. To address this mismatch, surface functionalization using self-assembled monolayers (SAM) is a common approach to modify surface polarity from hydrophilic to hydrophobic. This modification promotes the formation of well-ordered organic semiconductor layers, and it reduces the concentration of charge carrier trap states caused by surface hydroxyl groups, leading to improved charge carrier mobility and enhanced device stability.[43–46] According to that, we employed hexamethyldisilane (HMDS) and octadecyltrichlorosilane (OTS) as SAM reagents. On one hand, for the surface OTS functionalization, the substrates were immersed in a 3.0 mM solution of OTS using hexane as solvent for 1h. Then, the substrates were cleaned by sonication in hexane, acetone and ethanol for 10 minutes each and finally dried by blowing N_2. On the other hand, for HMDS treatment, the silicon cleaned substrates were exposed to HMDS vapor for a week in a closed air-free container.

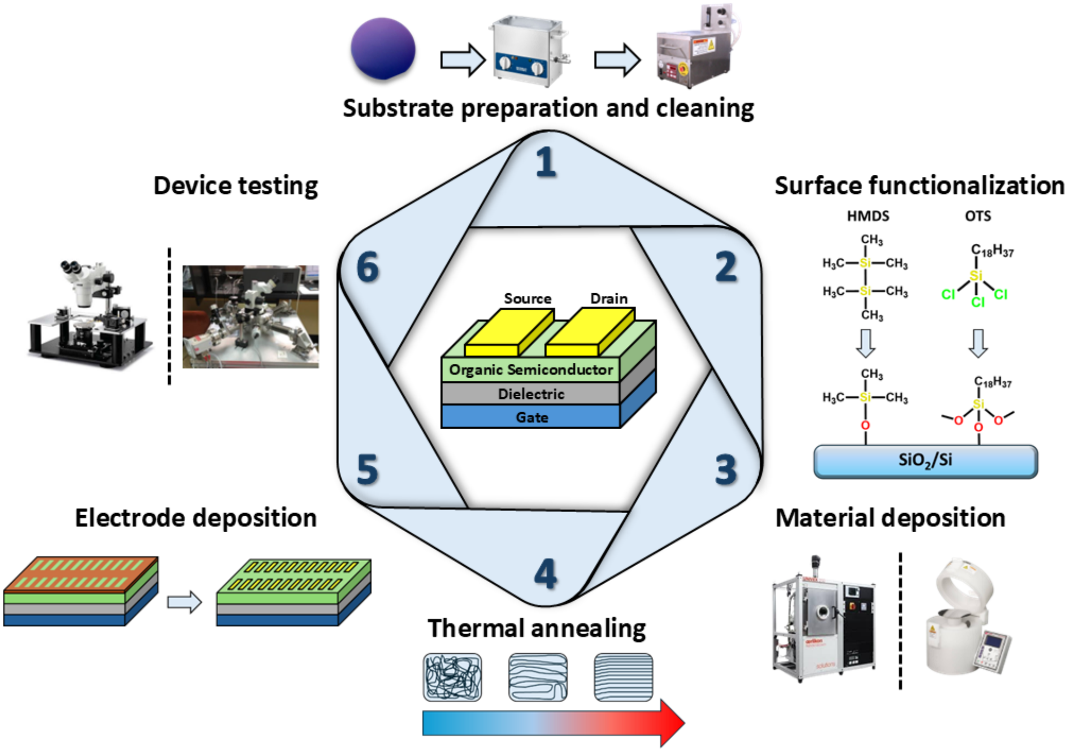

Figure 2.11. Steps for the fabrication of TC-BG OFETs.

After the dielectric surface functionalization, the organic semiconductor is deposited using slow sublimation under vacuum conditions or through solution-processed techniques. In vacuum evaporation, the organic semiconductor is sublimated under vacuum (around 10^{-6} torr) to form a thin film. In our case, we used an OERLIKON UNIVEX 250 evaporator to thermally deposit approximately 50 nm, determined by a quartz microbalance. This technique is commonly used for small molecules, oligomeric organic semiconductors and low-degree polymerization polymers. It is unsuitable for polymers with a higher degree of polymerization, since these are decomposed by cracking at high temperatures. The main advantages of vacuum evaporation are the precise control over the thickness and purity of the deposited film and the ability to achieve highly ordered films by monitoring the substrate temperature and deposition rate. As a result, this method can be excellent to get homogeneous and reproducible semiconductor films.[47]

In contrast to vacuum evaporation, solution process techniques are mainly used because they do not need high deposition temperatures or high vacuum conditions, making them ideal for devices on flexible substrates and to reduce costs. Spin coating is one of the most common techniques for the deposition of organic semiconductors, which consists on dissolving the organic semiconductor in an organic solvent, which is deposited onto a substrate. The substrate is turned at high speeds, and centrifugal forces cover the substrate which results in an uniform film. The thickness of the film in spin-coating is determined by factors such as the solution concentration, rotation speed or viscosity. Additionally, the organic semiconductor must have good solubility to ensure a good deposition process, since it requires concentrated solutions (5-10 mg/ml), and is not ideal for large-area fabrication. We have used a LAURELL TECHNOLOGIES WS-650MZ-23NPP spin-coater for all samples deposited by this technique at 1500 r.p.m. for 30s.[48,49] On the other hand, drop-casting is a simple deposition method, that involves dissolving the organic semiconductor in an organic solvent, depositing the solution onto the substrate and allowing the solvent to evaporate. However, this technique is limited by several drawbacks such as low reproducibility, difficulty in controlling film thickness, morphology and uniformity of the organic semiconductor thin film.[50]

The selection of solvent in solution process techniques plays a crucial role in determining the thin film properties. One of the most important characteristics of the solvent is its volatility. A slow evaporation of the solvent provides additional time to the deposited organic semiconductor molecules to arrange themselves into more crystalline domains. This enhanced crystallinity is generally advantageous, as it often improves charge carrier mobility.

After deposition, some of the organic active materials layers were then subjected to a thermal annealing process to improve the molecular order and crystallinity. Note that, the same thermal annealing process does not work properly for all organic materials. The annealing conditions are optimized for each compound by analysing their effect on the materials morphology, crystallinity and charge transport properties.

The last step in the fabrication of TC-BG OFETs is the deposition of source and drain electrodes. In this sense, gold is the most used metal because is stable and inert, although platinum and aluminium are commonly used as electrodes too. The same OERLIKON UNIVEX 250 evaporator previously used for the evaporation of organic semiconductors is utilized to thermally evaporate 40 nm gold source and drain electrodes through shadow masks. The channel width oscillated between 100 and 5000 µm, while the channel length varied between 10 and 100 µm.

2.4.2 Electrical characterization of OFETs

Electrical characterization of OFETs consists of recording the output and transfer curves that define the transport properties of organic semiconductors in saturation conditions.

The output curves are obtained by keeping the voltage at the gate electrode (V_{GS}) constant and sweeping the voltage between the source and drain electrodes (V_{DS}). To obtain the transfer curves in saturation mode, V_{DS} is kept constant at the value that assumes saturation regime, and a V_G sweep is performed. With the data from the transfer curves, we obtain the characteristic parameters of the OFETs: mobility (μ), intensity ratio (I_{ON}/I_{OFF}) and threshold voltage (V_T). The characterization of the transistors are carried out under vacuum and in air. Vacuum characterization (10^{-6} mbar) has been used due to the environmental instability of some organic semiconductors, especially n-type semiconductors. Atmospheric exposure to ambient O_2 and H_2O can inhibit electron transport, which makes measuring mobilities in inert atmospheres essential for the study of some organic semiconductors.

The following equipment have been used for the OFETs characterization:

- TRINOS VACUUM PROBE STATION: this probe station, custom-made by the company Trinos Vacuum, allows us to characterize the transistors in vacuum. It reaches pressures of 10^{-6} mbar.

- EVERBEING INT'L COMPANY PROBE STATION: commercial probe station that allows the characterization of transistors in atmospheric conditions.

- KEITHLEY 4200-SCS POTENTIOSTAT: this equipment can be connected to the aforementioned probe stations to vary the values of V_{GS} and V_{DS} to obtain the output and transfer curves.

2.5 Morphological characterization of semiconductor thin films

The morphology of thin films in organic semiconductors plays an important role in both injection and charge transport processes, which are key to device operation. Efficient charge transport demands highly ordered and uniform films, in which large crystalline domains are well interconnected.[51,52] Based on this considerations, two different techniques have been used to characterize the semiconductor film: X-ray diffraction (XRD) and Atomic Force Microscopy (AFM).

- X-rays are a form of high-energy, short-wavelength electromagnetic radiation. When an X-ray beam hits a solid material, some the beam is scattered in all directions. The rest of the beam can give rise to the phenomenon of X-ray diffraction, which occurs if there is an ordered arrangement of atoms and Bragg's Law is fulfilled (see equation [2.5]).

$$n \cdot \lambda = 2 \cdot d \cdot sen\,(\theta) \qquad [2.5]$$

Where n is an integer number, λ is the wavelength of the incident X-ray, d is the distance between the planes of the crystal lattice, and θ is the angle of incidence, as shown in Figure 2.12. X-ray diffractograms are a very useful tool for determining the degree of ordering and crystallinity of organic semiconductor thin films. The diffractograms have been obtained with the semiconductor thin film, deposited under the same conditions and on the same substrate used for fabricating OFETs. BRUKER D8 DISCOVER diffractometer was used to obtain X-ray diffraction patterns of organic semiconductor thin films by employing a scan (2θ) from 2 to 35º with CuK$_{\alpha 1}$ X-ray radiation (0.154 nm) was used.

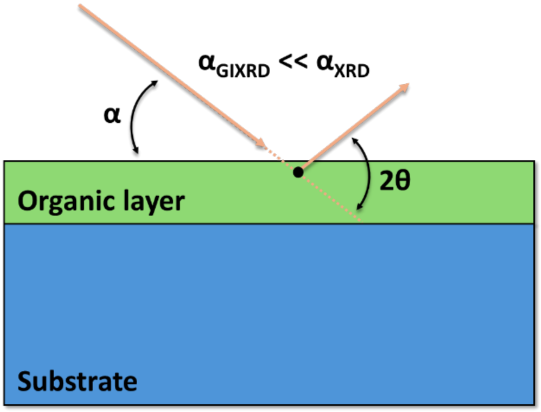

Figure 2.12. Representation of XRD characterization technique.

- The atomic force microscope is a mechanical-optical instrument capable of detecting forces in the order of nanonewtons between a tip of nanometric diameter and the sample. The tip is coupled to a microscopic bar. A laser beam reflected on its back can record the small deflections of the bar. A piezoelectric auxiliary system moves the sample three-dimensionally, while the tip (cantilever) runs along the surface, recording its topography. Consequently, AFM images help us to visualize the different topographies obtained from the semiconductor layers, see Figure 2.13. These topographies are highly dependent on the treatment performed on the dielectric and the thermal treatments. Therefore, AFM images have been recorded on the semiconductor deposited under equal conditions and on the same substrates as the semiconductor used for the fabrication of OFETs. To obtain AFM images of the thin films we have used a multimode atomic force microscope with a Nanoscope V Controller (Bruker Corporation, Billerica, MA, USA) working in tapping mode. An attractive-repulsive interaction is established between the tip and the sample with a separation in a range of 1 to 100 Å, depending on the amplitude and frequency of the vibration of the cantilever.

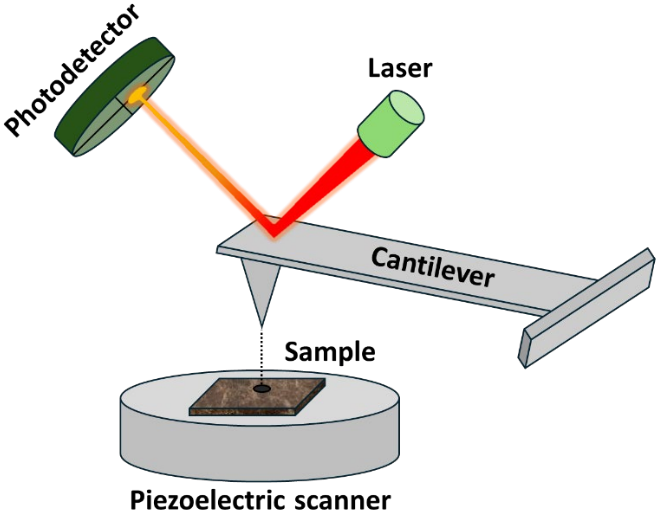

Figure 2.13. Scheme of the AFM characterization technique.

2.6 References

1 W. W. Parson and C. Burda, *Modern optical spectroscopy: From fundamentals to applications in chemistry, biochemistry and biophysics: Third edition*, 2023.

2 M. Bunzel and M. H. Penner, Basic Principles of Spectroscopy, 2024, 65–75.

3 Bertolucci, D. C, Harris and M. D, *Symmetry spectroscopy*, 1989.

4 P. J. Worsfold, UV—visible Spectroscopy and its Applications, *Anal Chim Acta*, 1993, **284**, 245.

5 C. A. Parker and W. T. Rees, Fluorescence spectrometry. A review, *Analyst*, 1962, **87**, 83–111.

6 H. G. M. Edwards, *Modern Raman spectroscopy—a practical approach. Ewen Smith and Geoffrey Dent . John Wiley and Sons Ltd, Chichester, 2005. Pp. 210. ISBN 0 471 49668 5 (cloth, hb); 0 471 49794 0 (pbk)* , 2005, vol. 36.

7 P. Rostron, S. Gaber and D. Gaber, Raman Spectroscopy , Review, 2016, **0869**, 50–64.

8 H. I. Gonev, E. Jones, C. Y. Chang, Y. Ie, S. Chatterjee and T. M. Clarke, Invariant Charge Carrier Dynamics Using a Non-Planar Non-Fullerene Acceptor across Multiple Processing Solvents, *Journal of Physical Chemistry C*, 2024, **128**, 6758–6766.

9 C. Castiglioni, M. Tommasini and G. Zerbi, Raman spectroscopy of polyconjugated molecules and materials: confinement effect in one and two dimensions, *Philosophical Transactions of the Royal Society of London. Series A: Mathematical, Physical and Engineering Sciences*, 2004, **362**, 2425–2459.

10 B. Stuart, Infrared Spectroscopy, *Kirk-Othmer Encyclopedia of Chemical Technology*, 2015, 1–18.

11 J. M. Thompson, Infrared Spectroscopy, DOI:10.1201/9781351206037.

12 T. Hong, J. Y. Yin, S. P. Nie and M. Y. Xie, Applications of infrared spectroscopy in polysaccharide structural analysis: Progress, challenge and perspective, *Food Chem X*, 2021, **12**, 100168.

13 G. P. Kissling, B. Ruhstaller and K. P. Pernstich, Measuring frontier orbital energy levels of OLED materials using cyclic voltammetry in solution, *Org Electron*, 2023, **122**, 106888.

14 C. M. Cardona, W. Li, A. E. Kaifer, D. Stockdale and G. C. Bazan, Electrochemical Considerations for Determining Absolute Frontier Orbital Energy Levels of Conjugated Polymers for Solar Cell Applications, *Advanced Materials*, 2011, **23**, 2367–2371.

15 R. E. M. Willems, C. H. L. Weijtens, X. de Vries, R. Coehoorn and R. A. J. Janssen, Relating Frontier Orbital Energies from Voltammetry and Photoelectron Spectroscopy to the Open-Circuit Voltage of Organic Solar Cells, *Adv Energy Mater*, 2019, **9**, 1803677.

16 A. de la Peña, I. Arrechea-Marcos, M. J. Mancheño, M. C. Ruiz Delgado, J. T. López Navarrete, J. L. Segura and R. Ponce Ortiz, Tuning of the Electronic Levels of Oligothiophene–Naphthalimide Assemblies by Chemical Modification, *Chemistry - A European Journal*, 2016, **22**, 13643–13652.

17 W. Kaim and J. Fiedler, Spectroelectrochemistry: the best of two worlds, *Chem Soc Rev*, 2009, **38**, 3373–3382.

18 P. Hohenberg and W. Kohn, Inhomogeneous electron gas, *Physical Review*, 1964, **136**, B864.

19 P. Hohenberg, W. K.-Phys. Rev and undefined 1964, Density functional theory (DFT), *nomad.fhi.mpg.de*.

20 W. Kohn, A. D. Becke and R. G. Parr, Density functional theory of electronic structure, *Journal of Physical Chemistry*, 1996, **100**, 12974–12980.

21 M. A. M. J. Frisch, G. W. Trucks, H. B. Schlegel, G. E. Scuseria, H. Robb, J. R. Cheeseman, G. Scalmani, V. Barone, G. A. Petersson, R. Nakatsuji, X. Li, M. Caricato, A. Marenich, J. Bloino, B. G. Janesko, and D. J. F. G. Gomperts, B. Mennucci, H. P. Hratchian, J. V. Ort and W. C. 2009. 09, Revision C.01. Gaussian, Inc., No Title.

22 and D. J. F. M. J. Frisch, G. W. T., H. B. Schlegel, G. E. Scuseria, M. A. Robb, J. R. Cheeseman, G. Scalmani, V. Barone, G. A. Petersson, H. Nakatsuji, X. Li, M. Caricato, A. V. Marenich, J. Bloino, B. G. Janesko, R. Gomperts, B. Mennucci, H. P. Hratchian, J. V. Orti, Gaussian 16, Revision A.03.

23 C. Lee, W. Yang and R. G. Parr, Development of the Colle-Salvetti correlation-energy formula into a functional of the electron density, *Phys Rev B*, 1988, **37**, 785.

24 A. D. Becke, Density-functional thermochemistry. I. The effect of the exchange-only gradient correction, *J Chem Phys*, 1992, **96**, 2155–2160.

25 T. Yanai, D. P. Tew and N. C. Handy, A new hybrid exchange–correlation functional using the Coulomb-attenuating method (CAM-B3LYP), *Chem Phys Lett*, 2004, **393**, 51–57.

26 J. Da Chai and M. Head-Gordon, Systematic optimization of long-range corrected hybrid density functionals, *Journal of Chemical Physics*, DOI:10.1063/1.2834918/71104.

27 J. Da Chai and M. Head-Gordon, Long-range corrected hybrid density functionals with damped atom-atom dispersion corrections, *Physical Chemistry Chemical Physics*, 2008, **10**, 6615–6620.

28 Y. Zhao and D. G. Truhlar, The M06 suite of density functionals for main group thermochemistry, thermochemical kinetics, noncovalent interactions, excited states, and transition elements: Two new functionals and systematic testing of four M06-class functionals and 12 other function, *Theor Chem Acc*, 2008, **120**, 215–241.

29 W. J. Hehre, K. Ditchfield and J. A. Pople, Self-consistent molecular orbital methods. XII. Further extensions of gaussian-type basis sets for use in molecular orbital studies of organic molecules, *J Chem Phys*, 1972, **56**, 2257–2261.

30 M. Francl, W. Pietro, W. Hehre, … J. B.-T. J. of and undefined 1982, Self-consistent molecular orbital methods. XXIII. A polarization-type basis set for second-row elements, *pubs.aip.org*.

31 J. Tomasi, B. Mennucci and R. Cammi, Quantum mechanical continuum solvation models, *Chem Rev*, 2005, **105**, 2999–3093.

32 R. Improta, V. Barone, G. Scalmani and M. J. Frisch, A state-specific polarizable continuum model time dependent density functional theory method for excited state calculations in solution, *Journal of Chemical Physics*, DOI:10.1063/1.2222364/908887.

33 Chemcraft - graphical software for visualization of quantum chemistry computations. https://www.chemcraftprog.com.

34 E. Runge and E. K. U. Gross, Density-functional theory for time-dependent systems, *Phys Rev Lett*, 1984, **52**, 997–1000.

35 H. H. Heinze, A. Görling and N. Rösch, An efficient method for calculating molecular excitation energies by time-dependent density-functional theory, *J Chem Phys*, 2000, **113**, 2088–2099.

36 K. Burke, J. Werschnik and E. K. U. Gross, Time-dependent density functional theory: Past, present, and future, *Journal of Chemical Physics*, DOI:10.1063/1.1904586/932825.

37 N. M. O'Boyle, A. L. Tenderholt and K. M. Langner, cclib: A library for package-independent computational chemistry algorithms, *J Comput Chem*, 2008, **29**, 839–845.

38 M. R. Pederson, T. Baruah, P. B. Allen and C. Schmidt, Density-functional-based determination of vibrational polarizabilities in molecules within the double-harmonic approximation: Derivation and application, *J Chem Theory Comput*, 2005, **1**, 590–596.

39 Chemcraft - Graphical program for visualization of quantum chemistry computations, www.chemcraftprog.coml.

40 V. Coropceanu, J. Cornil, D. A. da Silva Filho, Y. Olivier, R. Silbey and J. L. Brédas, Charge transport in organic semiconductors, *Chem Rev*, 2007, **107**, 926–952.

41 J. L. Brédas, D. Beljonne, V. Coropceanu and J. Cornil, Charge-transfer and energy-transfer processes in π-conjugated oligomers and polymers: A molecular picture, *Chem Rev*, 2004, **104**, 4971–5003.

42 B. C. Lin, C. P. Cheng and Z. P. M. Lao, Reorganization energies in the transports of holes and electrons in organic amines in organic electroluminescence studied by density functional theory, *Journal of Physical Chemistry A*, 2003, **107**, 5241–5251.

43 M. H. Yoon, C. Kim, A. Facchetti and T. J. Marks, Gate dielectric chemical structure-organic field-effect transistor performance correlations for electron, hole, and ambipolar organic semiconductors, *J Am Chem Soc*, 2006, **128**, 12851–12869.

44 S. Casalini, C. A. Bortolotti, F. Leonardi and F. Biscarini, Self-assembled monolayers in organic electronics, *Chem Soc Rev*, 2017, **46**, 40–71.

45 X. Cheng, Y. Y. Noh, J. Wang, M. Tello, J. Frisch, R. P. Blum, A. Vollmer, J. P. Rabe, N. Koch and H. Sirringhaus, Controlling Electron and Hole Charge Injection in Ambipolar Organic Field-Effect Transistors by Self-Assembled Monolayers, *Adv Funct Mater*, 2009, **19**, 2407–2415.

46 A. Tewari, K. Björkström, A. M. Ghafari, E. Macchia, L. Torsi and R. Österbacka, Stability of thiol-based self-assembled monolayer functionalized electrodes in EG-OFET-based applications, *FlatChem*, 2023, **42**, 100553.

47 R. A. Laudise, C. Kloc, P. G. Simpkins and T. Siegrist, Physical vapor growth of organic semiconductors, *J Cryst Growth*, 1998, **187**, 449–454.

48 D. M. DeLongchamp, B. M. Vogel, Y. Jung, M. C. Gurau, C. A. Richter, O. A. Kirillov, J. Obrzut, D. A. Fischer, S. Sambasivan, L. J. Richter and E. K. Lin, Variations in semiconducting polymer microstructure and hole mobility with spin-coating speed, *Chemistry of Materials*, 2005, **17**, 5610–5612.

49 G. Zhao, P. Gu, H. Dong, W. Jiang, Z. Wang and W. Hu, High-Mobility N-Type Organic Field-Effect Transistors of Rylene Compounds Fabricated by a Trace-Spin-Coating Technique, *Adv Electron Mater*, 2016, **2**, 1500430.

50 H. R. Tseng, H. Phan, C. Luo, M. Wang, L. A. Perez, S. N. Patel, L. Ying, E. J. Kramer, T. Q. Nguyen, G. C. Bazan and A. J. Heeger, High-mobility field-effect transistors fabricated with macroscopic aligned semiconducting polymers, *Advanced Materials*, 2014, **26**, 2993–2998.

51 H. N. Tsao and K. Müllen, Improving polymer transistor performance via morphology control, *Chem Soc Rev*, 2010, **39**, 2372–2386.

52 S. Chen, Z. Li, Y. Qiao and Y. Song, Solution-processed organic semiconductor crystals for field-effect transistors: from crystallization mechanism towards morphology control, *J Mater Chem C Mater*, 2021, **9**, 1126–1149.

3

Results and discussion

Table of contents

CONTENTS

Chapter I:

Tuning charge stabilization and transport in naphthalimide-based semiconductors: the role of fused-ring and core modifications

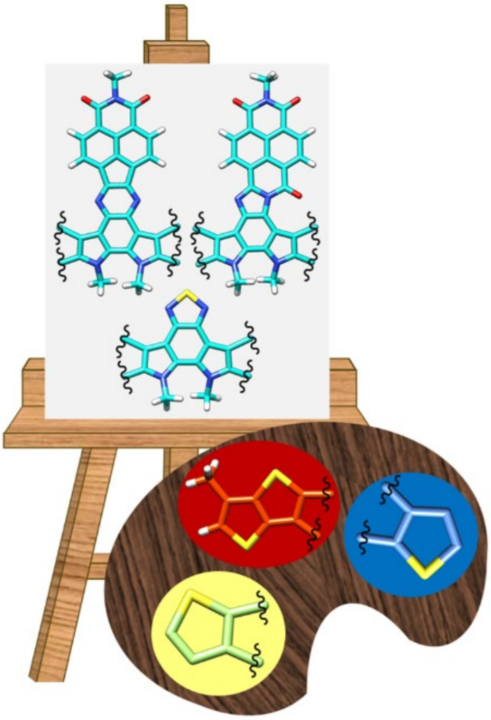

Table of contents

CONTENTS

I.1 Introduction

The development of small molecules and organic π-conjugated polymers has generated significant interest due to their tuneable electronic and structural properties. This, combined with their flexibility, low molecular weight, high solution processability, and lower cost compared to inorganic semiconductors, has brought organic electronics into the spotlight. These materials are used as active materials in a wide variety of devices, such as OLEDs[1,2], OPTs[3–5], OSCs[6–9], OFETs[10–13], and more recently in wearable electronics devices[14,15] and memory arrays[16,17]. However, despite the great advances in organic electronics in recent decades, their performance often lags behind that of their inorganic counterparts, primarily due to the lower mobility of charge carriers. Therefore, the design of new organic semiconductors with improved properties is essential to overcome these limitations.[18,19]

In this context, various molecular building blocks with tuneable properties and high performance have been employed in organic electronic devices.[20–22] In particular, the design and synthesis of new materials have gained great interest, as they allow obtaining compounds with efficient charge transport capacity and tuneable HOMO/LUMO energy levels.[23,24] In this sense, it has been shown that the combination of donor and acceptor units through different rigid and conjugated bonds can lead to functional materials with tuneable and even unexpected optical and electrochemical properties. Furthermore, these materials have shown remarkable performance in OFETs and OSCs devices[25–31]. Electron-acceptor imide units, particularly naphthalimide derivatives, are often employed as electron acceptors, facilitating the production of processable organic materials with low LUMO energy levels and excellent optical, electrochemical and electrical properties.[32–36] On the other hand, the covalent conjugation of naphthalimide units with strong donor structures, such as oligothiophenes or triarylamines, has proven to be a promising strategy for developing new materials.[37,38] In this chapter, we explore this type of D-A structures.

Over the past five years, the fused ring electron acceptor (FREA) strategy has proven to be an effective tool to modulate the donor capacity of organic materials without the need to introduce strong donor moieties. Representative examples of this approach are the ITIC, IDIC and Y6 molecules, which incorporate electron acceptors at terminal positions and allow a precise modulation of their donor capacity by controlling the length of the donor units.[39,40]

In this study, we have characterized a new family of compounds combining electron-withdrawing naphthalimide units and thiophene-based donor moieties connected by rigid and conjugated nitrogen connectivity units (Figure I.1). To fine-tune the HOMO energy levels, we have modified the length of the donor moiety (**BTD-ext**, **NDI-ext** and

NIP-ext) and explored different isomers (**BTD-inv**, **NDI-inv** and **NIP-inv**). As for the LUMO orbital, the incorporation of imidazole or pyrazine linkers, covalently linked to the naphthalimide unit, has allowed to precisely modulate its energy levels. Also, we demonstrate that the ring fusion strategy in the donor moiety can significantly modify the charge transport properties of these organic semiconductors.

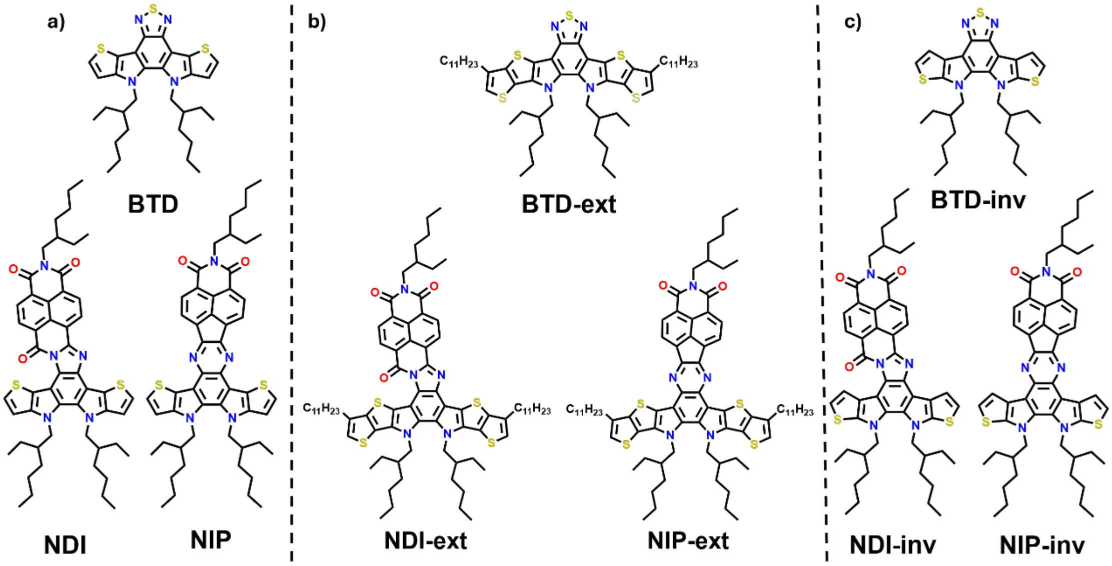

Figure I.1. Structure of the naphthalimide-based semiconductors described in this work: a) **BTD** derivatives, b) **BTD-ext** derivatives and c) **BTD-inv** derivatives.

I.2 Structural properties

The structure of the studied compounds was optimized by DFT. The calculations reveal a moderate distortion, of approximately 5-10 degrees, in the derived benzothiadiazole fragment in all the analyzed molecules. Furthermore, when comparing the different naphthalimide derivatives, we observed that the compounds with imidazole unit (**NDI** derivatives) present a higher torsion angle in the connecting unit of around 16° compared to the pyrazine derivatives (**NIP** derivatives), regardless of the length of the π-conjugation chain or the isomer considered. In contrast, the **NIP** derivatives showed practically planar structures, as shown in Figure I.2.

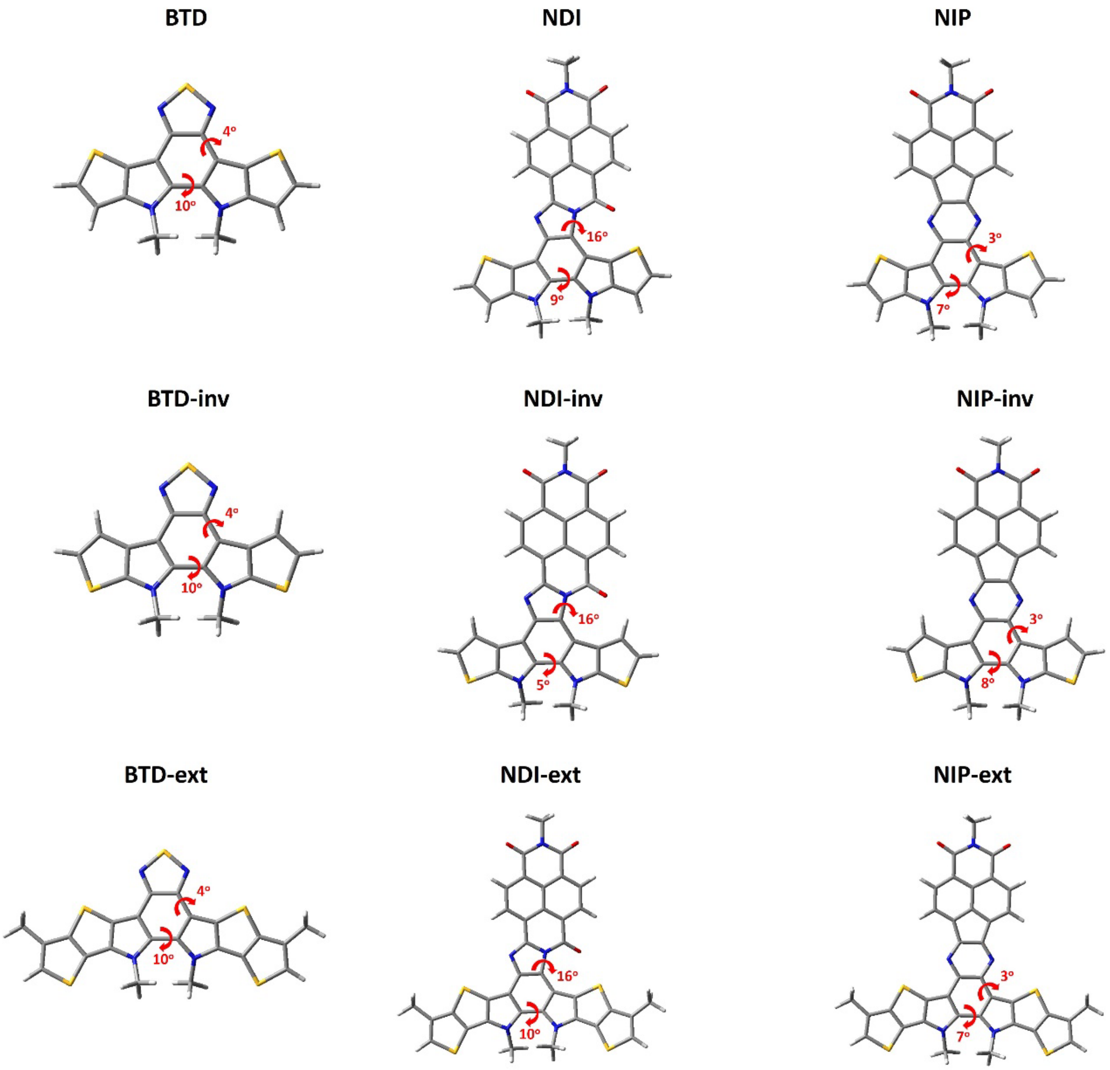

Figure I.2. DFT-computed global minimum structures for the different units studied at B3LYP/6-31G** level of theory.

Table I.1 presents the energy values of the calculated molecular orbitals (MO) for the studied compounds. The results show that the introduction of the naphthalimide unit significantly stabilizes the LUMO energy level from -1.71 eV in **BTD** to -2.77 eV and -3.14 eV in **NIP** and **NDI** respectively. This effect is less pronounced in the pyrazine derivatives compared to the imidazole derivatives, a trend also observed in other oligothiophene-naphthalimide assemblies, due to the lower electronegative character of pyrazine.[41] Furthermore, the LUMO energy values trend is similar within the family of the extended compounds, going from -1.79 eV in **BTD-ext** to -2.82 eV and -3.18 eV in **NIP-ext** and **NDI-ext**, and in the inverted compounds, where these values oscillate between -1.69 eV for **BTD-inv**, -2.81 eV and -3.17 eV for **NIP-inv** and **NDI-inv**, respectively. This scenery suggests that the energy of LUMO orbital is mainly determined by the naphthalimide unit, which is common in the extended and inverted compounds.

On the other hand, the incorporation of the arylenimide fragment has no remarkable impact on the HOMO energy levels. However, a slight destabilization of this level is observed when the number of fused thiophenes increases. We found values of -4.95 eV, -5.01 eV and -5.08 eV for **BTD**, **NDI** and **NIP**, respectively, compared with the values of -4.80 eV, -4.85 eV and -4.91 eV for **BTD-ext, NDI-ext and NIP-ext**. In the case of isomers with inversion of the more external thiophene rings a slight stabilization is observed, with values of -5.06 eV, -5.13 eV and -5.20 eV for **BTD-inv, NDI-inv and NIP-inv**, respectively. As a result, NDI derivatives, having the lower energy levels, exhibit substantially smaller energy gaps, with the extended derivative (**NDI-ext**) showing the lowest value of 1.67 eV. It is noteworthy that all the studied systems exhibit HOMO energy levels close to -5 eV, making them suitable for hole injection from gold electrodes. In contrast, only NDI derivatives show LUMO energy levels deep enough (lower than -3 eV) to facilitate electron injection.

Compound	LUMO (eV)	HOMO (eV)	E_{gap} (eV)
BTD	-1.71	-4.95	3.24
NDI	-3.14	-5.01	1.87
NIP	-2.77	-5.08	2.31
BTD-ext	-1.79	-4.80	3.01
NDI-ext	-3.18	-4.85	1.67
NIP-ext	-2.82	-4.91	2.09
BTD-inv	-1.69	-5.06	3.37
NDI-inv	-3.17	-5.13	1.96
NIP-inv	-2.81	-5.20	2.39

Table I.1. DFT-calculated (B3LYP/6-31G**) HOMO and LUMO energy levels.

The internal reorganization energies for electron and hole transport for the studied semiconductors are shown in Figure I.3. The reorganization energy (λ) is a key parameter reflecting the structural reorganization required to accommodate the charge defect during transport, with low λ values being a fundamental requirement for efficient charge conduction. In our study, all systems exhibit lower reorganization energies for p-type transport compared to n-type transport. This suggests that the accommodation of positive charges is more favourable than negative charges, thus facilitating hole transport. When analyzing the NIP and NDI families, the calculated values indicate that the reorganization energy for electron transport is similar within each family, regardless of the thienopyrrole core length or isomeric structure. This is in concordance with the electron density delocalization of the LUMO which is mainly localized in the naphthalimide unit as it will be discussed later. This suggests that the electron defect is mainly stabilized through the naphthalimide unit. In contrast, a decrease in the reorganization energy for hole transport is observed by extending the thienopyrrole unit, indicating a greater ease in accommodating positive charges in systems with a longer conjugated core.

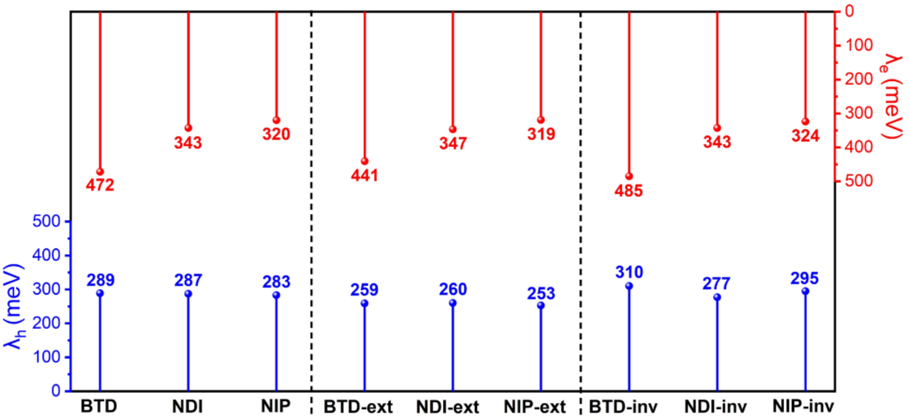

Figure I.3. Theoretically calculated (B3LYP/6-31G** level) hole (blue) and electron (red) reorganization energies for studied compounds.

I.3 Optical and electrochemical properties

The incorporation of branched alkyl chains in the imide and pyrrole sites of the studied compounds improves their solubility, reaching values higher than 30 mg/mL. This allows studying their optical and electrochemical properties by UV-Vis spectroscopy in solution and in the solid state (thin film), as well as by cyclic voltammetry analysis. Tables I.2 and I.3 summarize the most relevant optical and electrochemical parameters obtained from the experimental measurements.

			UV-Vis^a			
	[C] (µM)	$\lambda_{max}{}^b$ (nm)	$\varepsilon_{\lambda max}{}^c$ (nm)	λ_{ICT} (nm)	$\lambda_{onset}{}^d$ (nm)	$Eg^{opt,e}$ (eV)
BTD	5	316	26930	441	495	2.51
NIP	5	395	42360	583	690	1.79
NDI	5	374	35300	670	834	1.49
BTD-ext	5	369	73826	470	546	2.27
NIP-ext	5	372	197484	618	740	1.67
NDI-ext	5	360	73825	674	867	1.43
BTD-inv	5	368	14015	426	486	2.55
NIP-inv	5	398	22928	551	664	1.87
NDI-inv	5	363	21869	641	785	1.57

Table I.2. ^{a} UV-Vis absorption in $CHCl_3$ solution. ^{b} Absorption maxima in solution, ^{c} Molar extinction coefficient to the referred wavelength. ^{d} Onset wavelength for the absorption band. ^{e} Energy band gap derived from the low-energy absorption edge using the equation $E_g^{opt} = 1240/\lambda_{onset}$.

As observed in Figure I.4 and table I.2, the substitution of the benzothiadiazole core by naphthalimide units through planar and conjugated bonds induces a red-shift in the lowest absorption band (named as λ_{ICT} in Table I.2) of the UV-Vis spectra, with this effect been more pronounced in the NDI derivative as a consequence to the more pronounced electron-acceptor character of the imidazole group. In addition, an increase in the molar absorption coefficient (ε) is found for the naphthalimide-based derivatives. This effect is particularly noticeable in pyrazine-based (**NIP** derivatives) semiconductors, whose ε values are up to twice as high as those observed for BTD analogues, probably due to the extended π structure and the higher planarity,[42] as shown in Figure I.1.

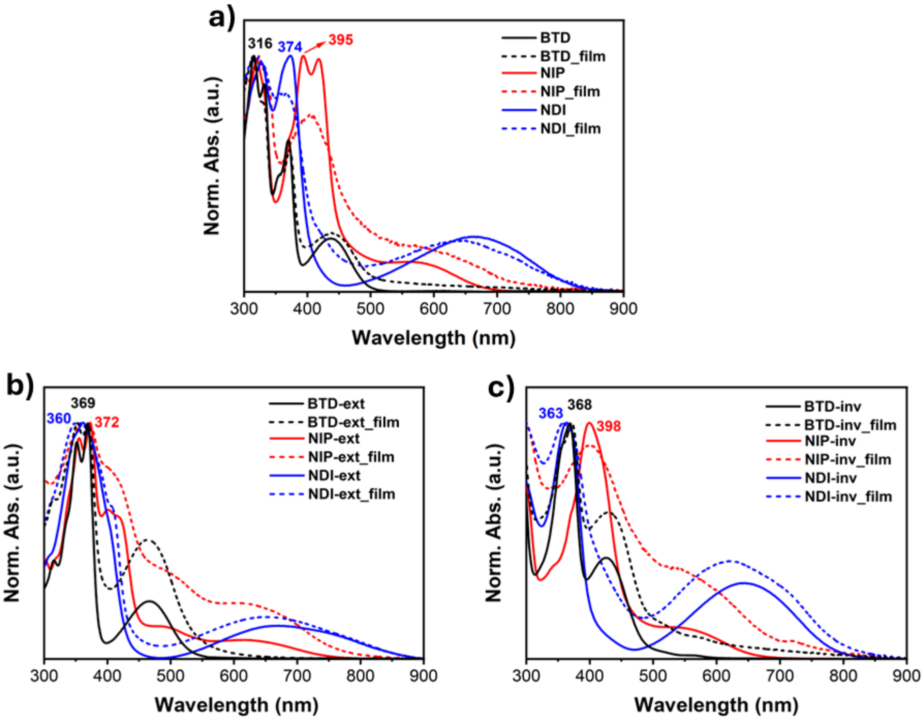

Figure I.4. UV-Vis absorption spectra of a) **BTD** (black), **NIP** (red) and **NDI** (blue) in solution (solid line) and thin-film (dashed line), b) **BTD-ext** (black), **NIP-ext** (red) and **NDI-ext** (blue) in solution (solid line) and thin-film (dashed line) and c), **BTD-inv** (black), **NIP-inv** (red) and **NDI-inv** (blue) in solution (solid line) and thin-film (dashed line).

Regarding the higher energy band (λ_{max}), it is observed that all pyrazine-based assemblies present a red-shifted absorption maximum compared to their imidazole-based analogues, especially in the smaller systems, with a maximum absorption band at 395 nm for **NIP** and 374 nm for **NDI**. Also, when evaluating the thiophene inversion, we observe a red-shift of λ_{max} in **NDI-inv** (363 nm) compared to **NIP-inv** (398 nm). However, when compared to **BTD-inv**, when an imidazole unit is introduced, a blue-shift occurs (363 nm in **NDI-inv** and 368 nm in **BTD-inv**). On the other hand, when analyzing the effect of thiophene extension in the π-conjugated systems, we found out that both **NIP-ext** and **NDI-ext** derivatives present similar λ_{max} values in solution (372 nm for **NIP-ext** and 360 nm for **NDI-ext**), compared to the non-functionalized **BTD-ext** analogue (369 nm).

Besides, as for the lowest energy absorption band, the extension of the donor fragment increases this absorption towards the NIR region, being more pronounced in the **NDI-ext** derivative, with a broad absorption band around 674 nm. On the other hand, **NDI-ext** shows a red-shift of 56 nm respect to **NIP-ext**. The same trend also has been observed in the smaller **NDI** and **NIP** semiconductors, with an absorption band at 583 nm for **NIP** and 670 nm for **NDI**, and for the inverted analogues (551 nm for **NIP-inv** and 641 nm for **NDI-inv**).

Furthermore, the modification of the π-conjugated chain involves changes in the optical properties of these materials, especially with the inversion of the fused thiophene unit, which leads to i) a significant decrease of the molar absorption coefficient (ε), probably due to the non-linearity of the donor fragment, and ii) a blue-shift in the ICT band, evidenced by the λ_{onset} values compared to the non-inverted systems. This latter trend is supported by TD-DFT calculations, as shown in Table I.3

Compound	Electronic transitions	Description	λ (nm)	f
BTD	$S_0 \rightarrow S_1$	H→L (97%)	450	0.14
NIP	$S_0 \rightarrow S_1$	H→L (98%)	629	0.11
NDI	$S_0 \rightarrow S_1$	H→L (91%)	810	0.10
BTD-ext	$S_0 \rightarrow S_1$	H→L (97%)	484	0.26
NIP-ext	$S_0 \rightarrow S_1$	H→L (99%)	698	0.12
NDI-ext	$S_0 \rightarrow S_1$	H→L (97%)	920	0.10
BTD-inv	$S_0 \rightarrow S_1$	H→L (99%)	435	0.12
NIP-inv	$S_0 \rightarrow S_1$	H→L (98%)	606	0.10
NDI-inv	$S_0 \rightarrow S_1$	H→L (64%)	771	0.04

Table I.3. The lowest-energy electronic transition obtained by TD-DFT (B3LYP/6-31G**) for **BTD**, **NIP** and **NDI** derivatives.

UV-Vis absorption spectra of **BTD**, **NDI** and **NIP** derivatives in thin film show almost negligible differences with solution spectra. All derivatives show a similar absorption profiles in solution and thin film, with two family of absorption bands around 400 and 650 nm. This coincidence suggests that, despite the extensive π-conjugated structure of these systems, the introduction of long branched alkyl chains into their structure not only improves processability, also prevents the formation of large supramolecular aggregates in the films.

TD-DFT theoretical calculations were performed to understand the nature of the electronic absorption bands. The lowest energy absorption bands in all studied systems are theoretically attributed to the HOMO-LUMO transition. As observed from the frontier molecular orbital topologies shown in Figure I.5, this electronic transition exhibits a clear intramolecular charge transfer (ICT) character. While the HOMO is localized on the most electron-rich region of the semiconductor, the thienopyrrolic part, the LUMO is localized on the most electron-deficient unit, the thiadiazol in the BTD systems, and the naphthalimide group in the NDI and NIP systems. This electronic absorption band is more intense and red-shifted in imidazole derivatives (**NDI** derivatives) compared to pyrazine derivatives (**NIP** derivatives).

To study the electrochemical properties of these organic semiconductors, cyclic voltammetry experiments were performed in an argon atmosphere, using dry solutions of dichloromethane and 0.1 M NBu_4PF_6 as supporting electrolyte. As shown in Table I.4 and Figure I.6, the results show amphoteric redox organic semiconductors, in NIP and NDI derivatives, with lower oxidation potentials compared to BTD derivatives. **BTD** system displays an oxidation potential of 0.42 eV, while **NIP** and **NDI** show a value of 0.37 eV**.** Furthermore, it is possible to modify the oxidation potential values by extending the thienopyrrole unit (extended systems) or, by modifying the position of the sulfur atom in the thiophene unit (inverted systems), as we will explore now in detail.

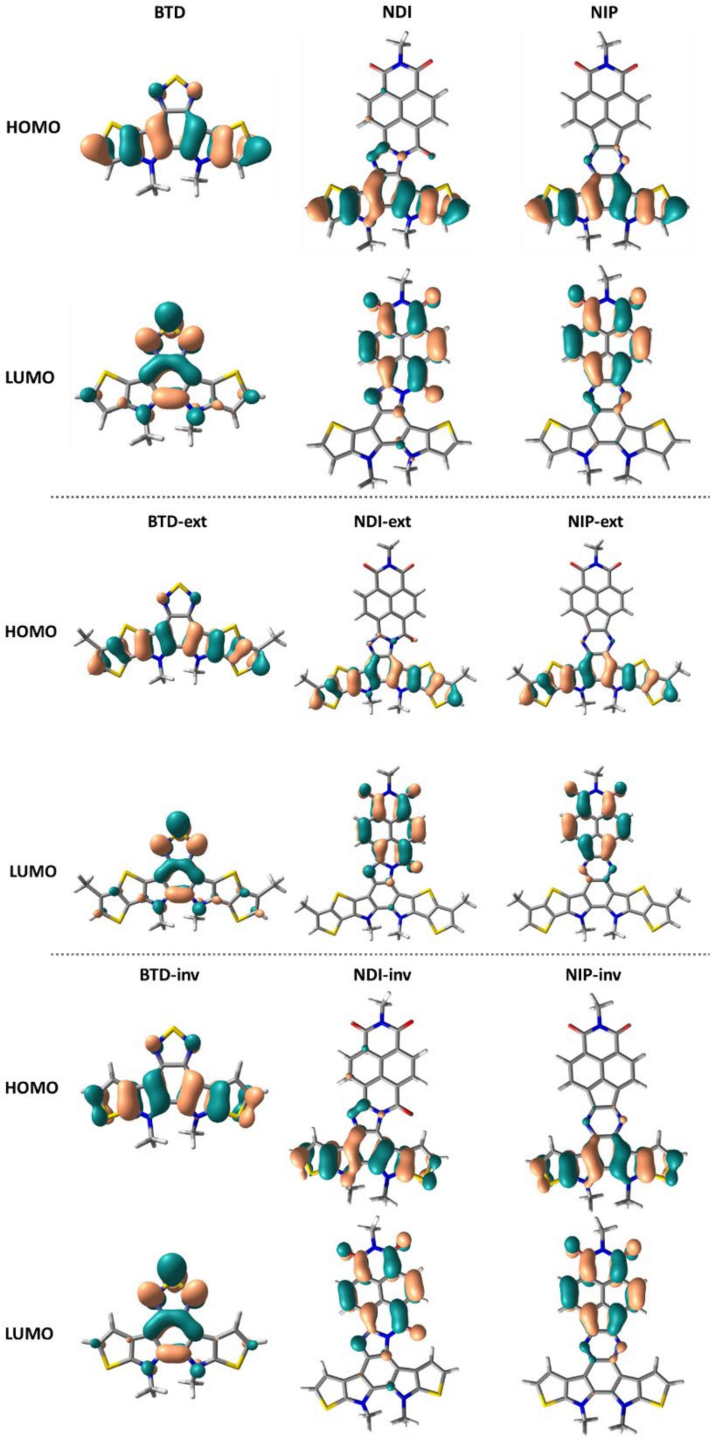

Figure I.5. DFT-calculated (B3LYP/6-31G**) molecular orbital topologies of all compounds under study (isovalue of 0.035 a.u.).

The experimental values summarized in Table I.4 demonstrate that, despite their similar chemical structures, slight changes in the position of the heterocyclic sulfur atoms can significantly alter the oxidation processes. For instance, the oxidation potentials increase to 0.56 eV in **BTD-inv** (0.42 eV for **BTD**), 0.49 eV in **NIP-inv** (0.37 eV for **NIP**) and 0.46 eV in **NDI-inv** (0.37 eV for **NDI**), compared to the non-inverted systems. Finally, the oxidative capacity of these semiconductors can be significantly improved by extending the effective conjugation at the thienopyrrole core. In fact, the values of oxidation potential decrease up to 0.26 eV for **BTD-ext** and **NDI-ext**, and 0.27 eV for **NIP-ext**. Thus, the larger semiconductors, **NIP-ext** and **NDI-ext**, exhibit a shift of approximately 0.10 V towards less positive potentials compared to their smaller derivatives, **NIP** and **NDI**, enhancing their oxidising ability.

	Cyclic Voltammetry^a					
	$E^{1/2}_{Red\ I}$ (V)	$E^{1/2}_{RedII}$ (V)	$E^{1/2}_{Ox\ I}$ (V)	$E_{HOMO}{}^{b}$ (eV)	$E_{LUMO}{}^{c}$ (eV)	$Eg^{elec,\ d}$ (eV)
BTD	-	-	0.42	-5.52	-3.01^e	-
NIP	-1.37	-1.74	0.37	-5.47	-3.73	1.73 (2.31)^f
NDI	-1.13	-1.43	0.37	-5.47	-3.97	1.50 (1.87)^f
BTD-ext	-	-	0.26	-5.36	-3.08^e	-
NIP-ext	-1.36	-1.65	0.27	-5.37	-3.74	1.63 (2.09)^f
NDI-ext	-1.12	-1.49	0.26	-5.36	-3.98	1.38 (1.67)^f
BTD-inv	-	-	0.56	-5.66	-3.11^e	-
NIP-inv	-1.37	-1.77	0.49	-5.59	-3.73	1.86 (2.39)^f
NDI-inv	-1.14	-1.49	0.46	-5.56	-3.96	1.60 (1.96)^f

Table I.4. ^{a}Electrochemical values obtained from experimental measurements for the organic semiconductors studied in this work. ^{a}Cyclic voltammetry recorded in DCM/TBAPF6 (0.1 M) at a scan rate of 0.10 V/s using Pt as working and the counter electrode, and Fc/Fc$^+$ as reference. ^{b}Estimated from E_{Homo} = -5.1 eV - $E^{1/2}$ox I. ^{c}Estimated from E_{LUMO} = -5.1 eV - $E^{1/2}$red I ^{d}Estimated from $E_{gap}{}^{elec}$ = E_{HOMO} - E_{LUMO}. ^{e}Estimated from $E_{gap}{}^{opt}$ = E_{HOMO} - E_{LUMO}. $^f E_{gap}$ for easier comparison with $E_{gap}{}^{elec}$.

As for the electron acceptor capacity of these organic semiconductors, it can be significantly modified upon insertion of naphthalimide units in the core, as shown in Table I.4. Note that our naphthalimide-based derivatives present reduction potentials around -1.13 V, which are lower values with respect to -2.2 V determined for other benzothiadiazole-based semiconductors shown in the literature.[43] It is important to note that in the benzothiadiazole-based systems studied (**BTD**, **BTD-ext** and **BTD-inv**) no reduction processes were recorded within the solvent window. However, for **NIP** two reduction processes are recorded at -1.37 V and -1.74 V, and for **NDI** at -1.13 V and -1.43 V. In addition, by extending the π-conjugated chain and by synthesizing different isomers, we have attempted to tune the acceptor-electronic properties of these naphthalimide-based semiconductors. These modifications have rendered reduction potentials of -1.36 V and -1.65 V when the thienopyrrole chain is elongated in **NIP-ext**, and -1.12 and -1.49 V in **NDI-ext**. On the other hand, the different isomers in the inverted compounds, give reduction potentials of -1.37 V and -1.77 V for **NIP-inv**, and -1.14 V and -1.49 V for **NDI-inv**. Both, in the extended and inverted semiconductors an improvement of approximately 0.2 V in the electron-acceptor properties is observed for NDI derivatives when compared to NIP derivatives.

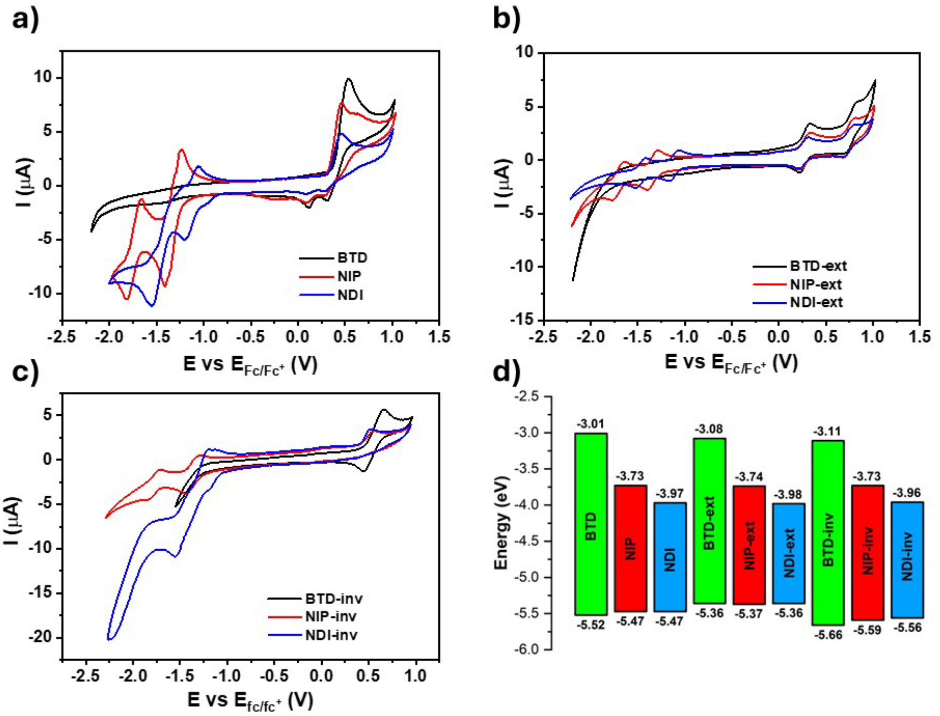

Figure I.6. Cyclic voltammetry of studied compounds: a) **BTD** (black), **NIP** (red) and **NDI** (blue) b) **BTD-ext** (black), **NIP-ext** (red) and **NDI-ext** (blue) c) **BTD-inv** (black), **NIP-inv** (red) and **NDI-inv** (blue). d) The corresponding energy levels diagram estimated from the experimental electrochemical values.

From the first reduction and oxidation potentials obtained by experimental cyclic voltammetry measurements (Figures I.6a, I6.b, I.6c and Table I.4) in dry dichloromethane, HOMO and LUMO levels of the studied compounds can be estimated. As shown in Figure

I.6d, the replacement of the thiadiazole core by a naphthalimide unit significantly stabilizes the LUMO energy level, also in the extended and inverted compounds, reaching values around -3.73 eV for NIP derivatives and around -3,97 eV for NDI derivatives, versus values around -3 eV obtained for BTD derivatives. This stabilization is less pronounced in pyrazine-containing derivatives (NIP derivatives) compared to their imidazole analogues (NDI derivatives), a behaviour that is in agreement with DFT calculations (Table I.1). This can be explained by the presence of three carbonyl groups in the naphthalimide structure that enhances its electron-acceptor capacity to a greater extent than pyrazine-based compounds. On the other hand, the introduction of these naphthalimide electroactive units affects very slightly the HOMO energy levels (i.e. 5.32 eV in **BTD**, 5.47 eV in **NIP** and **NDI**). Nevertheless, the HOMO energy level is moderately destabilized, with values up to -5.37 eV by increasing the number of fused thiophenes in extended derivatives, whereas the HOMO values are stabilized up to around -5.55 eV in inverted thienopyrrole derivatives.

Consequently, the strong impact on the LUMO energy level due to the incorporation of the naphthalimide units, combined with a subtle modification of the HOMO level, results in a reduction of the electrochemical bandgap in the NDI and NIP systems. Furthermore, a good correlation is observed between the values of the optical bandgap (E_{gap}^{opt}) and the electrochemical bandgap (E_{gap}^{elec}) determined for these donor-acceptor semiconductors (see Table I.4).

I.4 Spectroelectrochemical studies

In order to analyze the charged species, Figures I.7 to I.9 show the evolution of the UV-Vis/NIR spectra obtained by progressive spectroelectrochemical oxidation and reduction of a low concentration solution of the compounds studied, in the presence of a large excess of tetrabutylammonium hexafluorophosphate (NBu_4PF_6) as supporting electrolyte.

In this study, **BTD** is considered the main structural block common to all investigated systems. This compound stabilizes two positively charged species at 930 mV and 1200 mV, attributed to the radical cation and the dicationic species, respectively. During the reduction, a negatively charged species is formed at -1490 mV, corresponding to the radical anion. The incorporation of a naphthalimide unit into the benzothiadiazole core (in **NDI** and **NIP** compounds) significantly reduces the potential needed to stabilize two positively charged species during the oxidation process. In the case of **NDI**, the values decrease to 300 mV and 580 mV, while for **NIP** they are recorded at 680 mV and 1150 mV. This reduction in potential is remarkable, especially considering that the HOMO orbital, which is mainly located in the BTD fragment, undergoes minimal changes with the introduction of naphthalimide units. In addition, in both **NDI** and **NIP** semiconductors, two negatively charged species are stabilized during the reduction process, corresponding to the radical anion and dianion. The radical anion appears at potentials of -460 mV for **NDI** and -480 mV for **NIP**. In the case of dianion, this appears at -650 mV for **NDI** and -1000 mV for **NIP**. The stabilization of the dianion species observed in Figure I.7, together with the decrease in the reduction potentials, is consistent with the remarkable LUMO energy level adjustment upon the introduction of the naphthalimide unit.

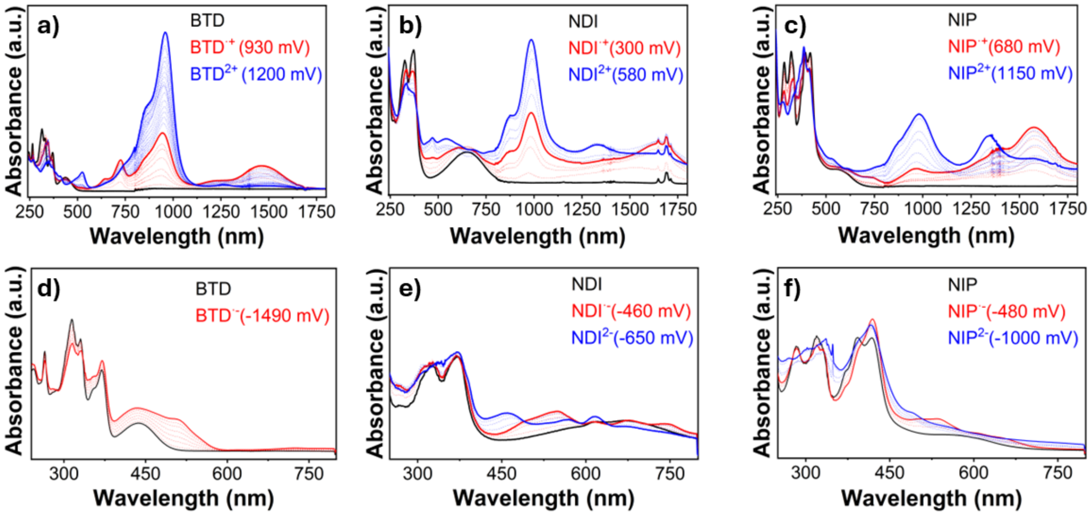

Figure I.7. UV-Vis/NIR spectra changes at room temperature upon oxidation for a) **BTD**, b) **NDI** and c) **NIP** and upon reduction for d) **BTD**, e) **NDI** and f) **NIP** within an OTTLE cell in dichloromethane in presence of 0.1M NBu_4PF_6 as the supporting electrolyte.

Furthermore, by extending the π-conjugated core in **BTD-ext**, two positive charges at 215 mV and 500 mV are stabilized, attributed to cation and dication species, respectively, as in **BTD**, but at remarkable lower potentials. In addition, as in **BTD**, this compound also stabilizes a negative charge at -1450 mV ascribed to anion species. Regarding to **NDI-ext** no new oxidized species are detected compared to **NDI**, as it also undergoes two oxidation processes at 850 mV and 1060 mV associated with the formation of cation and dication species, just like **NDI**, but at higher potentials (Figure I.7). For **NIP-ext** three distinct oxidized species are stabilized, at 380 mV, 520 mV and 800 mV, corresponding to the radical cation, dication and trication, respectively (Figure I.8). In contrast, in the **NIP** molecule only the first two species were identified (Figure I.7). This behaviour is explained because the extension of the thienopyrrole chain favours the stabilization of the positive charge along a more extensive conjugated pathway, as evidenced by the HOMO topology in Figure I.5, especially in **NIP-ext**, due to its higher planarity and the lower electrodeficient character compared to **NDI-ext**. On the other hand, chain extension does not generate significant differences in the stabilization of the reduced species. Both **NIP-ext** and **NDI-ext** presenting two reduction processes, just like **NIP** and **NDI**. **NIP-ext** stabilized two species at -550 mV and -620 mV attributed to the formation of radical anion and the dianion. For **NDI-ext**, radical anion and dianion are stabilized at -500 mV and -1500 mV.

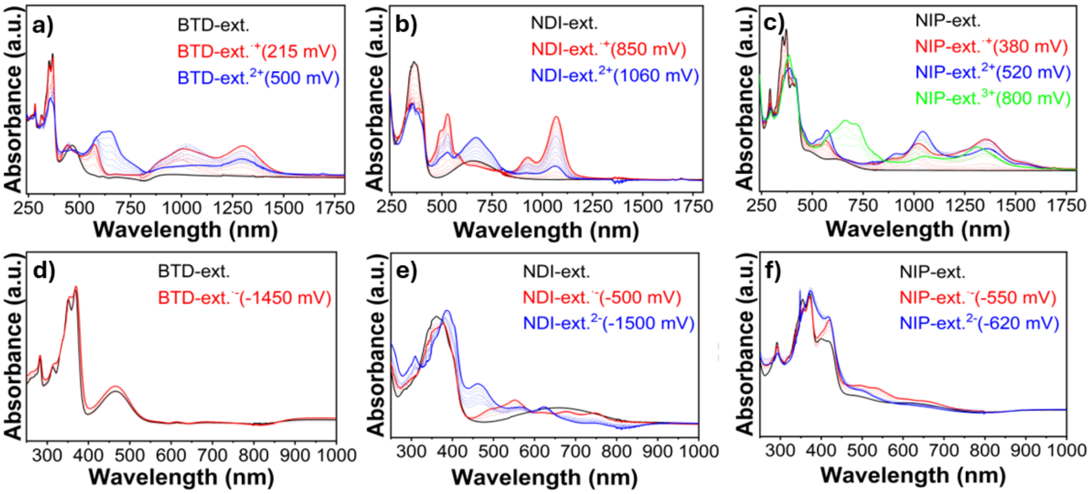

Figure I.8. UV-Vis/NIR spectra changes at room temperature upon oxidation for a) **BTD-ext**, b) **NDI-ext** and c) **NIP-ext,** and upon reduction for d) **BTD-ext**, e) **NDI-ext** and f) **NIP-ext** within an OTTLE cell in dichloromethane in presence of 0.1M NBu_4PF_6 as the supporting electrolyte.

On the other hand, π-conjugation in the thienopyrrole chain is partially hindered in the inverted derivatives, which also influences charge stabilization. In **BTD-inv** we observed a similar scenario that in the case of **BTD** and **BTD-ext**, with two oxidation processes at 850 mV and 1220 mV, albeit at higher potential, assigned to cation and dication species. In the same way this compound presents a reduction process at -1300 mV, indicating the formation of a radical anion, just like in the other BTD derivatives. However, the reduction processes are favoured in **NDI-inv**, where three new spectral profiles attributed to the radical anion (-830 mV), dianion (-1050 mV) and trianion (-1200 mV) species are recorded (Figure I.9), in contrast to the stabilization of only two reduced species in **NDI** (Figure I.7). Instead, only one oxidized species is formed at 1130 mV, indicating that the inversion in **NDI** significantly favours the reductive processes over the oxidative ones. In contrast, this effect is not observed in **NIP-inv**, whose spectral changes are similar to those of **NIP**, with the stabilization of two reduced species, radical anion at -1100 mV and dianion -1700mV and two oxidized species, radical cation at 1050 mV and dication 1220 mV. These results show that extending the π-conjugated chain is an effective way of stabilising positive charge. Conversely, inverting the thiophene in the π-conjugated chain is an effective way of stabilising a negative charge.

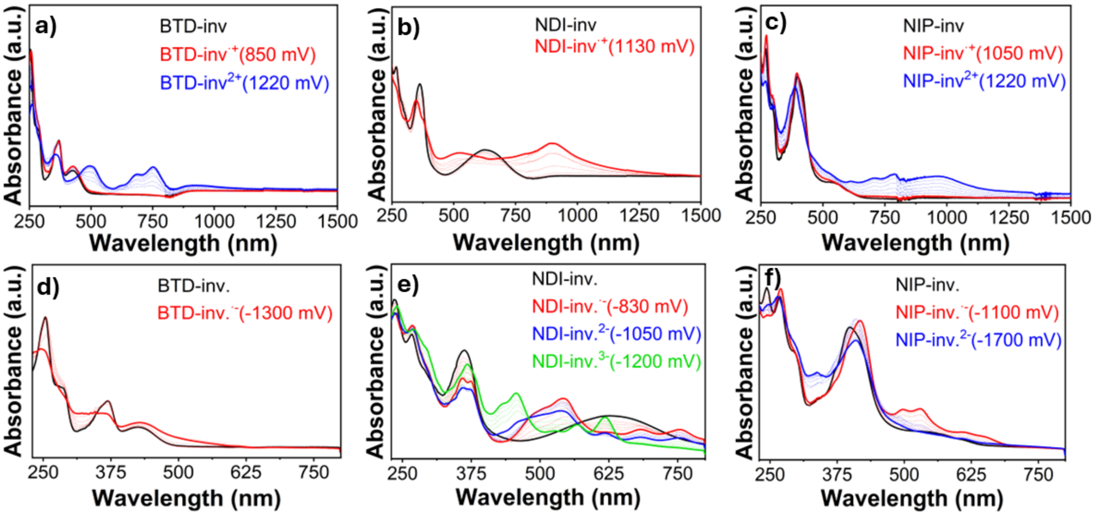

Figure I.9. UV-Vis/NIR spectra changes at room temperature upon oxidation for a) **BTD-inv**, b) **NDI-inv** and c) **NIP-inv** and upon reduction for d) **BTD-inv**, e) **NDI-inv** and f) **NIP-inv** within an OTTLE cell in dichloromethane in presence of 0.1M NBu_4PF_6 as the supporting electrolyte.

I.5 Field effect transistors and thin film characterization

Field-effect transistors were fabricated to evaluate the charge transport properties of the studied semiconductors. In particular, thin-film transistors with a top-contact and bottom-gate structure were developed by sublimation of semiconductor onto SAM-treated substrates. Octadecyltrichlorosilane (OTS) and hexamethyldisilazane (HMDS) were used as the regents for self-assembled monolayer treatment of the SiO_2 dielectric layer. The deposited thin films were characterized by atomic force microscopy (AFM, Figures I.10a) and X-ray diffraction (XRD, Figure I.10b).

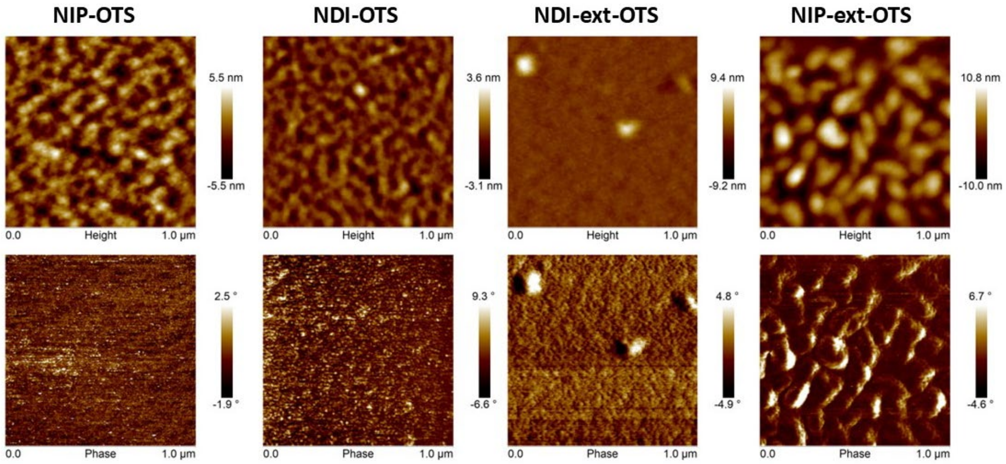

Figure I.10. AFM images of optimized OFETs thin films, on preheated OTS-treated substrates at 80ºC and thermally annealed at 150ºC for 3 hours for **NIP** and **NDI, NIP-ext** and **NDI-ext**.

Following semiconductor deposition, shadow masks were used to pattern gold electrodes with different predefined channel lengths and widths, finalizing the device fabrication process. Charge carrier mobilities (μ), threshold voltage (V_T), and on/off current ratio (I_{ON}/I_{OFF}) were extracted from the saturation region (see part 1.3.2 of introduction) in the device transfer curves, and the obtained parameters are summarized in Table I.5 (full device characterization is in appendix 5.2.1). BTD derivatives are inactive as semiconductors in OFETs. However, the naphthalimide derivatives show modest field-effect mobilities, achieving a maximum hole mobility value of 10^{-2} cm² V⁻¹ s⁻¹ for pyrazine derivative, **NIP** (see output and transfer plots in Figure I.12), in films deposited on substrates preheated at 80°C and after a thermal annealing at 150°C for 3 hours. Furthermore, the introduction of an imidazole ring as a spacer in **NDI** causes a decrease in field-effect mobility by two orders of magnitude (10^{-4} cm² V⁻¹ s⁻¹) under the same deposition conditions. When analyzing the effect of the extension of the π-conjugated system in these derivatives, a drastic decrease in field-effect mobility is observed in **NIP-ext** and **NDI-ext**, with values of 10^{-6} cm² V⁻¹ s⁻¹ for both semiconductors (see output and transfer in Figure I.12). **NDI** and **NIP** systems together with the extended analogues systems exhibit p-type mobility, in concordance with the values obtained for HOMO orbitals and the reorganization energy values**.** On the other hand, the inverted derivatives, **NDI-inv** and **NIP-inv**, do not present electrical activity.

XRD measurements and AFM images (Figure I.10) show a higher crystallinity in the **NIP** derivatives compared to the **NDI** ones, which can be one of the reasons explaining their higher field-effect mobilities. Furthermore, XRD analyses reveal that the **NIP-ext** and **NDI-ext** films (Figure I.11), as well as those of **NIP-inv** and **NDI-inv** are completely amorphous, which might be related to their poor electronic properties.

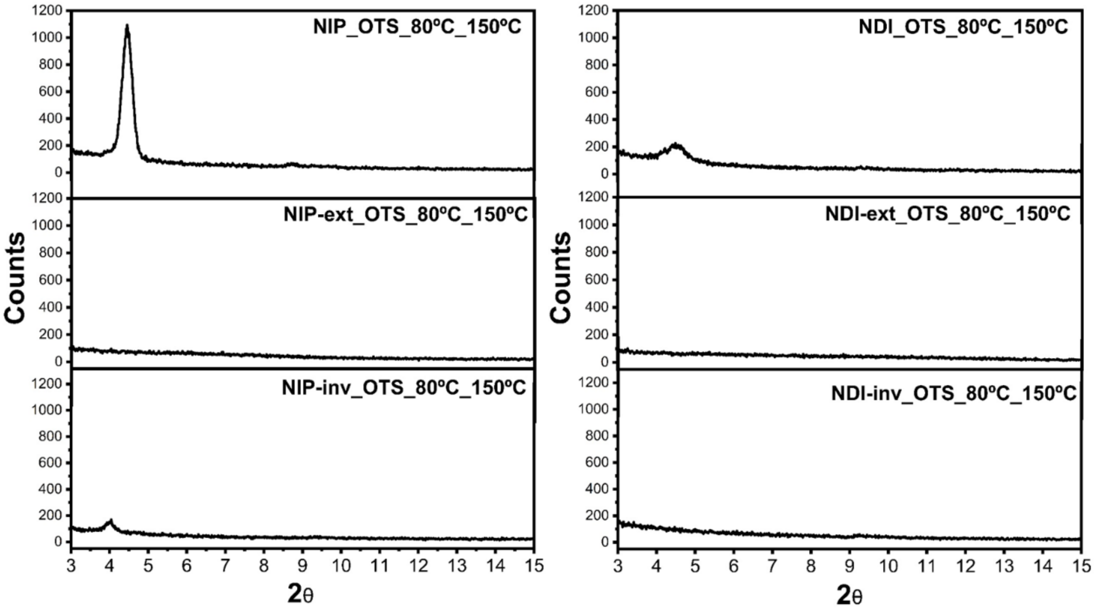

Figure I.11. XRD plots for **NIP**, **NDI**, **NIP-ext, NDI-ext, NIP-inv** and **NDI-inv** semiconductors on preheated OTS-treated substrates at 80ºC and thermally annealed at 150ºC for 3 hours.

In conclusion, the **NIP** compound exhibits a field-effect mobility two orders of magnitude higher than that of the **NDI** system, while the extension of the π-conjugated chain significantly deteriorates the mobility values in both cases (**NIP-ext** and **NDI-ext**).

Compound	Subst.^{a} Treatment	μ_h (cm^2 V^{-1} s^{-1})	V_T(V)	I_{ON}/I_{OFF}
NDI	OTS,(80°C,150°C)	2x10^{-4}	-6	2x10^{+4}
NIP	OTS,(80°C,150°C)	1x10^{-2}	-20	2x10^{+4}

Table I.5. OFETs electrical data recorded, under positive bias, for thin films of the indicated semiconductors measured in vacuum. ^{a}Substrates treated with octadecyltrichlorosilane (OTS) and preheated at 80°C during sublimation. Thin films were then thermal annealed at 150°C.

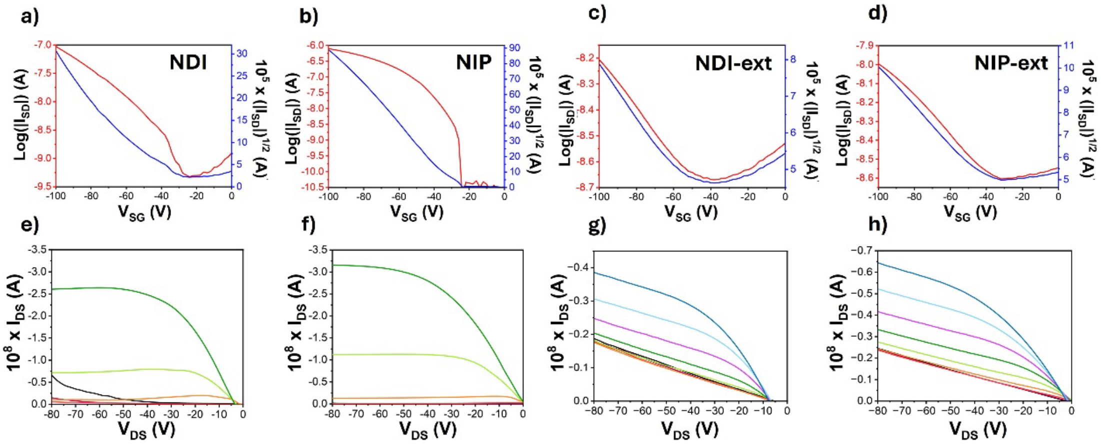

Figure I.12. OFET transfer and output characteristic of a), e) **NDI**, b), f) **NIP**, c), g) **NDI-ext** and d), h) **NIP-ext.** The transfer characteristics were measured at a constant source–drain voltage of -80 V. The gate voltage in the output plots varies from 0 to -80 V in steps of 10 V.

I.6 Conclusions

In this work we have characterized a family of compounds based on the combination of electron-withdrawing naphthalimide units with strong benzothiadiazole based donor groups, via two different conjugated and rigid nitrogen linkers (pyrazine and imidazoline). Various synthetic modifications were performed, in which the BTD unit was extended, or different isomers were employed. The effect of these synthetic approaches was analyzed by a complete physicochemical analysis, in which the stabilization of charged species was examined. In general, we observed notable differences in the LUMO energy levels upon the introduction of imidazole or pyrazine linkers, covalently attached to the naphthalimide unit. In contrast, the HOMO energy levels showed only moderate changes throughout the family of compounds.

Spectroelectrochemical studies demonstrated the formation of both reduced and oxidized charged species in all the studied systems. However, modifications in the chemical structures impact the stabilization of these charged species. In particular, the results highlight the role of the pyrazine linker in enhancing the communication between the naphthalimide and benzothiadiazole units, due to the more planar conjugated skeleton. Thus, the system that stabilizes the highest number of charged species is **NIP-ext**, showing two reduced species (radical anion and dianion) and up to three oxidized species (up to trication). Therefore, it is demonstrated that the use of the pyrazine linker is very efficient for charge stabilization.

Field-effect transistors were fabricated, finding that the use of this fused ring strategy in the donor group can drastically modify the charge transport properties of organic semiconductors, obtaining electrical behaviour as p-type semiconductors, in contrast to previously studied fused ring electron acceptor (FREA), where the compounds exhibit n-type or ambipolar mobilities. The electrical performance of the studied systems is modest, with a maximum hole mobility of 10^{-2} cm^2 V^{-1} s^{-1} for **NIP**. Furthermore, the introduction of imidazole as a spacer ring (**NDI**) causes a decrease in the field effect mobility by two orders of magnitude (10^{-4} cm^2 V^{-1} s^{-1}) under the same deposition conditions. Other derivatives, either by extending the conjugation or generating different isomers, showed decreased (10^{-6} cm^2 V^{-1} s^{-1} in extended compounds) or completely quenched electrical performances (in inverted compounds). XRD and AFM images showed rather amorphous films for all studied systems except for **NIP**, which might be one of the reasons behind its enhanced electrical performance.

I.7 References

1 S. Li, K. Liu, X. C. Feng, Z. X. Li, Z. Y. Zhang, B. Wang, M. Li, Y. L. Bai, L. Cui and C. Li, Synthesis and macrocyclization-induced emission enhancement of benzothiadiazole-based macrocycle, *Nature Communications 2022 13:1*, 2022, **13**, 1–7.

2 T. Tsukada, Y. Shoji, K. Takenouchi, H. Taka and T. Fukushima, A carbon-functionality-appended diborylacetylene available for a component of organic synthesis and OLEDs, *Chemical Communications*, 2022, **58**, 4973–4976.

3 Y. S. Guan, J. Qiao, Y. Liang, H. K. Bisoyi, C. Wang, W. Xu, D. Zhu and Q. Li, A high mobility air-stable n-type organic small molecule semiconductor with high UV–visible-to-NIR photoresponse, *Light: Science & Applications 2022 11:1*, 2022, **11**, 1–7.

4 Y. C. Lin, W. C. Yang, Y. C. Chiang and W. C. Chen, Recent Advances in Organic Phototransistors: Nonvolatile Memory, Artificial Synapses, and Photodetectors, *Small Science*, 2022, **2**, 2100109.

5 X. Huang, D. Ji, H. Fuchs, W. Hu and T. Li, Recent Progress in Organic Phototransistors: Semiconductor Materials, Device Structures and Optoelectronic Applications, *ChemPhotoChem*, 2020, **4**, 9–38.

6 W. Gao, F. Qi, Z. Peng, F. R. Lin, K. Jiang, C. Zhong, W. Kaminsky, Z. Guan, C.-S. Lee, T. J. Marks, H. Ade, A. K-Y Jen, W. Gao, K. Jiang, A. K-Y Jen, F. Qi, F. R. Lin, C. Lee, Z. Guan, Z. Peng, H. Ade, C. Zhong, W. Kaminsky and T. J. Marks, Achieving 19% Power Conversion Efficiency in Planar-Mixed Heterojunction Organic Solar Cells Using a Pseudosymmetric Electron Acceptor, *Advanced Materials*, 2022, **34**, 2202089.

7 D. Luo, W. Jang, D. D. Babu, M. S. Kim, D. H. Wang and A. K. K. Kyaw, Recent progress in organic solar cells based on non-fullerene acceptors: materials to devices, *J Mater Chem A Mater*, 2022, **10**, 3255–3295.

8 R. Ma, C. Yan, J. Yu, T. Liu, H. Liu, Y. Li, J. Chen, Z. Luo, B. Tang, X. Lu, G. Li and H. Yan, High-Efficiency Ternary Organic Solar Cells with a Good Figure-of-Merit Enabled by Two Low-Cost Donor Polymers, *ACS Energy Lett*, 2022, **7**, 2547–2556.

9 L. Xue, X. Liu, Q. Wang, M. Yang, S. Du, C. Yang, J. Tong, Y. Xia and J. Li, Improved Performance of Organic Solar Cells by Utilizing Green Non-Halogen Additive to Modulate Active-Layer Morphology, *Energy Technology*, 2022, **10**, 2200504.

10 J. Chen, J. Yang, Y. Guo, Y. Liu, J. Chen, J. Yang, Y. Guo and Y. Liu, Acceptor Modulation Strategies for Improving the Electron Transport in High-Performance Organic Field-Effect Transistors, *Advanced Materials*, 2022, **34**, 2104325.

11 K. Liu, B. Ouyang, X. Guo, Y. Guo and Y. Liu, Advances in flexible organic field-effect transistors and their applications for flexible electronics, *npj Flexible Electronics 2022 6:1*, 2022, **6**, 1–19.

12 B. Peng, Z. He, M. Chen, P. Kwok, L. Chan, B. Peng, Z. He, M. Chen and P. K. L. Chan, Ultrahigh On-Current Density of Organic Field-Effect Transistors Facilitated by Molecular Monolayer Crystals, *Adv Funct Mater*, 2022, **32**, 2202632.

13 X. Ren, Z. Lu, X. Zhang, S. Grigorian, W. Deng and J. Jie, Low-Voltage Organic Field-Effect Transistors: Challenges, Progress, and Prospects, *ACS Mater Lett*, 2022, **4**, 1531–1546.

14 D. Lv, Q. Jiang, Y. Shang and D. Liu, Highly efficient fiber-shaped organic solar cells toward wearable flexible electronics, *npj Flexible Electronics 2022 6:1*, 2022, **6**, 1–9.

15 J. Sang Heo, J. Eom, Y.-H. Kim, S. Kyu Park, J. S. Heo, S. K. Park, J. Eom and Y. Kim, Recent Progress of Textile-Based Wearable Electronics: A Comprehensive Review of Materials, Devices, and Applications, *Small*, 2018, **14**, 1703034.

16 Z. Chen, S. Duan, X. Zhang, B. Geng, Y. Xiao, J. Jie, H. Dong, L. Li and W. Hu, Organic Semiconductor Crystal Engineering for High-Resolution Layer-Controlled 2D Crystal Arrays, *Advanced Materials*, 2022, **34**, 2104166.

17 Y. Wei, Y. Geng, K. Wang, H. Gao, Y. Wu and L. Jiang, Organic ultrathin nanostructure arrays: materials, methods and applications, *Nanoscale Adv*, 2022, **4**, 2399–2411.

18 S. Wang, L. Peng, H. Sun and W. Huang, The future of solution processing toward organic semiconductor devices: a substrate and integration perspective, *J Mater Chem C*, 2022, **10**, 12468–12486.

19 H. Bronstein, C. B. Nielsen, B. C. Schroeder and I. McCulloch, The role of chemical design in the performance of organic semiconductors, *Nature Reviews Chemistry 2020 4:2*, 2020, **4**, 66–77.

20 J. Panidi, D. G. Georgiadou, T. Schoetz and T. Prodromakis, Advances in Organic and Perovskite Photovoltaics Enabling a Greener Internet of Things, *Adv Funct Mater*, 2022, **32**, 2200694.

21 C. Xu, Z. Zhao, K. Yang, L. Niu, X. Ma, Z. Zhou, X. Zhang and F. Zhang, Recent progress in all-small-molecule organic photovoltaics, *J Mater Chem A Mater*, 2022, **10**, 6291–6329.

22 D. Corzo, D. Rosas-Villalva, C. Amruth, G. Tostado-Blázquez, E. B. Alexandre, L. H. Hernandez, J. Han, H. Xu, M. Babics, S. De Wolf and D. Baran, High-performing organic electronics using terpene green solvents from renewable feedstocks, *Nature Energy 2022 8:1*, 2022, **8**, 62–73.

23 H. Lee, D. Lee, D. H. Sin, S. W. Kim, M. S. Jeong and K. Cho, Effect of donor–acceptor molecular orientation on charge photogeneration in organic solar cells, *NPG Asia Materials 2018 10:6*, 2018, **10**, 469–481.

24 J. Zhao, C. Yao, M. U. Ali, J. Miao and H. Meng, Recent advances in high-performance organic solar cells enabled by acceptor–donor–acceptor–donor–acceptor (A–DA'D–A) type acceptors, *Mater Chem Front*, 2020, **4**, 3487–3504.

25 R. Adel, E. Gala, M. J. Alonso-Navarro, E. Gutierrez-Fernandez, J. Martín, M. Stella, E. Martinez-Ferrero, A. De La Peña, A. Harbuzaru, M. M. Ramos, R. P. Ortiz, J. L. Segura and M. Campoy-Quiles, Comparing the microstructure and photovoltaic performance of 3 perylene imide acceptors with similar energy levels but different packing tendencies, *J Mater Chem C*, 2022, **10**, 1698–1710.

26 M. J. Alonso-Navarro, E. Gala, M. M. Ramos, R. Ponce Ortiz and J. L. Segura, Oligothiophene-Naphthalimide Hybrids Connected through Rigid and Conjugated Linkers in Organic Electronics: An Overview, *Electronic Materials 2021, Vol. 2, Pages 222-252*, 2021, **2**, 222–252.

27 M. J. Alonso-Navarro, A. Harbuzaru, P. De Echegaray, I. Arrechea-Marcos, A. Harillo-Baños, A. De La Peña, M. M. Ramos, J. T. López Navarrete, M. Campoy-Quiles, R. Ponce Ortiz and J. L. Segura, Effective interplay of donor and acceptor groups for tuning optoelectronic properties in oligothiophene–naphthalimide assemblies, *J Mater Chem C*, 2020, **8**, 15277–15289.

28 P. De Echegaray, M. J. Mancheño, I. Arrechea-Marcos, R. Juárez, G. López-Espejo, J. T. López Navarrete, M. M. Ramos, C. Seoane, R. P. Ortiz and J. L. Segura, Synthesis of

Perylene Imide Diones as Platforms for the Development of Pyrazine Based Organic Semiconductors, *Journal of Organic Chemistry*, 2016, **81**, 11256–11267.

29 A. de la Peña, I. Arrechea-Marcos, M. J. Mancheño, M. C. Ruiz Delgado, J. T. López Navarrete, J. L. Segura and R. Ponce Ortiz, Tuning of the Electronic Levels of Oligothiophene–Naphthalimide Assemblies by Chemical Modification, *Chemistry – A European Journal*, 2016, **22**, 13643–13652.

30 R. P. Ortiz, H. Herrera, C. Seoane, J. L. Segura, A. Facchetti and T. J. Marks, Rational Design of Ambipolar Organic Semiconductors: Is Core Planarity Central to Ambipolarity in Thiophene–Naphthalene Semiconductors?, *Chemistry – A European Journal*, 2012, **18**, 532–543.

31 R. Ponce Ortiz, H. Herrera, M. J. Mancheño, C. Seoane, J. L. Segura, P. Mayorga Burrezo, J. Casado, J. T. Lõpez Navarrete, A. Facchetti and T. J. Marks, Molecular and Electronic-Structure Basis of the Ambipolar Behavior of Naphthalimide–Terthiophene Derivatives: Implementation in Organic Field-Effect Transistors, *Chemistry – A European Journal*, 2013, **19**, 12458–12467.

32 X. Li, J. Guo, L. Yang, M. Chao, L. Zheng, Z. Ma, Y. Hu, Y. Zhao, H. Chen and Y. Liu, Low bandgap donor-acceptor p-conjugated polymers from diarylcyclopentadienone-fused naphthalimides, *Front Chem*, 2019, **7**, 461914.

33 I. Torres-Moya, J. R. Carrillo, M. V. Gómez, A. H. Velders, B. Donoso, A. M. Rodríguez, Á. Díaz-Ortiz, J. T. López Navarrete, R. P. Ortiz and P. Prieto, Synthesis of D-π-A high-emissive 6-arylalkynyl-1,8-naphthalimides for application in Organic Field-Effect Transistors and optical waveguides, *Dyes and Pigments*, 2021, **191**, 109358.

34 L. Wang, Y. Chen, W. Tao, K. Wang, Z. Peng, X. Zheng, C. Xiang, J. Zhang, M. Huang and B. Zhao, Polymerized Naphthalimide Derivatives as Remarkable Electron-Transport Layers for Inverted Organic Solar Cells, *Macromol Rapid Commun*, 2022, **43**, 2200119.

35 Z. Wang, J. Zhao, H. Dong, G. Qiu, Q. Zhang and W. Hu, An asymmetric naphthalimide derivative for n-channel organic field-effect transistors, *Physical Chemistry Chemical Physics*, 2015, **17**, 26519–26524.

36 M. J. Alonso-Navarro, A. Harbuzaru, M. Martínez-Fernández, P. Pérez Camero, J. T. López Navarrete, M. M. Ramos, R. Ponce Ortiz and J. L. Segura, Synthesis and electronic properties of nitrogen-doped π-extended polycyclic aromatic dicarboximides with multiple redox processes, *J Mater Chem C*, 2021, **9**, 7936–7949.

37 J. Zhang, X. Zhang, H. Xiao, G. Li, Y. Liu, C. Li, H. Huang, X. Chen and Z. Bo, 1,8-Naphthalimide-Based Planar Small Molecular Acceptor for Organic Solar Cells, *ACS Appl Mater Interfaces*, 2016, **8**, 5475–5483.

38 S. Gámez-Valenzuela, I. Torres-Moya, A. Sánchez, B. Donoso, J. T. López Navarrete, M. C. Ruiz Delgado, P. Prieto and R. Ponce Ortiz, Extended π-Conjugation and Structural Planarity Effects of Symmetrical D-π-A-π-D Naphthalene and Perylene Diimide Semiconductors on n-type Electrical Properties, *Chemistry – A European Journal*, 2023, **29**, e202301639.

39 B. Jia, J. Wang, Y. Wu, M. Zhang, Y. Jiang, Z. Tang, T. P. Russell and X. Zhan, Enhancing the Performance of a Fused-Ring Electron Acceptor by Unidirectional Extension, *J Am Chem Soc*, 2019, **141**, 19023–19031.

40 Z. Liu, X. Zhang, P. Li and X. Gao, Recent development of efficient A-D-A type fused-ring electron acceptors for organic solar, *Solar Energy*, 2018, **174**, 171–188.

41 M. J. Alonso-Navarro, A. Harbuzaru, R. González-Núñez, M. M. Ramos, J. L. Segura and R. Ponce Ortiz, Tunable electroactive oligothiophene-naphthalimide semiconductors via end-capped engineering: cumulative effects beyond the linker, *J Mater Chem C*, 2023, **11**, 10852–10863.

42 M. S. Vezie, S. Few, I. Meager, G. Pieridou, B. Dörling, R. S. Ashraf, A. R. Goñi, H. Bronstein, I. McCulloch, S. C. Hayes, M. Campoy-Quiles and J. Nelson, Exploring the origin of high optical absorption in conjugated polymers, *Nature Materials 2016 15:7*, 2016, **15**, 746–753.

43 S. I. Kato, T. Furuya, M. Nitani, N. Hasebe, Y. Ie, Y. Aso, T. Yoshihara, S. Tobita and Y. Nakamura, A Series of π-Extended Thiadiazoles Fused with Electron-Donating Heteroaromatic Moieties: Synthesis, Properties, and Polymorphic Crystals, *Chemistry – A European Journal*, 2015, **21**, 3115–3128.

Chapter II:

Tuning charge stabilization and transport in naphthalimide-based semiconductors: the effect of the insertion of halogen atoms into.

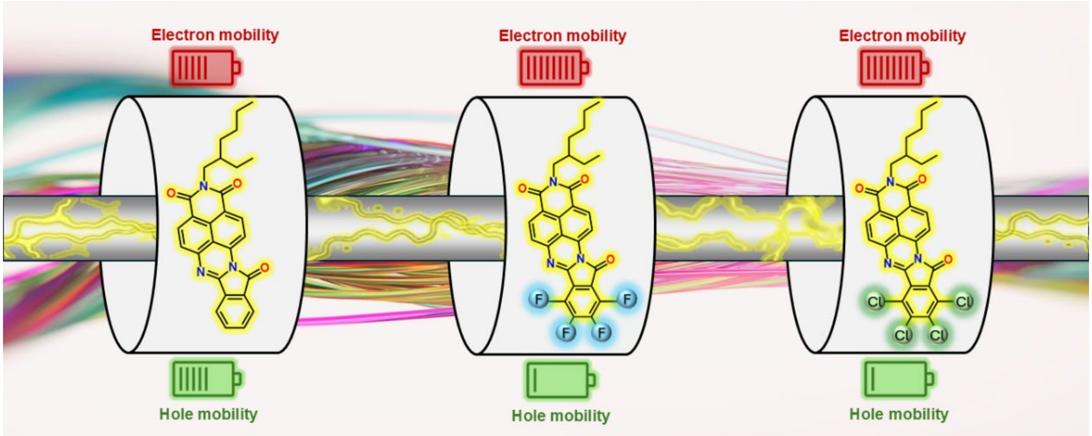

Table of contents

CONTENTS

II.1 Introduction

One of the reasons why organic semiconductor materials now attract much interest is for their great potential to be used in electronic devices, such as flexible displays[1–3] or sensors.[4,5] In recent years, considerable progress has been made to understand the energetic and structural mechanisms governing charge transport in molecular solids. In these organic electronic devices such as, OLEDs,[6] OPVs[7] or OFETs[8],one of the critical parameters employed to evaluate the suitability of organic semiconductors for optoelectronic applications is the carrier mobility, which is, in general, measured in OFETs. This is the major parameter affected by the molecular structure, the orbital energy levels[9–11] and the molecular packing.[12–14]

One technique that has proven to be effective in altering the electronic characteristics of organic semiconductors is halogenation.[15–17] The replacement of hydrogens by halogen atoms can significantly modify the energy levels and solid packing due to differences in electronegativity.[18–22] For instance, the incorporation of fluorine and chlorine into oligomers and polymers used in organic photovoltaic devices has been shown to result in higher performance due to reduced charge recombination.[23–26] In the case of linear polyacenes, the halogenation is often accompanied by little twisting of the conjugated core, and by a lowering of the lowest occupied molecular orbital (LUMO) level, while the highest occupied molecular orbital (HOMO) level remains almost unchanged. This variation of LUMO and HOMO permits the control of the semiconductor properties of the material.[27–29] A notable example is perfluorinated pentacene, which exhibits n-type mobility in contrast to its non-fluorinated counterpart, which exhibits p-type mobility.[30] This is due to the different electron density in both compounds induced by halogen atoms. Therefore, the degree of halogenation plays a significant role in the conjugated structure, meaning that both molecular and supramolecular materials properties will be altered.[31–36]

Polycyclic aromatic hydrocarbons (PAHs) represent a promising class of organic semiconductors due to their high solubility and stability.[37–40] In particular, these systems often self-assemble into supramolecular structures that favor charge transport in multiple directions.[41] It is postulated that halogenation of PAHs could significantly modify both their self-assembly and their electronic properties. Unlike halogenated linear polyacenes, halogenated PAHs have been less explored due to the synthetic challenges.

In this chapter, the characterization of a series of PAHs based on phenylene-naphthalimide assemblies has been carried out, in which both the phenylene unit and the electron-accepting naphthalimide group are directly conjugated through rigid inverted amidine (NAI)[42] linker. Different halogen atoms (F and Cl) have been introduced into the phenylene unit with the aim of modulating the electron-accepting and charge-transport properties in these systems (Figure II.1).[43–45] The effect of the insertion of halogens into the phenylene unit on the optical, electrochemical and charge-transport properties of these materials has been evaluated.

This study provides key insights into the impact of halogenation on planar PAHs, laying the foundation for future research aimed at the rational design of organic semiconductors with enhanced properties for advanced optoelectronic applications.

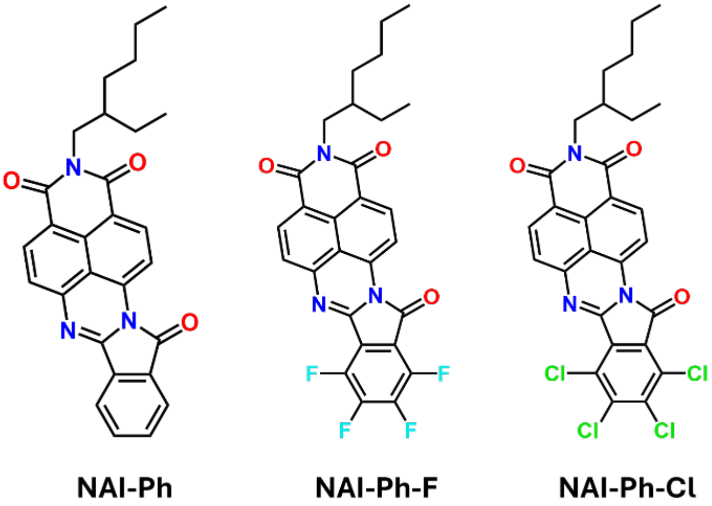

Figure II.1. Molecular structures of naphthalimide–oligothiophene derivatives studied in this chapter.

II.2 Structural and optical properties

The DFT optimization of the lowest-energy molecular structures of the analyzed compounds reveals a completely planar conformation in all three NAI-Ph systems (Figure II.2). In all derivatives, the torsion angle between the naphthalimide and phenylene units remains close to 0°, suggesting that the incorporation of halogen atoms into the conjugated skeleton does not alter the molecular structure of the compounds. Therefore, the selection of the halogen substitution positions is appropriate, since the preservation of the planarity and rigidity of these systems could favor optimal packing patterns in the solid state.

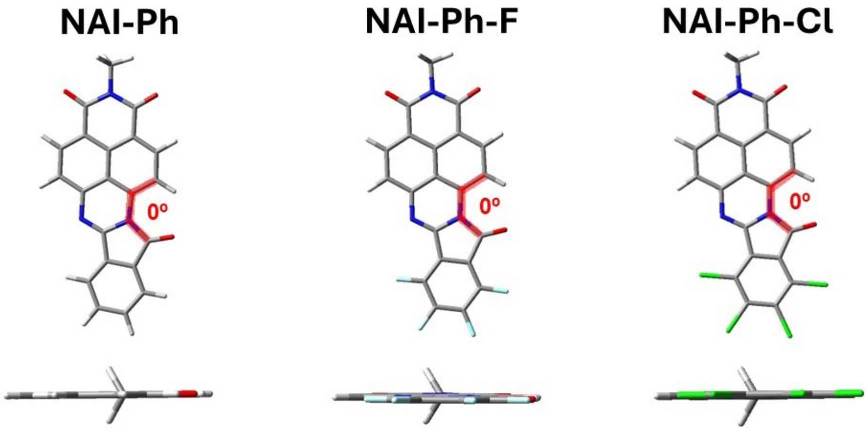

Figure II.2. DFT optimized structures for **NAI-Ph**, **NAI-Ph-F** and **NAI-Ph-Cl** at the B3LYP/6-31G** level of theory.

The UV–vis absorption spectra of the new semiconductors were recorded in dichloromethane solution (Figure II.3) and the most relevant data is summarized in Table II.1. Theoretical TD-DFT calculations appropriately support the experimental results (Table II.2).

The optical bandgaps were estimated from the onset of the lowest energy absorptions (λ_{onset}) in the UV–Vis spectra in solution (Table II.1). The incorporation of halogen atoms at the terminal positions of the phenylene unit resulted in a reduction of the bandgap values (2.24 eV for **NAI-Ph**, 2.16 eV for **NAI-Ph-F** and 2.11 eV for **NAI-Ph-Cl)**.[46]

	UV-Vis$_{\text{Solution}}$^{a}						UV-Vis$_{\text{Film}}$^{g}		Fluorescence^{j}		
	[C] (μM)	λ_{max} (nm)^{b}	$\varepsilon_{\lambda_{max}}$ (M^{-1} cm^{-1})^{c}	λ_{mrs} (nm)^{d}	λ_{onset} (nm)^{e}	E_g^{opt} (eV)^{f}	λ_{max} (nm)^{h}	λ_{onset} (nm)^{i}	[C] (μM)	λ_{exc} (nm)	λ_{em}^{k} (nm)
NAI-Ph	21	462	25 361	490	553	2.24	462	883	40	452	599
NAI-Ph-F	21	474	16 194	504	575	2.16	487	882	40	464	621
NAI-Ph-Cl	21	482	16 909	513	588	2.11	483	896	40	472	633

Table II.1. Photophysical properties of **NAI-Ph**, **NAI-Ph-F** and **NAI-Ph-Cl**. [a] UV-Vis absorption in dichloromethane solution. [b] Absorption maxima in solution. [c] Molar extinction coefficient to the referred wavelength. [d] Wavelength for the most red-shifted band. [e] Onset wavelength for the absorption band. [f] Energy band gap derived from the low energy absorption edge using the equation E_g^{opt}= 1240/λ_{onset}. [g] UV-Vis absorption in solid state thin film. [h] Absorption maxima in solid state thin film. [i] Onset wavelength for the absorption band. [j] Fluorescence emission in dichloromethane solution. [k] Emission maxima in solution.

For all the compounds studied**,** UV–Vis spectroscopy shows a broad spectral profile in the range from 330 to 560 nm, with two main contributions centered at 470 nm and 510 nm, associated to the n–π* and π–π* transitions, respectively.[47–49] The absorption at longer wavelength for each of the compounds shows the vibronic structure that is characteristic of naphthalimides derivatives. **NAI-Ph-F** and **NAI-Ph-Cl** display absorption maximum peaks at 474 and 482 nm, respectively, while the compound without halogen atoms (**NAI-Ph**) shows a blue-shifted absorption maximum at 462 nm. Thus, the principal absorptions wavelengths of **NAI-Ph-F** and **NAI-Ph-Cl,** are red-shifted by 12 and 20 nm, respectively, compared with **NAI-Ph**. This effect is attributed to the increase in effective conjugation due to the inductive effect and the delocalization of π electrons on the empty d-orbitals of the halogens, in the case of chlorine.[50,51] While fluorine exhibit a greater inductive effect due to its high electronegativity (3.98 for F versus 3.16 for Cl), chlorine has energetically accessible empty d orbitals, which allow a greater delocalization of π electrons, translating into a more pronounced red-shift in the absorption spectrum. It is significant that both **NAI-Ph-F** and **NAI-Ph-Cl** have lower absorption molar coefficients than **NAI-Ph**. Moreover, solubility tests indicate a reduction in the solubility of compounds upon incorporation of halogens.[52–54]

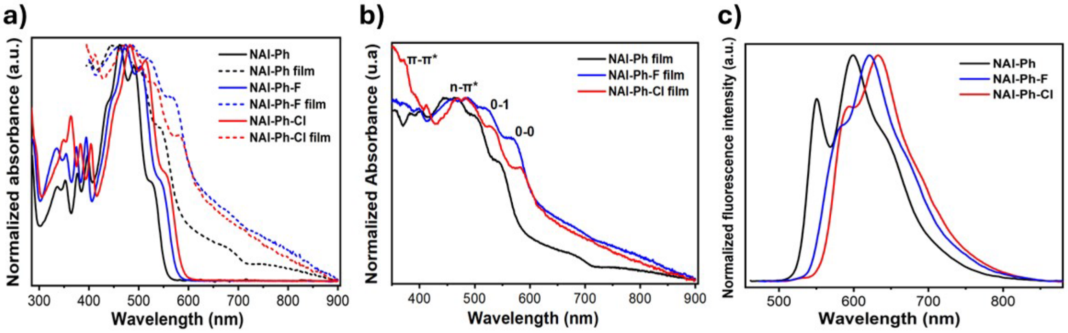

Figure II.3. a) Normalized UV−Vis absorption spectra of **NAI-Ph** (black), **NAI-Ph-F** (blue) and **NAI-Ph-Cl** (red) in dichloromethane solution (solid line) and thin film (dashed line). b) Normalized UV−Vis absorption spectra of **NAI-Ph** (black), **NAI-Ph-F** (blue) and **NAI-Ph-Cl** (red) in thin film. c) Normalized fluorescence spectra in dichloromethane solution of **NAI-Ph** (black), **NAI-Ph-F** (blue) and **NAI-Ph-Cl** (red).

In order to understand aggregation in the studied compounds, UV-Vis absorption in thin films has been recorded (Figure II.3a and II.3b). An increase in the intensity of the absorption peaks is observed in the thin film UV-Vis spectra of the three studied semiconductors. However, only **NAI-Ph-F** shows a slight displacement to larger frequencies, approximately 13 nm compared to its analogue spectrum in solution. This suggests the formation of supramolecular aggregates due to the strong π-π interactions and the possibility of intermolecular non-covalent bond interactions,[55–57] particularly in the fluorinated compound due to its high electronegativity and small size.[58,59] Moreover, thin film spectra of the three compounds display a higher 0-0/0-1 peaks intensity ratio than in solution spectra (Figure II.3b), which increases with the order and excitation-vibrational coupling due to the aggregation. This is a characteristic behaviour of J-aggregates and indicative of intramolecular charge transfer.[60] In this sense, the difference in the intensity ratio of the 0-0/0-1 peaks in thin film and in solution is similar to **NAI-Ph** and **NAI-Ph-Cl**, with a value of 0.24. In contrast, this value is higher for **NAI-Ph-F**, with a value of 0.36, suggesting a more pronounced aggregation for **NAI-Ph-F**. In addition, the increase in the ratio of the first two vibronic peaks intensities in the absorption spectra of the fluorinated compound (**NAI-Ph-F**) indicates an increased in the excitonic coupling for this compound, which is an important element to understand charge transport in organic materials.[61]

Compound	Description	λ_{max} (nm)	*f*
NAI-Ph	H→L (95%)	485	0.28
NAI-Ph-F	H→L (96%)	505	0.29
NAI-Ph-Cl	H→L (96%)	519	0.31

Table II.2. Electronic transitions obtained by TD-DFT (B3LYP/6-31G** level of theory) for **NAI-Ph**, **NAI-Ph-F**, **NAI-PhCl**.

Time-dependent density functional theory (TD-DFT) calculations have been carried out to analyse the nature of the electronic absorption bands. Table II shows the nature of the lowest energy transition, indicating a one electron excitation from the HOMO to the LUMO. Based on the molecular orbital topologies, the HOMO-LUMO transition involves an intramolecular charge transfer. It is observed that the HOMO orbital is located over the naphthalimide unit in the three systems, while the LUMO orbital is predominantly located on the phenylene fragment, although having also some contribution on the naphthalimide unit (Figure II.4).

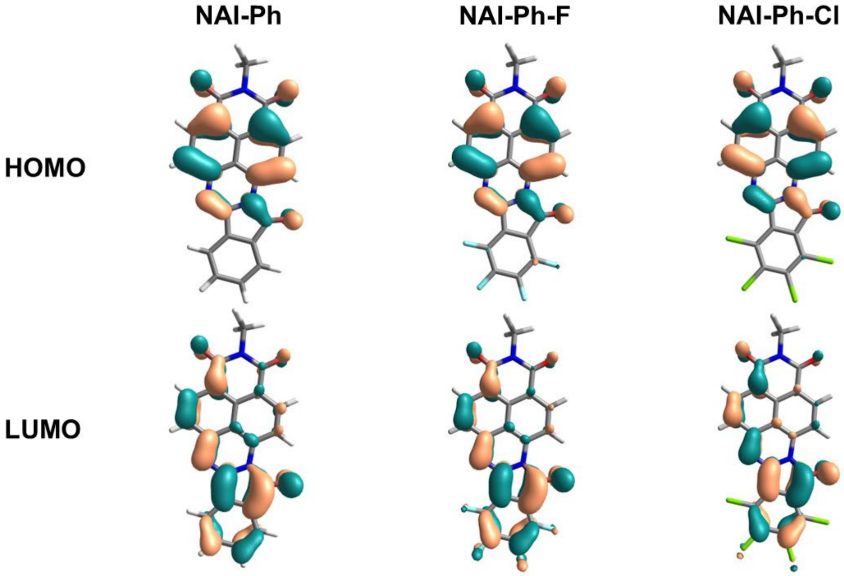

Figure II.4. Molecular orbital topologies of HOMO and LUMO orbitals of **NAI-Ph**, **NAI-Ph-F**, and **NAI-Ph-Cl** (isovalue of 0.035 a.u).

Furthermore, theoretical bandgaps were calculated at B3LYP/6-31G** level of theory, obtaining values in good agreement with the experimental results (Figure II.5). The theoretical data indicate that the HOMO and LUMO orbitals are progressively stabilized when going from **NAI-Ph** to **NAI-Ph-F** and **NAI-Ph-Cl**, as a consequence of the incorporation of halogen atoms. The electrodeficient nature of chlorine and fluorine induces the stabilization of both orbitals, being more significant in the LUMO. This effect is more pronounced in the compound with chlorine, which causes a moderate reduction of the HOMO-LUMO gap compared to **NAI-Ph** and **NAI-Ph-F**. Although, due to the higher electronegativity of fluorine atoms versus chlorine atoms, it is expected a higher decrease of the LUMO energy level in **NAI-Ph-F**, in literature it can be found that when comparing chlorination versus fluorination in organic semiconductors, the introduction of chlorine in the molecular structure usually lowers the LUMO orbital more efficiently than fluorine.[62–65] This behaviour is attributed to chlorine ability to accommodate a greater electron density through its empty 3d orbitals, whereas fluorine does not exhibit this possibility due to the absence of energetically accessible empty d orbitals.

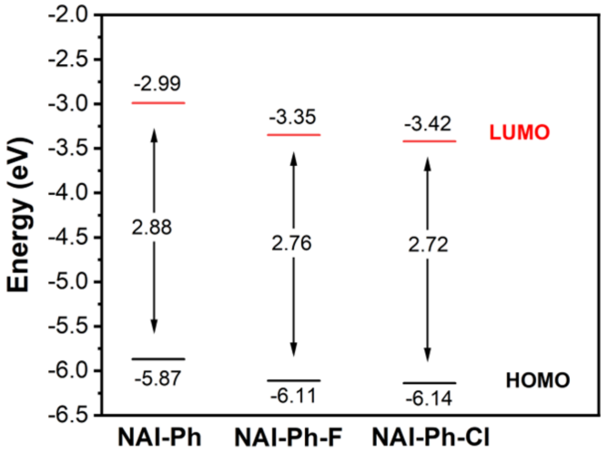

Figure II.5. DFT-calculated molecular orbital energies (B3LYP/6-31G**) for the studied molecules.

On the other hand, fluorescence spectra were obtained in dichloromethane solution (Table II.2 and Figure II.3c), revealing a moderate emission in the range of 510 nm to 830 nm. A bathochromic shift in the maximum peak was observed going from **NAI-Ph** (452 nm) to **NAI-Ph-F** (464 nm) and **NAI-Ph-Cl** (472 nm)**,** attributed to a higher effective conjugation upon halogenation. The Stokes shift was determined to be 27 nm (935 cm^{-1}) for **NAI-Ph**, 44 nm (1395 cm^{-1}) for **NAI-Ph-F**, and 43 nm (1314 cm^{-1}) for **NAI-Ph-Cl** (Figure II.6). The larger Stokes shifts observed in **NAI-Ph-F** and **NAI-Ph-Cl** indicate a higher electron-phonon coupling,[66] which normally decrease charge transport. However, note that for **NAI-Ph-F** and **NAI-Ph-Cl**, a decrease in the intensity of the shoulder around 700 nm is also observed. This indicates an increase in the ratio between 0-0 and 0-1 emission intensities, associated to an enhanced ordering in J-aggregates, which may favor charge transport.[67]

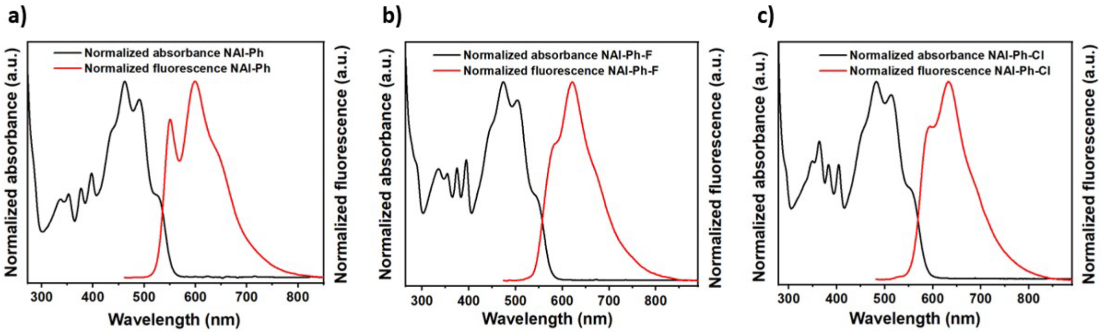

Figure II.6. Normalised UV-Vis and fluorescence spectra of **NAI-Ph, NAI-Ph-F and NAI-Ph-Cl** in dichloromethane.

II.3 Electrochemical and spectroelectrochemical studies

Electrochemical characterization of the studied materials has been performed by cyclic voltammetry (CV) in dichloromethane solution, using 0.1 M NBu_4PF_6 as supporting electrolyte and platinum as working and counter electrodes (Table II.3 and Figure II.7). The reference electrode used was Ag/AgCl, and the potentials were adjusted with respect to the ferrocene/ferrocenium redox couple (0.52 V vs. SCE). The ionization potentials (E_{HOMO}) and electron affinity (E_{LUMO}) values for the new semiconductors were estimated from the oxidation and reduction potential data, using standard approximations (Table II.3).[68–70]

In the cathodic scan, two reversible redox processes were observed for the three systems, corresponding to the formation of the radical anion and dianion species. The first reduction process appeared at similar potentials for **NAI-Ph-F** and **NAI-Ph-Cl**, –0.74 V and –0.66 V, respectively, being slightly lower in the second case due to its higher electron delocalization capacity. In contrast, the first reduction potential of **NAI-Ph** was shifted to a substantially more negative value, –0.99 V, compared to those of the halogenated analogues. In turn, the second reduction process follows the same trend with similar potentials for **NAI-Ph-F** and **NAI-Ph-Cl**, –1.10 V and –1.00 V, respectively, and a shifted reduction potential towards more negative values for **NAI-Ph** (-1.34 V).

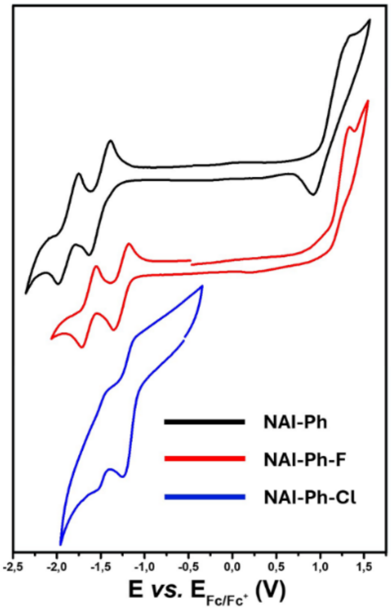

Figure II.7. Cyclic voltammograms of **NAI-Ph**, **NAI-Ph-F** and **NAI-Ph-Cl** 0.1M NBu_4PF_6 in dichloromethane. Potentials are referenced *vs*. SCE.

	Cyclic voltammetry[a]					
	$E^{1/2}_{\mathrm{Red\,I}}$ (V)	$E^{1/2}_{\mathrm{Red\,II}}$ (V)	$E^{1/2}_{\mathrm{Ox\,I}}$ (V)	E_{HOMO} (eV)[b]	E_{LUMO} (eV)[c]	$E^{\mathrm{elec}}_{\mathrm{g}}$ (eV)[d]
NAI-Ph	–0.99	–1.34	1.66	–6.10	–3.45	2.65
NAI-Ph-F	–0.74	–1.10	1.72	–6.16	–3.70	2.46
NAI-Ph-Cl	–0.66	–1.00	-	-	–3.78	-

Table II.3. [a] Cyclic voltammetry recorded in DCM/NBu_4PF_6 (0.1 M) at a scan rate of 0.10 V s^{-1} using Pt as working and the counter electrode, and Fc/Fc$^+$ as internal reference. [b] Estimated from $E_{\mathrm{HOMO}} = E_{\mathrm{LUMO}} - E^{\mathrm{elec}}_{\mathrm{g}}$. [c] Estimated from E_{LUMO} = –4.44 eV – $E^{1/2}_{\mathrm{Red\,I}}$. [d] Estimated from $E^{\mathrm{elec}}_{\mathrm{g}} = -E^{1/2}_{\mathrm{Red\,I}} + E^{1/2}_{\mathrm{Ox\,I}}$.

It should be noted that in the NAI derivatives, the nitrogen atoms, electron donors in the amidine bond, are directly connected to the electron acceptor of naphthalimide. The presence of halogens in the phenylene moiety reduces the electron-donating capacity of the nitrogen atoms of the amidine bond, causing the reduction potentials to shift to less negative values and the LUMO orbitals to stabilize. From these data, the LUMO energy levels were estimated at -3.45, -3.70 and -3.78 eV for **NAI-Ph**, **NAI-Ph-F** and **NAI-Ph-Cl**, respectively. Under these experimental conditions, the reduction processes are reversible for **NAI-Ph** and **NAI-Ph-F**, while quasi-reversible waves are recorded for **NAI-Ph-Cl**. This could be explained by the presence of aggregates, considering the stronger intermolecular interactions in the chlorinated material, as evidenced by the solubility tests. Therefore, different conditions were tested for **NAI-Ph-Cl**, obtaining reversible reductions processes using a 0.1 M solution of NBu_4PF_6 in dichloromethane at 40 °C (see Figure II.8).

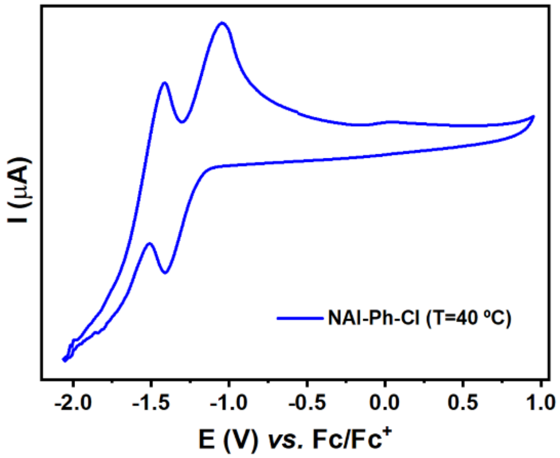

Figure II.8. Cyclic voltammetry reduction wave of **NAI-Ph-Cl** with 0.1 NBu_4PF_6 in dichloromethane solution at 40ºC.

On the other hand, both **NAI-Ph** and **NAI-Ph-F** show a quasi-reversible oxidation wave in the anodic scan, as we can see in Figure II.7. These oxidations processes appear at high potential values (1.66 V for **NAI-Ph** and 1.72 V for **NAI-Ph-F**) while no oxidation process is observed for **NAI-Ph-Cl** within the solvent window. The absence of this process in **NAI-Ph-Cl** is probably due to the lower solubility; thus, the oxidation wave is not clearly distinguished. In this way, the HOMO of **NAI-Ph-F** is calculated at -6.16 eV, which is stabilized by 0.06 eV compared to that of **NAI-Ph**, which is obtained at -6.10 eV. The presence of the fluorine atoms causes a reduction of the electrochemical bandgap of **NAI-Ph-F** (2.46 eV) with respect to **NAI-Ph** (2.65 eV), in agreement with the results obtained from the optical bandgap and the theoretical calculations.

To assess the ability of the studied compounds to stabilize charged species, Figure II.9 shows the evolution of the UV-Vis-NIR spectra, obtained by progressive reduction in the presence of NBu_4PF_6 as supporting electrolyte. In the case of **NAI-Ph**, the neutral spectral profile, with a maximum peak at 462 nm (black curve), evolves towards a new main band with a maximum peak at 465 nm (-1250 mV) (Figure II.9a), which is attributed to the formation of the radical anion. Upon introducing halogen atoms (F and Cl) into the chemical structure, no significant differences are observed in the spectral profiles of the radical anion species with respect to **NAI-Ph**. Only a bathochromic shift is observed due to the electrowithdrawing effect of the F and Cl atoms. The neutral spectra show the maximum peak at 473 nm for **NAI-Ph-F** and at 484 nm for **NAI-Ph-Cl**, with the reduction process causing the disappearance of the neutral spectral profile and the appearance of a new spectral profile with a main absorption band at 469 nm (-1250 mV) for **NAI-Ph-F** and at 470 nm (-1200 mV) for **NAI-Ph-Cl**. In both cases, this new band is associated with the formation of anion species (Figure II.9b and II.9c). It should be noted that both the spectral profiles and the applied potentials are comparable in the three cases, indicating similar capacities for charge formation and stabilization. Oxidation was attempted for **NAI-Ph**, **NAI-Ph-F**, and **NAI-Ph-Cl**, but none underwent oxidation processes under the tested experimental conditions.

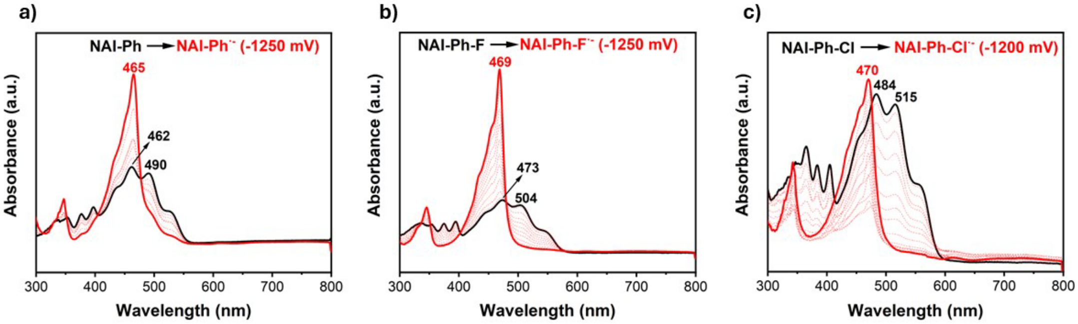

Figure II.9. UV-Vis/NIR spectra changes upon reduction of a) **NAI-Ph**, b) **NAI-Ph-F** and c) **NAI-Ph-Cl** within an OTTLE cell in dichloromethane in the presence of 0.1 M NBu_4PF_6 as the supporting electrolyte.

II.4 Field effect transistor and thin film characterization

Organic field-effect transistors (OFETs) with a top-contact/bottom-gate architecture were fabricated to evaluate the charge transport properties of the three studied compounds. The charge carrier mobility (μ), threshold voltage (V_T), and I_{ON}/I_{OFF} current ratio were extracted from the transfer plots obtained under saturation and vacuum conditions. The best parameters obtained for the devices are summarized in Tables II.4 and II.5.

The deposition of the active semiconductor film for all three compounds (**NAI-Ph**, **NAI-Ph-F**, and **NAI-Ph-Cl**) have been performed by sublimation of 10 mg of compound until reaching a thickness of 50 nm onto preheated substrates (doped Si wafers with a thermally grown 300 nm SiO_2 dielectric layer), either unfunctionalized or prefunctionalized with self-assembled monolayers of hexamethyldisilazane (HMDS) and octadecyltrichlorosilane (OTS) reactants.

Compound	Subst.[a] Treatment	μ_e ($cm^2 V^{-1} s^{-1}$)	V_T(V)	I_{ON}/I_{OFF}
NAI-Ph	OTS,(80°C,120°C)	$2x10^{-2}$	66	$1x10^{+3}$
NAI-Ph-F	OTS,(80°C,120°C)	$1x10^{-1}$	48	$2x10^{+4}$
NAI-Ph-Cl	OTS,(80°C,120°C)	$8x10^{-2}$	39	$2x10^{+4}$
NAI-Ph-Cl	HMDS,(110°C,120°C)	$2x10^{-1}$	57	$4x10^{+5}$

Table II.4. OFETs electrical data recorded, under positive bias, for thin films of the indicated semiconductors measured in vacuum. [a]Substrates treated with octadecyltrichlorosilane (OTS) and hexamethyldisilazane (HMDS) reagents and preheated at 80ºC or 110ºC during sublimation. Thin films were then thermal annealed at 120ºC.

Compound	Subst.^{a} Treatment	μ_h (cm^2 V^{-1} s^{-1})	V_T(V)	I_{ON}/I_{OFF}
NAI-Ph	OTS,(80ºC,120ºC)	3x10^{-3}	-60	1x10^{+4}
NAI-Ph-F	OTS,(80ºC,120ºC)	NA	NA	NA
NAI-Ph-Cl	OTS,(80ºC,120ºC)	NA	NA	NA
NAI-Ph-Cl	HMDS,(110ºC,120ºC)	NA	NA	NA

Table II.5. OFETs electrical data recorded, under positive bias, for thin films of the indicated semiconductors measured in vacuum. ^{a}Substrates treated with octadecyltrichlorosilane (OTS) and hexamethyldisilazane (HMDS) reagents and preheated at 80ºC or 110ºC during sublimation. Thin films were then thermal annealed at 120ºC.

NAI-Ph compound exhibits a maximum n-type field-effect mobility of 2 x 10^{-2} cm^{2}V^{-1}s^{-1} (see output and transfer plots in Figures II.10a and II.10b) for thin films deposited on OTS-treated substrates preheated to 80ºC and subsequently annealed at 120ºC for 3 hours. In addition, p-type mobility was also observed under the same deposition conditions, with a maximum field-effect mobility of 3 x 10^{-3} cm^{2}V^{-1}s^{-1} (see output and transfer plots in Figures II.10c and II.10d)

However, by introducing halogen atoms into the semiconductor's chemical structures, the compounds only exhibit n-type mobility. For **NAI-Ph-F** a maximum n-type mobility of 0.1 cm^{2}V^{-1}s^{-1} has been obtained, on OTS-treated substrates preheated to 80 °C and subjected to 3 hours annealing treatment at 120 °C, as for **NAI-Ph**. However, under these conditions the maximum n-type mobility for **NAI-Ph-Cl** is 8 x 10^{-2} cm^{2}V^{-1}s^{-1}, lower than the one obtained for **NAI-Ph-F**. In the case of **NAI-Ph-Cl** a maximum n-type mobility of 0.2 cm^{2}V^{-1}s^{-1} has been obtained on HMDS-treated substrates preheated to 110 °C and upon annealing treatment at 120 °C for 3 hours, (see output and transfer plots in Figures II.10e to II.10h).

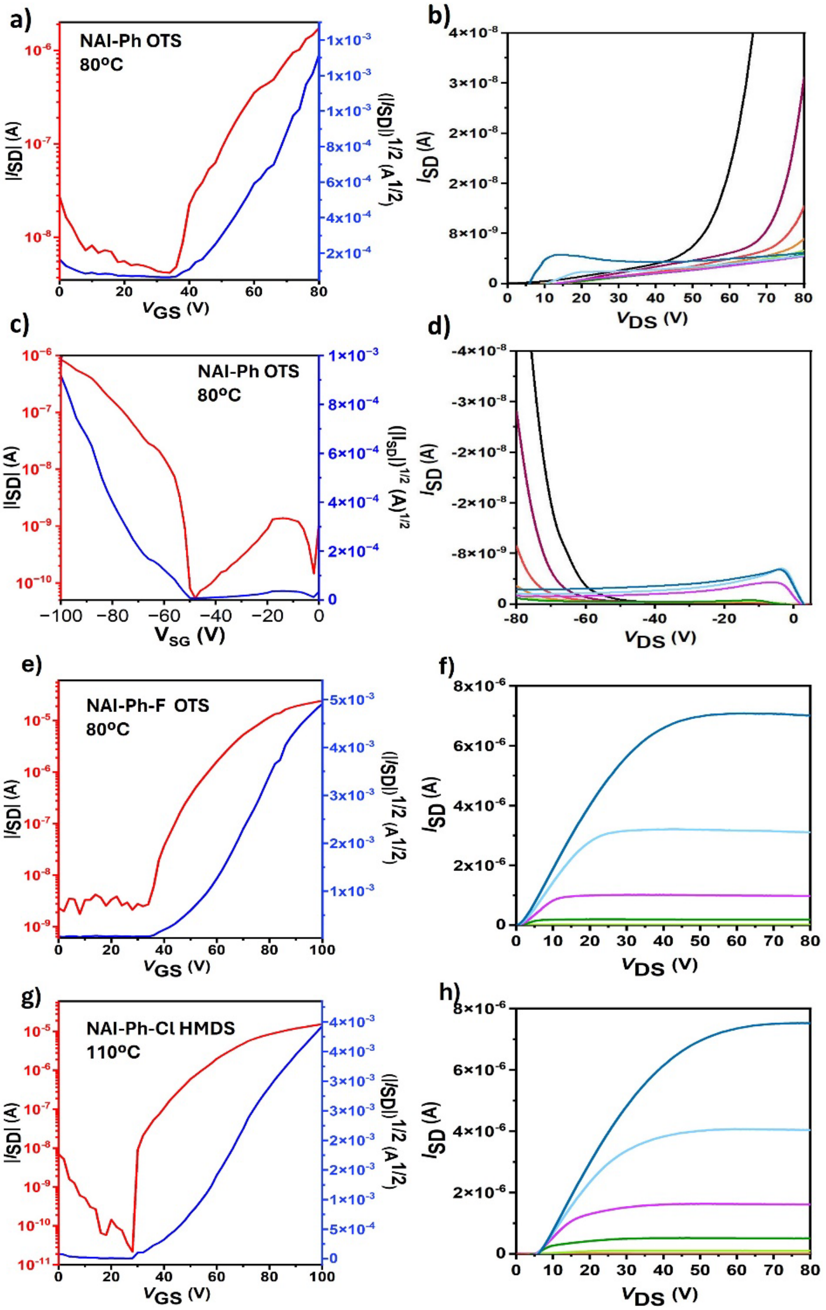

Figure II.10. Transfer a) and output b) plots of **NAI-Ph** under positive bias, transfer c) and output d) plots under negative bias of **NAI-Ph,** transfer e) and output f) plots of **NAI-Ph-F** under positive bias and transfer g) and output h) plots of **NAI-Ph-Cl** under positive bias. The transfer characteristics were measured at a constant source–drain voltage of ±80 V. The gate voltage in the output plots varies from 0 to ±80 V in steps of 10 V.

The semiconductor thin films were characterized by AFM (Figure II.11) and XRD (Figure II.12) techniques. The XRD spectra show that the films are quite amorphous for all three compounds, although enhanced crystallinity is observed for **NAI-Ph**. However, AFM images reveal some differences in the morphologies of the thin films when the compounds are deposited onto OTS-treated substrates preheated at 80 °C and after an annealing treatment at 120 °C for 3 hours, which could be one of the reasons for the different field effect mobilities between the three compounds. While **NAI-Ph-F** shows smooth films, **NAI-Ph-Cl** shows quite rough films. However, after optimization of **NAI-Ph-Cl** devices fabrication (HMDS-treated substrates preheated to 110 °C and annealing treatment at 120 °C for 3 hours), similar smooth films to **NAI-Ph-F** are obtained, resulting in an improvement in the field-effect mobility.

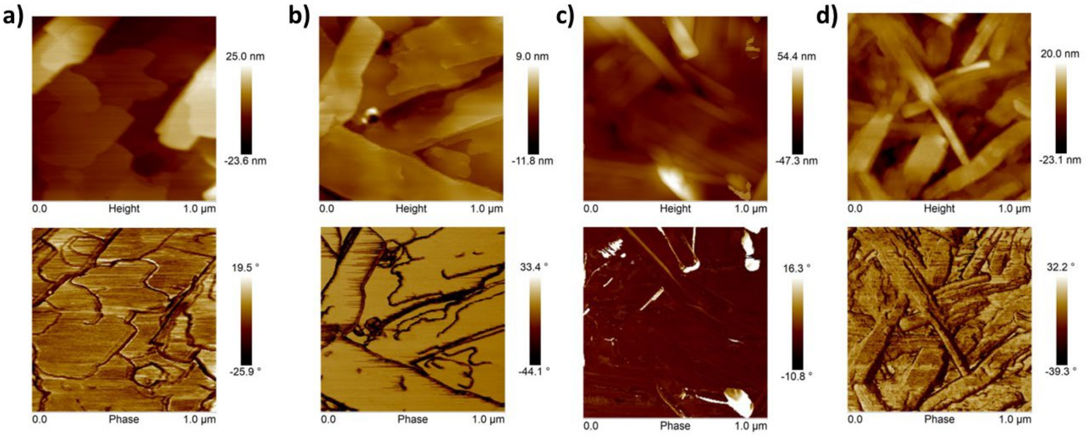

NAI-Ph OTS 80ºC Annealing 120ºC

NAI-Ph-F OTS 80ºC Annealing 120ºC

NAI-Ph-Cl OTS 80ºC Annealing 120ºC

NAI-Ph-Cl HMDS 110ºC Annealing 120ºC

Figure II.11. AFM images of semiconducting thin films deposited on preheated OTS-treated substrates at 80ºC and thermally annealed at 120ºC for 3 hours for a) **NAI-Ph**, b) **NAI-Ph-F** and c) **NAI-Ph-Cl.** d) AFM image of semiconducting thin film deposited on preheated HMDS-treated substrate at 110ºC and thermally annealed at 120ºC for 3 hours for **NAI-Ph-Cl.**

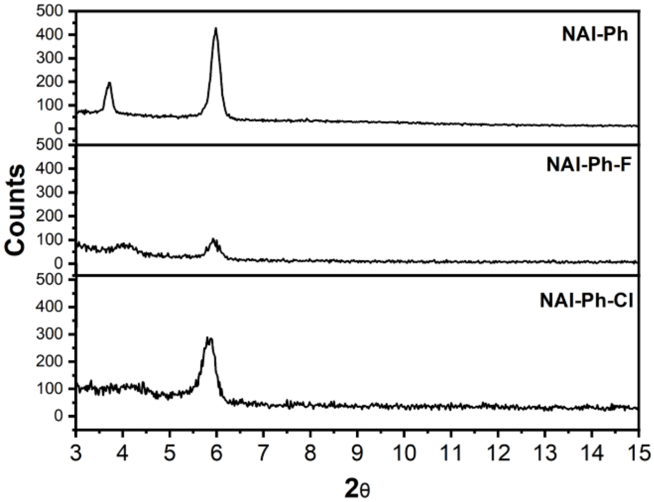

Figure II.12. Ɵ-2Ɵ X-ray diffraction scans of **NAI-Ph**, **NAI-Ph-F** and **NAI-Ph-Cl** thin films thermally deposited on preheated OTS-treated substrates at 80ºC and thermally annealed at 120ºC for 3 hours.

Therefore, the improved n-type electrical behaviour observed in halogenated compounds can be attributed to several reasons: (i) an enhanced charge injection at the electrodes due to a lower LUMO energy level compared to the **NAI-Ph** semiconductor; (ii) reversible and low-voltage reduction processes in the halogenated compounds favoring charge stabilization compared to **NAI-Ph**; (iii) an improvement in the film morphology for the compounds which contain F and Cl. Although the films are less crystalline, larger and more homogeneous domains are found, probably as a result of the enhanced supramolecular interactions thanks to the introduction of the halogen atoms.

II.5 Conclusions

In this chapter we characterize three polycyclic aromatic hydrocarbon molecules based on phenylene-naphthalimide assemblies connected by rigid inverted amidine (NAI) bonds and substituted with different halogen atoms (F and Cl), with the aim of modulating both the electron withdrawing characteristics and the charge transport properties. DFT calculations show rigid and planar structures, which favor charge transport, highlighting that substitution with halogen atoms at the phenylene ring is a good strategy to modulate the molecular electronic properties without sacrificing molecular planarity.

The physico-chemical analysis has pointed out that the introduction of halogen atoms has several implications on the molecular and electronic characteristics of the studied materials: (i) Higher electron-phonon coupling, especially in **NAI-Ph-F**. This effect normally inhibits the charge transport, although improvement of the supramolecular characteristics in the film due to the stronger interactions upon fluorination, may counteract that effect. (ii) Stabilization of the HOMO and LUMO energy levels, after introduction of F and Cl atoms, leading to a reduction of the energy gap. (iii) Lower reduction potentials compared to **NAI-Ph**. These two last effects are more evident in **NAI-Ph-Cl**, due to the higher capacity to delocalize charge through the empty 3d orbitals of chlorine atoms, which not are accessible in the fluorine atoms. The combination of these effects have an important impact on their electrical characteristics.

Electrical characterization in OFETs shows that, although ambipolar behaviour is observed when no halogen atoms are included in **NAI-Ph**, performance improves upon halogenation, although only electron transport is recorded. Thus, maximum n-type field effect mobilities of 0.1 $cm^2V^{-1}s^{-1}$ and 0.2 $cm^2V^{-1}s^{-1}$ were measured for **NAI-Ph-F** and **NAI-Ph-Cl**, respectively. In conclusion, the introduction of halogen atoms in **NAI-Ph** is an effective strategy to facilitate charge injection while maximising charge stabilisation and transport.

II.6 References

1 Q. Lin, Y. Zhu, Y. Wang, D. Li, Y. Zhao, Y. Liu, F. Li and W. Huang, Flexible Quantum Dot Light-Emitting Device for Emerging Multifunctional and Smart Applications, *Advanced Materials*, 2023, **35**, 2210385.

2 J. He, L. Cao, J. Cui, G. Fu, R. Jiang, X. Xu and C. Guan, Flexible Energy Storage Devices to Power the Future, *Advanced Materials*, 2024, **36**, 2306090.

3 M. Hassan, G. Abbas, N. Li, A. Afzal, Z. Haider, S. Ahmed, X. Xu, C. Pan, Z. Peng, M. Hassan, G. Abbas, N. Li, X. Xu, Z. Peng, A. Afzal, Z. Haider and S. Ahmed, Significance of Flexible Substrates for Wearable and Implantable Devices: Recent Advances and Perspectives, *Adv Mater Technol*, 2022, **7**, 2100773.

4 J. Ahn, S. H. Lee, I. Song, P. Chidchob, Y. Kwon and J. H. Oh, Chiral organic semiconducting materials for next-generation optoelectronic sensors, *Device*, 2023, **1**, 100176.

5 Z. Wang, J. Hu, J. Lu, X. Zhu, X. Zhou, L. Huang and L. Chi, Charge Transport Manipulation via Interface Doping: Achieving Ultrasensitive Organic Semiconductor Gas Sensors, *ACS Appl Mater Interfaces*, 2023, **15**, 8355–8366.

6 M. Tanaka, C. Y. Chan, H. Nakanotani and C. Adachi, Simultaneous control of carrier transport and film polarization of emission layers aimed at high-performance OLEDs, *Nature Communications 2024 15:1*, 2024, **15**, 1–9.

7 L. Zhu, M. Zhang, Z. Zhou, W. Zhong, T. Hao, S. Xu, R. Zeng, J. Zhuang, X. Xue, H. Jing, Y. Zhang and F. Liu, Progress of organic photovoltaics towards 20% efficiency, *Nature Reviews Electrical Engineering 2024 1:9*, 2024, **1**, 581–596.

8 Z. Chen, S. Duan, W. Hu, Z. Chen, S. Duan, W. Hu, S. Duan, W. Hu and X. Zhang, Novel solution-processed 2D organic semiconductor crystals for high-performance OFETs, *Mater Chem Front*, 2024, **8**, 2227–2272.

9 Y. Wu and W. Zhu, Organic sensitizers from D–π–A to D–A–π–A: effect of the internal electron-withdrawing units on molecular absorption, energy levels and photovoltaic performances, *Chem Soc Rev*, 2013, **42**, 2039–2058.

10 R. Zaier and S. Ayachi, DFT molecular modeling studies of D-π-A-π-D type cyclopentadithiophene-diketopyrrolopyrrole based small molecules donor materials for organic photovoltaic cells, *Optik (Stuttg)*, 2021, **239**, 166787.

11 K. Tanaka, New strategy for lowering the energy levels of one frontier molecular orbital in conjugated molecules and polymers based on Aza-substitution at the isolated HOMO or LUMO, *Polymer Journal 2023 56:2*, 2023, **56**, 61–70.

12 S. Fratini, M. Nikolka, A. Salleo, G. Schweicher and H. Sirringhaus, Charge transport in high-mobility conjugated polymers and molecular semiconductors, *Nature Materials 2020 19:5*, 2020, **19**, 491–502.

13 S. P. Wang, Y. Wang, F. Y. Chen, H. T. Wang, F. K. Sheong, F. Q. Bai and H. X. Zhang, Accurate Analysis of Anisotropic Carrier Mobility and Structure–property Relationships in Organic BOXD Crystalline Materials, *Front Chem*, 2021, **9**, 775747.

14 G.-Y. Ge, J.-T. Li, J.-R. Wang, M. Xiong, X. Dong, Z.-J. Li, J.-L. Li, X.-Y. Cao, T. Lei, J.-L. Wang, G.-Y. Ge, Z.-J. Li, J.-L. Wang, J.-T. Li, J.-R. Wang, J.-L. Li, T. Lei, M. Xiong, X. Dong and X.-Y. Cao, Unveiling the Interplay among End Group, Molecular Packing, Doping Level, and Charge Transport in N-Doped Small-Molecule Organic Semiconductors, *Adv Funct Mater*, 2022, **32**, 2108289.

15 H. Yao, J. Wang, Y. Xu, S. Zhang and J. Hou, Recent Progress in Chlorinated Organic Photovoltaic Materials, *Acc Chem Res*, 2020, **53**, 822–832.

16 Q. Zhang, M. A. Kelly, N. Bauer and W. You, The Curious Case of Fluorination of Conjugated Polymers for Solar Cells, *Acc Chem Res*, 2017, **50**, 2401–2409.

17 D. Mo, H. Wang, H. Chen, S. Qu, P. Chao, Z. Yang, L. Tian, Y. A. Su, Y. Gao, B. Yang, W. Chen and F. He, Chlorination of Low-Band-Gap Polymers: Toward High-Performance Polymer Solar Cells, *Chemistry of Materials*, 2017, **29**, 2819–2830.

18 Z. Fei, P. Boufflet, S. Wood, J. Wade, J. Moriarty, E. Gann, E. L. Ratcliff, C. R. Mcneill, H. Sirringhaus, J. S. Kim and M. Heeney, Influence of backbone fluorination in regioregular poly(3-alkyl-4-fluoro)thiophenes, *J Am Chem Soc*, 2015, **137**, 6866–6879.

19 A. A. Ahangar, R. Elancheran and A. A. Dar, Influence of halogen substitution on crystal packing, molecular properties and electrochemical sensing, *J Solid State Chem*, 2022, **314**, 123382.

20 H. Lai, H. Chen, Y. Shen, M. Wang, P. Chao, W. Xie, J. Qu, B. Yang and F. He, Using Chlorine Atoms to Fine-Tune the Intermolecular Packing and Energy Levels of Efficient Nonfullerene Acceptors, *ACS Appl Energy Mater*, 2019, **2**, 7679–7689.

21 Y. Zhang and W. Wang, Theoretical rationale for the role of the strong halogen bond in the design and synthesis of organic semiconductor materials, *Comput Theor Chem*, 2021, **1194**, 113074.

22 N. Alwadai, Z. M. Elqahtani, S. U. D. Khan, A. M. S. Pembere, A. Badshah, M. Y. Mehboob and M. F. Nazar, Impact of halogens on electronic and photovoltaic properties of organic semiconductors: A multiscale computational modeling, *J Phys Org Chem*, 2022, **35**, e4388.

23 W. Zhao, S. Li, H. Yao, S. Zhang, Y. Zhang, B. Yang and J. Hou, Molecular Optimization Enables over 13% Efficiency in Organic Solar Cells, *J Am Chem Soc*, 2017, **139**, 7148–7151.

24 D. Deng, Y. Zhang, J. Zhang, Z. Wang, L. Zhu, J. Fang, B. Xia, Z. Wang, K. Lu, W. Ma and Z. Wei, Fluorination-enabled optimal morphology leads to over 11% efficiency for inverted small-molecule organic solar cells, *Nature Communications*, 2016, **7**, 1–9.

25 Y. Chen, P. Lei, Y. Geng, T. Meng, X. Li, Q. Zeng, Q. Guo, A. Tang, Y. Zhong and E. Zhou, Selective fluorination on donor and acceptor for management of efficiency and energy loss in non-fullerene organic photovoltaics, *Sci China Chem*, 2023, **66**, 1190–1200.

26 K. Zuo, T. Dai, Q. Guo, Z. Wang, Y. Zhong, D. Mengzhen, H. Wang, A. Tang and E. Zhou, PTB7-Th-Based Organic Photovoltaic Cells with a High VOCof over 1.0 v via Fluorination and Side Chain Engineering of Benzotriazole-Containing Nonfullerene Acceptors, *ACS Appl Mater Interfaces*, 2022, **14**, 18764–18772.

27 J. U. Engelhart, F. Paulus, M. Schaffroth, V. Vasilenko, O. Tverskoy, F. Rominger and U. H. F. Bunz, Halogenated symmetrical tetraazapentacenes: Synthesis, structures, and properties, *Journal of Organic Chemistry*, 2016, **81**, 1198–1205.

28 L. T. Ming, H. O. Joon, A. D. Reichardt and Z. Bao, Chlorination: A general route toward electron transport in organic semiconductors, *J Am Chem Soc*, 2009, **131**, 3733–3740.

29 A. L. Appleton, S. M. Brombosz, S. Barlow, J. S. Sears, J. L. Bredas, S. R. Marder and U. H. F. Bunz, Effects of electronegative substitution on the optical and electronic properties of acenes and diazaacenes, *Nature Communications*, 2010, **1**, 1–7.

30 Y. Sakamoto, T. Suzuki, M. Kobayashi, Y. Gao, Y. Fukai, Y. Inoue, F. Sato and S. Tokito, Perfluoropentacene: High-performance p-n junctions and complementary circuits with pentacene, *J Am Chem Soc*, 2004, **126**, 8138–8140.

31 B. A. Jones, A. Facchetti, M. R. Wasielewski and T. J. Marks, Tuning orbital energetics in arylene diimide semiconductors. Materials design for ambient stability of n-type charge transport, *J Am Chem Soc*, 2007, **129**, 15259–15278.

32 R. Schmidt, J. H. Oh, Y. Sen Sun, M. Deppisch, A. M. Krause, K. Radacki, H. Braunschweig, M. Könemann, P. Erk, Z. Bao and F. Würthner, High-performance air-stable n-channel organic thin film transistors based on halogenated perylene bisimide semiconductors, *J Am Chem Soc*, 2009, **131**, 6215–6228.

33 S. Chai, S. H. Wen and K. L. Han, Understanding electron-withdrawing substituent effect on structural, electronic and charge transport properties of perylene bisimide derivatives, *Org Electron*, 2011, **12**, 1806–1814.

34 Z. Yuan, Y. Ma, T. Geßner, M. Li, L. Chen, M. Eustachi, R. T. Weitz, C. Li and K. Müllen, Core-fluorinated naphthalene diimides: Synthesis, characterization, and application in n-type organic field-effect transistors, *Org Lett*, 2016, **18**, 456–459.

35 M. Guo, L. Zhang, L. Liu and H. Hu, Synthesis, characterization, and charge-transport properties of halogenated dibenzo[a,j]perylenes, *Journal of Organic Chemistry*, 2020, **85**, 12243–12251.

36 L. Liu, G. Yang, Y. Duan, Y. Geng, Y. Wu and Z. Su, The relationship between intermolecular interactions and charge transport properties of trifluoromethylated polycyclic aromatic hydrocarbons, *Org Electron*, 2014, **15**, 1896–1905.

37 S. H. Pun and Q. Miao, Toward Negatively Curved Carbons, *Acc Chem Res*, 2018, **51**, 1630–1642.

38 M. R. Rao, S. Johnson and D. F. Perepichka, Aromatization of Benzannulated Perylene-3,9-diones: Unexpected Photophysical Properties and Reactivity, *Org Lett*, 2016, **18**, 3574–3577.

39 F. D. E. Ghorabe, A. S. Novikov, P. V. Nesterov, A. R. Galina, A. E. Dudaev, E. I. Shishatskaya and E. V. Skorb, Insight on relationship between crystallinity and band gap energies of polyhydroxyalkanoates polymers, *Mater Today Commun*, 2024, **39**, 108886.

40 J. Yang, J. Li, X. Zhang, W. Yang, S. Y. Jeong, E. Huang, B. Liu, H. Y. Woo, Z. Chen and X. Guo, Functionalized Phenanthrene Imide-Based Polymers for n-Type Organic Thin-Film Transistors, *Angewandte Chemie International Edition*, 2024, **63**, e202319627.

41 Y. T. Tao, S. Pola, S. Kumar and M. M. Islam, Synthesis and Characterization of Contorted Pentabenzo-Fused Coronenes as Semiconducting Materials, *Journal of Organic Chemistry*, 2017, **82**, 8067–8071.

42 A. de la Peña, I. Arrechea-Marcos, M. J. Mancheño, M. C. Ruiz Delgado, J. T. López Navarrete, J. L. Segura and R. Ponce Ortiz, Tuning of the Electronic Levels of Oligothiophene–Naphthalimide Assemblies by Chemical Modification, *Chemistry – A European Journal*, 2016, **22**, 13643–13652.

43 D. Meng, R. Wang, J. B. Lin, J. Lee Yang, S. Nuryyeva, Y.-C. Lin, S. Yuan, Z.-K. Wang, E. Zhang, C. Xiao, D. Zhu, L. Jiang, Y. Zhao, Z. Li, C. Zhu, K. N. Houk, Y. Yang, D. Meng, R. Wang, Y. Lin, E. Zhang, Y. Zhao, Y. Yang, J. B. Lin, S. Nuryyeva, K. N. Houk, J. L. Yang, S. Yuan, Z. Wang, C. Xiao, D. Zhu, L. Jiang, Z. Li and C. Zhu, Chlorinated Spiroconjugated Fused Extended Aromatics for Multifunctional Organic Electronics, *Advanced Materials*, 2021, **33**, 2006120.

44 Z. Li, W. Hu, Z. Li and Z. Wang, High performance n-type organic field-effect transistors based on halogenated derivatives of naphthalene tetracarboxylic diimides, *Mater Sci Semicond Process*, 2020, **120**, 105273.

45 Y. Luo, L. Yao, W. Gu, C. Xiao, H. Liao, M. K. Ravva, Y. Wang, Z. Li, L. Zhang, A. Lv and W. Yue, Effect of halogenated substituent on the properties of aza-octacenes, *Org Electron*, 2020, **85**, 105895.

46 M. S. Vezie, S. Few, I. Meager, G. Pieridou, B. Dörling, R. S. Ashraf, A. R. Goñi, H. Bronstein, I. McCulloch, S. C. Hayes, M. Campoy-Quiles and J. Nelson, Exploring the origin of high optical absorption in conjugated polymers, *Nature Materials 2016 15:7*, 2016, **15**, 746–753.

47 E. M. Kosower and J. R. de Souza, nπ-ct-π* Transitions: nπ* Transitions of the second kind, *Chem Phys*, 2006, **324**, 3–7.

48 R. Wang, P. Yang, S. Wang and X. Wang, Distorted carbon nitride nanosheets with activated n → π* transition and preferred textural properties for photocatalytic CO2 reduction, *J Catal*, 2021, **402**, 166–176.

49 Y. Zhang, J. He, P. J. G. Saris, H. U. Chae, S. Das, R. Kapadia and A. M. Armani, Multifunctional photoresponsive organic molecule for electric field sensing and modulation, *J Mater Chem C*, 2022, **10**, 1204–1211.

50 M. L. Tang and Z. Bao, Halogenated materials as organic semiconductors, *Chemistry of Materials*, 2011, **23**, 446–455.

51 F. Yang, C. Li, W. Lai, A. Zhang, H. Huang and W. Li, Halogenated conjugated molecules for ambipolar field-effect transistors and non-fullerene organic solar cells, *Mater Chem Front*, 2017, **1**, 1389–1395.

52 P. Ehrenreich, S. T. Birkhold, E. Zimmermann, H. Hu, K. D. Kim, J. Weickert, T. Pfadler and L. Schmidt-Mende, H-aggregate analysis of P3HT thin films-Capability and limitation of photoluminescence and UV/Vis spectroscopy, *Sci Rep*, 2016, **6**, 1–8.

53 A. Bakac, M. R. Lenze, K. Meerholz and F. Würthner, Enhanced photocurrent generation by folding-driven H-aggregate formation, *Chem Sci*, 2013, **4**, 2071–2075.

54 S. S. Wan, C. Chang, J. L. Wang, G. Z. Yuan, Q. Wu, M. Zhang and Y. Li, Effects of the Number of Bromine Substitution on Photovoltaic Efficiency and Energy Loss of Benzo[1,2-b:4,5-b']diselenophene-based Narrow-Bandgap Multibrominated Nonfullerene Acceptors, *Solar RRL*, 2019, **3**, 1800250.

55 M. J. Alonso-Navarro, A. Harbuzaru, M. Martínez-Fernández, P. Pérez Camero, J. T. López Navarrete, M. M. Ramos, R. Ponce Ortiz and J. L. Segura, Synthesis and electronic properties of nitrogen-doped π-extended polycyclic aromatic dicarboximides with multiple redox processes, *J Mater Chem C*, 2021, **9**, 7936–7949.

56 M. J. Alonso-Navarro, A. Harbuzaru, P. De Echegaray, I. Arrechea-Marcos, A. Harillo-Baños, A. De La Peña, M. M. Ramos, J. T. López Navarrete, M. Campoy-Quiles, R. Ponce Ortiz and J. L. Segura, Effective interplay of donor and acceptor groups for tuning optoelectronic properties in oligothiophene–naphthalimide assemblies, *J Mater Chem C Mater*, 2020, **8**, 15277–15289.

57 H. Chen, H. Liang, Z. Guo, Y. Zhu, Z. Zhang, Z. Li, X. Cao, H. Wang, W. Feng, Y. Zou, L. Meng, X. Xu, B. Kan, C. Li, Z. Yao, X. Wan, Z. Ma and Y. Chen, Central Unit Fluorination of Non-Fullerene Acceptors Enables Highly Efficient Organic Solar Cells with Over 18 % Efficiency, *Angewandte Chemie*, 2022, **134**, e202209580.

58 J. L. Wang, K. K. Liu, L. Hong, G. Y. Ge, C. Zhang and J. Hou, Selenopheno[3,2-b]thiophene-Based Narrow-Bandgap Nonfullerene Acceptor Enabling 13.3% Efficiency for Organic Solar Cells with Thickness-Insensitive Feature, *ACS Energy Lett*, 2018, **3**, 2967–2976.

59 F. Yang, C. Li, W. Lai, A. Zhang, H. Huang and W. Li, Halogenated conjugated molecules for ambipolar field-effect transistors and non-fullerene organic solar cells, *Mater Chem Front*, 2017, **1**, 1389–1395.

60 F. C. Spano, The spectral signatures of frenkel polarons in H- And J-aggregates, *Acc Chem Res*, 2010, **43**, 429–439.

61 V. Coropceanu, J. Cornil, D. A. da Silva Filho, Y. Olivier, R. Silbey and J. L. Brédas, Charge transport in organic semiconductors, *Chem Rev*, 2007, **107**, 926–952.

62 L. T. Ming, H. O. Joon, A. D. Reichardt and Z. Bao, Chlorination: A general route toward electron transport in organic semiconductors, *J Am Chem Soc*, 2009, **131**, 3733–3740.

63 A. M. Hiszpanski, J. D. Saathoff, L. Shaw, H. Wang, L. Kraya, F. Lüttich, M. A. Brady, M. L. Chabinyc, A. Kahn, P. Clancy and Y. L. Loo, Halogenation of a nonplanar molecular semiconductor to tune energy levels and bandgaps for electron transport, *Chemistry of Materials*, 2015, **27**, 1892–1900.

64 J. Qu, H. Chen, J. Zhou, H. Lai, T. Liu, P. Chao, D. Li, Z. Xie, F. He and Y. Ma, Chlorine Atom-Induced Molecular Interlocked Network in a Non-Fullerene Acceptor, *ACS Appl Mater Interfaces*, 2018, **10**, 39992–40000.

65 T. Hasegawa, M. Ashizawa, S. Kawauchi, H. Masunaga, N. Ohta and H. Matsumoto, Fluorination and chlorination effects on quinoxalineimides as an electron-deficient building block for n-channel organic semiconductors, *RSC Adv*, 2019, **9**, 10807–10813.

66 M. De Jong, L. Seijo, A. Meijerink and F. T. Rabouw, Resolving the ambiguity in the relation between Stokes shift and Huang–Rhys parameter, *Physical Chemistry Chemical Physics*, 2015, **17**, 16959–16969.

67 F. C. Spano, The spectral signatures of frenkel polarons in H- And J-aggregates, *Acc Chem Res*, 2010, **43**, 429–439.

68 R. P. Ortiz, H. Herrera, R. Blanco, H. Huang, A. Facchetti, T. J. Marks, Y. Zheng and J. L. Segura, Organic n-channel field-effect transistors based on arylenediimide-thiophene derivatives, *J Am Chem Soc*, 2010, **132**, 8440–8452.

69 R. P. Ortiz, J. Casado, V. Hernández, J. T. L. Navarrete, J. A. Letizia, M. A. Ratner, A. Facchetti and T. J. Marks, Thiophene–Diazine Molecular Semiconductors: Synthesis, Structural, Electrochemical, Optical, and Electronic Structural Properties; Implementation in Organic Field-Effect Transistors, *Chemistry – A European Journal*, 2009, **15**, 5023–5039.

70 M. H. Yoon, S. A. DiBenedetto, M. T. Russell, A. Facchetti and T. J. Marks, High-performance n-channel carbonyl-functionalized quaterthiophene semiconductors:

Thin-film transistor response and majority carrier type inversion via simple chemical protection/deprotection, *Chemistry of Materials*, 2007, **19**, 4864–4881.

Chapter III:

Tuning charge stabilization and transport in naphthalimide-based semiconductors: the effect of electroactive units.

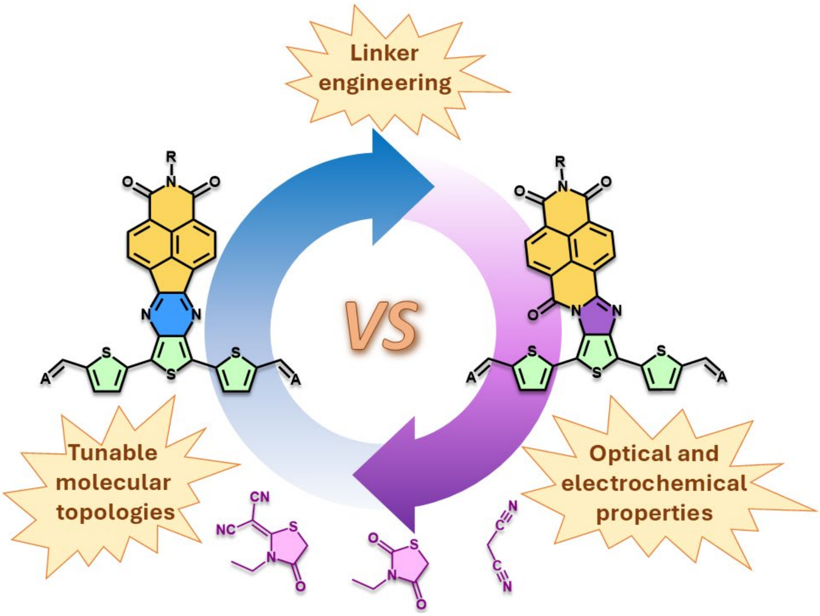

Table of contents

CONTENTS

III.1 Introduction

As we have indicated in the previous chapters, organic semiconductors have emerged as a promising alternative to inorganic semiconductors.[1] However, finding organic materials that can replace inorganic ones in devices remains a real challenge, so the development of these new materials is essential.[2–6] In this sense, the design and development of ambient stable and high-performance n-type organic semiconductor materials remains a challenge.

As we described in the previous chapters, introducing naphthalimide units with strong donor structures, such as oligothiophenes, is a promising strategy for developing new materials. Halogenation is also an effective way of altering electronic characteristics: replacing hydrogens with halogen atoms can significantly modify energy levels and solid packing due to differences in electronegativity. In this sense, developing electron charge carriers is an effective strategy to design electron deficient π-conjugated systems with planar structures functionalized with solubilizing alkyl chains.[7–9] Among the most promising materials for n-type organic semiconductors in OFETs, rylenimide derivatives have proven to be a prominent choice due to their stability, ease of functionalization, and tuneable optoelectronic properties.[10–12] In particular, naphthalimide-based assemblies have been employed as electron acceptors thanks to their electron-deficient structure, optimal LUMO energy levels, tuneable absorption spectrum, favourable supramolecular organization,[13–15] and excellent transport capacity in single-crystal structures.[16–18] In recent years, the A-D-A (acceptor-donor-acceptor) approach has been key to obtaining fullerene-free architectures with remarkable performance in OFETs[19–22] and OSCs devices.[23–26] Recently, our group have studied several series of donor-acceptor assemblies based on oligothiophene-naphthalimide (Figure III.1), connected by conjugated and planar bonds.[27] This strategy has allowed a precise control over the levels of the frontier orbitals, which is reflected in different optical, electrochemical and electronic properties.[28–30]

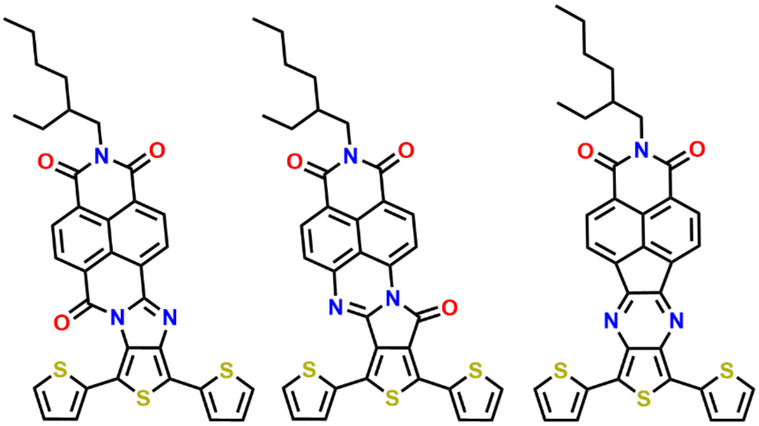

NDI3T **NAI3T** **NIP3T**

Figure III.1. Examples of oligothiophene-naphthalimide assemblies connected through different linkers.

In recent studies, it has been demonstrated that the incorporation of encapsulated terminal structures in pyrazine-based oligothiophene-naphthalimide architectures, named as **NIP3T** and **NIP3T-X**, (Figure III.2a) allows to tune the frontier orbital levels and improve the optoelectronic properties without altering the central molecular skeleton.[31] Motivated by these findings, we present in this chapter the characterization of several families of processable terthiophene-naphthalimide assemblies, denoted as **NDI3T** and **NDI3T-X** (Figure III.2b). In this sense, the introduction of an imidazole and pyrazine moieties together with three terminal protecting units with a strong electrowithdrawing effect, has allowed obtaining organic semiconductors with tuneable optical and electrochemical properties. This study provides a better understanding of the impact of the different linkers (comparison between pyrazine and imidazole linkers) conecting naphthalimide cores and terthiophene units and their functionalization with electroactive groups on the optical and electronic properties of these materials.

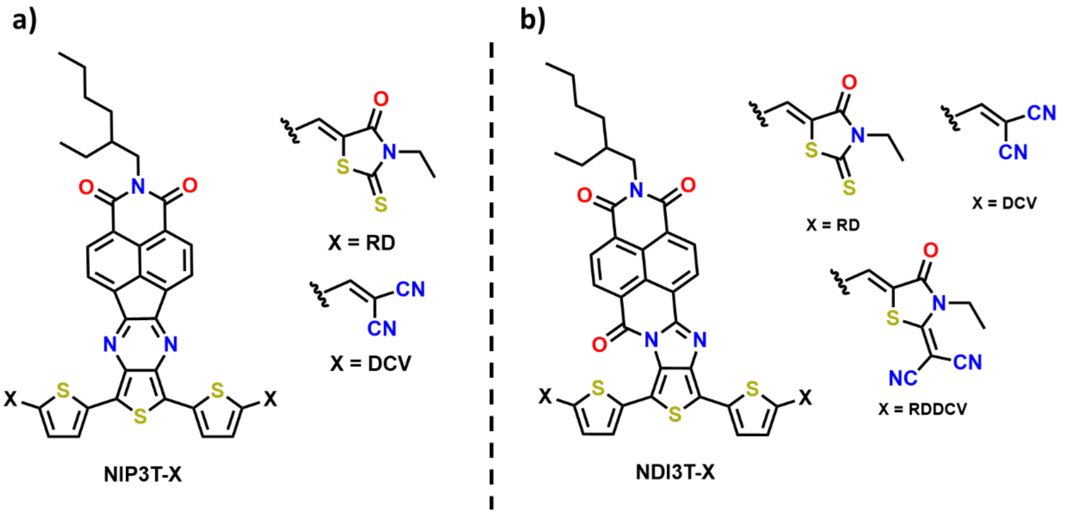

Figure III.2. a) Previous published end-capped thienopyrazine derivatives with A-D-A-D-A architectures. b) New end-capped oligothiophene-naphthalimide assemblies connected via imidazole linkers studied in this chapter.

III.2 Structural properties

Optimization of the lowest-energy molecular structures of the studied semiconductors reveals, for **NIP3T** an essentially planar structure (Figure III.3), whereas a non-coplanar configuration is found for **NDI3T-X**. Note that, in **NDI3T-X** the thiophene chain shows a distortion of approximately 140° due to the steric hindrance between the oxygen and sulphur atoms. This result underlines the importance of the choice of the central group (pyrazine *vs*. imidazole) in determining the molecular structure. Furthermore, modification of the linker group plays a key role in tuning the optoelectronic properties of these organic semiconductors, as will be discussed below.

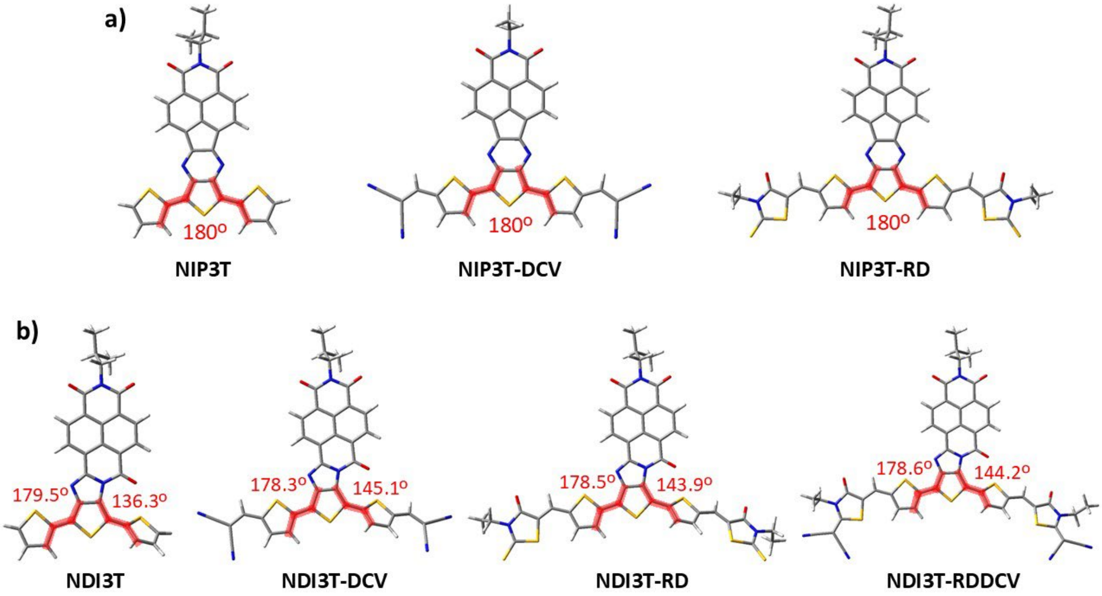

Figure III.3. DFT optimized molecular structures at the B3LYP/6-31G** level of theory for the systems under study: a) **NIP3T** and **NIP3T-X** and b) **NDI3T** and **NDI3T-X**.

FT-Raman spectra were recorded to evaluate the impact of lateral substituents on π-conjugation and molecular properties, being the data presented in Figure III.4. For this analysis, the ECC theory was employed,[32,33] which is widely studied for its effectiveness in the qualitative description of the degree of conjugation in molecular materials[34] and previously applied to naphthalene-modified oligothiophenes.[35]

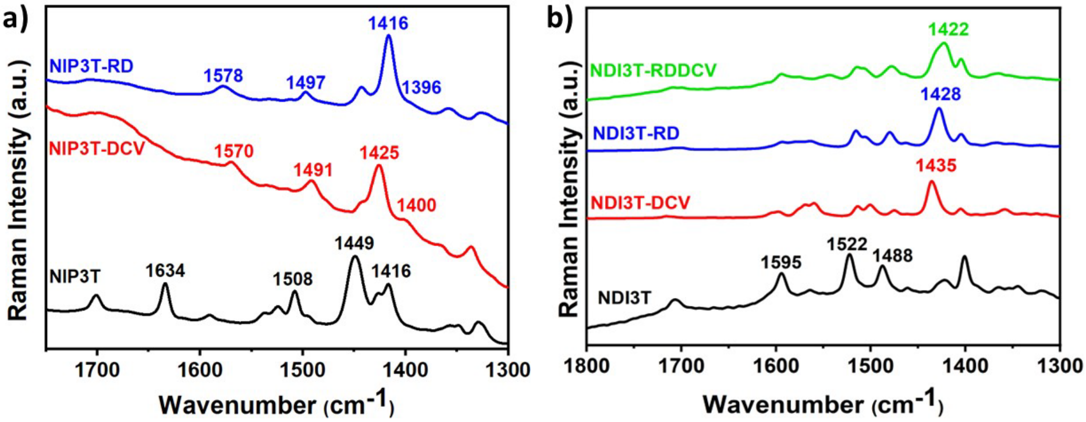

Figure III.4. FT-Raman spectra (λ=1064 nm) of a) **NIP3T** and **NIP3T-X systems** and b) **NDI3T** and **NDI3T-X** systems as bulk materials.

To analyze the Raman spectra in Figure III.4 and the selected eigenvectors in Figure III.5, we focused on the Raman vibrational modes associated with the fully symmetric ν(C=C) vibrational mode of the oligothiophene fragment. The position of this vibration allows to assess the extent of π-conjugation in this fragment. In **NDI3T** (Figure III.4b), this vibration appears at 1488 cm^{-1}, but it is significantly shifted to lower frequencies upon the incorporation of electrowithdrawing groups, being recorded at 1435 cm^{-1} in **NDI3T-DCV**, 1428 cm^{-1} in **NDI3T-RD**, and 1422 cm^{-1} in **NDI3T-RDDCV**. This red-shift of 53 cm^{-1} in **NDI3T-DCV**, 60 cm^{-1} in **NDI3T-RD** and 66 cm^{-1} in **NDI3T-RDDCV**, evidences the electronic delocalization improvement induced by the insertion of electrowithdrawing groups.

Furthermore, comparison with **NIP3T-X** systems (Figure III.4a) reveals a higher extent of π-conjugation in the oligothiophene fragment respect to NDI derivatives. This is reflected in the downward shift of the collectively fully symmetric ν(C=C) vibration mode, which appears at 1449 cm^{-1} in **NIP3T** (1488 cm^{-1} in **NDI3T**), 1425 cm^{-1} in **NIP3T-DCV** (1435 cm^{-1} in **NDI3T-DCV**) and 1416 cm^{-1} in **NIP3T-RD** (1428 cm^{-1} in **NDI3T-RD**). The higher π-conjugation in the NIP derivatives can be attributed to the planarization of the thiophene skeleton in these systems, due to the absence of repulsive S-O interactions, present in the NDI derivatives, and the appearance of attractive S-N interactions. On the other hand, the incorporation of electrowithdrawing lateral substituents in the NIP skeleton does not generate such a marked effect as in the NDI derivatives. While the downward shift in the ν(C=C) mode is 24 cm^{-1} and 33 cm^{-1} when passing from **NIP3T** to **NIP3T-DCV** and **NIP3T-RD** respectively, the same lateral modification causes a shift of 53 cm^{-1} and 60 cm^{-1} in the NDI derivatives. This indicates that the impact of lateral substituents on the degree of conjugation is more pronounced in NDI-based systems, due to the planarization of the terthiophene fragment, which is around 9° upon incorporation of electrowithdrawing groups (Figure III.3). In contrast, in the NIP derivatives, the terthiophene fragment remains completely planar both in the unsubstituted and laterally functionalized structures.

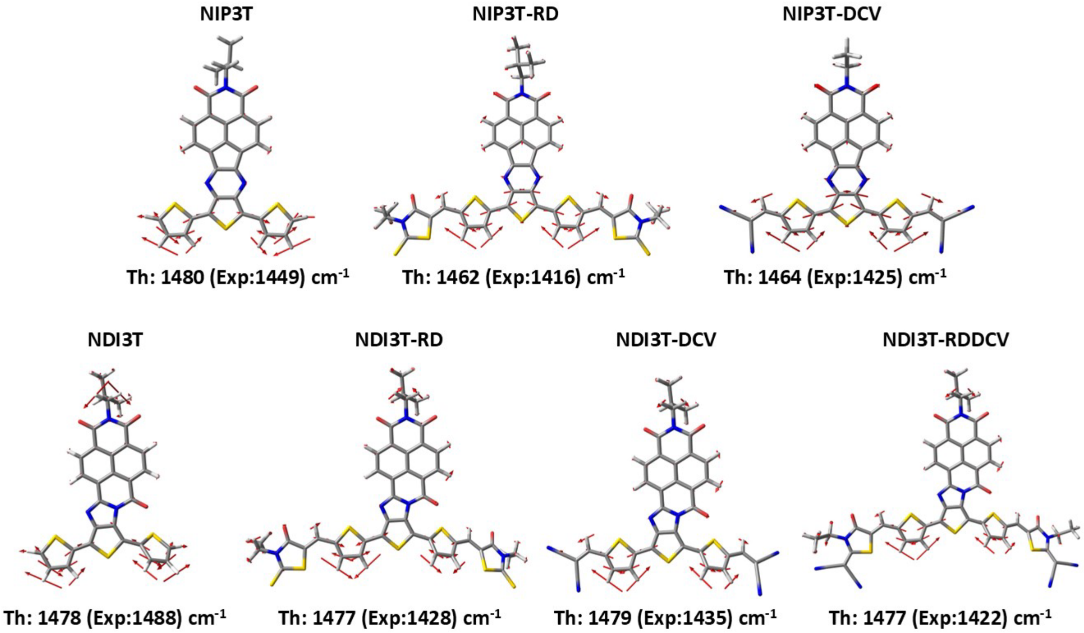

Figure III.5. B3LYP/6-31G** predicted eigenvectors for a) **NIP3T** and **NIP3T-X** systems and b) **NDI3T** and **NDI3T-X** systems

III.3 Optical and electrochemical properties

The good solubility of the studied compounds allows an adequate optical and electrochemical characterization in solution by UV-Vis and cyclic voltammetry techniques. The most important optical and electrochemical parameters of the NDI and NIP derivatives are summarized in Tables III.1 and III.4.

Figure III.6a shows the absorption profiles of the **NIP3T-X** derivatives. In the case of **NIP3T**, the spectrum shows a low-energy absorption band centered around 570 nm, which is attributed to intramolecular charge transfer (ICT) excitation. This behaviour has been theoretically confirmed by TD-DFT calculations (Table III.2) and can be described as a HOMO-

LUMO excitation, where the electron density shifts from the HOMO, located mainly in the oligothiophene fragment, towards the LUMO, located in the naphthalimide unit (Figure III.7a). It is observed that the end-capping functionalization of strong electron acceptors at the alpha position of the thiophene units has a significant impact on their optical properties, extending the absorption up to 800 nm compared to unfunctionalized **NIP3T**. In **NIP3T-DCV**, the spectrum shows a low-energy band located around 607 nm, consistent with a more extended conjugated system. However, unlike **NIP3T**, the HOMO and LUMO frontier orbitals are located mainly on the thiophene fragment, indicating that the electronic transition in **NIP3T-X** systems have a predominantly π-π* rather than ICT character. Similarly, in **NIP3T-RD**, a lower energy band is observed located around 646 nm, showing a red-shift with respect to the **NIP3T-DCV** compound. Again, the topology of the HOMO and LUMO frontier orbitals, which are located on the thiophene fragment, indicates that this transition has a π-π* rather than ICT character.

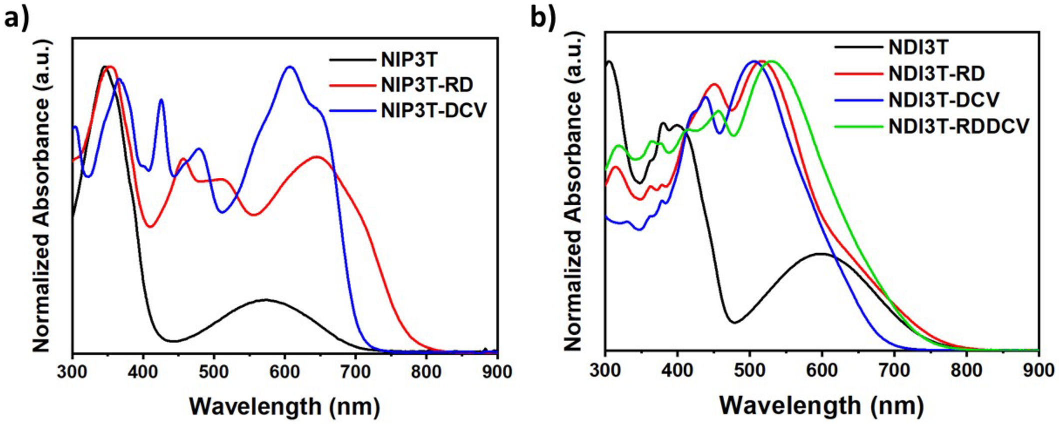

Figure III.6. Normalized UV-Vis absorption spectra for a) **NIP3T** (black), **NIP3T-RD** (red) and **NIP3T-DCV** (blue) and b) **NDI3T** (black), **NDI3T-RD** (red), **NDI3T-DCV** (blue) and **NDI3T-RDDCV** (green) in $CHCl_3$ solutions.

	UV-vis^a						
	[C] (μM)	$\lambda_{max}{}^b$ (nm)	$\varepsilon_{\lambda max}{}^c$ ($M^{-1}\cdot cm^{-1}$)	$\lambda_{ICT}{}^d$ (nm)	ε^d ($M^{-1}\cdot cm^{-1}$)	λ_{onset} (nm)	$E_g{}^{opt, e}$ (eV)
NDI3T	0.275	305	24473	599	8000	745	1.66
NDI3T-RD	0.275	516	44364	647	16364	758	1.64
NDI3T-DCV	0.275	505	40364	615	14909	681	1.82
NDI3T-RDDCV	0.275	529	54545	652	23273	737	1.68
NIP3T	0.275	346	68000	574	14910	698	1.77
NIP3T-RD	0.275	353	38180	-	17820	774	1.60
NIP3T-DCV	0.275	607	40360	-	11640	720	1.72

Table III.1. ^{a} UV-Vis absorption in $CHCl_3$ solution. ^{b} Absorption maxima in solution. ^{c} Molar extinction coefficient to the referred wavelength. ^{d} Wavelength for the most red-shifted absorption band. ^{e} Energy band gap derived from the low-energy absorption edge using the equation $E_g{}^{opt}=1240/\lambda_{onset}$.

On the other hand, as shown in Figure III.6b, **NDI3T** spectral profile displays the lowest energy absorption band centered around 599 nm, which is attributed to intramolecular charge transfer (ICT) excitation, such as in **NIP3T**. This behaviour has been theoretically confirmed by TD-DFT calculations (Table III.2) and can be described as a HOMO-LUMO excitation, where the electron density going from the HOMO, located mainly over oligothiophene fragment, towards the LUMO, located in the naphthalimide unit (Figure III.7b).

In the **NDI3T-X** derivatives, the lowest-energy absorption band is shifted with respect the nonfunctionalized derivative **NDI3T,** and a moderately shifting is found within the series as a function of the end-capping functionalization (i.e., 516 nm, 505 nm and 529 nm for **NDI3T-RD**, **NDI3T-DCV** and **NDI3T-RDDCV**, respectively). This phenomenon can be explained by considering the appearance of two different and competing ICT (intramolecular charge transfer) channels within **NDI3T-X** molecules, from terthiophene to the NDI unit and from terthiophene to the side substituents. These two ICT channels were confirmed by TD-DFT calculations, and are related to the one-electron transfer between HOMO→LUMO (experimental band shoulder around 650 nm) and HOMO→LUMO+1 (experimental band around 550 nm), phenomena described in bibliography for small molecules such as nitrophenols.[36,37] Regarding these two ICT pathways, it is interesting to note that the more highly conjugated chemical structure, the more red-shifted the HOMO→LUMO transition.

For this reason, **NDI3T-RDDCV** has the most extended and red-shifted absorption profile whereas the **NDI3T-DCV** presents the most blue-shifted ICT band. In the case of **NDI3T-DCV**, the limited extent of π-conjugation imparted by the lateral electrodeficient groups is not sufficient to counteract the effect of the two competing ICT channels, resulting in a blue-shifted absorption.

Compound	**Electronic transitions**	**Description**	**λ (nm)**	**f**
NIP3T	$S_0 \rightarrow S_1$	H→L (98%)	657	0.23
	$S_0 \rightarrow S_2$	H→L+1 (98%)	632	0.14
NIP3T-RD	$S_0 \rightarrow S_1$	H→L (98%)	725	1.04
	$S_0 \rightarrow S_2$	H→L+1 (98%)	681	0.24
NIP3T-DCV	$S_0 \rightarrow S_1$	H→L (98%)	665	0.85
	$S_0 \rightarrow S_2$	H→L+1 (98%)	610	0.19
NDI3T	$S_0 \rightarrow S_1$	H→L (99%)	736	0.22
	$S_0 \rightarrow S_4$	H→L+1 (91%)	419	0.23
NDI3T-RD	$S_0 \rightarrow S_1$	H→L (99%)	781	0.31
	$S_0 \rightarrow S_3$	H→L+1 (95%)	551	1.62
NDI3T-DCV	$S_0 \rightarrow S_1$	H→L (97%)	686	0.31
	$S_0 \rightarrow S_2$	H→L+1 (96%)	522	1.16
NDI3T-RDDCV	$S_0 \rightarrow S_1$	H→L (99%)	746	0.38
	$S_0 \rightarrow S_2$	H→L+1 (83%)	561	1.19

Table III.2. Lowest-energy transitions obtained by TD-DFT (B3LYP/6-31G**) for the studied compounds.

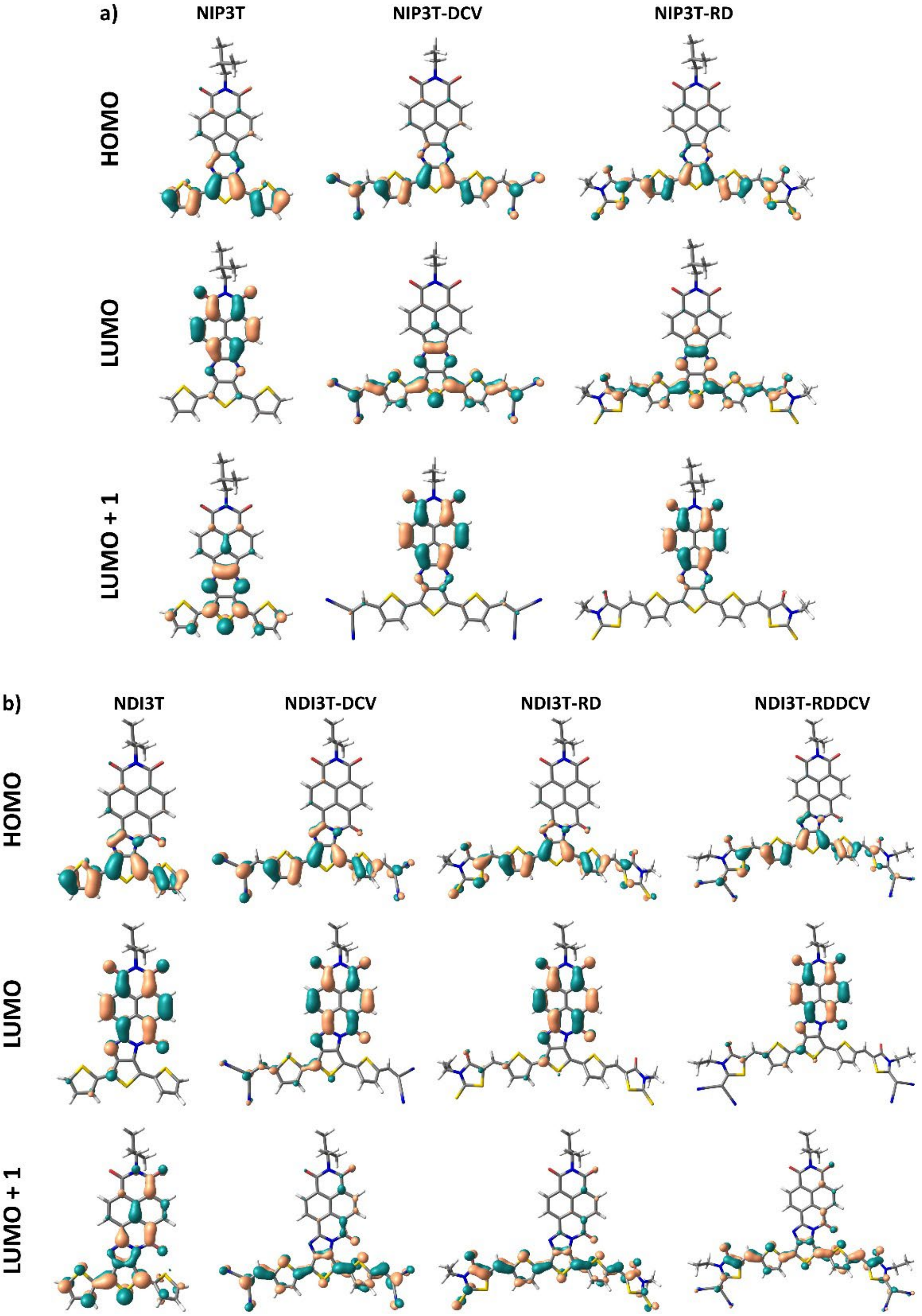

Figure III.7. Molecular orbital topologies of (a) **NIP3T** and **NIP3T-X** systems and (b) **NDI3T** and **NDI3T-X** systems at B3LYP/6-31G** level (isovalue of 0.035 a.u).

To gain insight into the nature of the lowest energy absorption band in the **NIP3T-X** and **NDI3T-X** systems, solvatochromic measurements were performed by varying the solvent polarity (Figure III.8).

The nonfunctionalized **NIP3T** and **NDI3T** systems exhibit clear solvatochromic behaviour, with a red-shift in the ICT absorption band in more polar solvents, indicating positive solvatochromism. This phenomenon suggests a larger dipole moment in the excited state (μ_{S_1}) than in the ground state (μ_{S_0}), in agreement with theoretical predictions (Table III.3). On the other hand, the terminally blocked **NDI3T-RD** and **NDI3T-DCV** derivatives exhibit a modest positive solvatochromic behaviour. In particular, the maximum absorption bands (around 515 nm) are red-shifted in more polar solvents, suggesting some intramolecular charge transfer character, in consonance with a larger dipole moment in the excited state than in the ground state, as predicted theoretically (Table III.3). In contrast, the **NDI3T-RDDCV** derivative shows a negative solvatochromism, indicating a lower dipole moment in the excited state compared to the ground state, in line with theoretical predictions (i.e., with a μ_{S_1} value of 6.20 D and μ_{S_0} value of 10.90 D). Thus, in terminally blocked **NDI3T-X** derivatives, the ICT nature of the lower energy absorption band, although moderately, can be demonstrated. This is reflected by the topologies of the HOMO and LUMO orbitals. It is possible to assume that the competition between the two ICT channels present, due to the coexistence of different acceptor units in the molecular structure, is behind the relatively discrete solvatochromic behaviour of the **NDI3T-X** systems compared to **NDI3T**.

However, in the capped **NIP3T-X** derivatives, the maximum absorption band demonstrated no shift when varying the solvent polarity, confirming the absence of an ICT absorption band. This is evidenced by the molecular orbital topologies (Figures III.7), where the HOMO and LUMO orbitals of **NIP3T-X** derivatives remain confined to the oligothiophene fragment.

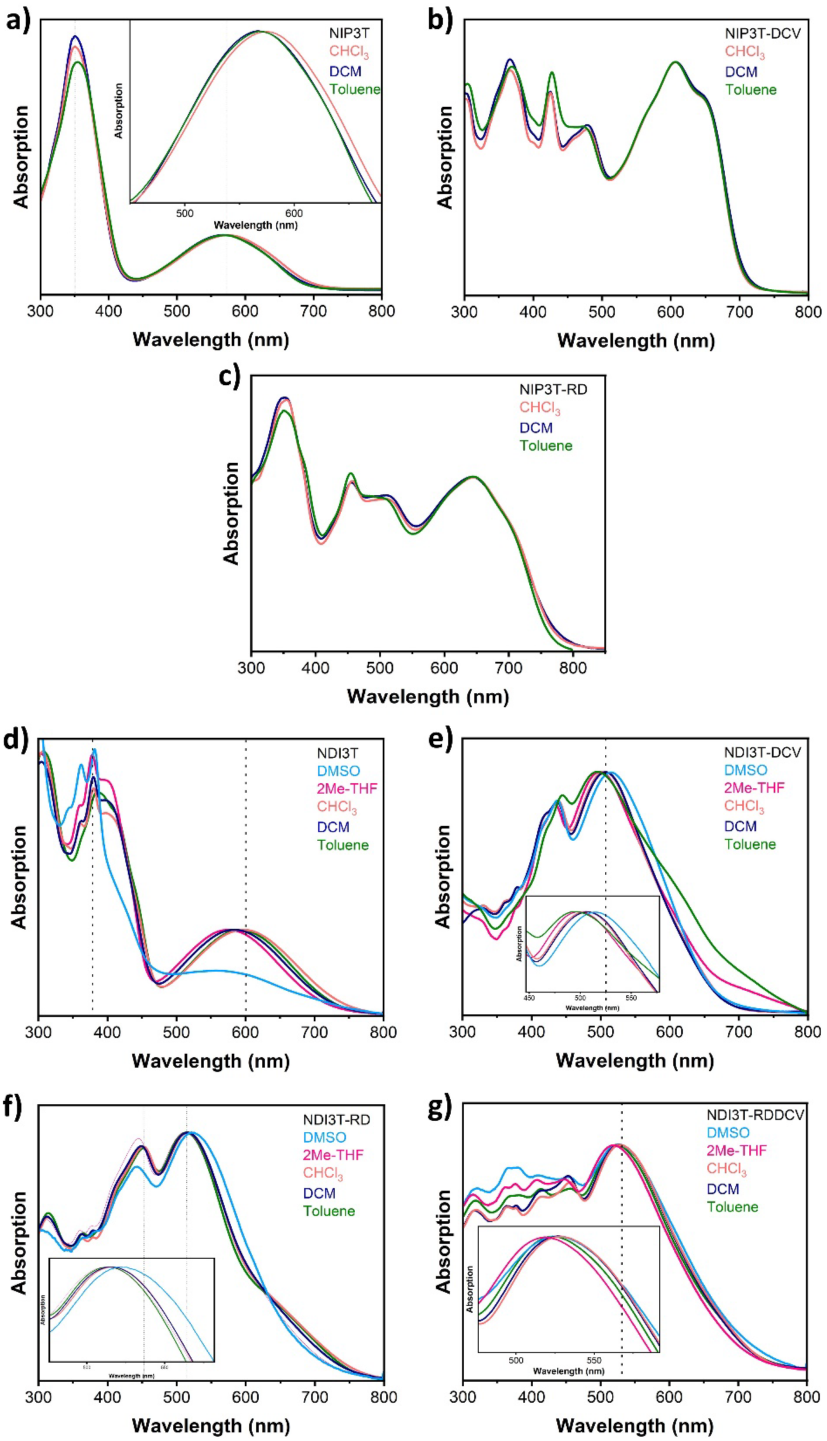

Figure III.8. Normalized UV-Vis spectra of a) **NIP3T**, b), c) **NIP3T-X** and d) **NDI3T** and e), f), g) **NDI3T-X** systems in various solvents.

Dipole moments (D)							
	NDI3T	NDI3T-RD	NDI3T-DCV	NDI3T-RDDCV	NIP3T	NIP3T-RD	NIP3T-DCV
μ_{S_0}	2.09	10.90	6.75	10.90	4.40	1.11	6.75
μ_{S_1}	14.06	12.90	8.29	6.20	16.90	3.60	0.40

Table III.3. B3LYP/6-31G** calculated dipole moments for **NDI3T-X** and **NIP3T-X** systems of the ground electronic state (μ_{S_0}) and the excited state (μ_{S_1}).

Cyclic voltammetry experiments were performed in an argon atmosphere using an electrochemical set-up at a scan rate of 100 mV/s at 20 °C. Tetrabutylammonium hexafluorophosphate (NBu_4PF_6, 0.1 mol/L) in dichloromethane was used as supporting electrolyte. All relevant data for NDI- and NIP-based organic semiconductors are compiled in Table III.4.

Cyclic voltammetry [a]					
	$E^{1/2}_{ox\,I}$ (V)	$E^{1/2}_{red\,I}$ (V)	E_{HOMO} [b] (eV)	E_{LUMO} [c] (eV)	$E_{gap}^{elec,\,d}$ (eV)
NDI3T	0.59	-1.09	-5.69	-4.00	1.69
NDI3T-RD	0.92	-0.98	-6.02	-4.12	1.90
NDI3T-DCV	0.94	-1.04	-6.04	-4.06	1.92
NDI3T-RDDCV	0.87	-0.98	-5.97	-4.12	1.85
NIP3T	0.50[e]	-1.30	-5.60	-3.80	1.80
NIP3T-RD	0.57[e]	-1.22	-5.67	-3.88	1.79
NIP3T-DCV	0.93[e]	-1.03	-6.03	-4.07	1.96

Table III.4. [a] Cyclic voltammetry recorded in DCM/TBAPF6 (0.1 M) at a scan rate of 0.15 V/s using Pt as working and the counter electrode, and Fc/Fc+ as reference. [b] Estimated from $E_{HOMO} = -5.1$ eV - $E^{1/2}$ox I. [c] Estimated from $E_{LUMO} = -5.1$ eV - $E^{1/2}$red I. [d] Estimated from $E_{gap}^{elec} = E_{HOMO} - E_{LUMO}$. [e] Anodic peak potential of the irreversible wave.

In Figure III.9 and Table III.4, it can be observed that, on the one hand, in unsubstituted systems, the substitution of a pyrazine linker (**NIP3T**) by an imidazole linkage (**NDI3T**) causes a shift of the reduction potential associated with the naphthalimide units, of approximately 0.2 V towards more positive values. This is due to the higher electron-accepting capacity of **NDI3T** compared to its analogue **NIP3T**. A similar phenomenon is observed in oxidation processes, with a shift of the oxidation potential of around 0.1 V, attributed in this case to the lower effective conjugation of the oligothiophene fragment in **NDI3T**, which reduces its capacity as an electron-donating unit due to the S···O steric interaction. This chemical modification stabilises both the HOMO and LUMO energy levels in the molecular assembly of **NDI3T** compared to its analogue NIP3T (Figures III.9c and III.9d).

On the other hand, the introduction of different electron-accepting units in the alpha position of the terthiophene fragment influences the electron-accepting capacity of these new materials. Thus, the electrochemical behaviour observed in the **NDI3T-X** series (Figure III.9b) follows the same trend as that observed in the **NIP3T-X** derivatives (Figure III.9a), showing an improvement in electron-accepting capacity compared to the unsubstituted **NDI3T** and **NIP3T** assemblies. Thus, the electrochemical data suggest that **NDI3T-X** systems are materials with an improved electron-accepting capacity compared to pyrazine-based **NIP3T-X** materials. Furthermore, the incorporation of these terminal units also affects the oxidation potential in **NDI3T-X** and **NIP3T-X** derivatives, showing a shift towards higher values when the electron-accepting units are covalently attached to the terthiophene unit, indicating a greater difficulty in the oxidation process. This effect is especially notable in **NDI3T-DCV**, **NDI3T-RD** and **NIP3T-DCV** compounds.

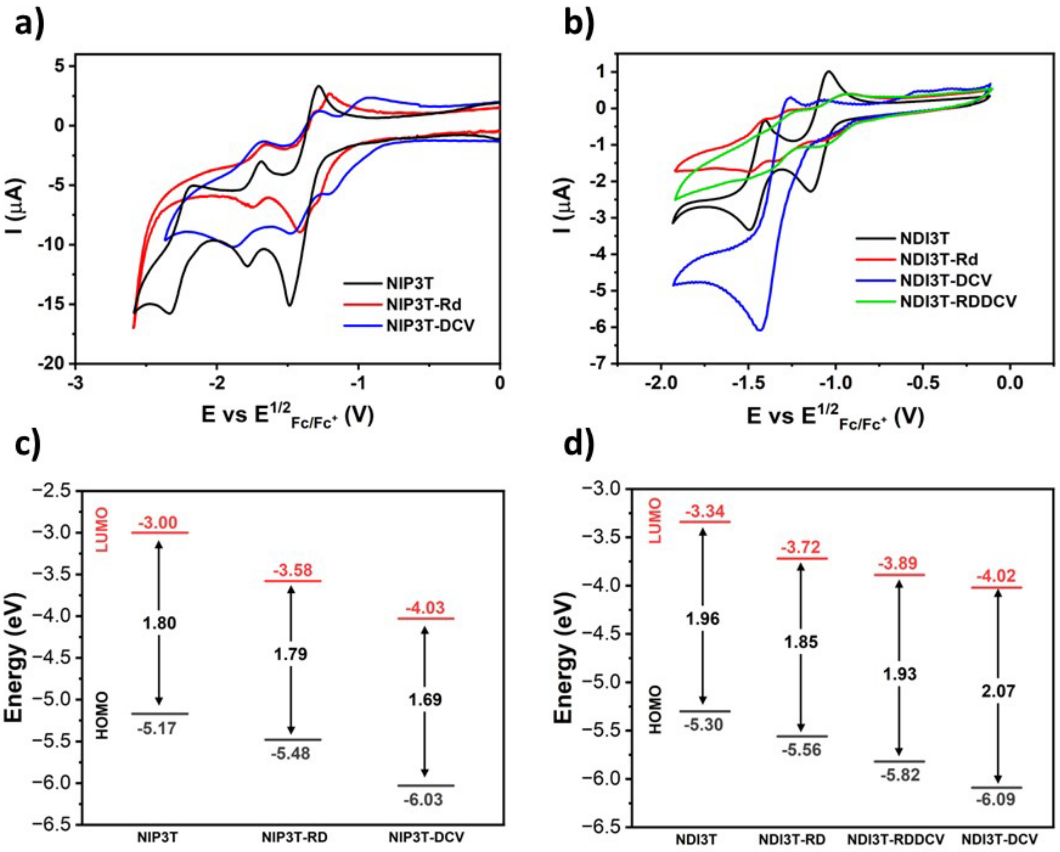

Figure III.9. Cyclic voltammetry comparison between a) **NIP3T**, **NIP3T-RD** and **NIP3T-DCV** b) **NDI3T**, **NDI3T-RD**, **NDI3T-DCV** and **NDI3T-RDDCV** reduction processes in dichloromethane solutions and c) and d) the corresponding energy levels diagram estimated from the experimental electrochemical values for both **NDI** and **NIP** based semiconductors.

As shown in Figures III.9c and III.9d, the introduction of electron-withdrawing units at the alpha position of the terminal thiophenes allows a precise control over the energy levels of the frontier molecular orbitals. It is observed that the introduction of electron-accepting units induces the stabilization of HOMO and LUMO orbitals in **NIP3T-X** compounds. Note that HOMO orbitals decrease from -5.17 eV in **NIP3T** to -5.48 eV and -6.03 eV in **NIP3T-RD** and **NIP3T-DCV** respectively, while LUMO orbital is stabilized from -3.00 eV to -3.58 eV and -4.03 eV. This shift indicates a lower capacity for the oxidation and a greater capacity to accept electrons. For its part, **NDI3T-X** derivatives show a similar trend. The HOMO orbitals decrease from -5.30 eV in **NDI3T** to -5.56 eV, -5.82 eV and -6.09 eV in **NDI3T-RD**, **NDI3T-RDDCV** and **NDI3T-DCV** respectively, while LUMO orbital is stabilized from

-3.34 eV to -3.72 eV, -3.89 eV and -4.02 eV. This increased stabilization in the HOMO and LUMO orbitals translate into shifted oxidation and reduction potentials and confirms the enhanced electron-withdrawing capacity of **NDI3T-X**. Furthermore, both **NDI3T-X** and **NIP3T-X** also display reduced bandgaps respect to unsubstituted **NDI3T** and **NIP3T**, with the exception of **NDI3T-DCV**, suggesting that the incorporation of strong electron-accepting units allows the fine tuning of the electronic properties of these semiconductors.

III.4 Spectroelectrochemical study

In this section, the structure and stability of the charge carriers present in the electron transport process are analysed by spectroelectrochemistry. The evolution of the UV-Vis-NIR spectra of the studied semiconductors was obtained by progressive spectroelectrochemical reduction and oxidation of low concentration solutions in the presence of a large excess of the supporting electrolyte Bu_4NPF_6. The results are supported by theoretical TD-DFT calculations at the B3LYP/6-31G** level. As shown in Figures III.10 and III.13, both spectroelectrochemical reduction and oxidation processes were recorded for the **NDI3T-X** and **NIP3T-X** systems, which was expected given their amphoteric redox behaviour demonstrated in the cyclic voltammetry.

The UV-Vis/NIR absorption spectra of **NIP3T** (Figure III.10a) as neutral species (black curve) after reduction potential, progressively evolve towards new absorption bands recorded at 365, 517 and 600 nm (red curve), which are attributed to the formation of anionic species. When the reduction potential is elevated two new absorption bands appear at 372 and 936 nm (blue curve) associated with the formation of dianion species. Focusing on NIP3T derivatives (**NIP3T-RD** and **NIP3T-DCV**), these show the typical spectral reduction profile of oligothiophenes, with a first spectral profile with two peaks (red curves), ascribed to the formation of radical anion species. A progressive reduction potential induces towards a new spectral profile, associated to dianion species, with a main absorption band located in the middle of the absorption bands of radical anion species.

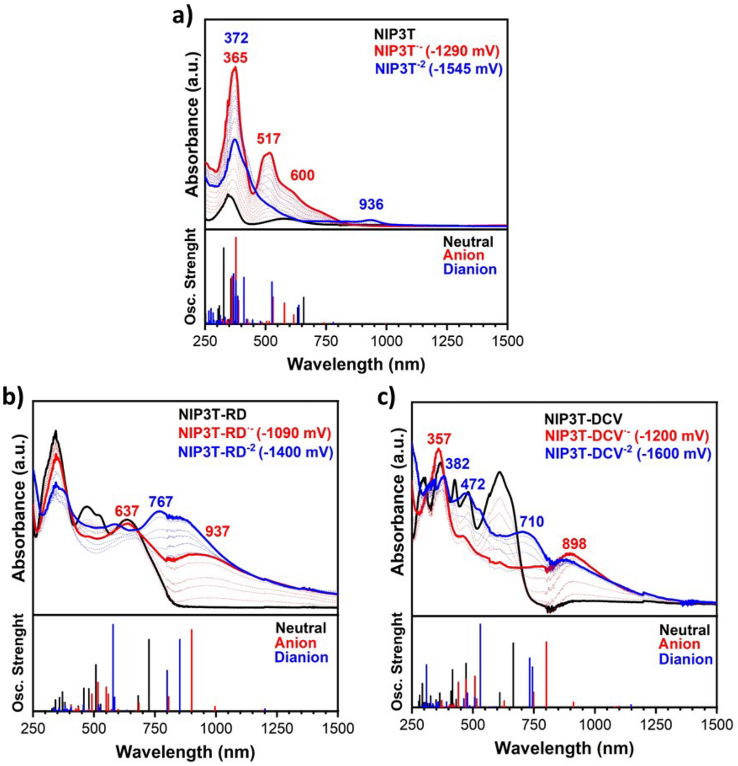

Figure III.10. UV-Vis/NIR absorption spectra recorded by electrochemical reduction and TD-DFT/B3LYP calculated vertical transitions energies of (a) **NIP3T**, (b) **NIP3T-RD** and (c) **NIP3T-RDCV** in dichloromethane in presence of Bu_4NBF_4 as supporting electrolyte within an OTTLE cell.

Looking at the oxidation processes (Figure III.11a), we can observe the capacity to accommodate two positive charges for **NIP3T**. Upon increasing the oxidation potential two new absorption bands appear at 814 and 1374 nm (red curve), related to the formation of radical cation species. Applying more positive potential the spectral profile change and we can found a new band at 968 nm (blue curve), associated with the formation of dication species. In **NIP3T-RD**, during the oxidation process the neutral spectral profile (black curve) evolve towards a new spectral profile with an absorption band at 876 nm (red curve) and other redshifted absorption band at 1380 nm, these new bans can be ascribed to the formation of radical cation species. Finally, for **NIP3T-DCV**, the gradual increase in the oxidation potential causes the spectral profile of neutral species (black curve) evolve towards a new profile with a new abroad absorption band (red curve) with two contributions at 1023 and 1164 nm, and another intense absorption band at 639 nm.

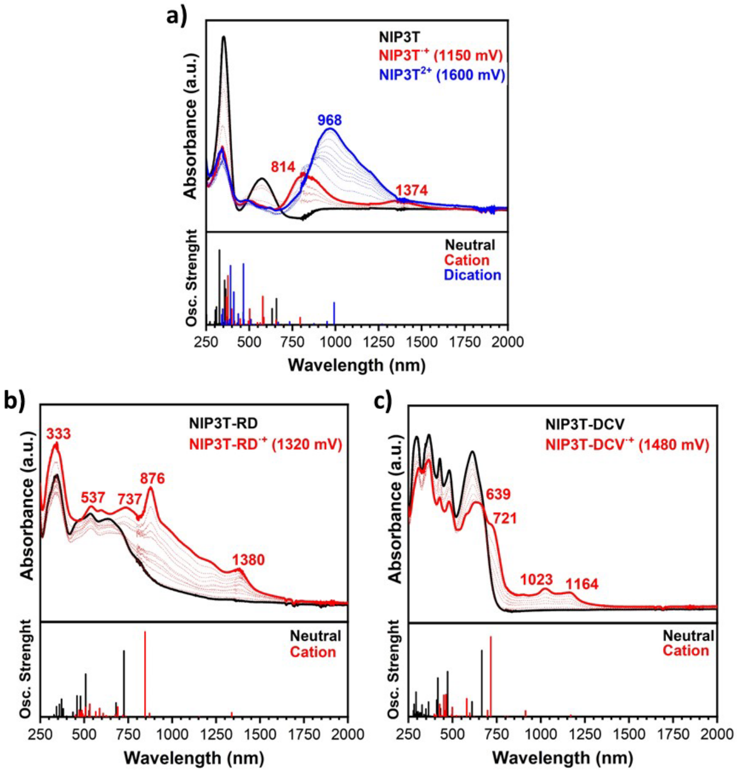

Figure III.11. UV-Vis/NIR absorption spectra recorded by electrochemical oxidation and TD-DFT/B3LYP calculated vertical transitions energies of (a) **NIP3T**, (b) **NIP3T-RD** and (c) **NIP3T-DCV** in dichloromethane in presence of Bu_4NBF_4 as supporting electrolyte within an OTTLE cell.

On the other hand, as we can observe in Figures III.12 and III.13, the UV-Vis-NIR absorption spectra of **NDI3T** (Figure III.12a) as a neutral species (black curve) progressively evolve towards new absorption bands recorded at 565 and 715 nm (red curve), which are attributed to the formation of radical anionic species. A further electrochemical reduction causes the disappearance of this spectral profile and the appearance of two new absorption peaks, one centered around 440 nm and another redshifted at 748 nm ascribed to the formation of dianion specie (blue curve).

The UV-Vis-NIR absorption spectra of **NDI3T-RD**, **NDI3T-DCV** (Figures III.12b-III.12d) show a similar behaviour. However, the spectral profile for **NDI3T-RDDCV** shows some differences**.** For **NDI3T-RD** and **NDI3T-DCV**, the neutral spectra (black curve) evolve towards a new spectral profile with two news absorption bands around 480 nm and 760 nm (red curves), attributed to the formation of radical anion species. A further increase in the applied potential causes these bands to decrease, while two news absorption bands emerge at higher energies, around 520 nm and 775 nm (blue curves), assigned to the dianion species. Finally, in **NDI3T-RDDCV** compound, the neutral spectral profile (black curve) changes towards a new spectral pattern with two new bands, just like in **NDI3T-RD** and **NDI3T-DCV**, at 495 nm and 776 nm (red curve), attributed to radical anion species. When the applied reduction potential is increased, unlike **NDI3T-RD** and **NDI3T-DCV,** the spectral profile evolves towards a new spectral profile with only one new absorption band at 441 nm (blue curve).

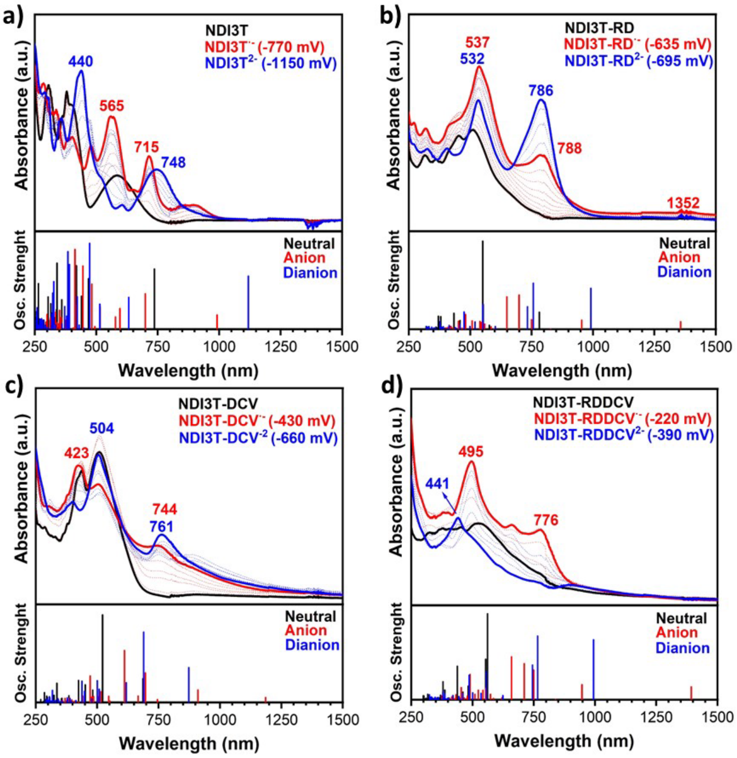

Figure III.12. UV-Vis/NIR absorption spectra recorded by electrochemical reduction and TD-DFT/B3LYP calculated vertical transitions energies of (a) **NDI3T**, (b) **NDI3T-RD**, (c) **NDI3T-DCV** and (d) **NDI3T-RDDCV** in dichloromethane in presence of Bu_4NBF_4 as supporting electrolyte within an OTTLE cell.

Progressive electrochemical oxidation of **NDI3T** (Figure III.13a) reduces the absorption of the neutral species (black curve), while leading to the formation of a broad, red-shifted absorption band at 1257 nm (red curve), and another band at 408 nm. According to the electrochemical results and TD-DFT calculations, these new absorptions can be attributed to the formation of the radical cation species. Further electrochemical oxidation leads to the appearance of a new broad absorption band (blue curve), which presents two contributions, one centered at 412 nm and another at 1038 nm, ascribed to the formation of dicationic species.

On the other hand, the progressive electrochemical oxidation of **NDI3T-RD**, **NDI3T-DCV** and **NDI3T-RDDCV** (Figure III.13b-III.13d) gives rise to the formation of a new cation species (red curve), which shows a similar absorption pattern, with the main absorption band appearing around 400 nm and other absorption band around 1150-1325 nm. A further increase of the applied potential does not lead to the formation of new species in the compounds with electrodeficient groups in the thiophene subunits.

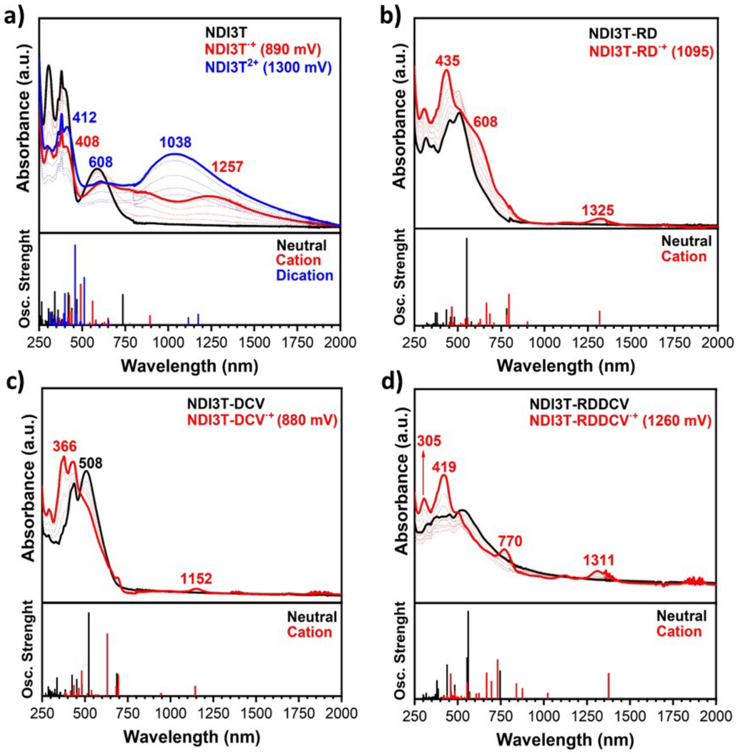

Figure III.13. UV-Vis/NIR absorption spectra recorded by electrochemical oxidation and TD-DFT/B3LYP calculated vertical transitions energies of (a) **NDI3T**, (b) **NDI3T-RDDCV**, (c) **NDI3T-RD** and (d) **NDI3T-DCV** in dichloromethane in presence of Bu_4NBF_4 as supporting electrolyte within an OTTLE cell.

However, the potentials at which both reduction and oxidation occur in the **NDI3T-X** systems are considerably lower than the **NIP3T-X** molecules. It is noteworthy that, in the latter, both the HOMO and the LUMO are located in the oligothiophene fragment, so the effect of the lateral substituents on the electron-donating properties of the thiophene chain is much more pronounced, indicating a reduced electron-donating nature of that molecular fragment. Therefore, the ability to stabilize positive charges is diminished in **NIP3T-X**. Furthermore, the injection of negative charges, which also goes directly to the oligothiophene fragment, is also hindered, so it appears at much higher voltages.

Furthermore, in the **NDI3T-X** systems, the injected negative charge is mainly stabilised on the naphthalimide fragment, as expected considering the LUMO topologies. DFT calculations of the charged species indicate that while in **NDI3T** the negative charge is localised over the NDI unit, the introduction of the terthiophene subunit laterally substituted with electrowithdrawing groups decreases this percentage, locating a 70% of the injected charge in the NDI units, while a 30% of the injected charge is localised over the end-capped electrowithdrawing groups (Figure III.14). A similar trend is observed in **NIP3T-X** systems. In **NIP3T,** the injected negative charge is localised over the NIP unit, whereas in **NIP3T-X** derivatives, after the introduction of electrowithdrawing groups in the terthiophene chain, the injected charge is localised around 50% between NIP units and lateral electrowithdrawing groups. This trend in **NDI3T-X** and **NIP3T-X** systems indicates the important role of both the central connecting unit and the lateral substituents in promoting the stabilisation of the negatively charged species.

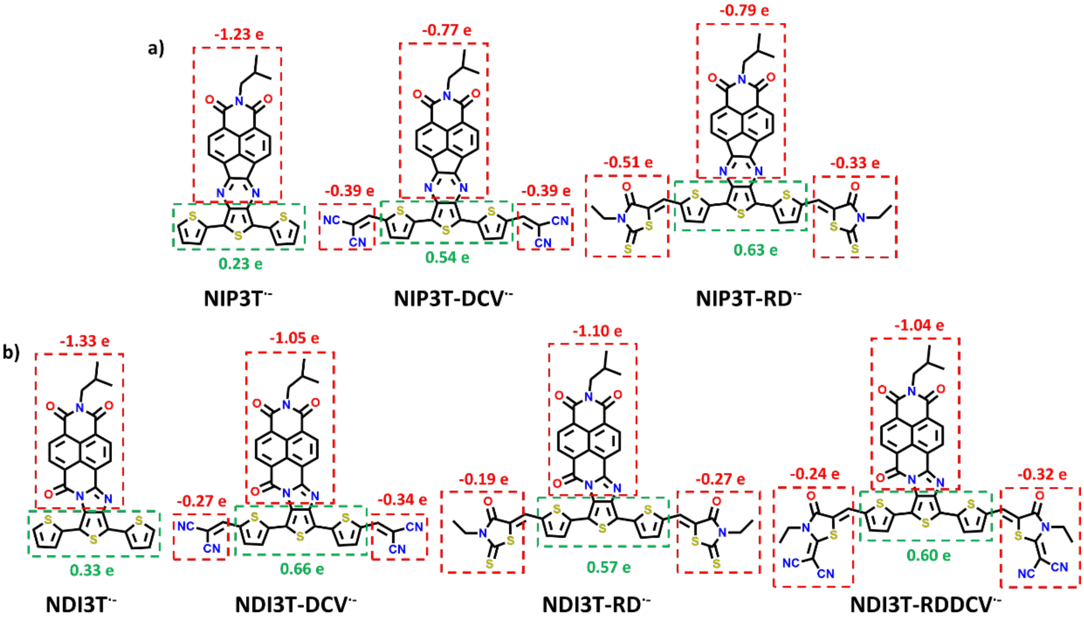

Figure III.14. DFT-calculated Mülliken atomic charges of the reduced species of a) **NIP3t** and **NIP3T-X** and b) **NDI3T** and **NDI3T-X**.

III.5 Conclusions

We study a novel family of amphoteric redox-behaving organic semiconductors featuring a combination of processable terthiophene-naphthalimide assemblies with imidazole and pyrazine linkers, and different terminal strong electron-withdrawing groups in order to tune their optoelectrochemical properties. All of these materials exhibit low LUMO energy levels and broad absorptions at around 800 nm, characteristics that are ideal for organic electronics.

The results indicate a complex electronic scenario that goes beyond the cumulative effects expected from the independent molecular units constituting the final molecular assembly. Thus, the modification of the connecting group in unsubstituted derivatives, such as **NIP3T** and **NDI3T**, has some impact on the optoelectronic properties, but does not modulate the topologies of the molecular orbitals, since the lowest energy absorption band has an ICT character. However, when electrowithdrawing lateral substituents are inserted into these molecular platforms, different effects are observed both on the energies and, especially, on the topologies of the frontier molecular orbitals. Here it has been shown that such effects have profound implications on the electronic properties of the materials, both on the optical absorption properties and on the stabilization of charged species. Thus, when electrowithdrawing groups are inserted into the **NIP3T** derivatives, the lowest energy absorption band acquires a π-π^* character, which causes the charge distribution in the LUMO to be localized over the oligothiophene fragment, instead of being located on the naphthalimide units, thus modulating the electron-donating nature of the oligothiophene chain. Nevertheless, both positive and negative charges are still stabilized, but at high potentials. In contrast, the introduction of electroactive groups into the **NDI3T** derivatives causes the appearance of two different and competing ICT channels within the molecule, which has interesting effects on the electronic absorption spectra. In addition, the electron densities at HOMO and LUMO are comparable to those of unsubstituted **NDI3T** system, so both positive and negative charges can be stabilized for **NDI3T-X** semiconductors, at much more accessible potentials than in **NIP3T-X** molecules.

III.6 References

1 C. Yan, S. Barlow, Z. Wang, H. Yan, A. K. Y. Jen, S. R. Marder and X. Zhan, Non-fullerene acceptors for organic solar cells, *Nature Reviews Materials 2018 3:3*, 2018, **3**, 1–19.

2 Y. Huang, X. Gong, Y. Meng, Z. Wang, X. Chen, J. Li, D. Ji, Z. Wei, L. Li and W. Hu, Effectively modulating thermal activated charge transport in organic semiconductors by precise potential barrier engineering, *Nature Communications 2021 12:1*, 2021, **12**, 1–9.

3 M. Wang, P. Baek, A. Akbarinejad, D. Barker and J. Travas-Sejdic, Conjugated polymers and composites for stretchable organic electronics, *J Mater Chem C*, 2019, **7**, 5534–5552.

4 A. Minotto, I. Bulut, A. G. Rapidis, G. Carnicella, M. Patrini, E. Lunedei, H. L. Anderson and F. Cacialli, Towards efficient near-infrared fluorescent organic light-emitting diodes, *Light: Science & Applications 2021 10:1*, 2021, **10**, 1–10.

5 W. Liu, X. Xu, J. Yuan, M. Leclerc, Y. Zou and Y. Li, Low-Bandgap Non-fullerene Acceptors Enabling High-Performance Organic Solar Cells, *ACS Energy Lett*, 2021, **6**, 598–608.

6 A. Velusamy, C. H. Yu, S. N. Afraj, C. C. Lin, W. Y. Lo, C. J. Yeh, Y. W. Wu, H. C. Hsieh, J. Chen, G. H. Lee, S. H. Tung, C. L. Liu, M. C. Chen and A. Facchetti, Thienoisoindigo (TII)-Based Quinoidal Small Molecules for High-Performance n-Type Organic Field Effect Transistors, *Advanced Science*, 2021, **8**, 2002930.

7 H. Bronstein, C. B. Nielsen, B. C. Schroeder and I. McCulloch, The role of chemical design in the performance of organic semiconductors, *Nature Reviews Chemistry 2020 4:2*, 2020, **4**, 66–77.

8 Y. Ran, Y. Guo and Y. Liu, Organostannane-free polycondensation and eco-friendly processing strategy for the design of semiconducting polymers in transistors, *Mater Horiz*, 2020, **7**, 1955–1970.

9 K. Tajima, K. Matsuo, H. Yamada, S. Seki, N. Fukui and H. Shinokubo, Acridino[2,1,9,8-klmna]acridine Bisimides: An Electron-Deficient π-System for Robust Radical Anions and n-Type Organic Semiconductors, *Angewandte Chemie*, 2021, **133**, 14179–14186.

10 A. Nowak-Król, K. Shoyama, M. Stolte and F. Würthner, Naphthalene and perylene diimides – better alternatives to fullerenes for organic electronics?, *Chemical Communications*, 2018, **54**, 13763–13772.

11 F. Suárez-Blas, L. Pandolfi, M. J. Alonso-Navarro, S. Riera-Galindo, J. I. Martínez, B. Dörling, A. Funes, A. Harillo-Baños, E. Venuti, M. M. Ramos, M. Campoy-Quiles and J. L. Segura, Tailoring the Electron-Deficient Central Core on Fused-Ring Nonfullerene Acceptors: Deciphering the Relationships Between Structure, Property, and Photovoltaic Performance, *Advanced Energy and Sustainability Research*, 2024, **5**, 2400028.

12 I. E. Park, A. Hoff, C. Beaumont, B. S. Gelfand, R. D. Pettipas and G. C. Welch, Cyclic secondary amine functionalized perylene diimide polymers for solution processed electrochromic devices, *J Mater Chem C*, 2024, **12**, 1710–1717.

13 S. V. Bhosale, M. Al Kobaisi, R. W. Jadhav, P. P. Morajkar, L. A. Jones and S. George, Naphthalene diimides: perspectives and promise, *Chem Soc Rev*, 2021, **50**, 9845–9998.

14 M. J. Sung, A. Luzio, W. T. Park, R. Kim, E. Gann, F. Maddalena, G. Pace, Y. Xu, D. Natali, C. de Falco, L. Dang, C. R. McNeill, M. Caironi, Y. Y. Noh and Y. H. Kim, High-Mobility Naphthalene Diimide and Selenophene-Vinylene-Selenophene-Based Conjugated Polymer: n-Channel Organic Field-Effect Transistors and Structure–Property Relationship, *Adv Funct Mater*, 2016, **26**, 4984–4997.

15 H. Liu, Y. Geng, Z. Xiao, L. Ding, J. Du, A. Tang and E. Zhou, The Development of Quinoxaline-Based Electron Acceptors for High Performance Organic Solar Cells, *Advanced Materials*, 2024, **36**, 2404660.

16 T. He, M. Stolte, C. Burschka, N. H. Hansen, T. Musiol, D. Kälblein, J. Pflaum, X. Tao, J. Brill and F. Würthner, Single-crystal field-effect transistors of new Cl2-NDI polymorph processed by sublimation in air, *Nature Communications 2015 6:1*, 2015, **6**, 1–9.

17 J. M. Fisher, M. L. Williams, J. R. Palmer, N. E. Powers-Riggs, R. M. Young and M. R. Wasielewski, Long-Lived Charge Separation in Single Crystals of an Electron Donor Covalently Linked to Four Acceptor Molecules, *J Am Chem Soc*, 2024, **146**, 9911–9919.

18 B. Lu, M. Stolte, D. Liu, X. Zhang, L. Zhao, L. Tian, C. D. Frisbie, F. Würthner, X. Tao, T. He, B. Lu, D. Liu, X. Zhang, L. Zhao, L. Tian, X. Tao, T. He, M. Stolte, F. Würthner and C. D. Frisbie, High Sensitivity and Ultra-Broad-Range NH3 Sensor Arrays by Precise

Control of Step Defects on The Surface of Cl2-Ndi Single Crystals, *Advanced Science*, 2024, **11**, 2308036.

19 Y. Park, C. Fuentes-Hernandez, X. Jia, F. A. Larrain, J. Zhang, S. R. Marder and B. Kippelen, Measurements of the field-effect electron mobility of the acceptor ITIC, *Org Electron*, 2018, **58**, 290–293.

20 T. Duan, J. Wang, W. Shi, Y. Li, K. Tu, X. Bi, C. Zhong, J. Lv, K. Yang, Z. Xiao, B. Kan and Y. Zhao, Fully Fused Indacenodithiophene-Centered Small-Molecule n-Type Semiconductors for High-Performance Organic Electronics, *Angewandte Chemie*, 2024, **136**, e202407890.

21 X. Liao, M. Liu, W. Xie, J. Wang, P. Zhu, S. Yu, Y. Fu, X. Lu, K. Feng, X. Guo and Y. Chen, Manipulating Molecular Stacking to Achieve High Electron Mobility in 2D Conjugated Ultra-Narrow Bandgap Non-Fullerene Acceptors with Absorption Beyond 1000 nm, *Adv Funct Mater*, 2024, **34**, 2405728.

22 B. Balambiga, P. Devibala, P. M. Imran and S. Nagarajan, Tunable Charge Transport Using Heterocycles-Flanked Alkoxyphenanthrenes for High-Performing OFETs, *ACS Omega*, DOI:10.1021/ACSOMEGA.4C01166/ASSET/IMAGES/LARGE/AO4C01166_0006.JPEG.

23 W. Tang, D. Huang, C. He, Y. Yi, J. Zhang, C. Di, Z. Zhang and Y. Li, Solution-processed small molecules based on indacenodithiophene for high performance thin-film transistors and organic solar cells, *Org Electron*, 2014, **15**, 1155–1165.

24 X. Zhou, S. Pang, B. Wu, J. Zhou, H. Tang, K. Lin, Z. Xie, C. Duan, F. Huang and Y. Cao, Noncovalent Interactions Induced by Fluorination of the Central Core Improve the Photovoltaic Performance of A-D-A’-D-A-Type Nonfused Ring Acceptors, *ACS Appl Energy Mater*, 2022, **5**, 7710–7718.

25 S. Khanam, S. J. Akram, R. A. Khera, S. T. Zohra, A. M. Shawky, N. S. Alatawi, M. A. A. Ibrahim and E. U. Rashid, Exploration of charge transfer analysis and photovoltaics properties of A-D-A type non-fullerene phenazine based molecules to enhance the organic solar cell properties, *J Mol Graph Model*, 2023, **125**, 108580.

26 A. Mishra and G. D. Sharma, Harnessing the Structure-Performance Relationships in Designing Non-Fused Ring Acceptors for Organic Solar Cells, *Angewandte Chemie*, 2023, **135**, e202219245.

27 M. J. Alonso-Navarro, E. Gala, M. M. Ramos, R. Ponce Ortiz and J. L. Segura, Oligothiophene-Naphthalimide Hybrids Connected through Rigid and Conjugated

Linkers in Organic Electronics: An Overview, *Electronic Materials 2021, Vol. 2, Pages 222-252*, 2021, **2**, 222–252.

28 A. de la Peña, I. Arrechea-Marcos, M. J. Mancheño, M. C. Ruiz Delgado, J. T. López Navarrete, J. L. Segura and R. Ponce Ortiz, Tuning of the Electronic Levels of Oligothiophene–Naphthalimide Assemblies by Chemical Modification, *Chemistry – A European Journal*, 2016, **22**, 13643–13652.

29 R. P. Ortiz, H. Herrera, R. Blanco, H. Huang, A. Facchetti, T. J. Marks, Y. Zheng and J. L. Segura, Organic n-channel field-effect transistors based on arylenediimide-thiophene derivatives, *J Am Chem Soc*, 2010, **132**, 8440–8452.

30 R. Ponce Ortiz, H. Herrera, M. J. Mancheño, C. Seoane, J. L. Segura, P. Mayorga Burrezo, J. Casado, J. T. Lõpez Navarrete, A. Facchetti and T. J. Marks, Molecular and Electronic-Structure Basis of the Ambipolar Behavior of Naphthalimide–Terthiophene Derivatives: Implementation in Organic Field-Effect Transistors, *Chemistry – A European Journal*, 2013, **19**, 12458–12467.

31 M. J. Alonso-Navarro, A. Harbuzaru, P. De Echegaray, I. Arrechea-Marcos, A. Harillo-Baños, A. De La Peña, M. M. Ramos, J. T. López Navarrete, M. Campoy-Quiles, R. Ponce Ortiz and J. L. Segura, Effective interplay of donor and acceptor groups for tuning optoelectronic properties in oligothiophene–naphthalimide assemblies, *J Mater Chem C*, 2020, **8**, 15277–15289.

32 C. Castiglioni, J. T. Lopez Navarrete, G. Zerbi and M. Gussoni, A simple interpretation of the vibrational spectra of undoped, doped and photoexcited polyacetylene: Amplitude mode theory in the GF formalism, *Solid State Commun*, 1988, **65**, 625–630.

33 G. Zerbi, M. Veronelli, S. Martina, A. -D Schlüter and G. Wegner, π-Electron delocalization in conformationally distorted oligopyrroles and ploypyrrole, *Advanced Materials*, 1994, **6**, 385–388.

34 J. Albero, P. Atienzar, A. Corma and H. Garcia, Efficiency Records in Mesoscopic Dye-Sensitized Solar Cells, *The Chemical Record*, 2015, **15**, 803–828.

35 S. R. González, J. Casado, J. T. López Navarrete, R. Blanco and J. L. Segura, A β-naphthaleneimide-modified terthiophene exhibiting charge transfer and polarization through the short molecular axis. Joint spectroscopic and theoretical study, *Journal of Physical Chemistry A*, 2008, **112**, 6732–6740.

36 S. K. Panja, N. Dwivedi and S. Saha, Tuning the intramolecular charge transfer (ICT) process in push–pull systems: effect of nitro groups, *RSC Adv*, 2016, **6**, 105786–105794.

37 Y. Rout, C. Montanari, E. Pasciucco, R. Misra and B. Carlotti, Tuning the Fluorescence and the Intramolecular Charge Transfer of Phenothiazine Dipolar and Quadrupolar Derivatives by Oxygen Functionalization, *J Am Chem Soc*, 2021, **143**, 9933–9943.

Chapter IV:

Impact of supramolecular interactions by hydrogen bonding on the electronic and charge transport properties of DPP-based organic semiconductors

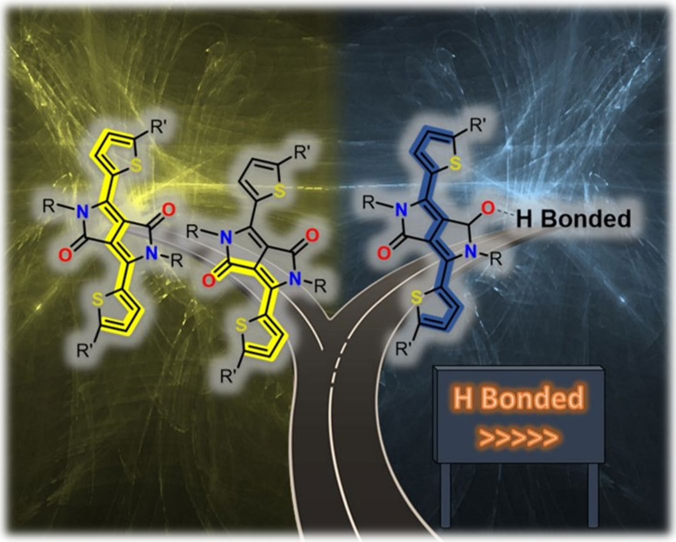

Table of contents

CONTENTS

IV.1 Introduction

The versatility of organic synthesis allows the design of small molecules or polymers with desired optoelectronic properties.[1–5] The design of the molecules is important for device efficiency, although the way in which the materials are assembled is equally important.[6–8] Noncovalent interactions play an important role in the direct self-assembly of small molecules in solution and the thin-film deposition process. For organic semiconductors composed of conjugated segments and aromatic moieties, π-stacking is usually the most important noncovalent interaction that defines their molecular packing. This noncovalent π-stacking interaction, when combined with hydrogen bonding, has been observed to be an extremely efficient way to improve the morphology of the active layer in organic electronic devices by forming enhanced interconnected regions in which charge can be easily transported.[9–16]

Despite promising results highlighting the beneficial role of hydrogen bonds, the incorporation of these moieties into organic semiconductors for the fabrication of various electronic devices is still poorly explored. In addition, the search for better-performing organic semiconductors that could be commercially viable has mostly focused on optimising the structure-property relationships of organic semiconducting materials over the years. The aim is to find the right balance between molecular and intermolecular characteristics to enable efficient charge transport. However, there is growing attention on the use of molecular dopants because they allow tailoring the energy gap as well as the optical and electrical functionalities of the semiconductor materials.[17,18] This approach has been demonstrated to enhance the electrical properties of the materials by increasing the ease of charge injection and transport within the devices.[19–25] Nevertheless, the selection and design of effective organic dopants is a challenge. In this context, self-doping in molecular materials can be more straightforward because it does not need the synthesis of extra dopants. In luminescent organic semiconductors, self-doping has been achieved by incorporating impurities with higher conjugation (usually reaction by-products) that act as molecular dopants.[26,27] Other strategies include doping the semiconductor main chain by introducing functional groups in the side chains[28] or the use of quinoidal semiconductors, where the coexistence of closed and open shell structures can give rise to self-doping characteristics.[29–31] In any case, these strategies lead to the generation of free charge carriers, which improves the electrical performance of the material. Furthermore, some examples of hydrogen-bonded assisted self-doped conductors have been reported in the literature, where it has been shown that this supramolecular interaction is responsible for the self-doping mechanism.[32–34] However, in organic transistors, self-doping, understood as the unintentional formation of doped species in the pure material, often produces non-ideal results, since improving the charge mobility by field effect without decreasing the ON/OFF ratio remains a challenge.[35] Therefore, it is essential to explore new strategies that allow modulating the electronic characteristics of the materials and facilitate charge formation without the need to add external dopants.

DPP is a widely known π-conjugated system used in numerous organic electronic devices due to its excellent electronic properties and stability.[36–39] Generally, this system appears as a component of high molecular weight semiconductor polymers or as part of more sophisticated discrete molecules employed in organic electronic devices.[40–42] In some cases, devices fabricated from DPP cores have been reported in the literature.[43–45] Although the structures obtained using this technique are well organized, the low solubility of non-alkylated systems requires their processing by sublimation or the application of the latent pigment technique (protection and acid post-treatment) to make their processing in solution possible. Furthermore, this strategy is not versatile, since the assembly process always follows the same trend, which limits the possibility of adjusting the optoelectronic properties of the materials based on their intra or intermolecular interactions.

In this chapter, we investigate whether is possible to achieve good charge carrier mobility values using small, discrete π-conjugated basic cores containing hydrogen-bonding units. To this end, we have selected a simple electroactive segment based on diketopyrrolopyrrole (DPP) with thiophene ends and amide groups as hydrogen-bonding units. A control molecule, without amide groups, thus without the possibility to form hydrogen bonds, was also analyzed (Figure IV.1). In order to measure their electrical characteristics we have fabricated solution-processed organic field-effect transistors (OFETs).

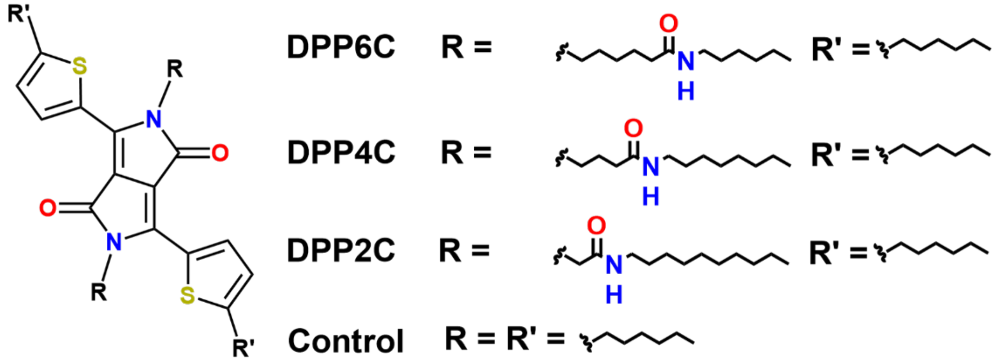

Figure IV.1. Chemical structure of **Control**, **DPP2C**, **DPP4C** and **DPP6C**.

IV.2 Structural and optical properties

To analyze the structural and electronic properties of the derivatives with amide groups, as well as the control molecule, density functional theory (DFT) calculations were performed. The results show that **Control**, **DPP4C**, and **DPP6C** compounds have similar molecular skeleton arrangements, with a thiophene-DPP-thiophene planar structure, due to the interaction between the hydrogen of the thiophene ring and the carbonyl of the lactam of the DPP unit. This interaction occurs at a distance of 2.1 Å, as observed in Figure IV.2. However, DFT calculations indicate a twisted structure for **DPP2C**, with torsion angles of approximately 15° between the DPP core and the thiophene groups, which is due to the intramolecular interaction between the hydrogen of the amide group and the carbonyl of DPP, that prevents the aforementioned interaction with the thiophene ring that planarizes the π-conjugated core. Note that**,** the distance between the hydrogen atom of the N−H amide group and the C=O carbonyl group of DPP in **DPP2C** is 2.02 Å. This distance is less than the sum of the van der Waals radii of the two atoms (2.72 Å), indicating the presence of an intramolecular hydrogen bond interaction.

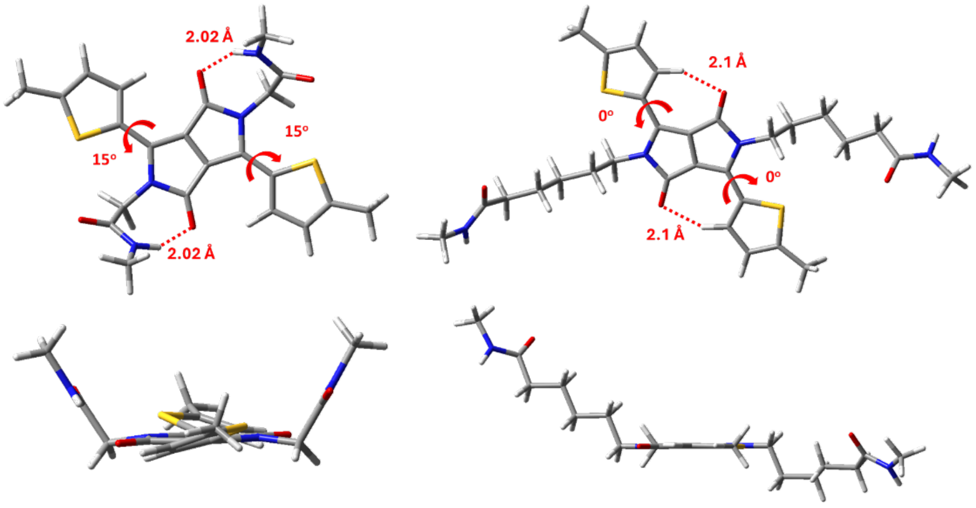

DPP2C **DPP6C**

Figure IV.2. DFT-computed global minimum energy geometries for **DPP2C** and **DPP6C** at B3LYP/6-31G** level of theory.

As expected, the frontier molecular orbitals in the studied molecules are delocalized along the entire conjugated skeleton, with a greater contribution at the DPP core, see Figure IV.3. The **Control**, **DPP4C** and **DPP6C** systems exhibit similar HOMO-LUMO energy gaps around 2.42 eV. However, **DPP2C** exhibits a slightly higher HOMO-LUMO gap compared to the other compounds, at 2.47 eV. In particular, a slight destabilization of the HOMO and LUMO orbitals is predicted for **DPP4C** and **DPP6C** respect to **Control** molecule. In contrast, the opposite trend is observed in the **DPP2C**, where HOMO and LUMO orbitals are stabilized respect **Control** compound. This difference in the energies of HOMO and LUMO energies of **DPP2C** can be attributed to the lower electronic communication between the thiophenes and the DPP, which accentuates the electron-deficient character of the DPP and provokes the stabilization of both HOMO and LUMO orbitals. Stabilization is more pronounced in the HOMO orbital, increasing the HOMO-LUMO gap.

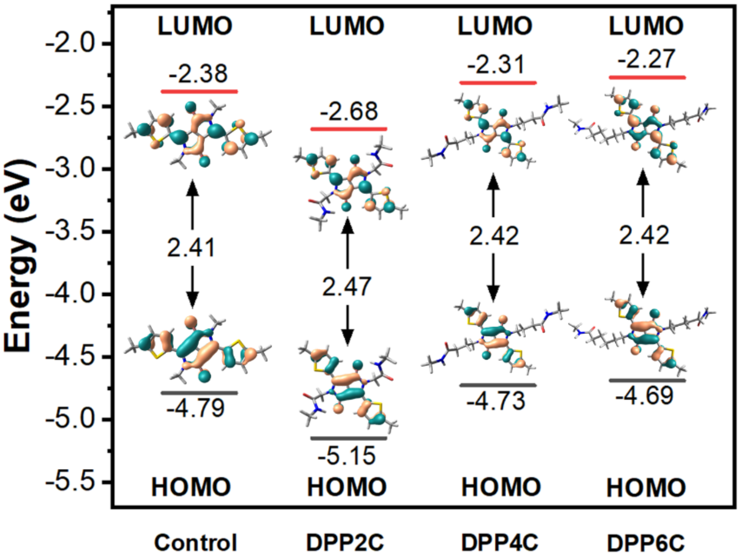

Figure IV.3. DFT-calculated molecular orbital energies (B3LYP/6-31G**) for the studied molecules along with topologies of the HOMO and LUMO orbitals.

The optical properties in solution and in thin film of **Control**, **DP2C**, **DPP4C** and **DPP6C** were studied by UV-Vis absorption spectroscopy (Figure IV.4) and analyzed with the help of time-dependent density functional theory (TD-DFT) calculations. **Control**, **DPP4C** and **DPP6C** present a similar spectrum in solution, due to the minimization of intermolecular interactions between the molecules in dilute solution, showing a main band around 560 nm, with vibronic features at 520 nm and 482 nm. However, **DPP2C** absorption spectra is slightly blue-shifted respect to those of the other studied compounds, with a main absorption band at 554 nm and vibronic features at 516 and 479 nm, indicating a decrease in the π-conjugation. This effect in **DPP2C** can be attributed to the intramolecular hydrogen interaction between the amide hydrogen and the DPP carbonyl, which decreases planarity and thus, π-conjugation. TD-DFT calculations correctly predict these experimental results and assign the lowest energy band to a single-electron excitation from the HOMO to the LUMO (Table IV.1). Furthermore, the thin film spectra of all studied materials show a broader and red-shifted spectral profile, with three main bands around 490 nm and 610 nm.

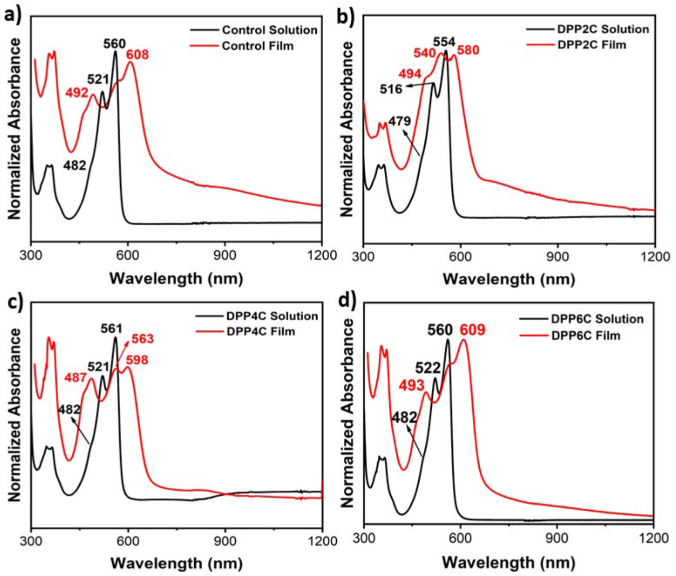

Figure IV.4. UV-Vis absorption spectra in chloroform solutions (black) and thin film (red) of a) **Control**, b) **DPP2C**, c) **DPP4C** and d) **DPP6C**.

Compound	Description	λ_{max}	*f*
Control	H→L (100%)	523 nm	0.59
DPP2C	H→L (100%)	514 nm	0.61
DPP4C	H→L (100%)	524 nm	0.60
DPP6C	H→L (100%)	525 nm	0.61

Table IV.1. Electronic transitions calculated by TD-DFT B3LYP/6-31G** level of theory for **Control**, **DPP2C**, **DPP4C** and **DPP6C**.

The effect of modifying the alkyl side chains was analyzed by recording the emission spectra and measuring the corresponding Stokes shifts both in solution and in the solid state (see Figure IV.5). While small Stokes shifts of approximately 11-15 nm were observed in solution, significantly larger shifts were found in the solid state. Particularly, for molecules where intermolecular hydrogen bonds are favourable, **DPP4C** and **DPP6C**, we observed Stokes shifts of 137 nm and 140 nm, respectively. Large Stokes shifts induced by hydrogen bond interactions have previously been reported in the literature.[46,47] However, the **Control** and **DPP2C** compounds show lower shifts in the solid state (108 nm and 117 nm, respectively) than **DPP4C** and **DPP6C**, probably compounds due to the presence of π-π interactions in these compounds.

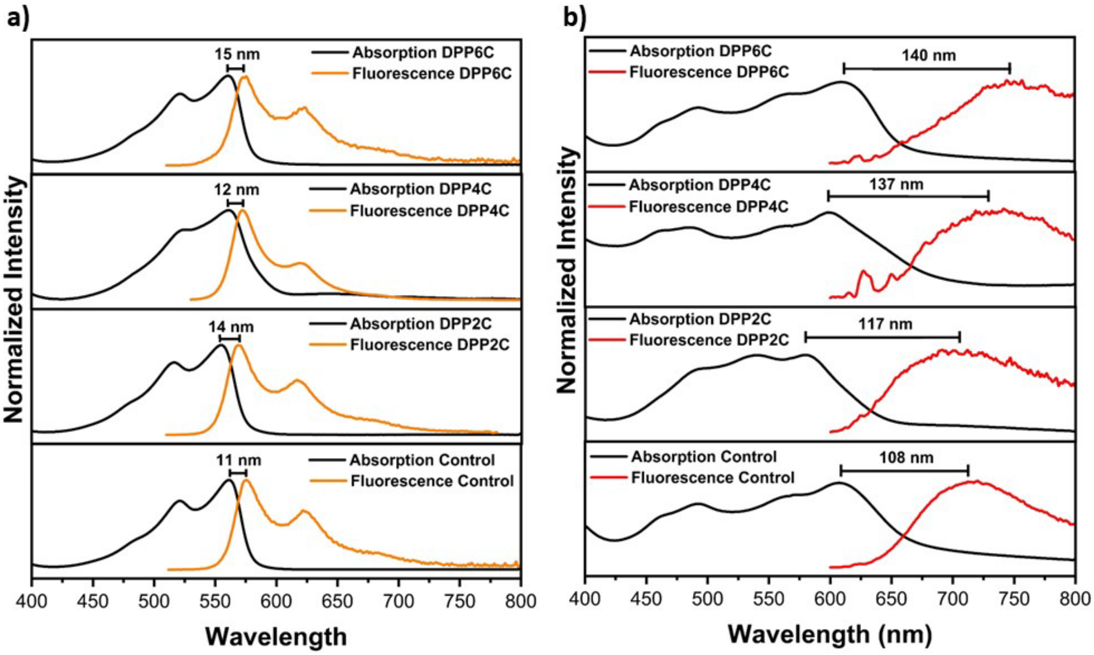

Figure IV.5. a) UV-Vis absorption spectra in chloroform solution (black) and emission spectra (orange) of **Control**, **DPP2C**, **DPP4C** and **DPP6C**. b) UV-Vis absorption spectra in film (black) and emission spectra (red) of **Control**, **DPP2C**, **DPP4C** and **DPP6C**.

IV.3 Vibrational Spectroscopical analysis

Attenuated total reflectance (ATR) IR and FT-Raman spectra of the studied semiconductors in powder form were recorded to analyse hydrogen bond formation and its impact on the electronic structures of the conjugated backbones.

In the ATR spectrum of the **Control** compound (Figure IV.6a), a single ν(C=O) vibration is observed at 1656 cm^{-1}, corresponding to the cross-conjugated carbonyl group of the DPP lactam. In contrast, in the **DPP4C** and **DPP6C** compounds, as expected, two distinct bands appear around 1658 cm^{-1} and 1642 cm^{-1}. The IR band around 1658 cm^{-1} is associated with the ν(C=O) vibration of the lactam ring, while the band at 1642 cm^{-1} is attributed to the ν(C=O) vibration of amide groups in the alkyl chains, being involved in hydrogen bonds. Theoretical calculations do not predict this shift, with the frequency of this latter band being significantly lower than the one predicted for isolated **DPP4C** and **DPP6C** molecules (1710 cm^{-1} for **DPP4C** and 1709 cm^{-1} for DPP6C). This indicates a lengthening of the C=O double bond due to intermolecular interactions, see Figure IV.6b and eigenvectors in Figure IV.7. On the other hand, for **DPP2C** the band attributed to ν(C=O) vibration of the amide groups in the alkyl chains appears at a higher wavenumber, (1670 cm^{-1}) whereas the ν(C=O) vibration of the DPP appear at 1653 cm^{-1}. This shift to higher wavenumber of the ν(C=O) vibration of the amide groups is consistent with the amide carbonyl group of the alkyl chains no participating in hydrogen bond interactions. Theoretical calculations are in consonance with experimental data, showing two bands at 1714 cm^{-1} and 1654 cm^{-1}, ascribed to the ν(C=O) vibration of the amide groups in the alkyl chains and the ν(C=O) vibration of the lactam ring, respectively. This latter band is shifted to lower frequencies compared to the other compounds, indicating that the carbonyl of DPP in **DPP2C** takes part in intramolecular hydrogen bonds, as previously indicated.

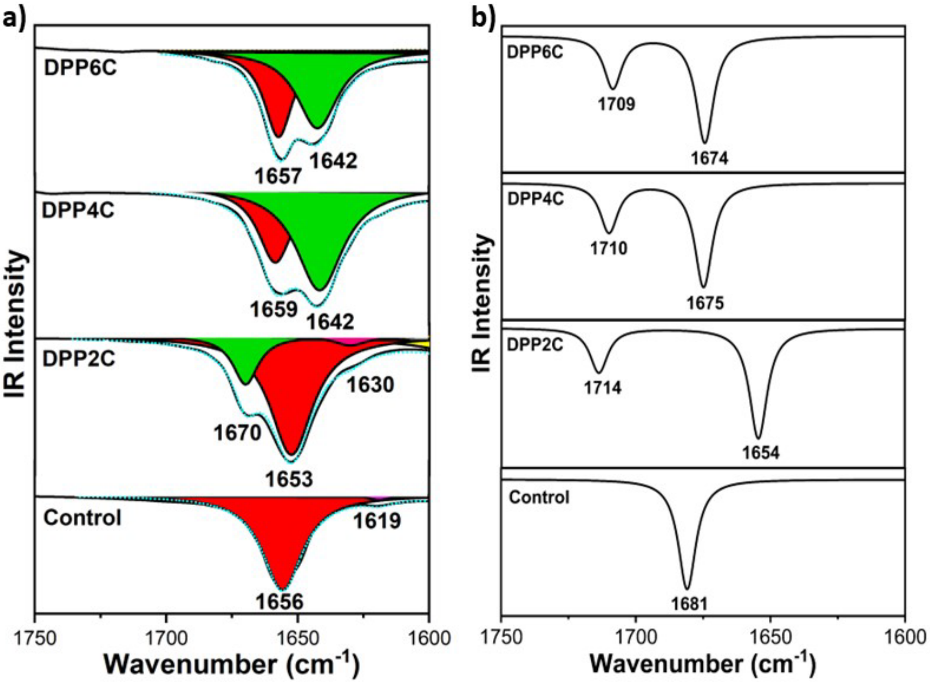

Figure IV.6. a) IR spectra of **Control**, **DPP2C**, **DPP4C** and **DPP6C** and b) B3LYP/6-31G** IR theoretical spectra for **Control**, **DPP2C**, **DPP4C** and **DPP6C**.

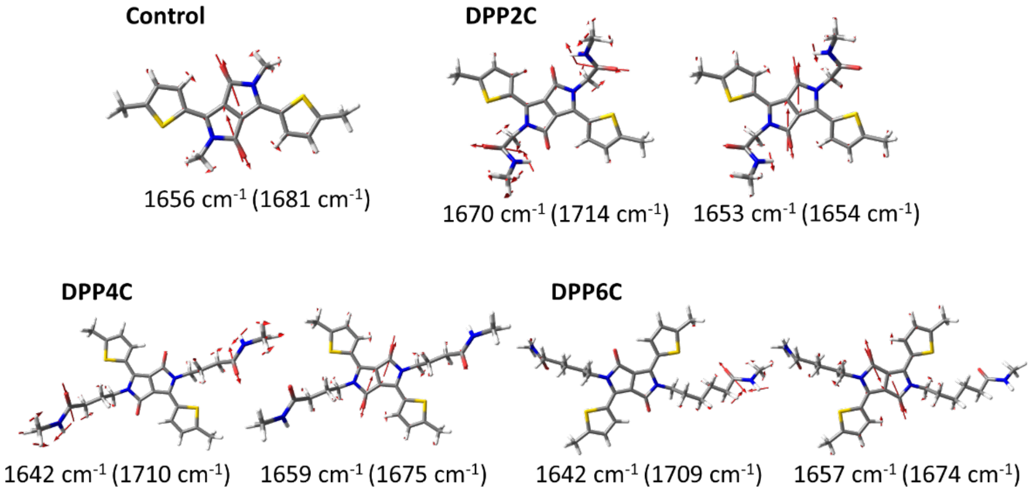

Figure IV.7. B3LYP/6-31G** predicted eigenvectors for the IR bands discussed in the text for **Control**, **DPP2C**, **DPP4C** and **DPP6C.** Experimental and theoretical data (in parenthesis).

In order to further corroborate the intramolecular hydrogen bonds in **DPP2C**, we focus our attention in the ν(N−H) vibration (Figure IV.8). The experimental data exhibit a comparable position of the ν(N−H) vibration for the compounds **DPP2C**, **DPP4C** and **DPP6C**, with a maximum difference of approximately 17 cm^{-1}. However, theoretical calculations show a shift of this molecular mode towards lower frequencies in **DPP2C** (around 120 cm^{-1}) respect to **DPP4C** and **DPP6C**, indicating that the N−H of the amide is probably forming hydrogen bonds. Since the theoretical calculation is performed on an isolated molecule in a vacuum and predicts the lengthening of the N-H bond in **DPP2C**, this bond can only be intramolecular, linking the hydrogen atom of the amide group with the C=O of the DPP lactam. This indicates that all amides are capable of forming hydrogen bonds, however with different characteristics. In the case of **DPP2C**, the bond is intramolecular, whereas in **DPP4C** and **DPP6C**, it is intermolecular. This explains the fact that theoretical calculations of a single molecule in a vacuum do not reproduce the displacement towards lower frequencies of the N-H vibration for **DPP4C** and **DPP6C**.

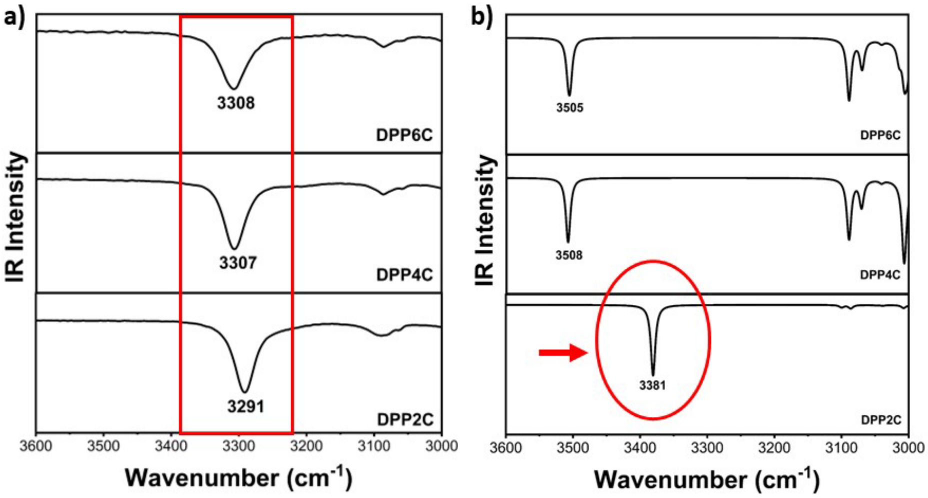

Figure IV.8. a) IR spectra of **DPP2C**, **DPP4C** and **DP6C in** the amides region and b) IR theoretical spectra (B3LYP/6-31G**) for **DPP2C**, **DPP4C** and **DP6C** in the amides zone.

In the same way, the Raman spectra reveal modifications in the electronic properties of the conjugated skeletons as a result of hydrogen bond formation. To examine this effect, we focused on the collective vibration along the thiophene-DPP-thiophene chain. In the case of **Control**, this vibration is recorded at 1528 cm^{-1} (Figure IV.9a). However, in **DPP4C** and

DPP6C, where intermolecular hydrogen bonding is present, this band broadens and shows two distinct contributions at 1526-1527 cm^{-1} and 1530 cm^{-1}. The presence of these two signals suggests that the carbonyl group of the lactam ring may participate, in some extent, in the supramolecular hydrogen bonding interaction, which favors greater π-conjugation in molecules that exhibit this interaction. This phenomenon can be explained by considering that, when the carbonyl group of the lactam participates in hydrogen bond formation, the cross-conjugated pathway associated with that carbonyl is blocked, which in turn favors greater π -conjugation along the linear pathway (Figure IV.9b). However, it is reasonable to assume that only a fraction of the molecules interacts through the carbonyl groups of the DPP unit, with hydrogen bonds more likely to form primarily through the amide groups of the alkyl side chains.

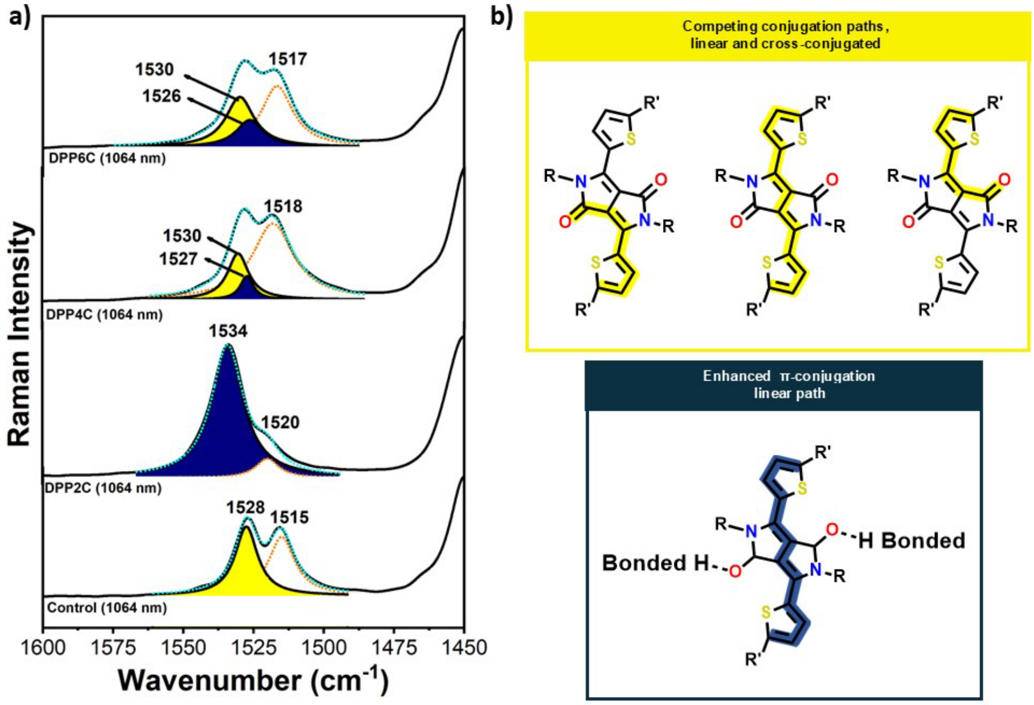

Figure IV.9. a) Raman spectra of **Control**, **DPP2C**, **DPP4C** and **DP6C** and b) Schematic representation of molecular π-conjugation: (yellow) showing the presence of different competing paths (linear and cross-conjugated) in molecules with no hydrogen-bonds formation, and (dark blue) showing the enhanced π-conjugation linear path after hydrogen bond formation through the carbonyl of the lactam ring.

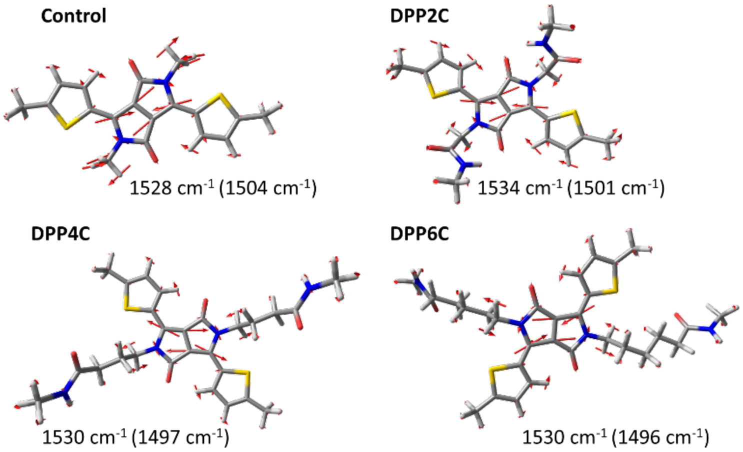

Figure IV.10. B3LYP/6-31G** Raman predicted eigenvectors of **Control**, **DPP2C**, **DPP4C** and **DPP6C** for the collective Ramanν (C=C/C-C) vibration. Experimental and theoretical data (in parenthesis)

On the contrary, the Raman spectra of **DPP2C** show the collective ν(C=C/C-C) vibration at 1534 cm^{-1} with a single contribution, in consonance with the presence of only intramolecular hydrogen bond interactions between the carbonyl group of the DPP and N-H of the amide group in all molecules. However, this vibration appears at 1534 cm^{-1}, exhibiting a slightly shift towards higher frequencies. This shift can be attributed to the loss of the planarity in **DPP2C**, as predicted by theoretical calculations. The theoretical calculations indicate that the ν(C=C/C-C) vibration mode frequency for **DPP2C** is 1501 cm^{-1}, 1497 cm^{-1}, for **DPP4C** and 1496 cm^{-1} for **DPP6C** (see eigenvectors in Figure IV.10).

IV.4 Analysis by spectroelectrochemistry: charge carriers stabilization

In order to evaluate the ability of the studied compounds to stabilize charge carriers and determine whether noncovalent interactions influence the formation of these charged species, *in situ* spectroelectrochemical studies were carried out.

Initially, these studies were performed in dilute dichloromethane solution (10^{-4} M) at room temperature, using 0.1 M NBu_4PF_6 as the supporting electrolyte and an optically transparent thin-film electrochemical (OTTLE) cell. As shown in Figure IV.11, the studied compounds exhibit similar behaviour in solution, considering that intermolecular interactions are avoided at low concentrations. Under these conditions, all compounds stabilize a positive charge at similar applied potentials. Note that, however, that the applied potential is slightly higher for **DPP2C** in consonance with the stabilization of the HOMO level due to the molecular planarity loss.

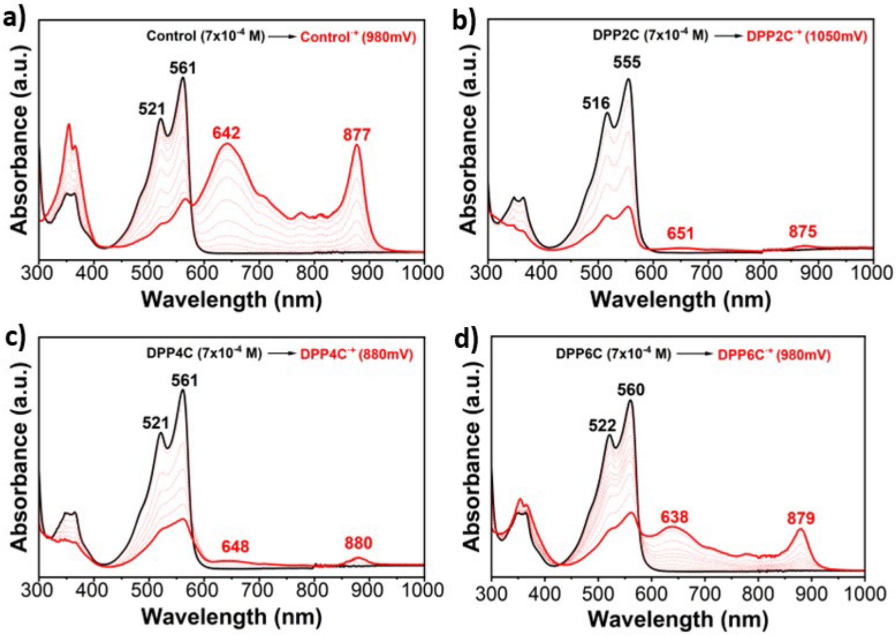

Figure IV.11. UV-Vis-NIR absorption spectra of a) **Control** b) **DPP2C**, c) **DPP4C** and d) **DPP6C** electrochemically oxidized by progressive increase of the oxidation potentials.

In order to evaluate the role of intermolecular interactions in charge injection and stabilization, thin films were oxidized by exposing them to iodine vapor, a weak oxidant, for 24 hours (Figure IV.12). Differences were observed between the hydrogen-bonding semiconductor, **DPP6C**, and the reference material, **Control**. While UV-Vis displays that intermolecular hydrogen-bonded compound showed the formation of a positively charged species, **Control** showed no signs of oxidation, suggesting that the absence of hydrogen-bonding interactions prevents this process. Furthermore, in the IR spectra of **Control** molecule, not remarkable differences are found before and after the oxidation with iodine. However, in the case of **DPP6C** remarkable spectral changes are recorded, according to the radical cation formation. Therefore, the enhanced π-conjugated path, formed through intermolecular hydrogen bonding via the carbonyl group of the imide of the alkyl chains, and the different supramolecular aggregation, have a significant impact on charge injection and stabilisation, thereby improving charge carrier mobility. Unfortunately, for **DPP2C** and **DPP4C** it was not possible to obtain reproducible results.

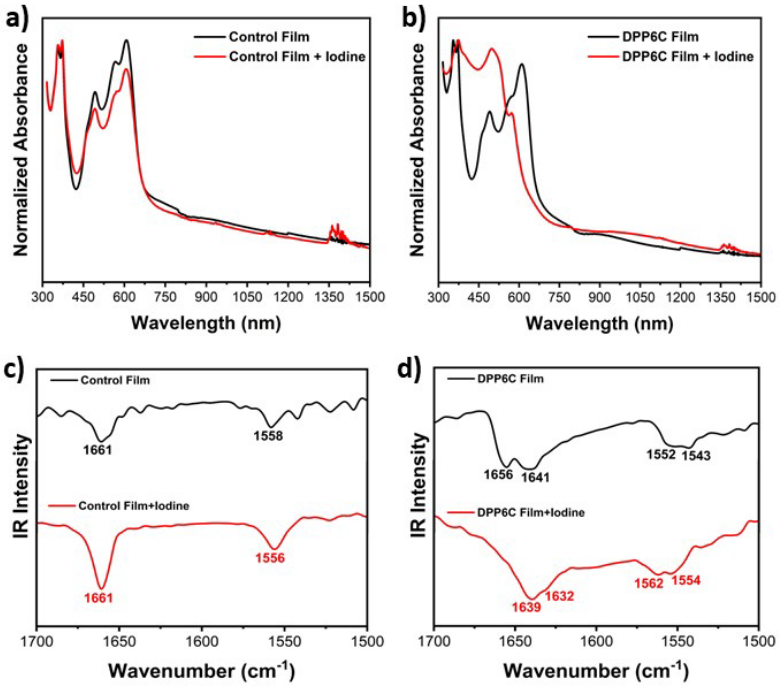

Figure IV.12. Solid state oxidation for **Control** and **DPP6C**, upon iodine vapor exposition: a) and b) UV-Vis spectra and c) and d) IR spectra.

IV.5 Field effect transistor and thin film characterization

To evaluate the electrical properties of the tested compounds, solution-processed OFET transistors with a top-contact/bottom-gate structure were fabricated. From the saturation region in the device transfer curves, the charge carrier mobility (μ), threshold voltage (V_T), and on/off current ratio (I_{ON}/IO_{FF}) were determined. The electrical parameters of the best-performing devices are presented in Table IV.2, while the full device characterization is provided in the appendix 6.2.4.

Thin films of **Control**, **DPP2C**, **DPP4C** and **DPP6C** were deposited by drop casting onto Si/SiO_2 substrates from solutions of the semiconductor materials in chloroform (3 mg/ml). After deposition, a thermal annealing was carried out at 120 °C for 3 hours. Importantly, while **Control** showed no activity in OFETs, p-type field-effect mobilities of 4 × 10^{-6} cm^2 V^{-1} s^{-1}, 5 × 10^{-3} cm^2 V^{-1} s^{-1} and 2 × 10^{-2} cm^2 V^{-1} s^{-1} were recorded for **DPP2C**, **DPP4C** and **DPP6C,** respectively (see output and transfer plots in Figure IV.13). Thus, the field effect mobilities increase as the amide unit moves further away from the DPP core, due to the presence of intermolecular bonds in **DPP4C** and **DPP6C**, which favor charge transport. In contrast, **DPP2C** with the amide close to the π-conjugated skeleton, forms intramolecular hydrogen bonds, which has two effects; i) inhibit the formation of hydrogen bonded supramolecular aggregates; ii) has a clear impact on the molecular structure, increasing the oxidation potential and thus, decreasing the ability to inject and stabilize charge carriers.

Compound	Subst.[a] Treatment	μ_h (cm^2 V^{-1} s^{-1})	V_T(V)	I_{ON}/I_{OFF}
Control	OTS (120)	NA	NA	NA
DPP2C	OTS (120)	$4x10^{-6}$	-10	$4x10^{+1}$
DPP4C	OTS (120)	$5x10^{-3}$	-15	$3x10^{+3}$
DPP6C	OTS (120)	$2x10^{-2}$	-12	$2x10^{+4}$

Table IV.2. OFET electrical data for best-performing deposited films of the indicated semiconductors measured in vacuum. [a]Substrates treated with OTS and thermal annealed at 120ºC.

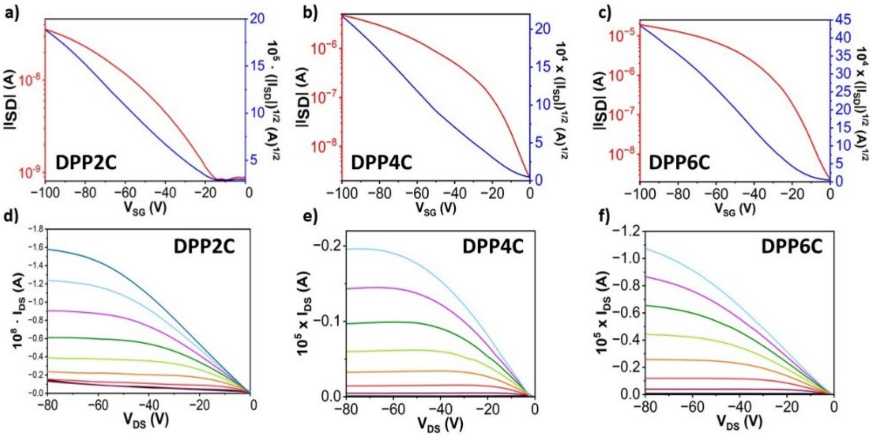

Figure IV.13. Transfer (a-c) and output (d-f) of **Control**, **DPP2C**, **DPP4C** and **DPP6C**. The transfer characteristics were measured at a constant source–drain voltage of -80 V. The gate voltage in the output plots varies from 0 to -80 V in steps of 10 V.

The morphologies of the thin films were analyzed by atomic force microscopy (AFM). Clear differences were found when comparing the studied compounds. While the **Control** and **DPP2C** molecules forms crystalline structures (Figure IV.14a and IV.14b), due to the predominance of self-assembles through π-π interactions,[48] **DPP4C** and **DPP6C** exhibit a morphology composed of smaller fibers, (Figures IV.14c and IV.14c). This is attributed to the formation of J-type aggregates in **DPP4C** and **DPP6C**, due to the formation of intermolecular hydrogen bonds.

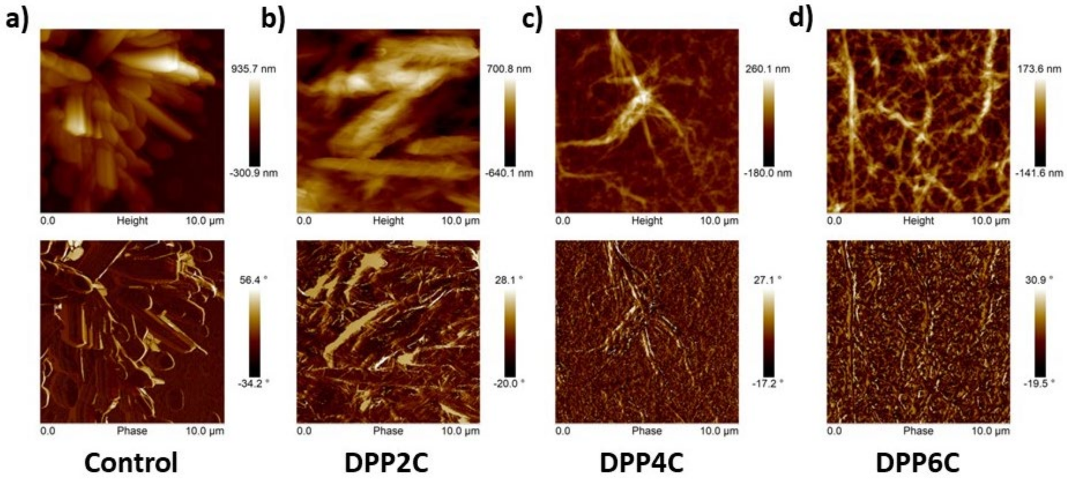

Figure IV.14. AFM images of semiconducting thin films deposited on OTS-treated Si/SiO$_2$ substrates with a posterior thermal treatment of 120º during 3 hours. a) **Control**, b) **DPP2C**, **c**) **DPP4C** and d) **DPP6C**.

XRD measurements were also performed on the thin films (Figure IV.15), which indicated an enhanced crystallinity structure for **Control** and **DPP2C**, through π-π interactions. Although crystallinity is desirable to achieve efficient charge transport, **DPP4C** and **DPP6C** exhibit interconnected amorphous fibrillar networks. We believe that these two morphological scenarios are crucial to compare their charge transport properties, since interconnection between amorphous aggregates is sometimes beneficial in polymeric semiconductors and other hydrogen-bonded oligomers.[49,50]

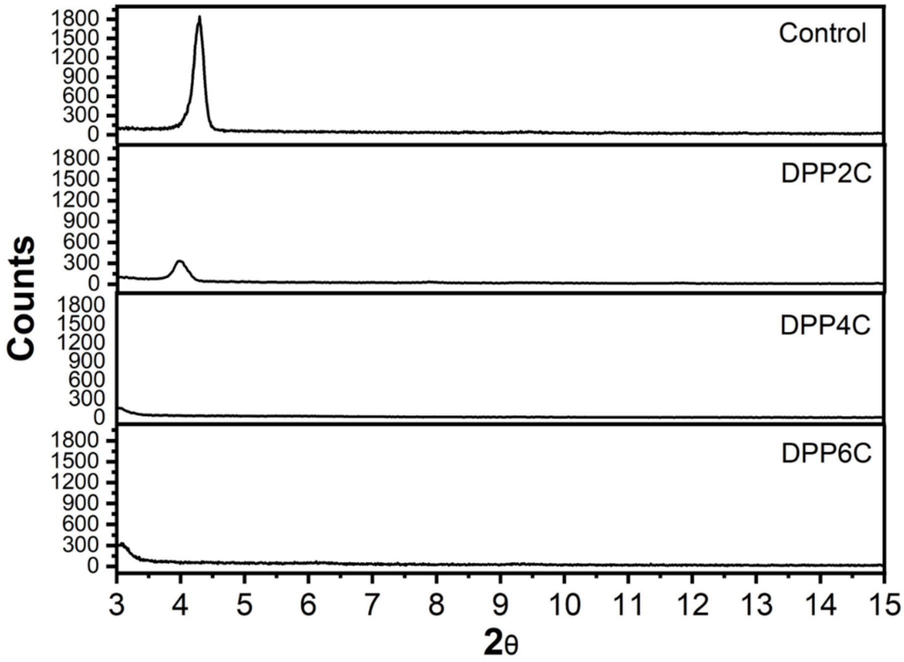

Figure IV.15. Θ-2Θ X-ray diffraction scans of solution deposited **Control**, **DPP2C**, **DPP4C** and **DPP6C** thin films grown on OTS-treated Si/SiO$_2$ substrates with a posterior thermal treatment of 120º during 3 hours.

IV.6 Conclusions

In conclusion, we present a molecular engineering strategy that allows simultaneous control of the intrinsic morphological and electronic properties of semiconductors by promoting hydrogen bonding in small-sized DPP derivatives. Our results demonstrate that the electrical enhancement observed in semiconductors with amide groups is not solely due to the supramolecular organization in thin films, but it can be also attributed to the modulation of their electronic properties through (intra/inter) hydrogen bonding interactions. By analysing the intermolecular versus intramolecular hydrogen bond interactions, we can observe the following effects: i) **Control**, **DPP4C** and **DPP6C** exhibit a planar structure due to the interaction between the hydrogen of the thiophene ring and the carbonyl of the lactam. In contrast, **DPP2C** exhibits a twisted structure due to intramolecular hydrogen bond interactions between the hydrogen of the amide group of the alkyl chains and the carbonyl of the DPP, which prevents the aforementioned interaction with the thiophene ring that planarizes the structure. The twisted structure of **DPP2C** implies lower π-conjugation and charged stabilisation compared to **DPP4C** and **DPP6C**, as shown by UV-Vis, Raman and IR spectra. ii) The different hydrogen bond interactions in **DPP2C** compared to **DPP4C** and **DPP6C** have been demonstrated by IR spectroscopy aided by DFT calculations. iii) AFM and XRD also show enhanced crystallinity for **Control** and **DPP2C** due to self-assembly through π-π interactions. On the other hand, **DPP4C** and **DPP6C** exhibit interconnected amorphous fibrillar networks due to intermolecular hydrogen bonding. iv) **DPP4C** and **DPP6C** compounds show improved charge transport in OFETs compared to **Control** and **DPP2C** compounds. While the **Control** and **DPP2C** compounds are practically inactive in OFETs, the **DPP4C** and **DPP6C** molecules exhibit field effect mobilities of 5×10^{-3} $cm^2\ V^{-1}\ s^{-1}$ and 2×10^{-2} $cm^2\ V^{-1}\ s^{-1}$, respectively. These results corroborate our initial hypothesis that modifying the position of functional groups on side chains is a highly effective strategy for promoting π-conjugation, stabilising charged species and generating supramolecular aggregates.

IV.7 References

1 B. Raj, P. Kaur, P. Kumar and S. S. Gill, Comparative Analysis of OFETs Materials and Devices for Sensor Applications, *Silicon*, 2022, **14**, 4463–4471.

2 Z. Chen, S. Duan, W. Hu, Z. Chen, S. Duan, W. Hu, S. Duan, W. Hu and X. Zhang, Novel solution-processed 2D organic semiconductor crystals for high-performance OFETs, *Mater Chem Front*, 2024, **8**, 2227–2272.

3 K. Ditte, T. A. Nguyen Le, O. Ditzer, D. I. Sandoval Bojorquez, S. Chae, M. Bachmann, L. Baraban and F. Lissel, Rapid Detection of SARS-CoV-2 Antigens and Antibodies Using OFET Biosensors Based on a Soft and Stretchable Semiconducting Polymer, *ACS Biomater Sci Eng*, 2023, **9**, 2140–2147.

4 P. Ding, D. Yang, S. Yang and Z. Ge, Stability of organic solar cells: toward commercial applications, *Chem Soc Rev*, 2024, **53**, 2350–2387.

5 S. Luo, C. Li, J. Zhang, X. Zou, H. Zhao, K. Ding, H. Huang, J. Song, J. Yi, H. Yu, K. S. Wong, G. Zhang, H. Ade, W. Ma, H. Hu, Y. Sun and H. Yan, Auxiliary sequential deposition enables 19%-efficiency organic solar cells processed from halogen-free solvents, *Nature Communications 2023 14:1*, 2023, **14**, 1–11.

6 F. Liu, C. Wang, J. K. Baral, L. Zhang, J. J. Watkins, A. L. Briseno and T. P. Russell, Relating chemical structure to device performance via morphology control in diketopyrrolopyrrole-based low band gap polymers, *J Am Chem Soc*, 2013, **135**, 19248–19259.

7 X. Cao, C. Xu, H. Li, Y. Han, Y. Deng, H. Tian, J. Liu and L. Wang, Enabling close backbone stacking in near-amorphous n-type polymer semiconductors via side-chain engineering, *Mater Chem Front*, 2024, **8**, 2002–2010.

8 H. Quan, Z. Zhong, T. Hao, K. An, W. Zhong, C. Wang, F. Liu, L. Ying and F. Huang, High-performance organic photodetectors enabled by a refined fibrillar multiphase morphology, *Chemical Engineering Journal*, 2023, **452**, 139295.

9 T. Aytun, L. Barreda, A. Ruiz-Carretero, J. A. Lehrman and S. I. Stupp, Improving solar cell efficiency through hydrogen bonding: A method for tuning active layer morphology, *Chemistry of Materials*, 2015, **27**, 1201–1209.

10 A. Ruiz-Carretero, T. Aytun, C. J. Bruns, C. J. Newcomb, W. W. Tsai and S. I. Stupp, Stepwise self-assembly to improve solar cell morphology, *J Mater Chem A Mater*, 2013, **1**, 11674–11681.

11 X. Shi and W. Bao, Hydrogen-Bonded Conjugated Materials and Their Application in Organic Field-Effect Transistors, *Front Chem*, 2021, **9**, 723718.

12 J. H. Oh, W. Y. Lee, T. Noe, W. C. Chen, M. Könemann and Z. Bao, Solution-shear-processed quaterrylene diimide thin-film transistors prepared by pressure-assisted thermal cleavage of swallow tails, *J Am Chem Soc*, 2011, **133**, 4204–4207.

13 J. Yao, C. Yu, Z. Liu, H. Luo, Y. Yang, G. Zhang and D. Zhang, Significant Improvement of Semiconducting Performance of the Diketopyrrolopyrrole-Quaterthiophene Conjugated Polymer through Side-Chain Engineering via Hydrogen-Bonding, *J Am Chem Soc*, 2016, **138**, 173–185.

14 J. Ma, Z. Liu, J. Yao, Z. Wang, G. Zhang, X. Zhang and D. Zhang, Improving Ambipolar Semiconducting Properties of Thiazole-Flanked Diketopyrrolopyrrole-Based Terpolymers by Incorporating Urea Groups in the Side-Chains, *Macromolecules*, 2018, **51**, 6003–6010.

15 C. Wang, M. Liu, S. Rahman, H. P. Pasanen, J. Tian, J. Li, Z. Deng, H. Zhang and P. Vivo, Hydrogen bonding drives the self-assembling of carbazole-based hole-transport material for enhanced efficiency and stability of perovskite solar cells, *Nano Energy*, 2022, **101**, 107604.

16 Y. C. Lin, C. C. Shih, Y. C. Chiang, C. K. Chen and W. C. Chen, Intrinsically stretchable isoindigo–bithiophene conjugated copolymers using poly(acrylate amide) side chains for organic field-effect transistors, *Polym Chem*, 2019, **10**, 5172–5183.

17 Z. Qin, C. Gao, W. W. H. Wong, M. K. Riede, T. Wang, H. Dong, Y. Zhen and W. Hu, Molecular doped organic semiconductor crystals for optoelectronic device applications, *J Mater Chem C Mater*, 2020, **8**, 14996–15008.

18 J. Guo, C. Shi, Y. Zhen and W. Hu, Rational Control of Packing Arrangements in Organic Semiconducting Materials toward High-Performance Optoelectronics, *Acc Mater Res*, 2024, **5**, 907–919.

19 A. D. Scaccabarozzi, A. Basu, F. Aniés, J. Liu, O. Zapata-Arteaga, R. Warren, Y. Firdaus, M. I. Nugraha, Y. Lin, M. Campoy-Quiles, N. Koch, C. Müller, L. Tsetseris, M. Heeney and T. D. Anthopoulos, Doping Approaches for Organic Semiconductors, *Chem Rev*, 2022, **122**, 4420–4492.

20 A. F. Paterson, N. D. Treat, W. Zhang, Z. Fei, G. Wyatt-Moon, H. Faber, G. Vourlias, P. A. Patsalas, O. Solomeshch, N. Tessler, M. Heeney and T. D. Anthopoulos, Small Molecule/Polymer Blend Organic Transistors with Hole Mobility Exceeding 13 cm2V−1s−1, *Advanced Materials*, 2016, **28**, 7791–7798.

21 S. Hunter, A. D. Mottram and T. D. Anthopoulos, Temperature and composition-dependent density of states in organic small-molecule/polymer blend transistors, *J Appl Phys*, DOI:10.1063/1.4955282/143340.

22 J. Smith, W. Zhang, R. Sougrat, K. Zhao, R. Li, D. Cha, A. Amassian, M. Heeney, I. McCulloch and T. D. Anthopoulos, Solution-processed small molecule-polymer blend organic thin-film transistors with hole mobility greater than 5 cm 2/Vs, *Advanced Materials*, 2012, **24**, 2441–2446.

23 J. Panidi, A. F. Paterson, D. Khim, Z. Fei, Y. Han, L. Tsetseris, G. Vourlias, P. A. Patsalas, M. Heeney and T. D. Anthopoulos, Remarkable Enhancement of the Hole Mobility in Several Organic Small-Molecules, Polymers, and Small-Molecule:Polymer Blend Transistors by Simple Admixing of the Lewis Acid p-Dopant B(C6F5)3, *Advanced Science*, 2018, **5**, 1700290.

24 S. Lan, Y. Yan, H. Yang, G. Zhang, Y. Ye, F. Li, H. Chen and T. Guo, Improving device performance of n-type organic field-effect transistors via doping with a p-type organic semiconductor, *J Mater Chem C Mater*, 2019, **7**, 4543–4550.

25 L. Cao, C. Ren and T. Wu, Recent advances in doped organic field-effect transistors: mechanism, influencing factors, materials, and development directions, *J Mater Chem C Mater*, 2023, **11**, 3428–3447.

26 A. D. Kuimov, C. S. Becker, N. A. Shumilov, I. P. Koskin, A. A. Sonina, V. Y. Komarov, I. K. Shundrina and M. S. Kazantsev, Synthetic approach for the control of self-doping in luminescent organic semiconductors, *Mater Chem Front*, 2022, **6**, 2244–2255.

27 O. D. Parashchuk, A. A. Mannanov, V. G. Konstantinov, D. I. Dominskiy, N. M. Surin, O. V. Borshchev, S. A. Ponomarenko, M. S. Pshenichnikov and D. Y. Paraschuk, Molecular Self-Doping Controls Luminescence of Pure Organic Single Crystals, *Adv Funct Mater*, 2018, **28**, 1800116.

28 P. Chen, D. Wang, L. Luo, J. Meng, Z. Zhou, X. Dai, Y. Zou, L. Tan, X. Shao, C.-A. Di, C. Jia, H.-L. Zhang, Z. Liu, P. Chen, L. Luo, J. Meng, Z. Zhou, X. Shao, H.-L. Zhang, Z. Liu, D. Wang, X. Dai, Y. Zou, C.-A. Di and L. Tan, Self-Doping Naphthalene Diimide Conjugated Polymers for Flexible Unipolar n-Type OTFTs, *Advanced Materials*, 2023, **35**, 2300240.

29 K. Yang, X. Zhang, A. Harbuzaru, L. Wang, Y. Wang, C. Koh, H. Guo, Y. Shi, J. Chen, H. Sun, K. Feng, M. C. Ruiz Delgado, H. Y. Woo, R. P. Ortiz and X. Guo, Stable Organic Diradicals Based on Fused Quinoidal Oligothiophene Imides with High Electrical Conductivity, *J Am Chem Soc*, 2020, **142**, 4329–4340.

30 Y. Zhang, Y. Zheng, H. Zhou, M.-S. Miao, F. Wudl, T.-Q. Nguyen, Y. Zhang, Y. Zheng, F. Wudl, T.-Q. Nguyen, H. Zhou and M. Miao, Temperature Tunable Self-Doping in Stable Diradicaloid Thin-Film Devices, *Advanced Materials*, 2015, **27**, 7412–7419.

31 D. Yuan, Y. Guo, Y. Zeng, Q. Fan, J. Wang, Y. Yi and X. Zhu, Air-Stable n-Type Thermoelectric Materials Enabled by Organic Diradicaloids, *Angewandte Chemie - International Edition*, 2019, **58**, 4958–4962.

32 Y. Kobayashi, M. Yoshioka, K. Saigo, D. Hashizume and T. Ogura, Hydrogen-bonding-assisted self-doping in tetrathiafulvalene (TTF) conductor, *J Am Chem Soc*, 2009, **131**, 9995–10002.

33 Y. Kobayashi, M. Yoshioka, K. Saigo, D. Hashizume and T. Ogura, Hydrogen-bonding tetrathiafulvalene (TTF) conductors: Carrier generation by self-doping, *Physica B Condens Matter*, 2010, **405**, S23–S26.

34 S. C. Kim, J. Whitten, J. Kumar, F. F. Bruno and L. A. Samuelson, Self-doped carboxylated polyaniline: Effect of hydrogen bonding on the doping of polymers, *Macromol Res*, 2009, **17**, 631–637.

35 Z. B. Henson, Y. Zhang, T. Q. Nguyen, J. H. Seo and G. C. Bazan, Synthesis and properties of two cationic narrow band gap conjugated polyelectrolytes, *J Am Chem Soc*, 2013, **135**, 4163–4166.

36 D. Chandran and K. S. Lee, Diketopyrrolopyrrole: A versatile building block for organic photovoltaic materials, *Macromol Res*, 2013, **21**, 272–283.

37 M. Grzybowski and D. T. Gryko, Diketopyrrolopyrroles: Synthesis, Reactivity, and Optical Properties, *Adv Opt Mater*, 2015, **3**, 280–320.

38 Z. He, K. Asare-Yeboah and S. Bi, Advances in Charge Carrier Mobility of Diketopyrrolopyrrole-Based Organic Semiconductors, *Coatings 2024, Vol. 14, Page 1080*, 2024, **14**, 1080.

39 Z. He, · Kyeiwaa Asare-Yeboah and · Sheng Bi, Diketopyrrolopyrrole based organic semiconductors: pioneering advances in organic electronic devices, *Discover Electronics 2025 2:1*, 2025, **2**, 1–28.

40 Q. Liu, H. Sun, C. Blaikie, C. Caporale, S. Manzhos, K. Feron, J. M. Macleod, M. Massi, S. E. Bottle, J. Bell, Y. Y. Noh and P. Sonar, Naphthalene flanked diketopyrrolopyrrole based organic semiconductors for high performance organic field effect transistors, *New Journal of Chemistry*, 2018, **42**, 12374–12385.

41 Q. Liu, S. Chavhan, H. Zhang, H. Sun, A. J. Brock, S. Manzhos, Y. Chen, K. Feron, S. E. Bottle, J. C. McMurtrie, J. H. Jou, H. S. Chen, M. R. Nagar, W. Hu, Y. Y. Noh, Y. Zhen and P. Sonar, Short Alkyl Chain Engineering Modulation on Naphthalene Flanked Diketopyrrolopyrrole toward High-Performance Single Crystal Transistors and Organic Thin Film Displays, *Adv Electron Mater*, 2021, **7**, 2000804.

42 Q. Liu, H. Sun, S. P. Ponnappa, K. Feron, S. Manzhos, M. W. M. Jones, S. E. Bottle, J. Bell, Y. Y. Noh and P. Sonar, Naphthalene flanked diketopyrrolopyrrole: A new DPP family member and its comparative optoelectronic properties with thiophene- and furan- flanked DPP counterparts, *Org Electron*, 2019, **74**, 290–298.

43 E. D. Głowacki, H. Coskun, M. A. Blood-Forsythe, U. Monkowius, L. Leonat, M. Grzybowski, D. Gryko, M. S. White, A. Aspuru-Guzik and N. S. Sariciftci, Hydrogen-bonded diketopyrrolopyrrole (DPP) pigments as organic semiconductors, *Org Electron*, 2014, **15**, 3521–3528.

44 A. Ruiz-Carretero, N. R. Ávila Rovelo, S. Militzer and P. J. Mésini, Hydrogen-bonded diketopyrrolopyrrole derivatives for energy-related applications, *J Mater Chem A Mater*, 2019, **7**, 23451–23475.

45 J. Dhar, D. P. Karothu and S. Patil, Herringbone to cofacial solid state packing via H-bonding in diketopyrrolopyrrole (DPP) based molecular crystals: influence on charge transport, *Chemical Communications*, 2014, **51**, 97–100.

46 Y. Liu, X. Tao, F. Wang, J. Shi, J. Sun, W. Yu, Y. Ren, D. Zou and M. Jiang, Intermolecular hydrogen bonds induce highly emissive excimers: Enhancement of solid-state luminescence, *Journal of Physical Chemistry C*, 2007, **111**, 6544–6549.

47 V. F. Traven, D. A. Cheptsov and C. Lodeiro, Control of Fluorescence of Organic Dyes in the Solid-State by Supramolecular Interactions, *Journal of Fluorescence 2022 33:3*, 2022, **33**, 799–847.

48 N. R. Ávila-Rovelo, G. Martinez, W. Matsuda, S. Sinn, P. Lévêque, D. Schwaller, P. Mésini, S. Seki and A. Ruiz-Carretero, Hydrogen-Bonded Organic Semiconductors with Long Charge Carrier Lifetimes, *Journal of Physical Chemistry C*, 2022, **126**, 10932–10939.

49 R. Noriega, J. Rivnay, K. Vandewal, F. P. V. Koch, N. Stingelin, P. Smith, M. F. Toney and A. Salleo, A general relationship between disorder, aggregation and charge transport in conjugated polymers, *Nature Materials 2013 12:11*, 2013, **12**, 1038–1044.

50 G. J. Thapa, M. Chauhan, R. R. Cranston, B. Guo, B. H. Lessard, D. B. Dougherty and A. Amassian, Linking Electronic and Structural Disorder Parameters to Carrier Transport in a Modern Conjugated Polymer, *ACS Appl Mater Interfaces*, 2024, **16**, 48016–48024.

4

Conclusions

Conclusions

In this thesis, a series of π-conjugated organic semiconductors have been studied for their application in organic field effect transistors (OFETs). The main objective of this study is to understand how molecular and supramolecular properties influence charge transport mechanisms. In order to address the aforementioned objectives, spectroscopic, electrochemical, spectroelectrochemical and quantum-chemical methods have been employed, providing detailed information on the structure and electronic properties of the studied compounds. These analyses are crucial to understand the electronic and optical properties of these conjugated materials and to guide the development of compounds with improved properties for application in OFETs.

In Chapter I, we have studied a family of compounds combining electron-withdrawing naphthalimides units and thiophene-derived donor moieties connected by rigid and conjugated nitrogen-containing rings (imidazole or pyrazine). The effect of conjugated chain length and heteroatom substitution is studied.

The results indicate that the modification of the chemical structure impacts charge stabilization in the studied compounds. We demonstrate the importance of the pyrazine linkers and the extension of the π-conjugated chain in the stabilization of charges in solution. In particular, the combination of the pyrazine linker with an extended π-conjugated chain allows the stabilization up to two reduced species and three oxidated species.

To evaluate the charge transport in these compounds, OFETs were fabricated, obtaining p-type electrical behaviour. We found that smaller systems with less extended π-conjugation render more organized films, resulting in better field effect mobilities, up to 10^{-2} $cm^2\ V^{-1}\ s^{-1}$.

In Chapter II our study focused on a series of compounds based on phenylene-naphthalimide assemblies, in which the phenylene and naphthalimide units are directly conjugated via rigid amidine (NAI) bonds. The effect of halogen insertion was approached, which modify the electron-accepting and charge-transport properties of these systems.

Physico-chemical analysis shows that the introduction of halogen atoms into the structure induces enhanced π-conjugation and stabilization of the HOMO and LUMO energy levels, leading to a reduction of the energy gap. The introduction of halogen atoms also render lower reduction potentials compared to non-halogenated compound facilitating charge stabilization.

Finally, electrical characterization in OFETs shows ambipolar behaviour in non-halogenated compound, but performance improves upon halogenation, despite only electron transport being recorded, with maximum n-type field effect mobility of 0.2 $cm^2V^{-1}s^{-1}$.

In Chapter III, we have studied a family of compounds based on terthiophene-naphthalimide assemblies with imidazole and pyrazine linkers, in which different electrodeficient groups have been introduced in order to tune their optoelectrochemical properties.

The results suggested that the introduction of electrowithdrawing substituents into the molecular structures affects both the energies and the topologies of the frontier molecular orbitals. It has been demonstrated here that these effects have a significant impact on the electronic properties of the studied materials, including optical absorption properties and stabilisation of charged species. Therefore, a good balance between donor and acceptor groups allows fine modulation of electronic and molecular properties.

Finally, in Chapter IV, we have studied the role of hydrogen bonds in supramolecular interactions and molecular packing in small-sized molecular semiconductors based on DPP, as the electroactive component, and amide groups as hydrogen-bonding units.

We have found that the control of intra- and intermolecular hydrogen bond interactions has a remarkable effect on the molecular and electronic properties of the studied compounds. The presence of intermolecular hydrogen bonds interaction is an effective approach to promoting π-conjugation, stabilising charged species, and forming supramolecular aggregates. This is corroborated by OFETs fabrication, where the compounds having intermolecular hydrogen bonds show enhanced field effect mobilities, up to 2×10^{-2} cm^2 V^{-1} s^{-1}.

In conclusion, the results obtained from the different chapters of this thesis demonstrate how the distinct structural modifications influence the electrical properties of the studied semiconductors. It has been demonstrated that the modification of the π-conjugated chain, through extension or heteroatom substitution (Chapter I), in conjunction with the supramolecular interaction due to hydrogen bonds (Chapter IV), results in p-type field effect mobilities of up to 10^{-2} cm^2 V^{-1} s^{-1}. However, the incorporation of halogen atoms within the molecular structure (Chapter II) has been demonstrated to enhance the electrical properties, with n-type mobilities reaching up to 10^{-1} cm^2 V^{-1} s^{-1}. This approach has been identified as a promising strategy for the design of novel organic semiconductors. The most relevant electrical performances are summarized in Table 4.1.

Compound	Subst.[a] Treatment	μ_e (cm^2 V^{-1} s^{-1})	V_T(V)	I_{ON}/I_{OFF}
NDI	OTS,(80°C,150°C)	2×10^{-4}	-6	$2\times10^{+4}$
NIP	OTS,(80°C,150°C)	1×10^{-2}	-20	$2\times10^{+4}$
NAI-Ph	OTS,(80°C,120°C)	2×10^{-2}	66	$1\times10^{+3}$
NAI-Ph-F	OTS,(80°C,120°C)	1×10^{-1}	48	$2\times10^{+4}$
NAI-Ph-Cl	OTS,(80°C,120°C)	8×10^{-2}	39	$2\times10^{+4}$
NAI-Ph-Cl	HMDS,(110°C,120°C)	2×10^{-1}	57	$4\times10^{+5}$
DPP2C	OTS (120°C)	4×10^{-6}	-10	$4\times10^{+1}$
DPP4C	OTS (120°C)	5×10^{-3}	-15	$3\times10^{+3}$
DPP6C	OTS (120°C)	2×10^{-2}	-12	$2\times10^{+4}$

Table 4.1. OFETs electrical data recorded, for thin films of the indicated semiconductors measured in vacuum. [a]Substrates treated with octadecyltrichlorosilane (OTS) and hexamethyldisilazane (HMDS) reagents and preheated either at 80°C or 110°C during sublimation and room temperature. Thin films were then thermal annealed either at 120°C or 150°C.

5

Resumen

Tabla de contenidos

CONTENIDOS

5.1 Introducción

Vivimos en un mundo cargado de tecnología, en una sociedad en la que la mayor parte de nuestras actividades diarias implican el uso de dispositivos electrónicos. Diferentes aspectos como la economía, la salud o las relaciones sociales están principalmente relacionados con el avance tecnológico, ver Figura 5.1.[1] Esta dependencia está creciendo a un ritmo vertiginoso y los sistemas electrónicos ocupan una parte cada vez mayor de nuestras vidas. Hasta ahora, esta necesidad se ha satisfecho utilizando silicio y otros materiales inorgánicos. Sin embargo, la escasez de recursos y la fabricación en masa de dispositivos plantean problemas urgentes que deben resolverse, con especial atención a los aspectos ambientales asociados a la fabricación, el uso y la posterior eliminación de estos dispositivos electrónicos. En este sentido, la electrónica orgánica, con procesos de fabricación y eliminación más sostenibles, abre un nuevo campo. Además de ofrecernos materiales que ofrecen estructuras electrónicas con propiedades únicas, posicionándose como una alternativa en la electrónica del futuro.[2,3]

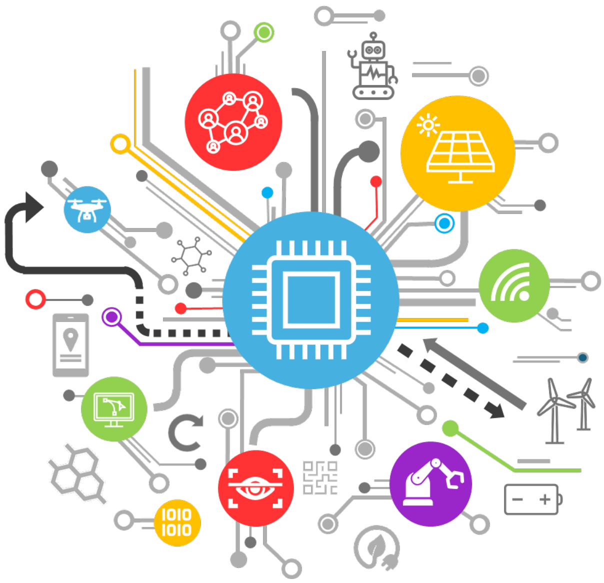

Figure 5.1 Esquema representativo del uso de la tecnología en la sociedad.

Actualmente, ya estamos rodeados de dispositivos electrónicos fabricados con materiales orgánicos: pantallas de teléfonos móviles, células solares portátiles, televisores, etc.[4] Esto es posible gracias al enorme desarrollo que ha experimentado la electrónica orgánica y a la mejora en la miniaturización de los semiconductores orgánicos.[5] Hoy en día, existen microprocesadores con una tecnología que permite una distancia entre transistores de 5 nm. A esta escala, el comportamiento de los electrones está regido por incertidumbres cuánticas, lo que hace que los transistores sean poco fiables. La tecnología que reduce el tamaño del transistor está llegando a su límite, esto significa que reducir el tamaño de un transistor ya no aumenta la velocidad ni disminuye el consumo de energía.[6] Con lo cual, se deben desarrollar nuevas tecnologías para solventar este problema. En este sentido, existen varias vías a seguir en el futuro, como son: la integración tridimensional de sistemas en paquete,[7] el uso de chiplets,[8] memorias no volátiles,[9] computación basada en fotones,[10] biocomputación, [11] computadora cuántica,[12] polímeros y moléculas orgánicas.[13]

Los semiconductores orgánicos destacan por su flexibilidad, respeto al medio ambiente, facilidad de producción a gran escala y capacidad de procesamiento a bajas temperaturas mediante métodos sencillos como la impresión por inyección de tinta.[14] Por lo que, este tipo de materiales pueden integrarse en sustratos tales como: vidrio, polímeros, tejidos y papel, ampliando así sus posibles aplicaciones. Gracias a su capacidad de producción a gran escala, con métodos químicos modulables, son más respetuosos con el medio ambiente y compatibles con innovaciones de diseño. Los semiconductores orgánicos se caracterizan por estar basados en estructuras formadas principalmente por átomos de carbono. La propiedad más relevante de estos materiales reside en la deslocalización electrónica a lo largo de una estructura π-conjugada.[15] Los orbitales π enlazantes constituyen el orbital molecular ocupado de mayor energía (HOMO), mientras que los orbitales π* antienlazantes forman el orbital molecular desocupado de menor energía (LUMO). La diferencia de energía entre estos dos orbitales se denomina HOMO-LUMO gap. En sistemas lineales π-conjugados, el valor del gap depende de varios factores estructurales, como la longitud de la cadena y el grado de planaridad.

Los semiconductores orgánicos desempeñan un papel fundamental en diversas aplicaciones de la electrónica orgánica, como células solares (OPVs),[16] diodos emisores de luz (OLEDs)[17] y transistores de efecto de campo orgánicos (OFETs).[18] Un transistor de efecto de campo (FET) es un dispositivo en el que un campo eléctrico induce una carga espacial neta en el semiconductor. Esta carga se polariza mediante la aplicación de una diferencia de potencial entre los electrodos. Los FETs son elementos esenciales en los circuitos electrónicos, donde desempeñan funciones como interruptores o amplificadores de señal, entre otros. En el caso específico de los OFET, la capa activa está compuesta de materiales orgánicos, ya sean polímeros o moléculas conjugadas.

Un OFET es un dispositivo de tres electrodos en el que un voltaje aplicado al electrodo puerta (*gate*) controla el flujo de corriente entre los electrodos de fuente (*source*) y sumidero (*drain*) mediante un voltaje impuesto (Figura 5.2).

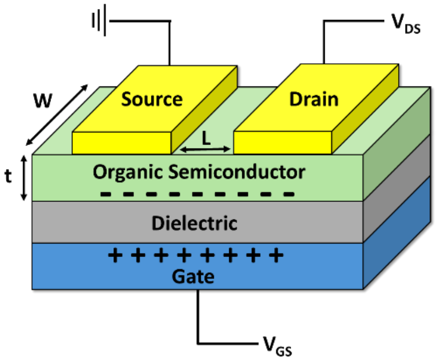

Figure 5.2 Representación de un transistor orgánico de efecto de campo "top contact-bottom gate". L es la longitud del canal; W es el ancho del canal y t es el espesor de la capa semiconductora.

Los elementos que componen un transistor orgánico de efecto campo son:[19]

- **Electrodos:** puerta, fuente y sumidero. Normalmente, los electrodos fuente y sumidero están hechos de oro, mientras que el electrodo puerta está hecho de silicio dopado.
- **Material dieléctrico:** suele ser un óxido metálico, siendo el dióxido de silicio (SiO_2) el material más utilizado. Los polímeros también son una buena alternativa debido a sus propiedades aislantes y se utilizan ampliamente como dieléctricos.
- **Semiconductor orgánico:** material que conecta los electrodos de fuente y sumidero, formando el canal por el que fluye la corriente. Si el dispositivo transporta huecos, se clasifica como de tipo p, si transporta electrones, es de tipo n. Los semiconductores capaces de transportar tanto huecos como electrones se denominan ambipolares.

Para alcanzar un completo desarrollo de estos semiconductores orgánicos en dispositivos electrónicos, hay que entender cómo funciona el transporte de carga y los factores de los cuales éste depende. A diferencia de los semiconductores inorgánicos, en los semiconductores orgánicos el ordenamiento depende de interacciones intermoleculares no covalentes,[20] pudiendo distinguir entre semiconductores orgánicos desordenados, amorfos, y semiconductores orgánicos con estructuras cristalinas.[21] En estos semiconductores el transporte de carga se describe principalmente mediante un transporte de carga mediante bandas, un mecanismo de salto (*hopping mechnism*) o mediante un mecanismo de salto de rango variable (*Variable range hopping*).

Por otro lado, diferentes características moleculares pueden afectar a las propiedades del material y, por tanto, al transporte de carga: la extensión de la cadena π-conjugada[22], sustitución con heteroátomos,[23] sustitución con grupos dadores o aceptores,[24] empaquetamiento molecular o la introducción de grupos solubilizantes[25]. La extensión de la cadena π-conjugada aumenta la π-conjugación y por consiguiente puede favorecer el transporte de carga. En cuanto a la sustitución con heteroátomos, se trata de una estrategia eficiente para optimizar las propiedades electrónicas y el empaquetamiento molecular. A su vez, la sustitución con grupos dadores o aceptores de electrones es otra estrategia consolidada en la modificación de las propiedades electrónicas de este tipo de semiconductores, ya que la introducción de este tipo de grupos modifica las propiedades oxidativas y de estabilidad. Otro factor que juega un papel importante en el transporte de carga en semiconductores orgánicos es el empaquetamiento molecular, ya que el grado de orden molecular influye drásticamente en las propiedades macroscópicas del material. Por último, la introducción de grupos solubilizantes tiene una gran importancia en la mejora de la procesabilidad de los materiales.

5.1.1 Materiales a estudio

En esta tesis doctoral, se investigan diversos semiconductores orgánicos π-conjugados para su aplicación en transistores orgánicos de efecto de campo (OFETs), con el objetivo principal de profundizar en la comprensión del transporte de carga de estos materiales. Concretamente, se estudian varios factores que afectan al transporte de carga: (i) El efecto de la longitud de la cadena conjugada y la sustitución de heteroátomos (Capítulo I); (ii) La introducción de átomos electronegativos (Capítulo II); (iii) La introducción de grupos electroactivos (Capítulo III); (iv) Las interacciones intermoleculares y el empaquetamiento molecular (Capítulo IV).

Para el estudio de los semiconductores descritos en esta tesis se han empleado métodos espectroscópicos, electroquímicos, espectroelectroquímicos y químico-cuánticos, los cuales proporcionan información detallada sobre la estructura y las propiedades electrónicas.

5.2 Metodología

En esta tesis, se ha llevado a cabo un estudio sistemático que combina técnicas espectroscópicas y electroquímicas junto con cálculos químico-cuánticos.

En primer lugar, los compuestos estudiados se han caracterizado tanto en disolución como en estado sólido mediante el uso de técnicas como la absorción UV-Vis, emisión, Raman e Infrarrojo (IR), así como mediante técnicas electroquímicas, como la voltamperometría cíclica y espectroelectroquímica. Este estudio nos permite evaluar el efecto que producen las diferentes modificaciones químicas sobre la estructura molecular y el grado de conjugación de los diferentes materiales estudiados. Posteriormente, los resultados obtenidos experimentalmente han sido interpretados con la ayuda de cálculos químico-cuánticos a nivel DFT, los cuales nos han permitido interpretar los espectros en profundidad, obteniendo la mayor información posible sobre el efecto de las modificaciones químicas establecidas, sobre las propiedades optoelectrónicas de nuestros sistemas.

Una vez los compuestos estudiados se han caracterizado, estos se han implementado en dispositivos electrónicos, en nuestro caso OFETs. Con esto, evaluamos la capacidad de transporte de carga en los semiconductores estudiados, pudiendo relacionarla con las propiedades observadas anteriormente.

Finalmente, la morfología de las láminas delgadas semiconductoras se analizan mediante técnicas cómo la microscopía de fuerza atómica (AFM) o difracción de rayos X (XRD), con el objetivo de obtener la mayor información posible sobre el efecto que tiene la morfología y el grado de cristalinidad en la eficiencia de los dispositivos electrónicos fabricados.

5.3 Resultados y discusión

A continuación, detallaremos los resultados más relevantes obtenidos de los materiales estudiados en esta tesis.

5.3.1 Capítulo I: Modulación de la estabilización y el transporte de carga en semiconductores basados en naftalimidas: el papel de las modificaciones del esqueleto fusionado y del núcleo conector.

En este primer capítulo, se aborda la caracterización de una nueva familia de compuestos basados en BTD, el cual se considera el principal bloque común en todos los sistemas estudiados, combinado con unidades electroatractoras de naftalimidas con potentes unidades dadoras de electrones derivadas de tiofeno, conectadas a través de unidades nitrogenadas rígidas y conjugadas (Figura 5.4).[26] Para ajustar con precisión los niveles de energía del orbital HOMO, extendimos la longitud de las unidades de tiofeno y evaluamos diferentes isómeros.

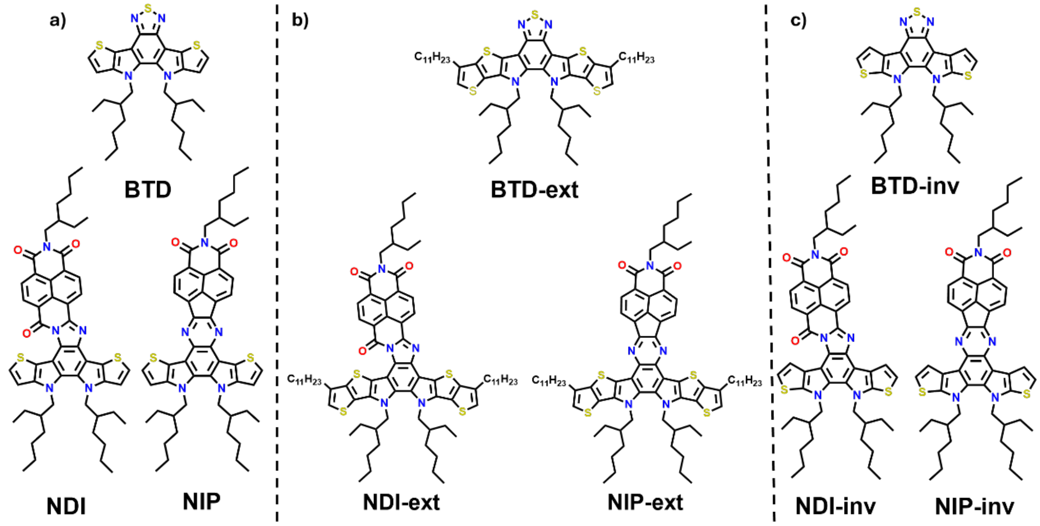

Figure 5.4 Estructura de los semiconductores basados en naftalimida descritos en el capítulo I, a) derivados **BTD**, b) derivados **BTD-ext** y c) derivados **BTD-inv**.

La estructura de mínima energía de los compuestos estudiados fue optimizada mediante cálculos DFT, observándose cómo los derivados de **NDI** presentan una estructura distorsionada, en contraste con los derivados de **NIP**, los cuales muestran una estructura totalmente plana.

Según muestran los niveles energéticos calculados de los orbitales moleculares, la introducción del grupo naftalimida en los diferentes derivados estabiliza la energía del orbital LUMO. Al contrario, la incorporación del fragmento de arilenimida no tiene un impacto notable en los niveles de energía del HOMO.

La figura 5.5 muestra un resumen de la experimentación realizada en este capítulo.

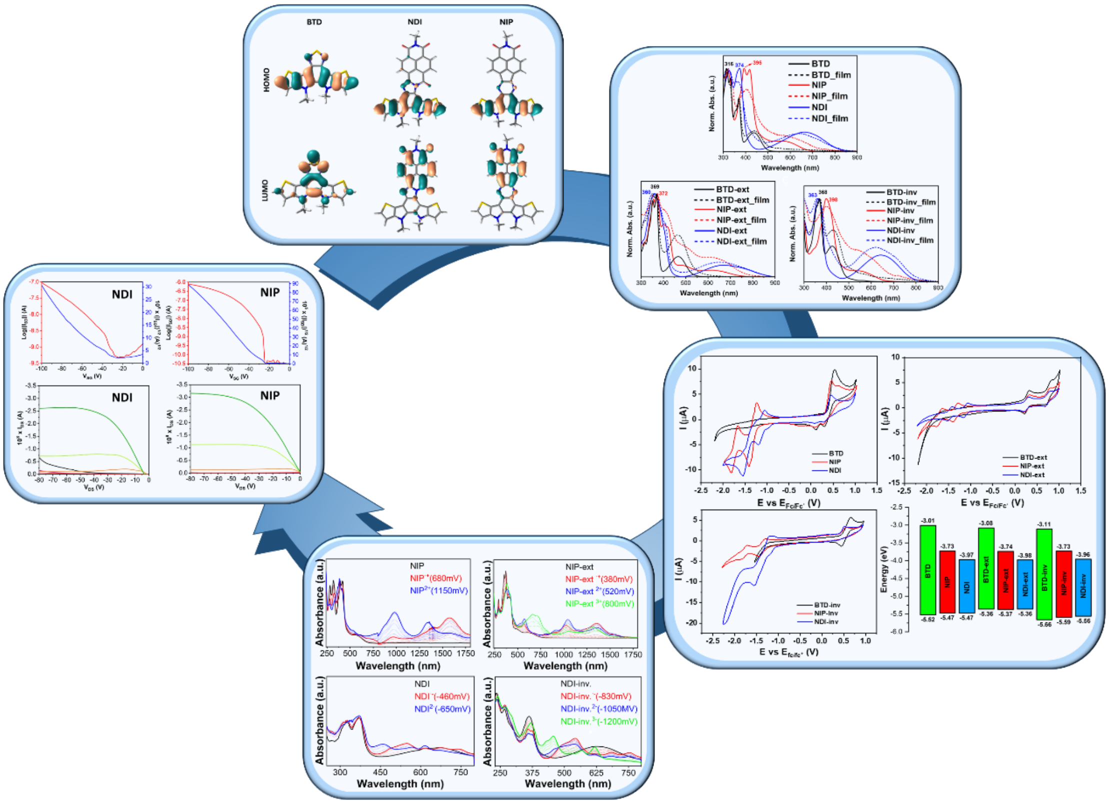

Figure 5.5 Resumen del estudio experimental y teórico llevado a cabo en el capítulo I.

La sustitución del núcleo de benzotiadiazol por unidades de naftalimida mediante enlaces planos y conjugados induce un desplazamiento al rojo en la banda de absorción más baja en energía de los espectros UV-Vis en los compuestos **NDI** y **NIP**. Sin embargo, al comparar los derivados invertidos, vemos que, al introducir una unidad de imidazol (**ND-inv**), se produce un ligero desplazamiento al azul en comparación con el derivado no funcionalizado (**BTD-inv**). También se estudió el efecto de la extensión de la cadena de tiofenos en los sistemas π-conjugados, encontrando que en la banda de absorción más baja en energía, la extensión del fragmento dador aumenta esta absorción hacia la región NIR, siendo más pronunciada en el derivado **NDI-ext**. A su vez, los espectros de absorción UV-Vis de los diferentes derivados de **BTD**, **NDI** y **NIP** en sólido muestran diferencias prácticamente nulas con los espectros en disolución. Todos los derivados presentan un perfil espectral similar con dos familias de bandas sobre 400 nm y 650 nm.

Se realizaron cálculos teóricos de TD-DFT para comprender la naturaleza de las transiciones electrónicas, mostrando que las bandas de absorción de menor energía en todos los sistemas estudiados se atribuyen teóricamente a la transición HOMO-LUMO. Esta transición electrónica exhibe una clara transferencia de carga intramolecular, como evidencia la topología de los orbitales moleculares, donde vemos cómo la densidad electrónica va desde la región más rica en electrones del semiconductor, la parte tienopirrólica, hasta la unidad más deficiente en electrones, el tiadiazol en los sistemas BTD, y el grupo naftalimida en los derivados NDI y NIP.

Para estudiar las propiedades electroquímicas de estos semiconductores orgánicos, se realizaron experimentos de voltamperometría cíclica en atmósfera de argón. Además, es posible modificar los valores del potencial de oxidación extendiendo la unidad tienopirrol (**BTD-ext**, **NDI-ext** y **NIP-ext**), o por otro lado, modificando la posición del átomo de azufre en la unidad tiofeno (**BTD-inv**, **NDI-inv** y **NIP-inv**). De esa forma vemos cómo la capacidad oxidativa de estos semiconductores puede mejorarse significativamente extendiendo la conjugación efectiva en el núcleo de tienopirrol.

En cuanto a la capacidad aceptora de electrones de estos semiconductores orgánicos, se observan potenciales de reducción un poco menores cuando la cadena de tienopirrol se alarga (**NIP-ext** y **NDI-ext)** y cuando invertimos la posición de los tiofenos terminales (**NIP-inv** y **NDI-inv**).

Para analizar las especies cargadas, se ha hecho uso de espectroelectroquímica UV-Vis/NIR. En este estudio, cómo se ha mencionado anteriormente, el **BTD** se considera el principal bloque estructural común a todos los sistemas investigados. Este compuesto es capaz de estabilizar dos especies con carga positiva y una especie con carga negativa. La incorporación de una unidad de naftalimida al núcleo de benzotiadiazol (**NDI** y **NIP**) reduce significativamente el potencial necesario para estabilizar también dos especies con carga positiva durante el proceso de oxidación. Además, tanto en semiconductores **NDI** como **NIP**, dos especies con carga negativa se estabilizan durante el proceso de reducción.

Al extender el núcleo π-conjugado en **BTD-ext**, se estabilizan dos cargas positivas, como en **BTD**, pero a potenciales notablemente más bajos. Además, como en **BTD**, este compuesto también estabiliza una carga negativa. Con respecto a **NDI-ext** no se detectan nuevas especies oxidadas en comparación con **NDI**. En cambio, para **NIP-ext** se estabilizan tres especies oxidadas distintas, al contrario que en la molécula de **NIP** donde solo se identificaron las dos primeras especies. Por otro lado, la extensión de la cadena no genera diferencias significativas en la estabilización de las especies reducidas. Tanto **NIP-ext** como **NDI-ext** presentan dos procesos de reducción, al igual que **NIP** y **NDI**.

A su vez, la π-conjugación en la cadena de tienopirrol se ve parcialmente obstaculizada en los derivados invertidos, lo que también influye en la estabilización de la carga. En **BTD-inv** observamos un escenario similar que en el caso de **BTD** y **BTD-ext**. Sin embargo, los procesos de reducción se ven favorecidos en **NDI-inv**, donde se registran tres nuevos perfiles espectrales en contraste con la estabilización de solo dos especies reducidas en **NDI**. En cambio, solo se forma una especie oxidada, lo que indica que la inversión en NDI favorece significativamente los procesos de reducción sobre los oxidativos. Por el contrario, este efecto no se observa en **NIP-inv**, cuyos cambios espectrales son similares a los de **NIP**.

Finalmente se fabricaron transistores de efecto de campo para evaluar las propiedades de transporte de carga de los semiconductores estudiados. Los derivados de BTD mostraron ser inactivos como semiconductores en OFET. Sin embargo, los derivados de naftalimida muestran movilidades de efecto de campo modestas, alcanzando un valor máximo de movilidad de huecos de 10^{-2} cm^2 V^{-1} s^{-1} para **NIP**. Además, la introducción de un anillo de imidazol como espaciador en **NDI** causa una disminución en la movilidad de efecto de campo en dos órdenes de magnitud (10^{-4} cm^2 V^{-1} s^{-1}). Al analizar el efecto de la extensión del sistema π-conjugado en estos derivados, se observa una disminución drástica en la movilidad de efecto de campo en **NIP-ext** y **NDI-ext**, con valores de 10^{-6} cm^2 V^{-1} s^{-1} para ambos semiconductores. Por otro lado, los derivados invertidos, **NDI-inv** y **NIP-inv**, no presentan actividad eléctrica.

5.3.2 Capítulo II: Modulación de la estabilización y el transporte de carga en semiconductores basados en naftalimidas: efecto de la inserción de átomos de halógenos.

En este capítulo hemos estudiado una serie de compuestos basados en derivados fenileno-naftalimida (**NAI-Ph**, **NAI-Ph-F** y **NAI-Ph-Cl**) (Figure 5.6),[27] donde las unidades de fenileno y las unidades de la naftalimida están directamente conjugadas mediante uniones amidina rígidas (NAI). Para modificar las propiedades aceptoras de electrones y de transporte de carga de estos nuevos sistemas, se incorporaron diferentes átomos de halógeno (F y Cl) a la unidad de fenileno. Se estudió el efecto de la incorporación de átomos electronegativos a la unidad de fenileno sobre las propiedades ópticas, electroquímicas y de transporte de carga.

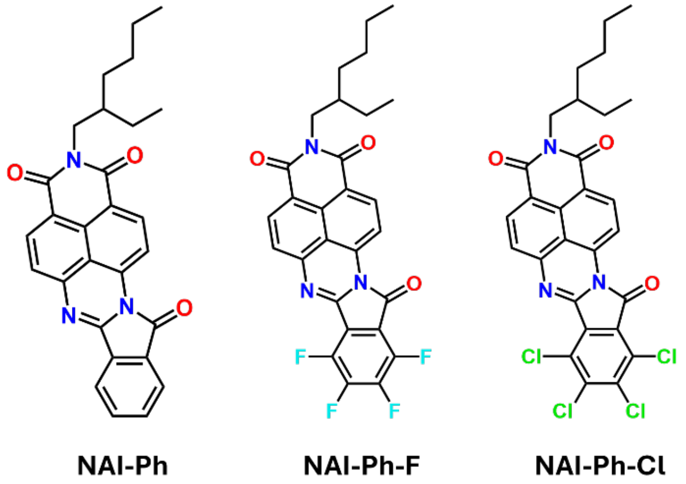

Figure 5.6 Estructuras moleculares de los derivados de naftalimida-oligotiofeno estudiados en el capítulo II.

La optimización DFT de las estructuras moleculares de los compuestos analizados, revela una conformación completamente plana en los tres sistemas estudiados, lo que sugiere que la incorporación de átomos de halógeno al esqueleto conjugado no altera la estructura molecular de los compuestos.

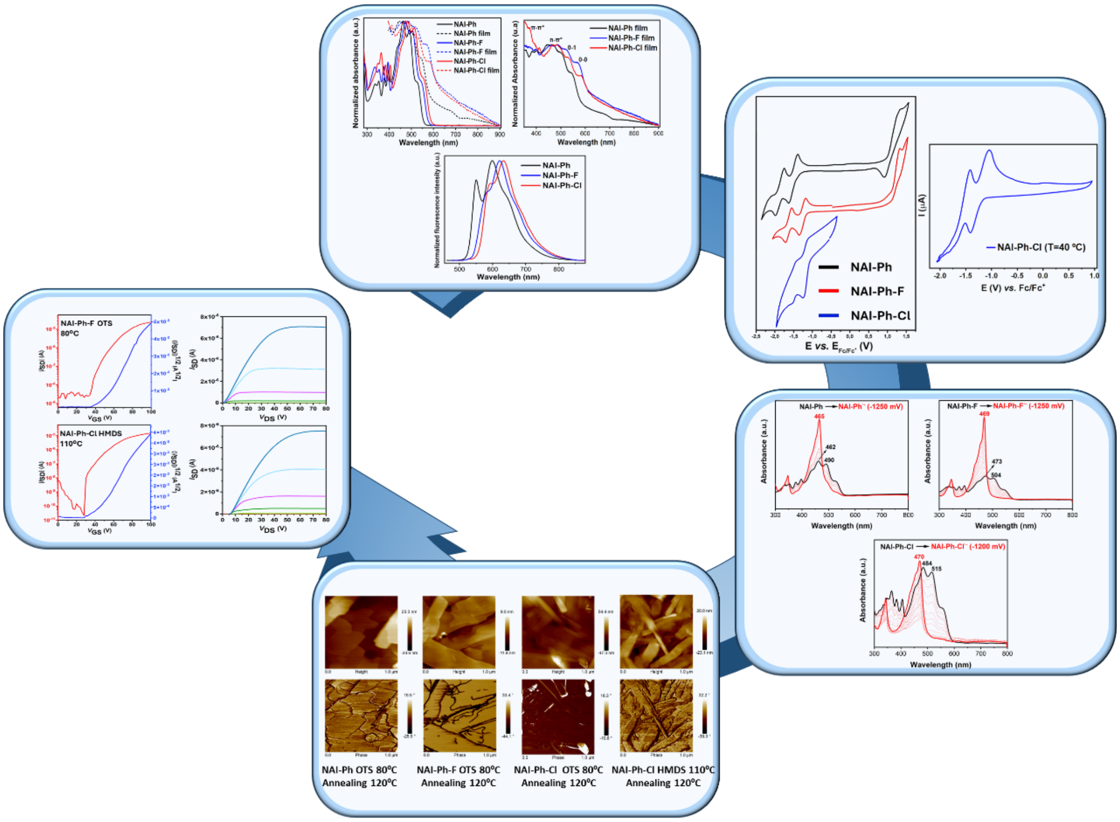

Figure 5.7 Resumen del estudio experimental y teórico llevado a cabo en el capítulo II.

La figura 5.7 muestra un resumen de la experimentación realizada en este capítulo. En primer lugar, los espectros de absorción UV-vis de los compuestos muestran que la incorporación de átomos de halógeno en las posiciones terminales de la unidad de fenileno resulta en una reducción del gap óptico. Para todos los compuestos estudiados, la espectroscopía UV-Vis muestra un amplio perfil espectral en el rango de 335 a 551 nm. En cuanto a los máximos de las principales bandas de absorción en **NAI-Ph-F** y **NAI-Ph-Cl**, estos se desplazan al rojo 12 y 20 nm, respectivamente, en comparación con **NAI-Ph**.

Para comprender la agregación en los compuestos estudiados, se ha registrado la absorción UV-Vis en películas delgadas, donde se observan cambios en los espectros UV-Vis de película delgada respecto a los espectros en disolución de los tres semiconductores estudiados. Esto sugiere la formación de agregados supramoleculares debido a las fuertes interacciones π-π y la posibilidad de interacciones intermoleculares de enlaces no covalentes, particularmente en el compuesto fluorado debido a la alta electronegatividad y pequeño tamaño de los átomos de F.

Se calcularon los gaps electrónicos teóricos a nivel teórico B3LYP/6-31G**, obteniendo valores que concuerdan con los resultados experimentales. Los datos teóricos indican que los orbitales HOMO y LUMO se estabilizan progresivamente al pasar de **NAI-Ph** a **NAI-Ph-F** y **NAI-Ph-Cl**, como consecuencia de la incorporación de átomos de halógeno. La naturaleza electrodeficiente del cloro y el flúor induce la estabilización de ambos orbitales, siendo más significativa esta estabilización en el LUMO. Aunque, la introducción de cloro en la estructura molecular reduce de forma más eficiente la energía del orbital LUMO, debido a la capacidad del cloro de acomodar mayor densidad electrónica a través de sus orbitales 3d vacíos, mientras que el flúor no tiene orbitales d energéticamente accesibles.

Por otra parte, los espectros de fluorescencia revelan una emisión moderada en el rango de 510 nm a 830 nm. Se observó un desplazamiento batocrómico en el pico de mayor intensidad cuando vamos de **NAI-Ph** (452 nm) a **NAI-Ph-F** (464 nm) y **NAI-Ph-Cl** (472 nm), atribuido a una conjugación efectiva más alta tras la halogenación.

La caracterización electroquímica de los materiales estudiados se realizó mediante voltamperometría cíclica (CV) en soluciones de diclorometano. En el barrido catódico, se observaron dos procesos redox reversibles para los tres sistemas, correspondientes a la formación de dos especies aniónicas. El primer proceso de reducción se observó a potenciales similares para **NAI-Ph-F** y **NAI-Ph-Cl**, alcanzándose este proceso a un potencial de reducción más negativo en **NAI-Ph**. A su vez, el segundo proceso de reducción siguió la misma tendencia con potenciales similares para **NAI-Ph-F** y **NAI-Ph-Cl** y un potencial de reducción más negativo para **NAI-Ph**.

Cabe destacar que, la presencia de halógenos en la unidad de fenileno reduce la capacidad dadora de electrones de los átomos de nitrógeno del enlace amidina, provocando que los potenciales de reducción se desplacen a valores menos negativos y que los orbitales LUMO se estabilicen.

Por otro lado, tanto **NAI-Ph** como **NAI-Ph-F** muestran una onda de oxidación cuasi-reversible en el barrido anódico. Estos procesos de oxidación aparecen a altos potenciales, mientras que no se observa ningún proceso de oxidación para **NAI-Ph-Cl**.

Para evaluar la capacidad de los compuestos estudiados en estabilizar especies cargadas se realizó un estudio espectroelectroquímico. En el caso de **NAI-Ph**, es capaz de estabilizar una especie aniónica. Al introducir átomos de halógeno (F y Cl) en la estructura química, no se observan diferencias significativas en los perfiles espectrales con respecto a

NAI-Ph. Solo se observa un desplazamiento batocrómico debido al efecto electroaceptor de los átomos de F y Cl. Se intentó la oxidación para **NAI-Ph**, **NAI-Ph-F** y **NAI-Ph-Cl**, pero ninguno experimentó procesos de oxidación en las condiciones experimentales probadas.

Para finalizar, se fabricaron transistores orgánicos de efecto de campo (OFET) para evaluar las propiedades de transporte de carga de los tres compuestos estudiados. El compuesto **NAI-Ph** exhibe una movilidad máxima de efecto de campo tipo n de 2×10^{-2} cm² V^{-1} s^{-1}, y una movilidad de tipo p de 3×10^{-3} cm² V^{-1} s^{-1}. Sin embargo, al introducir átomos de halógeno en la estructura química del semiconductor, los compuestos solo exhiben movilidad de tipo n. Para **NAI-Ph-F** se ha obtenido una movilidad tipo n máxima de 0,1 cm² V^{-1} s^{-1}, y para **NAI-Ph-Cl** se ha obtenido una movilidad tipo n máxima de 0,2 cm² V^{-1} s^{-1}.

5.3.3 Capítulo III: Modulación de la estabilización y el transporte de carga en semiconductores basados en naftalimidas: inclusión de grupos electroactivos.

En este capítulo, estudiamos varias familias de compuestos basadas en tertiofeno-naftalimida (Figure 5.8).[28] En estas familias de compuestos, se han introducido tres unidades terminales distintas con fuerte capacidad de atracción de electrones produciendo nuevos semiconductores orgánicos con propiedades optoelectroquímicas ajustables. Además, se ha modificado el grupo conector, pirazina (**NIP3T-X**) e imidazol (**NDI3T-X**).

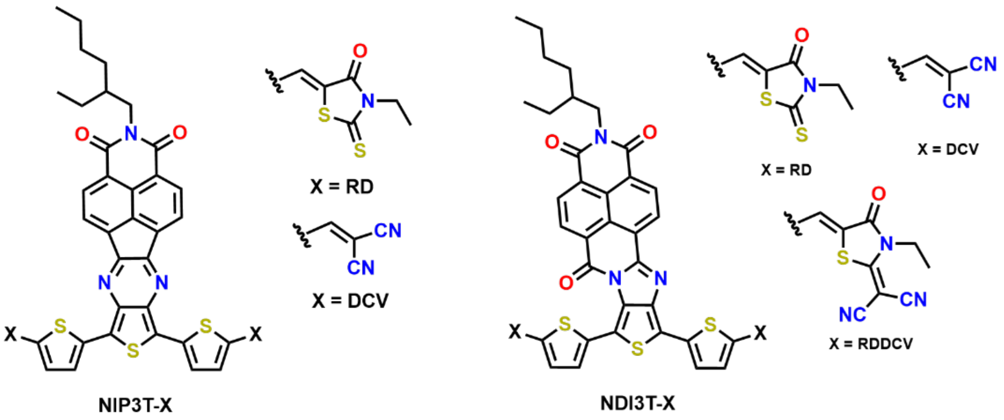

Figure 5.8 Compuestos derivados de oligotiofeno-naftalimida con sustitución terminal estudiados en el capítulo III.

La optimización a nivel DFT de las estructuras moleculares a estudio revela una conformación no plana para **NDI3T-X**, mientras que los sistemas **NIP3T-X** estudiados, presentan una estructura principalmente plana.

La figura 5.9 muestra un resumen de la experimentación realizada en este capítulo. Primero, para evaluar el impacto de los sustituyentes laterales en la π-conjugación y las propiedades moleculares se usó FT-Raman. Al analizar los espectros Raman, nos centramos en los modos vibracionales Raman asociados con el modo vibracional ν(C=C) completamente simétrico del fragmento de oligotiofeno. Esta vibración se desplaza significativamente a frecuencias más bajas tras la incorporación de grupos electroaceptores en **NDI3T-X**. Además, la comparación con los sistemas **NIP3T-X** revela un mayor grado de π-conjugación de los derivados basados en NIP, debido a la planaridad del esqueleto conjugado.

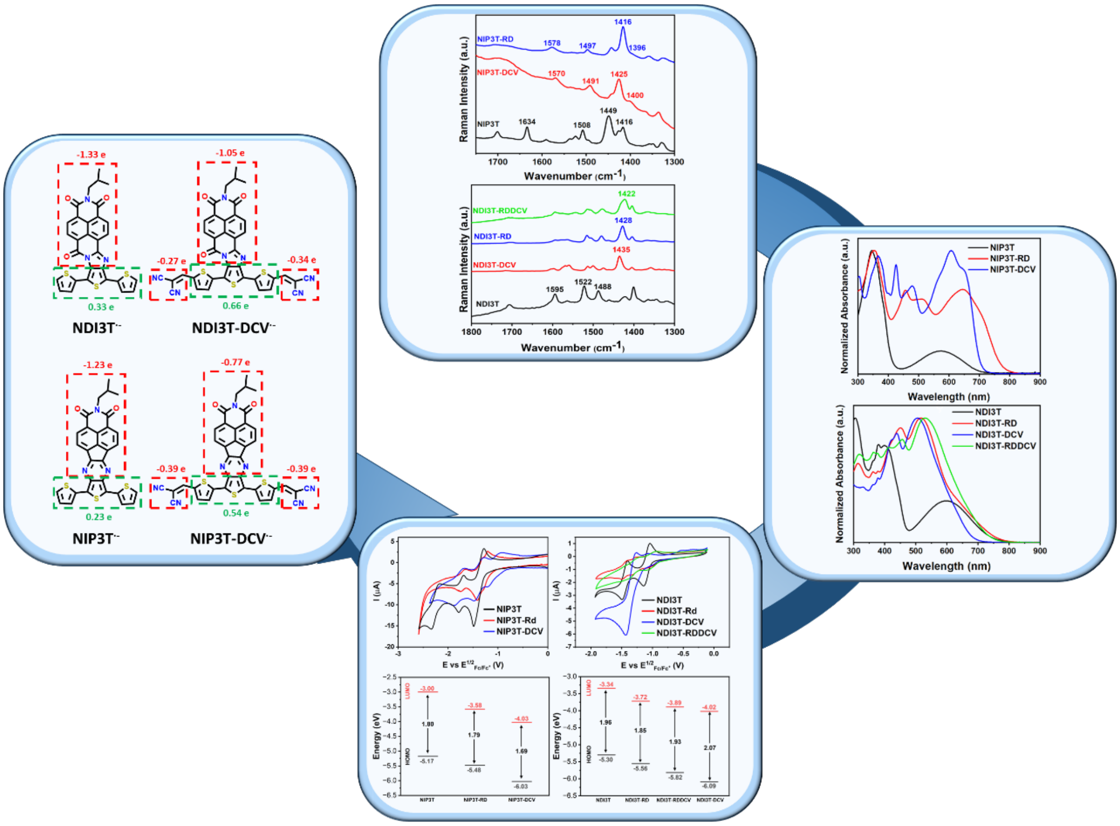

Figure 5.9 Resumen del estudio experimental y teórico llevado a cabo en el capítulo III.

La buena solubilidad de los compuestos estudiados permite una adecuada caracterización óptica y electroquímica en disolución mediante técnicas de UV-Vis y voltamperometría cíclica. El perfil del espectro de absorción de **NIP3T** muestra una banda de absorción a menor energía, que se atribuye a la excitación por transferencia de carga intramolecular (ICT). Esto se ha confirmado teóricamente mediante cálculos de TD-DFT y puede describirse como una excitación HOMO-LUMO, donde la densidad electrónica se desplaza desde el HOMO, ubicado principalmente en el fragmento de oligotiofeno, hacia el LUMO, ubicado en la unidad de naftalimida. Se observa que la funcionalización con aceptores electrónicos fuertes en la posición alfa de las unidades de tiofeno tiene un impacto significativo en sus propiedades ópticas, extendiendo la absorción hasta 800 nm en los compuestos funcionalizados. Sin embargo, a diferencia de **NIP3T**, los orbitales HOMO y LUMO de **NIP3T-X** se ubican principalmente en el fragmento de tiofeno, lo que indica que la transición electrónica tiene un carácter predominantemente π-π^* en lugar de ICT.

Por otro lado, el perfil espectral de **NDI3T** muestra también una banda de absorción de menor energía, que se atribuye a la excitación por transferencia de carga intramolecular (ICT), como en **NIP3T**. En los derivados de **NDI3T-X**, la funcionalización con fuertes aceptores de electrones causa un ligero desplazamiento de la absorción, dependientemente de la unidad aceptora de electrones introducida. Concretamente, la absorción a menor energía se desplaza para todos los derivados de **NDI3T-X**. Este fenómeno se puede explicar considerando la aparición de dos canales ICT diferentes y en competencia. Estos dos canales ICT se confirmaron mediante cálculos de TD-DFT y están relacionados con la transferencia electrónica entre HOMO→LUMO y HOMO→LUMO+1.

Para comprender mejor la naturaleza de la banda de absorción situada a menor energía en los sistemas **NIP3T-X** y **NDI3T-X**, se realizaron medidas solvatocrómicas variando la polaridad del disolvente. Los sistemas **NDI3T y NIP3T** exhiben un claro comportamiento solvatocrómico, con un desplazamiento al rojo en la banda de absorción ICT en disolventes más polares. Sin embargo, en los derivados **NIP3T-X**, la banda de absorción no mostró desplazamiento al variar la polaridad del disolvente, lo que confirma la ausencia de una banda de absorción ICT. A su vez, los derivados **NDI3T-RD** y **NDI3T-DCV** exhiben un solvatocromismo positivo con cierto carácter de transferencia de carga intramolecular. Por el contrario, el derivado **NDI3T-RDDCV** muestra un solvatocromismo negativo.

Mediante experimentos de voltamperometría cíclica se puede observar que, por un lado, en sistemas no sustituidos, la sustitución de un conector de pirazina (**NIP3T**) por un conector imidazol (**NDI3T**) provoca un desplazamiento del potencial de reducción asociado a las unidades de naftalimida hacia valores más positivos. Esto se debe a la mayor capacidad aceptora de electrones de **NDI3T** en comparación con su análogo **NIP3T**. Un fenómeno similar se observa en procesos de oxidación. Por otro lado, la introducción de diferentes unidades aceptoras de electrones en la posición alfa del fragmento de tertiofeno muestra en la serie **NDI3T-X** la misma tendencia que la observada en los derivados **NIP3T-X**, con una mejora en la capacidad aceptora de electrones en comparación con los compuestos **NDI3T** y **NIP3T** no sustituidos. Por lo tanto, los datos electroquímicos sugieren que los sistemas **NDI3T-X** son materiales con una capacidad aceptora de electrones mejorada en comparación con los materiales **NIP3T-X**.

Finalmente, se han analizado mediante espectroelectroquímica la estructura y estabilidad de los portadores de carga presentes en el proceso de transporte de electrones. En el caso de **NIP3T, NIP3T-RD** y **NIP3T-DCV**, la aplicación de potencial negativo da lugar a la formación de dos especies reducidas. En cuanto, a los procesos de oxidación, podemos observar la capacidad de **NIP3T** para acomodar dos cargas positivas. En cambio, **NIP3T-RD** y **NIP3T-DCV**, sólo estabilizan una especie positiva.

Centrándonos en los derivados de imidazol, **NDI3T** muestra la capacidad de estabilizar dos especies aniónicas. Del mismo modo, **NDI3T-RD** y **NDI3T-DCV**, muestran la capacidad de estabilizar dos especies negativas. Finalmente, en el compuesto **NDI3T-RDDCV** tenemos dos procesos de reducción, pero a diferencia de **NDI3T-RD** y **NDI3T-DCV**, el perfil espectral muestra ciertas diferencias. En cuanto a la oxidación electroquímica progresiva de **NDI3T,** se observa la presencia de dos procesos oxidativos. Por otro lado, la oxidación electroquímica progresiva de **NDI3T-RD**, **NDI3T-DCV** y **NDI3T-RDDCV** da lugar a la formación de una sola especie catiónica.

Finalmente, podemos ver cómo en los sistemas **NDI3T-X**, la carga negativa inyectada se estabiliza principalmente en el fragmento de naftalimida, como se esperaba considerando las topologías del LUMO. Los cálculos DFT de las especies cargadas de **NDI3T-X** indican que mientras que en **NDI3T** la carga negativa se localiza principalmente sobre la unidad NDI, la introducción de la subunidad de tertiofeno sustituida lateralmente con grupos electroaceptores disminuye este porcentaje, localizando un 70% de la carga inyectada en las unidades NDI, mientras que un 30% de la carga inyectada se localiza sobre los grupos electroaceptores. Una tendencia similar se observa en los sistemas **NIP3T-X**, donde podemos ver en **NIP3T** como la carga negativa inyectada se localiza sobre la unidad NIP. Mientras que en los derivados de **NIP3T-X**, después de la introducción de grupos electroaceptores en la cadena de tertiofeno, la carga inyectada se deslocaliza alrededor del 50% entre las unidades NIP y los grupos electroaceptores. Esta tendencia en los sistemas **NDI3T-X** y **NIP3T-X** indica el importante papel tanto de la unidad de conexión central como de los sustituyentes laterales en la estabilización de las especies cargadas negativamente.

5.3.4 Capítulo IV: Impacto de las interacciones supramoleculares mediante enlaces de hidrógeno en las propiedades electrónicas y de transporte de carga de semiconductores orgánicos basados en DPP

En este capítulo, se ha estudiado el papel de los enlaces de hidrógeno en el orden supramolecular de los derivados de diketopirrolopirrol (DPP), así como su efecto en la estructura molecular y electrónica. Nuestro objetivo es optimizar la generación de portadores de carga en dispositivos con el fin de mejorar el rendimiento eléctrico de semiconductores moleculares de tamaño excepcionalmente pequeño. Concretamente, se han estudiado sistemas de DPP unidos a tiofenos como componentes electroactivos y cadenas laterales que incorporan grupos amida como potenciales formadores de enlaces de hidrógeno. Se investigaron tres posiciones diferentes de los grupos amidas, **DPP2C**, **DPP4C** y **DPP6C**, y los resultados se compararon con una molécula **Control**, sin grupos amida en las cadenas laterales. (Figura 5.10)[29] Experimentos espectroelectroquímicos, complementados con espectroscopia vibracional y cálculos DFT, revelaron que la formación de enlaces de hidrógeno induce no solo modificaciones a nivel supramolecular, sino también en la longitud de conjugación efectiva de los semiconductores.

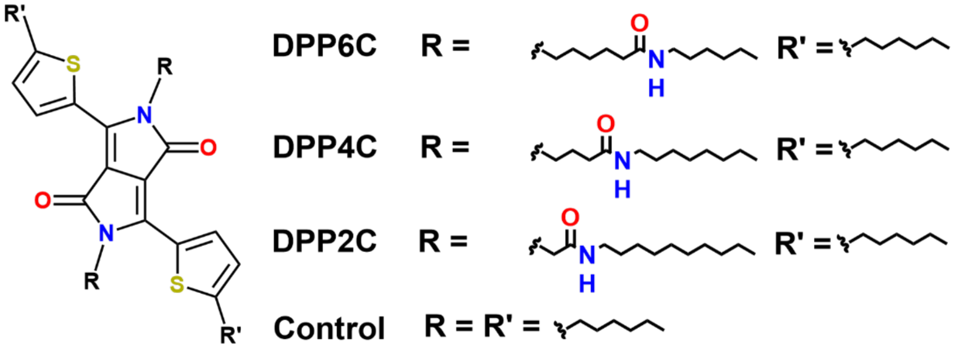

Figure 5.10 Compuestos derivados de DPP estudiados en el capítulo IV.

Los cálculos a nivel DFT muestran que los compuestos **Control**, **DPP4C** y **DPP6C** tienen esqueletos moleculares planos, debido a la interacción entre el hidrógeno del tiofeno y el oxígeno del grupo carbonilo del DPP. Sin embargo, la molécula **DPP2C** muestra una estructura distorsionada con ángulos de torsión de aproximadamente 15° entre el núcleo de DPP y los grupos tiofeno, debido a la formación de una interacción intramolecular mediante puente de hidrógeno entre el hidrógeno del grupo amida y el carbonilo de DPP. Como se esperaba, los orbitales moleculares frontera en las moléculas estudiadas están deslocalizados a lo largo de todo el esqueleto conjugado, con una mayor contribución en el núcleo DPP. Los compuestos **Control**, **DPP4C** y **DPP6C** presentan un HOMO-LUMO gap similar, alrededor de 2.42 eV. Sin embargo, **DPP2C** muestra un gap HOMO-LUMO ligeramente más alto en comparación con los otros compuestos, a 2.47 eV. Esta diferencia en las energías de los orbitales HOMO y LUMO de **DPP2C** puede atribuirse a la menor comunicación electrónica entre los tiofenos y el DPP, por la distorsión del esqueleto conjugado, lo que aumenta el carácter deficiente en electrones del DPP y estabiliza los orbitales HOMO y los LUMO.

La figura 5.11 muestra un resumen de la experimentación realizada en este capítulo. Las propiedades ópticas en disolución y en película delgada del **Control**, **DP2C**, **DPP4C** y **DPP6C** se estudiaron mediante espectroscopia de absorción UV-Vis y se analizaron con la ayuda de cálculos TD-DFT. Las moléculas **Control**, **DPP4C** y **DPP6C** presentan un espectro similar en disolución, mostrando una banda principal alrededor de 560 nm. Sin embargo, los espectros de absorción de **DPP2C** están desplazados hacia el azul con respecto a los de los otros compuestos estudiados, lo que indica una disminución en la π-conjugación. Este efecto en **DPP2C** puede atribuirse a la interacción intramolecular entre el hidrógeno de la amida y el carbonilo de DPP, que disminuye la planaridad y la π-conjugación. Además, los espectros de película delgada de todos los materiales estudiados muestran un perfil espectral más amplio y desplazado al rojo.

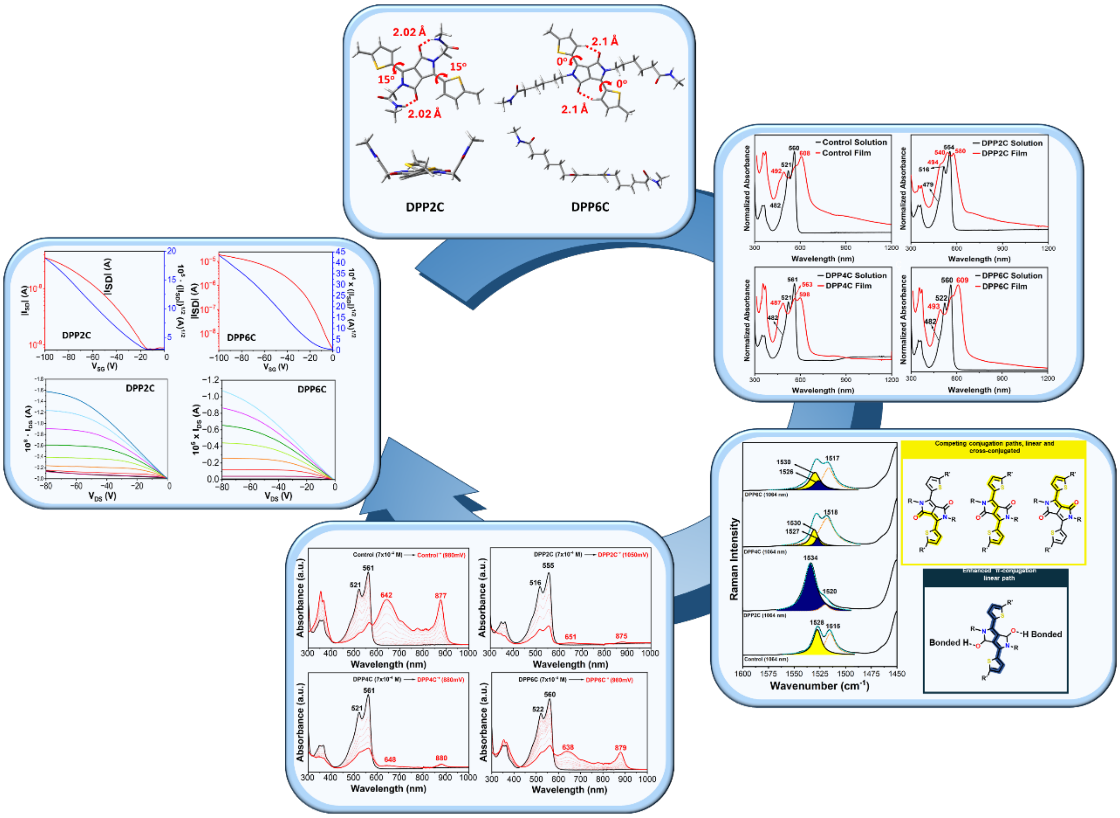

Figure 5.11 Resumen del estudio experimental y teórico llevado a cabo en el capítulo IV.

Por otro lado, se analizó el efecto producido por modificación de las cadenas laterales alquílicas mediante el registro de espectros de emisión y midiendo los desplazamientos de Stokes correspondientes tanto en disolución como en estado sólido. Se observaron pequeños desplazamientos de Stokes para todos los compuestos estudiados en disolución. En cambio, se observaron desplazamientos significativamente mayores en estado sólido. Concretamente, mayores desplazamientos se obtienen para los compuestos **DPP4C** y **DPP6C** comparados con la molécula **Control** y **DPP2C,** lo que indica diferentes tipos de agregación.

A su vez, se registraron los espectros IR de reflectancia total atenuada (ATR) y FT-Raman de los semiconductores **Control**, **DPP2C**, **DPP4C** y **DPP6C** en polvo para analizar la formación de enlaces de hidrógeno y su impacto en la estructura electrónica de las cadenas principales conjugadas. En el espectro ATR del compuesto **Control**, se observa una única vibración ν(C=O) correspondiente al grupo carbonilo del DPP. Por el contrario, en los compuestos **DPP4C** y **DPP6C**, aparecen dos bandas distintas asociadas con la vibración ν(C=O) del anillo de lactama y la vibración ν(C=O) de los grupos amida en las cadenas alquílicas, que forman enlaces de hidrógeno. La vibración ν(C=O) experimental de los grupos amida se posiciona a menores frecuencias que la predicha por los cálculos teóricos para moléculas aisladas de **DPP4C** y **DPP6C**, lo que indica un alargamiento del doble enlace C=O debido a interacciones intermoleculares. Por otro lado, para **DPP2C,** la banda atribuida a la vibración ν(C=O) de los grupos amida aparece a mayores frecuencias, en concordancia con la ausencia de participación del grupo carbonilo de la amida en los enlaces de hidrógeno intermoleculares. Como se observó mediante cálculos teóricos, dado que en **DPP2C**, el grupo carbonilo de la amida participa en enlaces de hidrógeno intramoleculares. Para corroborar aún más la presencia de estos enlaces de hidrógeno intramoleculares en **DPP2C**, centramos nuestra atención en la vibración ν(N−H). Dado que los cálculos teóricos de la molécula individual en el vacío predicen el alargamiento del enlace N-H en el caso del **DPP2C** y los datos experimentales muestran una posición similar para la vibración ν(N−H) de los compuestos **DPP2C**, **DPP4C** y **DPP6C**, todas las amidas deben estar formando enlaces de hidrógeno, aunque de diferente naturaleza: en el caso de **DPP2C**, este enlace es intramolecular, mientras que en **DPP4C** y **DPP6C** es intermolecular, ya que los cálculos teóricos de la molécula aislada en vacío no reproducen esta interacción.

De igual manera, los espectros Raman revelan modificaciones en las propiedades electrónicas de los esqueletos conjugados como resultado de la formación de enlaces de hidrógeno. Para examinar este efecto, nos centramos en la vibración colectiva a lo largo de la cadena tiofeno-DPP-tiofeno. En el caso del **Control**, esta vibración tiene una sola contribución. Sin embargo, en **DPP4C** y **DPP6C**, donde hay enlaces de hidrógeno intermoleculares, esta banda muestra dos contribuciones distintas. La presencia de estas dos señales sugiere que el grupo carbonilo del DPP puede participar, en cierta medida, en la interacción supramolecular de enlaces de hidrógeno, lo que favorece una mayor π-conjugación en moléculas que presentan esta interacción. Por el contrario, los espectros Raman de **DPP2C** muestran la vibración colectiva ν(C=C/C-C) con solo una contribución, en consonancia con la presencia de enlaces de hidrógeno intramoleculares en todas las moléculas.

Para evaluar la capacidad de los compuestos estudiados en estabilizar especies cargadas y determinar si las interacciones no covalentes influyen en la formación de estas especies, se realizaron estudios espectroelectroquímicos *in situ*. Los compuestos estudiados exhiben un comportamiento similar en disolución, considerando que se suprimen las interacciones intermoleculares a bajas concentraciones. En estas condiciones, todos los compuestos estabilizan una carga positiva a potenciales aplicados similares. Sin embargo, cabe destacar que el potencial aplicado es ligeramente mayor para **DPP2C**, debido a la menor π-conjugación. A su vez, para evaluar el papel de las interacciones intermoleculares en la inyección y estabilización de carga, se oxidaron películas delgadas exponiéndolas a vapor de yodo, durante 24 horas. Se observaron diferencias entre el semiconductor con enlaces de hidrógeno intermoleculares, **DPP6C**, y el material de referencia, **Control**. Mientras que el UV-Vis muestra que el compuesto con enlaces de hidrógeno intermoleculares estabiliza una especie con carga positiva, el **Control** no mostró signos de oxidación, lo que sugiere que la ausencia de interacciones mediante enlaces de hidrógeno previene este proceso. Además, en los espectros IR de la molécula **Control**, no se encontraron diferencias notables antes y después de la oxidación con yodo. Sin embargo, en el caso de **DPP6C** se registraron cambios atribuidos la formación del catión radical. Para **DPP2C** y **DPP4C** no se obtuvieron resultados reproducibles

Por último, para evaluar las propiedades eléctricas, se fabricaron transistores orgánicos de efecto campo (OFETs). Es importante destacar que, si bien el **Control** no mostró actividad, se registraron movilidades de efecto campo de tipo p de 4×10^{-6} cm^2 V^{-1} s^{-1}, 5×10^{-3} cm^2 V^{-1} s^{-1} y 2×10^{-2} cm^2 V^{-1} s^{-1} para **DPP2C**, **DPP4C** y **DPP6C**, respectivamente.

5.4 Conclusiones

En esta tesis, hemos estudiado una serie de semiconductores orgánicos π-conjugados para su aplicación en transistores orgánicos de efecto de campo (OFETs). El objetivo principal es comprender el impacto de diferentes modificaciones estructurales en la deslocalización intramolecular π-electrónica, así como las implicaciones de estas modificaciones en la organización supramolecular, que desempeña un papel importante en el transporte de carga de los materiales.

En el Capítulo I, estudiamos una familia de compuestos basados en unidades de naftalimidas con potentes grupos dadores derivados del tiofeno, conectados mediante enlaces de nitrógeno rígidos y conjugados (imidazol o pirazina), donde se estudia el efecto de la longitud de la cadena conjugada y la sustitución de heteroátomos. En este sentido, la modificación de la estructura química influye en la estabilización de la carga de los compuestos estudiados. En particular, los resultados destacan el papel de los enlaces de pirazina en la mejora de la comunicación electrónica entre la naftalimida y la cadena π-conjugada, debido al esqueleto conjugado más plano. Los OFETs fabricados demuestran un comportamiento eléctrico como semiconductores de tipo p con una movilidad máxima de huecos de 10^{-2} cm^2 V^{-1} s^{-1} para el derivado de pirazina (**NIP**). Además, la introducción de imidazol como anillo espaciador causa una disminución en la movilidad de efecto de campo en dos órdenes de magnitud (10^{-4} cm^2 V^{-1} s^{-1}). Otros derivados, mostraron propiedades eléctricas muy bajas (10^{-6} cm^2 V^{-1} s^{-1} en compuestos extendidos) o completamente nulas (en compuestos invertidos).

El Capítulo II de nuestro estudio se centró en una serie de compuestos basados en unidades fenileno-naftalimida (**NAI-Ph**, **NAI-Ph-F** y **NAI-Ph-Cl**), en los que las unidades de fenileno y naftalimida se conjugan directamente mediante enlaces rígidos de amidina (NAI). Estudiamos el efecto de la inserción de halógenos, el cual modifica las propiedades aceptoras de electrones y de transporte de carga de estos sistemas. Los cálculos DFT muestran estructuras rígidas y planas para los compuestos estudiados, lo que favorece el transporte de carga, destacando que la sustitución con átomos de halógeno en el anillo de fenileno es una buena estrategia para modular las propiedades electrónicas moleculares sin sacrificar la planaridad molecular.

El análisis fisicoquímico muestra que la introducción de átomos de halógeno en la estructura induce una mayor conjugación efectiva. Además, la introducción de flúor y cloro provoca una estabilización de los niveles de energía HOMO y LUMO, lo que conlleva una reducción del gap electrónico. Finalmente, la introducción de átomos de halógeno muestra potenciales de reducción más bajos en comparación con **NAI-Ph**.

La caracterización eléctrica en OFETs muestra un comportamiento ambipolar en **NAI-Ph**, pero el rendimiento mejora con la halogenación, a pesar de que solo se registra el transporte de electrones. Se midieron movilidades máximas de efecto de campo tipo n de 0,1 cm^{2}V^{-1}s^{-1} y 0,2 cm^{2}V^{-1}s^{-1} para **NAI-Ph-F** y **NAI-Ph-Cl**, respectivamente. En conclusión, la introducción de átomos de halógeno en **NAI-Ph** es una estrategia eficaz para facilitar la inyección de carga y maximizar la estabilización y el transporte de carga.

En el Capítulo III, estudiamos una familia de compuestos basados en tertiofeno-naftalimida con enlaces imidazol (**NDI3T-X**) y pirazina (**NIP3T-X**), en los que analizaos el efecto de la inserción de grupos electrodeficientes en el ajuste sus propiedades optoelectroquímicas.

Los espectros UV-Vis muestran un carácter de ICT en la banda de absorción de menor energía. Sin embargo, al insertar sustituyentes laterales electroaceptores en estas estructuras moleculares, se observan diferentes efectos en las energías de los orbitales frontera y especialmente en las topologías moleculares. Se ha demostrado que estos efectos tienen un impacto significativo en las propiedades electrónicas de los materiales, incluyendo las propiedades de absorción óptica y la estabilización de especies cargadas. Así, cuando se insertan grupos electroaceptores en derivados de pirazina (**NIP3T-X**), la banda de absorción de menor energía adquiere un carácter π-π*. Esto es debido a que la distribución de carga en el LUMO se localiza en el fragmento de oligotiofeno en lugar de en las unidades de naftalimida, modulando la naturaleza dadora de electrones de la cadena de oligotiofeno. Por el contrario, la introducción de grupos electroactivos en derivados de imidazol crea dos canales ICT diferentes y competitivos dentro de la molécula, lo que tiene un efecto interesante en los espectros de absorción electrónica y en la estabilización de especies cargadas.

Finalmente, en el Capítulo IV, estudiamos el papel de los enlaces de hidrógeno en las interacciones intra e intermoleculares y el empaquetamiento molecular en semiconductores moleculares de pequeño tamaño basados en DPP-tiofeno con cadenas laterales que incorporan grupos amida, como unidades formadoras de enlace de hidrógeno. Se investigaron tres posiciones diferentes de la amida: **DPP2C**, **DPP4C** y **DPP6C**, y los resultados se compararon con una molécula **Control**, que no contiene grupos formadores de enlaces de hidrógeno.

Al analizar la estructura molecular de los compuestos estudiados observamos que los compuestos **DPP4C** y **DPP6C**, presentan una estructura plana debido a la interacción entre el hidrógeno del anillo de tiofeno y el carbonilo del DPP. Por el contrario, **DPP2C** presenta una estructura distorsionada debido a la interacción de hidrógeno entre el hidrógeno del grupo amida y el oxígeno de carbonilo del DPP, lo que impide la interacción con el anillo de tiofeno. La estructura distorsionada en **DPP2C** implica una menor π-conjugación y estabilización de carga, como lo muestran los espectros UV-Vis, Raman e IR. Hemos comprobado la diferente interacción molecular en **DPP2C** con respecto a **DPP4C** y **DPP6C** mediante la comparación de los datos de IR y Raman teóricos y experimentales. En el IR teórico de **DPP2C**, la banda asociada al grupo amida se desplaza a frecuencias más bajas en comparación con **DPP4C** y **DPP6C**. Sin embargo, esta banda aparece en el mismo rango para los tres compuestos en los espectros experimentales, lo que indica que los tres compuestos forman enlaces de hidrógeno, pero en el caso de **DPP2C** este enlace de hidrógeno debe ser intramolecular, ya que los cálculos teóricos de la molécula aislada en el vacío predicen el alargamiento del enlace N-H. Finalmente, mientras que los compuestos **Control** y **DPP2C** son prácticamente inactivos en OFETs, las moléculas **DPP4C** y **DPP6C** exhiben movilidades de efecto de campo de 5×10^{-3} cm^2 V^{-1} s^{-1} y 2×10^{-2} cm^2 V^{-1} s^{-1}, respectivamente. Estos resultados respaldan la idea de que modificar la posición de los grupos funcionales amida en las cadenas laterales es un enfoque eficaz para promover la π-conjugación, estabilizar las especies cargadas y formar agregados supramoleculares.

5.5 Referencias

1 S.-H. Sunwoo, S. I. Han, C. S. Park, J. H. Kim, J. S. Georgiou, S.-P. Lee, D.-H. Kim and T. Hyeon, Soft bioelectronics for the management of cardiovascular diseases, *Nature Reviews Bioengineering 2023 2:1*, 2023, **2**, 8–24.

2 K. Liu, B. Ouyang, X. Guo, Y. Guo and Y. Liu, Advances in flexible organic field-effect transistors and their applications for flexible electronics, *npj Flexible Electronics 2022 6:1*, 2022, **6**, 1–19.

3 B. King, B. H. Lessard, B. Benoıˆ, B. H. Lessard, B. Benoıˆt and H. Lessard, Review of recent advances and sensing mechanisms in solid-state organic thin-film transistor (OTFT) sensors, *J Mater Chem C Mater*, 2024, **12**, 5654–5683.

4 X. Wei, W. Zhang and G. Yu, Semiconducting Polymers Based on Isoindigo and Its Derivatives: Synthetic Tactics, Structural Modifications, and Applications, *Adv Funct Mater*, 2021, **31**, 2010979.

5 L. Xia, Y. Liu, R. T. Chen, B. Weng and Y. Zou, Advancements in miniaturized infrared spectroscopic-based volatile organic compound sensors: A systematic review, *Appl Phys Rev*, DOI:10.1063/5.0197236/20039816/031306_1_5.0197236.AM.PDF.

6 F. Zhu, P. Xu and J. Zong, Moore's Law: The potential, limits, and breakthroughs, *Applied and Computational Engineering*, 2023, **10**, 307–315.

7 W. Tian, B. Li, Z. Li, H. Cui, J. Shi, Y. Wang and J. Zhao, Using Chiplet Encapsulation Technology to Achieve Processing-in-Memory Functions, *Micromachines 2022, Vol. 13, Page 1790*, 2022, **13**, 1790.

8 X. Ma, Y. Wang, Y. Wang, X. Cai and Y. Han, Survey on chiplets: interface, interconnect and integration methodology, *CCF Transactions on High Performance Computing*, 2022, **4**, 43–52.

9 D. Bittman, P. Alvaro, U. Santa Cruz, U. Pankaj Mehra, I. Member, U. D. Darrell E Long, U. L. Ethan Miller, P. Mehra and D. D. E Long, Twizzler: A Data-centric OS for Non-volatile Memory, *ACM Transactions on Storage (TOS)*, 2021, **17**, 31.

10 N. Maring, A. Fyrillas, M. Pont, E. Ivanov, P. Stepanov, N. Margaria, W. Hease, A. Pishchagin, A. Lemaître, I. Sagnes, T. H. Au, S. Boissier, E. Bertasi, A. Baert, M. Valdivia, M. Billard, O. Acar, A. Brieussel, R. Mezher, S. C. Wein, A. Salavrakos, P. Sinnott, D. A. Fioretto, P. E. Emeriau, N. Belabas, S. Mansfield, P. Senellart, J. Senellart and N.

Somaschi, A versatile single-photon-based quantum computing platform, *Nat Photonics*, 2024, **18**, 603–609.

11 F. Deng, J. Pan, Z. Liu, L. Zeng and J. Chen, Programmable DNA biocomputing circuits for rapid and intelligent screening of SARS-CoV-2 variants, *Biosens Bioelectron*, 2023, **223**, 115025.

12 R. Rietsche, C. Dremel, S. Bosch, L. Steinacker, M. Meckel and J. M. Leimeister, Quantum computing, *Electronic Markets*, 2022, **32**, 2525–2536.

13 Q. Lin, Polymeric electronic materials for microelectronics manufacturing: A review, *Polymer (Guildf)*, 2023, **286**, 126395.

14 A. D. Scaccabarozzi, A. Basu, F. Aniés, J. Liu, O. Zapata-Arteaga, R. Warren, Y. Firdaus, M. I. Nugraha, Y. Lin, M. Campoy-Quiles, N. Koch, C. Müller, L. Tsetseris, M. Heeney and T. D. Anthopoulos, Doping Approaches for Organic Semiconductors, *Chem Rev*, 2022, **122**, 4420–4492.

15 H. Wang, W. Wang and W. J. Jin, σ-Hole Bond vs π-Hole Bond: A Comparison Based on Halogen Bond, *Chem Rev*, 2016, **116**, 5072–5104.

16 G. L. Ong, T. S. Ong, S. L. Yap, D. J. Liaw, T. Y. Tou, S. S. Yap and C. H. Nee, A brief review of nanoparticles-doped PEDOT:PSS nanocomposite for OLED and OPV, *Nanotechnol Rev*, 2022, **11**, 1870–1889.

17 J. Y. Woo, M. H. Park, S. H. Jeong, Y. H. Kim, B. Kim, T. W. Lee and T. H. Han, Advances in Solution-Processed OLEDs and their Prospects for Use in Displays, *Advanced Materials*, 2023, **35**, 2207454.

18 Y. Zhou, K. Zhang, Z. Chen and H. Zhang, Molecular Design Concept for Enhancement Charge Carrier Mobility in OFETs: A Review, *Materials 2023, Vol. 16, Page 6645*, 2023, **16**, 6645.

19 C. R. Newman, C. D. Frisbie, D. A. Da Silva Filho, J. L. Brédas, P. C. Ewbank and K. R. Mann, Introduction to organic thin film transistors and design of n-channel organic semiconductors, *Chemistry of Materials*, 2004, **16**, 4436–4451.

20 S. Fratini, M. Nikolka, A. Salleo, G. Schweicher and H. Sirringhaus, Charge transport in high-mobility conjugated polymers and molecular semiconductors, *Nat Mater*, 2020, **19**, 491–502.

21 D. Schwarz, A. Acharjya, A. Ichangi, Y. S. Kochergin, P. Lyu, M. V. Opanasenko, J. Tarábek, J. Vacek Chocholoušová, J. Vacek, J. Schmidt, J. Čejka, P. Nachtigall, A.

Thomas and M. J. Bojdys, Tuning the Porosity and Photocatalytic Performance of Triazine-Based Graphdiyne Polymers through Polymorphism, *ChemSusChem*, 2019, **12**, 194–199.

22 R. Khatua, S. R. Sahoo, S. Sharma and S. Sahu, Anisotropic charge transport and optoelectronic properties of wide band gap organic semiconductors based on biphenyl derivatives: A computational study, *Synth Met*, 2020, **267**, 116474.

23 S. E. Root, S. Savagatrup, A. D. Printz, D. Rodriquez and D. J. Lipomi, Mechanical Properties of Organic Semiconductors for Stretchable, Highly Flexible, and Mechanically Robust Electronics, *Chem Rev*, 2017, **117**, 6467–6499.

24 L. Feriancová, M. Cigáň, J. Kožíšek, K. Gmucová, V. Nádaždy, T. Dubaj, M. Sobota, M. Novota, M. Weis and M. Putala, Dithienylnaphthalenes and quaterthiophenes substituted with electron-withdrawing groups as n-type organic semiconductors for organic field-effect transistors, *J Mater Chem C Mater*, 2022, **10**, 10058–10074.

25 Z. Chen, S. Duan, W. Hu, Z. Chen, S. Duan, W. Hu, S. Duan, W. Hu and X. Zhang, Novel solution-processed 2D organic semiconductor crystals for high-performance OFETs, *Mater Chem Front*, 2024, **8**, 2227–2272.

26 R. González-Núñez, M. J. Alonso-Navarro, F. Suárez-Blas, E. Gala, M. M. Ramos, J. L. Segura and R. Ponce Ortiz, Tuning the charge stabilization and transport in naphthalimide-based semiconductors via a fused-ring and core-engineering strategy, *Mater Chem Front*, 2024, **8**, 1981–1992.

27 R. González-Núñez, A. de la Peña, C. Valderrama-Callejón, J. L. Segura and R. Ponce Ortiz, Small asymmetric halogenated Phenylene–Naphthalimide molecules for organic field-effect transistors, *Dyes and Pigments*, 2025, **242**, 112984.

28 M. J. Alonso-Navarro, A. Harbuzaru, R. González-Núñez, M. M. Ramos, J. L. Segura and R. Ponce Ortiz, Tunable electroactive oligothiophene-naphthalimide semiconductors via end-capped engineering: cumulative effects beyond the linker, *J Mater Chem C Mater*, 2023, **11**, 10852–10863.

29 R. González-Núñez, G. Martinez, N. R. Avila-Rovelo, K. I. Hong, A. Ruiz-Carretero and R. Ponce Ortiz, The effect of hydrogen bond interactions on the electronic nature of DPP-based organic semiconductors: implications on charge transport, *J Mater Chem C Mater*, 2024, **12**, 18264–18273.

6

Appendices

Table of contents

CONTENTS

6.1 Acronyms and symbols

Acronyms	
D-A	Donor-Acceptor
DFT	Density Functional Theory
H-L_{gap}	Homo-LUMO gap
HOMO	Highest Occupied Molecular Orbital
ISC	Intersystem Crossing
LUMO	Lowest Unoccupied Molecular Orbital
NIR	Near Infrared
OFET	Organic Field-Effect Transistor
OLED	Organic Light-Emitting Diode
OTS	Octadecyltrichlorosilane
RT	Room Temperature
TD	Time Dependent
UV-Vis	Ultraviolet-Visible
DPP	Diketopyrrolopyrrole
TIPS	Triisopropylsilylethynyl
NDI	Naphthalenediimide
OLED	Organic Light-Emitting Diode
OPV	Organic Photovoltaic Cells
BC-BG	Bottom Contact – Bottom Gate
TC-BG	Top Contact – Bottom Gate
BC-TG	Bottom Contact – Top Gate
TC-TG	Top Contact – Top Gate
XRD	X-Ray Diffraction
ICT	Intramolecular Charge Transfer
FT	Fourier Transform
HMDS	Hexamethyldisiloxane
C8	Octyl
Ph	Phenylene
BTD	Benzothidiadiazole
TPA	Triphenylamine
AFM	Atomic Force Microscopy
CV	Cyclic Voltammetry
VB	Valence Band
CB	Conduction Band
K	Kelvin
DCM	Dichloromethane

Symbols

S_0	Ground electronic state
S_n	Electronic excited state "n"
$I_{on/off}$	Intensities on/off ratio
a.u.	Arbitrary units
μ_e	Electron field-effect mobility
μ_h	Hole field-effect mobility
I_o/I	Fluorescence intensity ratio
λ_{max}	Absorption maxima wavelength
I_{DS}	Drain-source current
σ	Electrical conductivity
W_F	Work function of an electrode
ϕB	Injection barrier
λ_h	Hole reorganization energy
λ_e	Electron reorganization energy
λ_{exc}	Excitation wavelength
ε	Dielectric constant
V_{GS}	Gate-source electric potential
V_{DS}	Drain-source electric potential
V_T	Threshold voltage
E_{onset}	Potential Onset
E_g^{opt}	Optical HOMO-LUMO gap
E_{pc}	Potential catodic peak
E_{pa}	Potential anodic peak

6.2 DFT calculations, experimental data and OFETs performance optimization

6.2.1 Chapter I

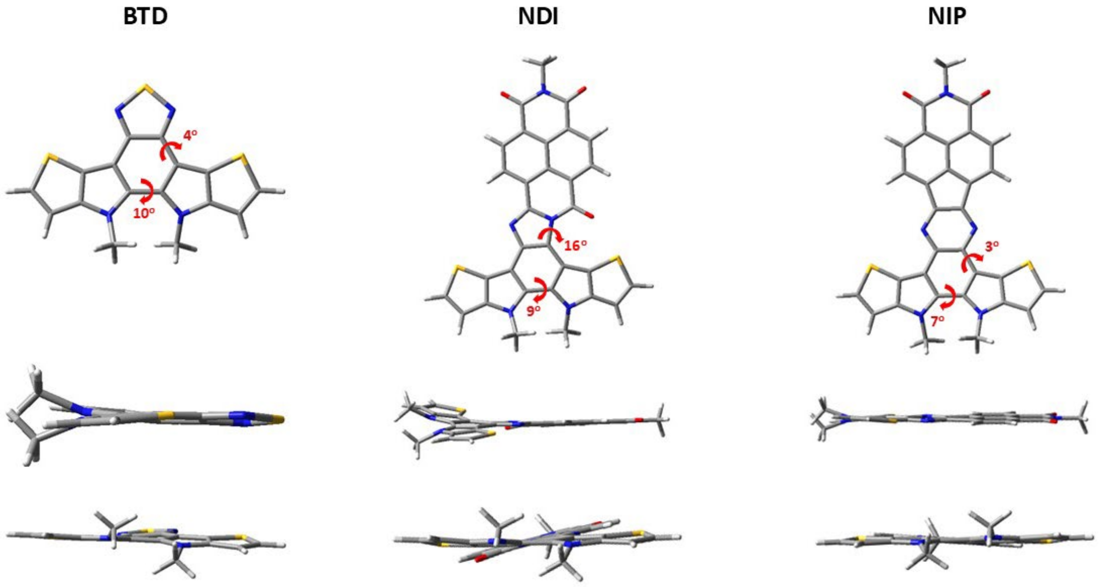

Figure 6.1. DFT-computed global minimum structure for **BTD**, **NDI** and **NIP** at B3LYP/6-31G** level of theory.

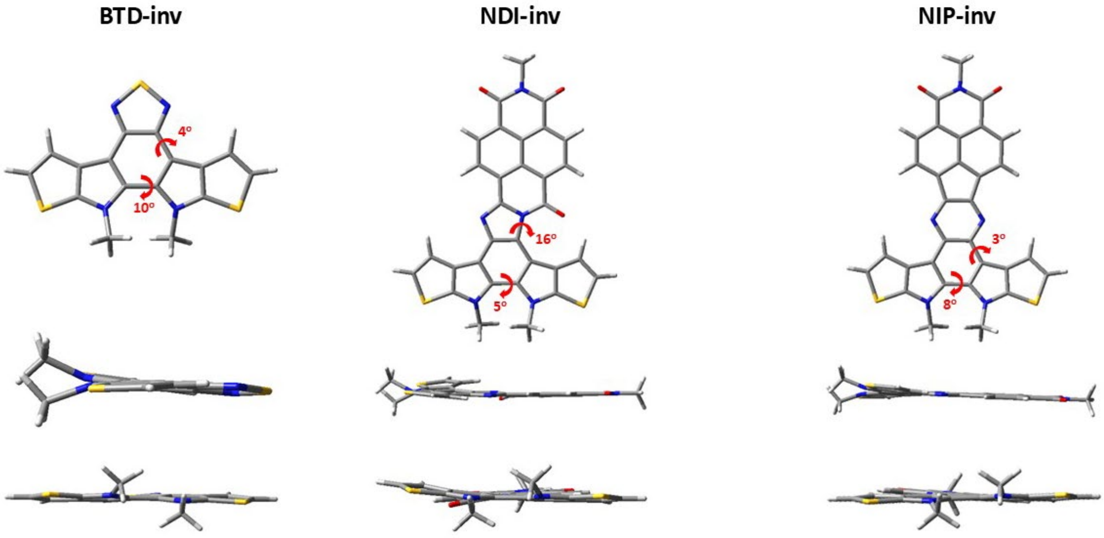

Figure 6.2. DFT-computed global minimum structure for **BTD-inv**, **NDI-inv** and **NIP-inv** at B3LYP/6-31G** level of theory.

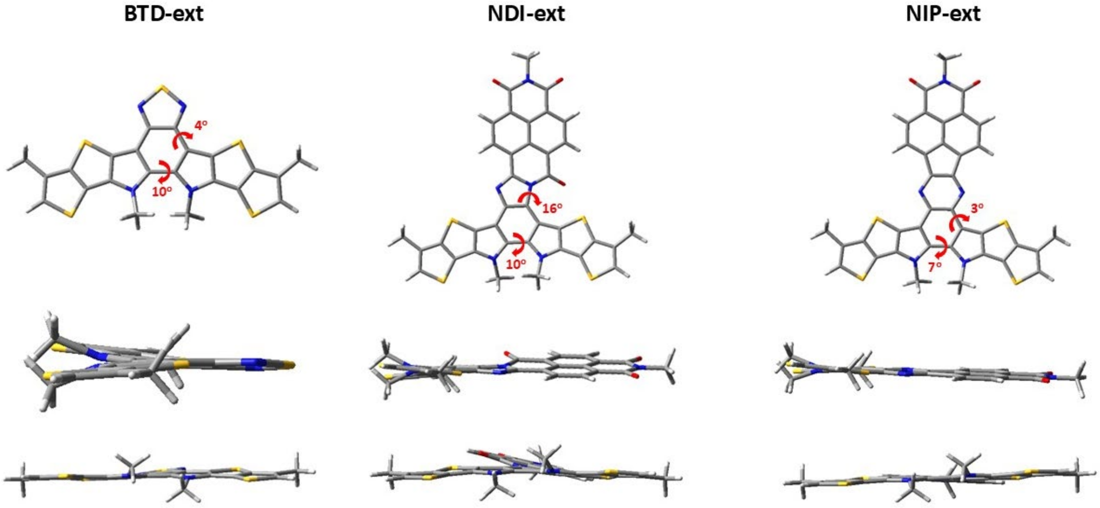

Figure 6.3. DFT-computed global minimum structure for **BTD-ext**, **NDI-ext** and **NIP-ext** at B3LYP/6-31G** level of theory.

Electronic transitions	Description	E_{max} (λ_{max})	*f*
$S_0 \rightarrow S_1$	H→L (97%)	2.8 eV (450 nm)	0.136
$S_0 \rightarrow S_2$	H-1→L (93%)	3.6 eV (343 nm)	0.200
$S_0 \rightarrow S_3$	H-2→L (58%) H→L (40%)	3.8 eV (324 nm)	0.117
$S_0 \rightarrow S_4$	H-2→L (41%) H→L+1 (56%)	4.0 eV (308 nm)	0.527
$S_0 \rightarrow S_{16}$	H-3→L+1 (30%) H→L+4 (20%) H→L+5 (37%)	5.3 eV (234 nm)	0.125
$S_0 \rightarrow S_{25}$	H-5→L+1 (13%) H-1→L+4 (27%) H-1→L+5 (38%) H→L+7 (15%)	5.8 eV (212 nm)	0.270

Table 6.1. Electronic transitions obtained by TD-DFT B3LYP/6-31G** level of theory for **BTD**.

Electronic transitions	Description	E_{max} (λ_{max})	*f*
$S_0 \rightarrow S_1$	H→L (91%)	1.5 eV (810 nm)	0.10
$S_0 \rightarrow S_2$	H-1→L (91%)	1.7 eV (733 nm)	0.14
$S_0 \rightarrow S_9$	H-5→L (59%) H-1→L+1 (31%)	3.5 eV (358 nm)	0.52
$S_0 \rightarrow S_{18}$	H-9→L (17%) H-1→L+2 (31%) H→L+4 (28%)	4.0 eV (312 nm)	0.19
$S_0 \rightarrow S_{19}$	H-1→L+3 (13%) H-1→L+4 (50%) H→L+4 (20%)	4.0 eV (312 nm)	0.18
$S_0 \rightarrow S_{20}$	H-9→L (38%) H-1→L+3 (19%) H-1→L+4 (25%)	4.0 eV (307 nm)	0.18
$S_0 \rightarrow S_{26}$	H-1→L+5 (87%)	4.7 eV (266 nm)	0.11

Table 6.2. Electronic transitions obtained by TD-DFT B3LYP/6-31G** level of theory for **NDI**.

Electronic transitions	**Description**	**E_{max} (λ_{max})**	***f***
$S_0 \rightarrow S_1$	H→L (98%)	2.0 eV (629 nm)	0.11
$S_0 \rightarrow S_6$	H-2→L (14%) H-1→L+1 (80%)	3.3 eV (381 nm)	0.83
$S_0 \rightarrow S_9$	H-3→L (94%)	3.4 eV (360 nm)	0.25
$S_0 \rightarrow S_{15}$	H-9→L (18%) H→L+2 (59%)	3.9 eV (316 nm)	0.29
$S_0 \rightarrow S_{16}$	H-9→L (24%) H-3→L+1 (41%) H→L+2 (20%)	4.0 eV (311 nm)	0.25
$S_0 \rightarrow S_{24}$	H-11→L (21%) H-6→L+1 (16%) H-1→L+3 (47%)	4.4 eV (279 nm)	0.16
$S_0 \rightarrow S_{25}$	H-12→L (17%) H-1→L+4 (73%)	4.5 eV (275 nm)	0.24

Table 6.3. Electronic transitions obtained by TD-DFT B3LYP/6-31G** level of theory for **NIP**.

Electronic transitions	**Description**	**E_{max} (λ_{max})**	***f***
$S_0 \rightarrow S_1$	H→L (99%)	2.8 eV (435 nm)	0.12
$S_0 \rightarrow S_2$	H-1→L (95%)	3.6 eV (347 nm)	0.17
$S_0 \rightarrow S_{10}$	H-1→L+1 (21%) H→L+3 (68%)	4.8 eV (259 nm)	0.10
$S_0 \rightarrow S_{14}$	H-5→L (65%) H-1→L+1 (26%)	5.1 eV (242 nm)	0.18
$S_0 \rightarrow S_{15}$	H-5→L (31%) H-1→L+1 (47%) H→L+3 (13%)	5.1 eV (242 nm)	0.56
$S_0 \rightarrow S_{21}$	H-8→L (40%) H-2→L+2 (52%)	5.5 eV (226 nm)	0.15
$S_0 \rightarrow S_{23}$	H-2→L+1 (56%) H→L+7 (26%)	5.5 eV (225 nm)	0.13

Table 6.4. Electronic transitions obtained by TD-DFT B3LYP/6-31G** level of theory for **BTD-inv**.

Electronic transitions	**Description**	**E_{max} (λ_{max})**	***f***
$S_0 \rightarrow S_1$	H-1→L (36%) H→L (64%)	1.6 eV (771 nm)	0.04
$S_0 \rightarrow S_2$	H-1→L (64%) H→L (36%)	1.7 eV (733 nm)	0.19
$S_0 \rightarrow S_8$	H-5→L (16%) H-1→L+1 (74%)	3.4 eV (365 nm)	0.16
$S_0 \rightarrow S_9$	H-5→L (67%) H-1→L+1 (18%)	3.5 eV (358 nm)	0.42
$S_0 \rightarrow S_{27}$	H-1→L+5 (56%) H→L+4 (12%)	4.7 eV (263 nm)	0.26

Table 6.5. Electronic transitions obtained by TD-DFT B3LYP/6-31G** level of theory for **NDI-inv**.

Electronic transitions	**Description**	**E_{max} (λ_{max})**	***f***
$S_0 \rightarrow S_1$	H→L (98%)	2.0 eV (606 nm)	0.10
$S_0 \rightarrow S_6$	H-2→L (11%) H-1→L+1 (85%)	3.2 eV (387 nm)	0.82
$S_0 \rightarrow S_9$	H-3→L (94%)	3.5 eV (357 nm)	0.18
$S_0 \rightarrow S_{19}$	H-11→L (13%) H-4→L+1 (51%) H→L+3 (22%)	4.2 eV (292 nm)	0.36
$S_0 \rightarrow S_{23}$	H-11→L (66%) H-6→L+1 (22%)	4.5 eV (276 nm)	0.26
$S_0 \rightarrow S_{27}$	H-1→L+3 (16%) H→L+4 (42%) H→L+5 (30%)	4.7 eV (266 nm)	0.25
$S_0 \rightarrow S_{29}$	H→L+4 (19%) H→L+5 (52%)	4.7 eV (263 nm)	0.12

Table 6.6. Electronic transitions obtained by TD-DFT B3LYP/6-31G** level of theory for **NIP-inv**.

Electronic transitions	**Description**	**E_{max} (λ_{max})**	***f***
$S_0 \rightarrow S_1$	H→L (97%)	2.6 eV (484 nm)	0.26
$S_0 \rightarrow S_2$	H-1→L (86%)	3.5 eV (358 nm)	0.16
$S_0 \rightarrow S_3$	H-2→L (10%) H→L+1 (83%)	3.5 eV (358 nm)	0.64
$S_0 \rightarrow S_4$	H-2→L (89%) H→L+1 (10%)	3.6 eV (341 nm)	0.21
$S_0 \rightarrow S_6$	H-3→L (14%) H→L+2 (80%)	4.0 eV (310 nm)	0.12
$S_0 \rightarrow S_{13}$	H-3→L+1 (91%)	4.7 eV (266 nm)	0.14

Table 6.7. Electronic transitions obtained by TD-DFT B3LYP/6-31G** level of theory for **BTD-ext**.

Electronic transitions	**Description**	**E_{max} (λ_{max})**	***f***
$S_0 \rightarrow S_1$	H→L (97%)	1.3 eV (920 nm)	0.10
$S_0 \rightarrow S_2$	H-1→L (91%)	1.7 eV (741 nm)	0.14
$S_0 \rightarrow S_6$	H→L+1 (96%)	3.0 eV (413 nm)	0.18
$S_0 \rightarrow S_9$	H-5→L (21%) H-1→L+1 (57%) H→L+3 (11%)	3.4 eV (369 nm)	0.47
$S_0 \rightarrow S_{10}$	H-1→L+1 (10%) H→L+2 (80%)	3.4 eV (362 nm)	0.52
$S_0 \rightarrow S_{11}$	H-6→L (55%) H→L+3 (30%)	3.5 eV (359 nm)	0.15
$S_0 \rightarrow S_{12}$	H-6→L (35%) H→L+3 (46%)	3.5 eV (356 nm)	0.20
$S_0 \rightarrow S_{23}$	H-11→L (41%) H-1→L+4 (33%) H→L+5 (10%)	4.0 eV (309 nm)	0.14

Table 6.8. Electronic transitions obtained by TD-DFT B3LYP/6-31G** level of theory for **NDI-ext**.

Electronic transitions	Description	E_{max} (λ_{max})	f
$S_0 \rightarrow S_1$	H→L (99%)	1.8 eV (698 nm)	0.12
$S_0 \rightarrow S_3$	H→L+1 (92%)	2.4 eV (507 nm)	0.12
$S_0 \rightarrow S_9$	H-1→L+1 (88%)	3.3 eV (371 nm)	0.53
$S_0 \rightarrow S_{10}$	H-5→L (92%)	3.3 eV (369 nm)	0.50
$S_0 \rightarrow S_{11}$	H-2→L+1 (23%) H→L+2 (75%)	3.4 eV (361 nm)	0.55
$S_0 \rightarrow S_{12}$	H-2→L+1 (75%) H→L+2 (22%)	3.5 eV (352 nm)	0.35
$S_0 \rightarrow S_{16}$	H-1→L+2 (13%) H→L+3 (77%)	3.8 eV (330 nm)	0.14
$S_0 \rightarrow S_{21}$	H-8→L (10%) H-4→L+1 (70%)	4.0 eV (314 nm)	0.25
$S_0 \rightarrow S_{27}$	H-1→L+3 (87%)	4.3 eV (286 nm)	0.20

Table 6.9. Electronic transitions obtained by TD-DFT B3LYP/6-31G** level of theory for **NIP-ext**.

Compound	Subst. Treatment	μ_h (cm^2 V^{-1} s^{-1})	V_T(V)	I_{ON}/I_{OFF}
NDI-ext	HMDS,(RT)	$3x10^{-6}$ ($2x10^{-6}$)	2	4
NDI-ext	HMDS,(RT,150ºC)	NA	NA	NA
NDI-ext	HMDS,(80ºC)	$2x10^{-6}$ ($1x10^{-6}$)	35	2
NDI-ext	HMDS,(80ºC,150ºC)	NA	NA	NA

Table 6.10. OFET electrical data for deposited films of **NDI-ext**. Both best and average (in parenthesis) mobility values are shown.

Compound	Subst. Treatment	μ_h (cm^2 V^{-1} s^{-1})	V$_T$(V)	I$_{ON}$/I$_{OFF}$
NDI	OTS,(RT)	2x10^{-4} (2x10^{-4})	-41	8x10^{+4}
NDI	OTS,(RT,150ºC)	NA	NA	NA
NDI	OTS,(80ºC)	2x10^{-4} (1x10^{-4})	-40	2x10^{+2}
NDI	OTS,(80ºC,150ºC)	2x10^{-4} (2x10^{-4})	-3	4x10^{+1}
NDI	HMDS,(RT)	1x10^{-4} (9x10^{-5})	-42	1x10^{+2}
NDI	HMDS,(RT,150ºC)	2x10^{-5} (1x10^{-5})	-27	4x10^{+3}
NDI	HMDS,(80ºC)	8x10^{-5} (7x10^{-5})	-48	2x10^{+2}
NDI	HMDS,(80ºC,150ºC)	8x10^{-5} (5x10^{-5})	-10	2x10^{+5}

Table 6.11. OFET electrical data for deposited films of **NDI**. Both best and average (in parenthesis) mobility values are shown.

Compound	Subst. Treatment	μ_h (cm^2 V^{-1} s^{-1})	V$_T$(V)	I$_{ON}$/I$_{OFF}$
NIP-ext	HMDS,(RT)	4x10^{-6} (4x10^{-6})	12	12
NIP-ext	HMDS,(RT,150ºC)	NA	NA	NA
NIP-ext	HMDS,(80ºC)	2x10^{-6} (3x10^{-6})	43	2
NIP-ext	HMDS,(80ºC,150ºC)	NA	NA	NA

Table 6.12. OFET electrical data for deposited films of **NIP-ext.** Both best and average (in parenthesis) mobility values are shown.

Compound	Subst. Treatment	μ_h (cm^2 V^{-1} s^{-1})	V_T(V)	I_{ON}/I_{OFF}
NIP	OTS,(RT)	$2x10^{-3}$ $(1x10^{-3})$	-32	$6x10^{+5}$
NIP	OTS,(RT,150ºC)	NA	NA	NA
NIP	OTS,(80ºC)	NA	NA	NA
NIP	OTS,(80ºC,150ºC)	$1x10^{-2}$ $(1x10^{-2})$	-19	$3x10^{+4}$
NIP	HMDS,(RT)	NA	NA	NA
NIP	HMDS,(RT,150ºC)	$9x10^{-4}$ $(9x10^{-4})$	-21	$4x10^{+5}$
NIP	HMDS,(80ºC)	$1x10^{-4}$ $(1x10^{-4})$	-49	$2x10^{+2}$
NIP	HMDS,(80ºC,150ºC)	$2x10^{-3}$ $(2x10^{-3})$	-24	$4x10^{+4}$

Table 6.13. OFET electrical data for deposited films of **NIP.** Both best and average (in parenthesis) mobility values are shown.

6.2.2 Chapter II

Compound	**Subst. Treatment**	μ_e (cm^2 V^{-1} s^{-1})	V_T(V)	I_{ON}/I_{OFF}
NAI-Ph	OTS,(80ºC,120ºC)	2x10^{-2} (1x10^{-2})	66	1x10^{+3}
NAI-Ph	OTS,(110ºC,120ºC)	NA	NA	NA
NAI-Ph	OTS,(110ºC,150ºC)	NA	NA	NA
NAI-Ph	OTS,(110ºC,180ºC)	NA	NA	NA
NAI-Ph	OTS,(110ºC,200ºC)	NA	NA	NA
NAI-Ph	OTS,(RT,120ºC)	1x10^{-2} (3x10^{-3})	87	3x10^{+2}
NAI-Ph	OTS,(RT,150ºC)	NA	NA	NA
NAI-Ph	OTS,(RT,180ºC)	NA	NA	NA
NAI-Ph	OTS,(RT,200ºC)	NA	NA	NA
NAI-Ph	HMDS,(80ºC,120ºC)	5x10^{-4} (3x10^{-4})	60	1x10^{+3}
NAI-Ph	HMDS,(110ºC,120ºC)	5x10^{-3} (2x10^{-3})	95	2x10^{+5}
NAI-Ph	HMDS,(110ºC,150ºC)	4x10^{-3} (2x10^{-3})	98	1x10^{+4}
NAI-Ph	HMDS,(110ºC,180ºC)	5x10^{-3} (4x10^{-3})	87	1x10^{+4}
NAI-Ph	HMDS,(110ºC,200ºC)	NA	NA	NA
NAI-Ph	HMDS,(RT,120ºC)	1x10^{-3} (6x10^{-4})	52	2x10^{+2}
NAI-Ph	HMDS,(RT,150ºC)	7x10^{-4} (4x10^{-4})	91	2x10^{+5}
NAI-Ph	HMDS,(RT,180ºC)	2x10^{-3} (1x10^{-3})	82	2x10^{+5}
NAI-Ph	HMDS,(RT,200ºC)	NA	NA	NA

Table 6.14. n-channel OFET derived electrical data for **NAI-Ph**. Both best and average (in parenthesis) mobility values are shown.

Compound	Subst. Treatment	μ_h (cm^2 V^{-1} s^{-1})	V$_T$(V)	I$_{ON}$/I$_{OFF}$
NAI-Ph	OTS,(80ºC,120ºC)	3x10^{-3} (3x10^{-3})	-60	1x10^{+4}
NAI-Ph	OTS,(110ºC,120ºC)	4x10^{-4} (2x10^{-4})	-54	6x10^{+4}
NAI-Ph	OTS,(110ºC,150ºC)	2x10^{-3} (7x10^{-4})	-53	1x10^{+4}
NAI-Ph	OTS,(110ºC,180ºC)	8x10^{-3} (2x10^{-3})	-66	6x10^{+2}
NAI-Ph	OTS,(110ºC,200ºC)	2x10^{-3} (1x10^{-3})	-56	5x10^{+2}
NAI-Ph	OTS,(RT,120ºC)	3x10^{-3} (2x10^{-3})	-48	2x10^{+2}
NAI-Ph	OTS,(RT,150ºC)	6x10^{-4} (5x10^{-4})	-59	2x10^{+3}
NAI-Ph	OTS,(RT,180ºC)	1x10^{-3} (7x10^{-4})	-61	5x10^{+2}
NAI-Ph	OTS,(RT,200ºC)	1x10^{-3} (4x10^{-4})	-46	6x10^{+2}
NAI-Ph	HMDS,(80ºC,120ºC)	4x10^{-3} (1x10^{-3})	-72	3x10^{+4}
NAI-Ph	HMDS,(110ºC,120ºC)	3x10^{-4} (2x10^{-4})	-67	1x10^{+5}
NAI-Ph	HMDS,(110ºC,150ºC)	2x10^{-3} (6x10^{-4})	-70	5x10^{+3}
NAI-Ph	HMDS,(110ºC,180ºC)	9x10^{-3} (5x10^{-3})	-57	2x10^{+3}
NAI-Ph	HMDS,(110ºC,200ºC)	6x10^{-3} (3x10^{-3})	-48	4x10^{+3}
NAI-Ph	HMDS,(RT,120ºC)	6x10^{-4} (3x10^{-4})	-43	5x10^{+4}
NAI-Ph	HMDS,(RT,150ºC)	1x10^{-3} (6x10^{-4})	-66	3x10^{+3}
NAI-Ph	HMDS,(RT,180ºC)	3x10^{-3} (1x10^{-3})	-61	7x10^{+2}
NAI-Ph	HMDS,(RT,200ºC)	3x10^{-6} (2x10^{-6})	-34	5x10^{+0}

Table 6.15. p-channel OFET derived electrical data for **NAI-Ph**. Both best and average (in parenthesis) mobility values are shown.

Compound	**Subst. Treatment**	**μ_e (cm^2 V^{-1} s^{-1})**	**V_T(V)**	**I_{ON}/I_{OFF}**
NAI-Ph-F	OTS,(80ºC,120ºC)	$1x10^{-1}$ ($9x10^{-2}$)	48	$2x10^{+4}$
NAI-Ph-F	OTS,(110ºC,120ºC)	$9x10^{-2}$ ($9x10^{-2}$)	63	$2x10^{+5}$
NAI-Ph-F	OTS,(110ºC,150ºC)	$7x10^{-2}$ ($6x10^{-2}$)	62	$2x10^{+5}$
NAI-Ph-F	OTS,(110ºC,180ºC)	$3x10^{-2}$ ($2x10^{-2}$)	65	$1x10^{+6}$
NAI-Ph-F	OTS,(110ºC,200ºC)	$1x10^{-2}$ ($9x10^{-3}$)	90	$1x10^{+5}$
NAI-Ph-F	OTS,(RT,120ºC)	$7x10^{-2}$ ($5x10^{-2}$)	57	$2x10^{+4}$
NAI-Ph-F	OTS,(RT,150ºC)	$6x10^{-2}$ ($4x10^{-2}$)	75	$1x10^{+5}$
NAI-Ph-F	OTS,(RT,180ºC)	$5x10^{-2}$ ($4x10^{-2}$)	62	$5x10^{+4}$
NAI-Ph-F	OTS,(RT,200ºC)	NA	NA	NA
NAI-Ph-F	HMDS,(80ºC,120ºC)	$2x10^{-2}$ ($2x10^{-2}$)	29	$3x10^{+4}$
NAI-Ph-F	HMDS,(110ºC,120ºC)	$9x10^{-2}$ ($7x10^{-2}$)	37	$5x10^{+5}$
NAI-Ph-F	HMDS,(110ºC,150ºC)	$3x10^{-2}$ ($1x10^{-2}$)	35	$1x10^{+5}$
NAI-Ph-F	HMDS,(110ºC,180ºC)	$3x10^{-2}$ ($2x10^{-2}$)	46	$3x10^{+3}$
NAI-Ph-F	HMDS,(110ºC,200ºC)	$1x10^{-2}$ ($6x10^{-3}$)	46	$2x10^{+4}$
NAI-Ph-F	HMDS,(RT,120ºC)	$4x10^{-2}$ ($3x10^{-2}$)	56	$1x10^{+5}$
NAI-Ph-F	HMDS,(RT,150ºC)	$3x10^{-2}$ ($3x10^{-2}$)	54	$2x10^{+4}$
NAI-Ph-F	HMDS,(RT,180ºC)	$3x10^{-2}$ ($3x10^{-2}$)	40	$1x10^{+5}$
NAI-Ph-F	HMDS,(RT,200ºC)	$1x10^{-2}$ ($9x10^{-3}$)	61	$1x10^{+4}$

Table 6.16. n-channel OFET derived electrical data for **NAI-Ph-F**. Both best and average (in parenthesis) mobility values are shown.

Compound	Subst. Treatment	μ_e (cm^2 V^{-1} s^{-1})	V_T(V)	I_{ON}/I_{OFF}
NAI-Ph-Cl	OTS,(80ºC,120ºC)	8x10^{-2} (3x10^{-2})	39	2x10^{+4}
NAI-Ph-Cl	OTS,(110ºC,120ºC)	1x10^{-1} (9x10^{-2})	56	7x10^{+6}
NAI-Ph-Cl	OTS,(110ºC,150ºC)	1x10^{-1} (1x10^{-1})	68	2x10^{+6}
NAI-Ph-Cl	OTS,(110ºC,180ºC)	1x10^{-1} (1x10^{-1})	58	2x10^{+6}
NAI-Ph-Cl	OTS,(110ºC,200ºC)	4x10^{-2} (3x10^{-2})	56	4x10^{+6}
NAI-Ph-Cl	OTS,(RT,120ºC)	7x10^{-2} (6x10^{-2})	61	3x10^{+5}
NAI-Ph-Cl	OTS,(RT,150ºC)	5x10^{-2} (4x10^{-2})	60	4x10^{+5}
NAI-Ph-Cl	OTS,(RT,180ºC)	4x10^{-2} (3x10^{-2})	48	4x10^{+6}
NAI-Ph-Cl	OTS,(RT,200ºC)	2x10^{-2} (2x10^{-2})	62	2x10^{+4}
NAI-Ph-Cl	HMDS,(80ºC,120ºC)	5x10^{-2} (3x10^{-2})	44	7x10^{+4}
NAI-Ph-Cl	HMDS,(110ºC,120ºC)	2x10^{-1} (7x10^{-2})	57	4x10^{+5}
NAI-Ph-Cl	HMDS,(110ºC,150ºC)	6x10^{-2} (6x10^{-2})	53	5x10^{+5}
NAI-Ph-Cl	HMDS,(110ºC,180ºC)	8x10^{-2} (7x10^{-2})	54	4x10^{+4}
NAI-Ph-Cl	HMDS,(110ºC,200ºC)	3x10^{-2} (3x10^{-2})	42	1x10^{+6}
NAI-Ph-Cl	HMDS,(RT,120ºC)	5x10^{-2} (4x10^{-2})	43	3x10^{+5}
NAI-Ph-Cl	HMDS,(RT,150ºC)	2x10^{-2} (2x10^{-2})	30	5x10^{+6}
NAI-Ph-Cl	HMDS,(RT,180ºC)	4x10^{-2} (4x10^{-2})	40	1x10^{+5}
NAI-Ph-Cl	HMDS,(RT,200ºC)	4x10^{-2} (4x10^{-2})	50	5x10^{+4}

Table 6.17. n-channel OFET derived electrical data for **NAI-Ph-Cl**. Both best and average (in parenthesis) mobility values are shown.

6.2.3 Chapter III

Electronic transitions	**Description**	**E_{max} (λ_{max})**	***f***
$S_0 \rightarrow S_1$	$H \rightarrow L$ (99%)	1.68 eV (736 nm)	0.22
$S_0 \rightarrow S_2$	$H\text{-}1 \rightarrow L$ (96%)	2.65 eV (468 nm)	0.18
$S_0 \rightarrow S_4$	$H \rightarrow L+1$ (91%)	2.96 eV (419 nm)	0.23
$S_0 \rightarrow S_{11}$	$H\text{-}5 \rightarrow L+1$ (17%) $H \rightarrow L+2$ (59%)	3.64 eV (340 nm)	0.24

Table 6.18. Electronic transitions obtained by TD-DFT B3LYP/6-31G** level of theory for **NDI3T**.

Electronic transitions	**Description**	**E_{max} (λ_{max})**	***f***
$S_0 \rightarrow S_1$	$H \rightarrow L$ (99%)	1.59 eV (781 nm)	0.31
$S_0 \rightarrow S_3$	$H \rightarrow L+1$ (95%)	2.25 eV (551 nm)	1.62
$S_0 \rightarrow S_{10}$	$H\text{-}5 \rightarrow L$ (73%)	2.86 eV (434 nm)	0.29

Table 6.19. Electronic transitions obtained by TD-DFT B3LYP/6-31G** level of theory for **NDI3T-RD**.

Electronic transitions	**Description**	**E_{max} (λ_{max})**	***F***
$S_0 \rightarrow S_1$	$H \rightarrow L$ (97%)	1.81 eV (686 nm)	0.31
$S_0 \rightarrow S_2$	$H \rightarrow L+1$ (96%)	2.38 eV (522 nm)	1.16
$S_0 \rightarrow S_5$	$H\text{-}2 \rightarrow L$ (62%) $H\text{-}1 \rightarrow L+1$ (18%)	2.92 eV (424 nm)	0.29

Table 6.20. Electronic transitions obtained by TD-DFT B3LYP/6-31G** level of theory for **NDI3T-DCV**.

Electronic transitions	Description	E_{max} (λ_{max})	*F*
$S_0 \rightarrow S_1$	H→L (99%)	1.66 eV (746 nm)	0.38
$S_0 \rightarrow S_2$	H→L+1 (83%) H-1→L (16%)	2.21 eV (561 nm)	1.19
$S_0 \rightarrow S_3$	H-1→L (82%) H→L+1 (15%)	2.24 eV (554 nm)	0.56
$S_0 \rightarrow S_6$	H-3→L (60%) H-1→L+1 (27%)	2.83 eV (438 nm)	0.46

Table 6.21. Electronic transitions obtained by TD-DFT B3LYP/6-31G** level of theory for **NDI3T-RDDCV**.

Electronic transitions	Description	E_{max} (λ_{max})	*F*
$S_0 \rightarrow S_1$	H→L (98%)	1.89 eV (657 nm)	0.23
$S_0 \rightarrow S_2$	H→L+1 (98%)	1.96 eV (632 nm)	0.14
$S_0 \rightarrow S_6$	H-1→L+1 (92%)	3.30 eV (376 nm)	0.24
$S_0 \rightarrow S_{10}$	H-2→L (90%)	3.41 eV (363 nm)	0.31
$S_0 \rightarrow S_{11}$	H-1→L (17%) H-1→L+2 (48%)	3.48 eV (357 nm)	0.38
$S_0 \rightarrow S_{18}$	H-5→L+1 (53%) H-3→L+1 (37%)	3.79 eV (327 nm)	0.64

Table 6.22. Electronic transitions obtained by TD-DFT B3LYP/6-31G** level of theory for **NIP3T**.

Electronic transitions	**Description**	**E_{max} (λ_{max})**	***F***
$S_0 \rightarrow S_1$	H→L (98%)	1.71 eV (725 nm)	1.04
$S_0 \rightarrow S_2$	H→L+1 (98%)	1.82 eV (681 nm)	0.24
$S_0 \rightarrow S_6$	H-1→L+2 (89%)	2.44 eV (508 nm)	0.68
$S_0 \rightarrow S_7$	H-1→L+1 (93%)	2.59 eV (479 nm)	0.33
$S_0 \rightarrow S_8$	H-1→L (20%) H→L+3 (72%)	2.70 eV (458 nm)	0.33
$S_0 \rightarrow S_{21}$	H-1→L+3 (59%) H→L+4 (36%)	3.35 eV (370 nm)	0.28

Table 6.23. Electronic transitions obtained by TD-DFT B3LYP/6-31G** level of theory for **NIP3T-RD**.

Electronic transitions	**Description**	**E_{max} (λ_{max})**	***F***
$S_0 \rightarrow S_1$	H→L (98%)	1.86 eV (665 nm)	0.85
$S_0 \rightarrow S_2$	H→L+1 (98%)	2.03 eV (610 nm)	0.19
$S_0 \rightarrow S_4$	H-1→L+2 (90%)	2.63 eV (472 nm)	0.58
$S_0 \rightarrow S_6$	H-1→L+2 (32%) H→L+3 (51%)	2.98 eV (416 nm)	0.50
$S_0 \rightarrow S_8$	H-1→L +1(89%)	3.03 eV (410 nm)	0.21
$S_0 \rightarrow S_{13}$	H-3→L (22%) H-2→L+1 (45%)	3.41 eV (364 nm)	0.19

Table 6.24. Electronic transitions obtained by TD-DFT B3LYP/6-31G** level of theory for **NIP3T-DCV**.

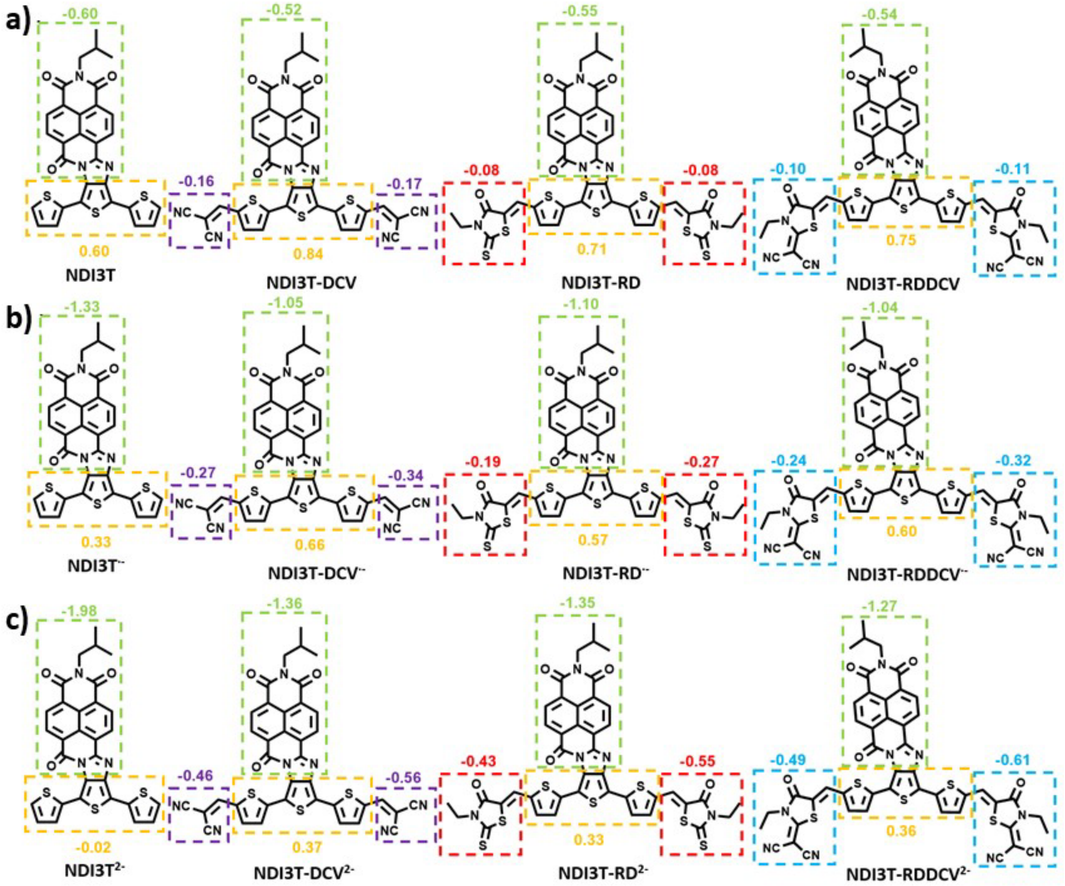

Figure 6.4. B3LYP/6-31G** charge distributions for **NDI3T**, **NIP3T-DCV**, **NIP3T-Rd** and **NIP3T-RDDCV** as a) neutral b) anion and c) dianion.

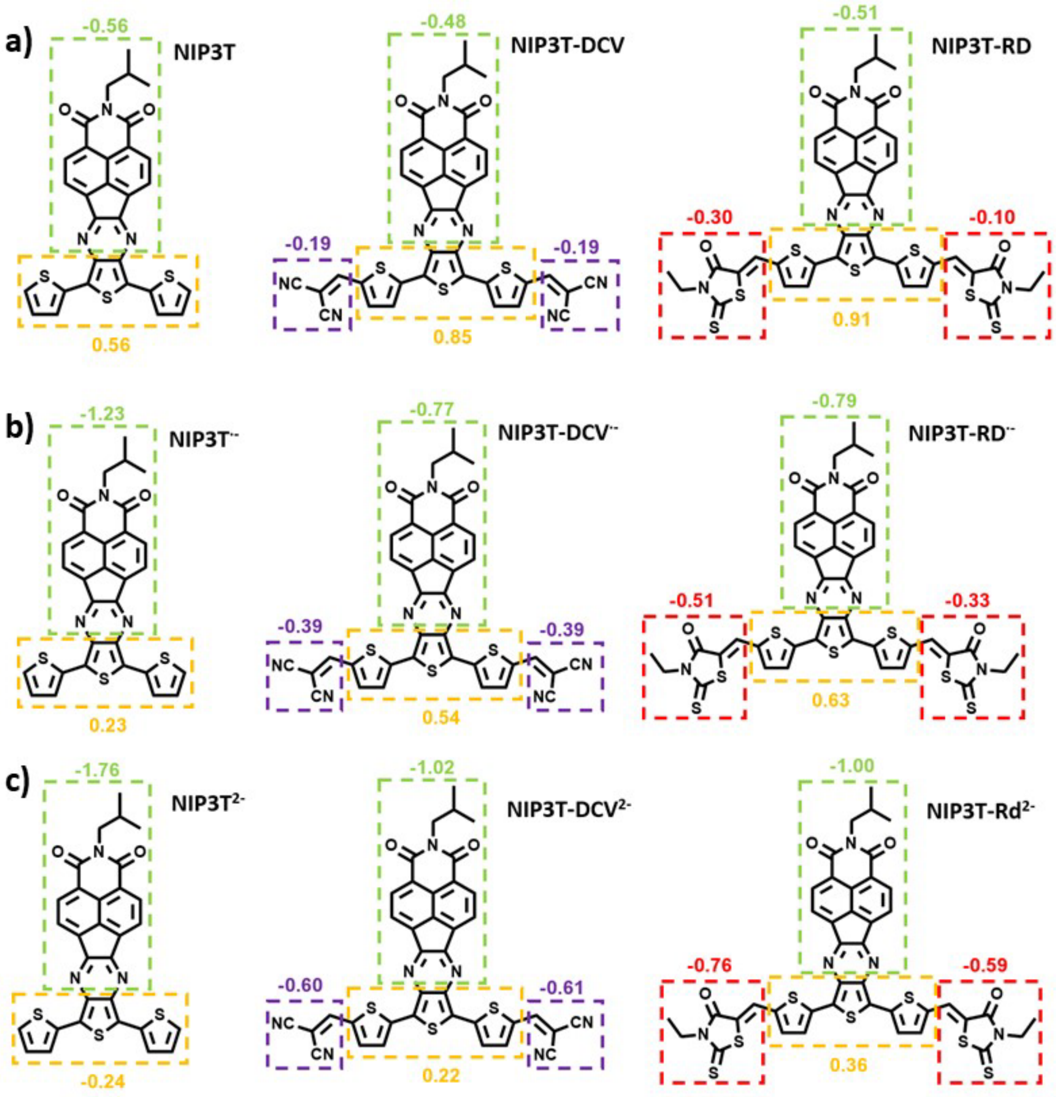

Figure 6.5. B3LYP/6-31G** charge distributions for **NIP3T**, **NIP3T-DCV** and **NIP3T-Rd** as a) neutral b) anion and c) dianion.

6.2.4 Chapter IV

Compound	Subst. Treatment	μ_h (cm^2 V^{-1} s^{-1})	V_T(V)	I_{ON}/I_{OFF}
DPP2C	OTS,(RT)	8x10^{-6} (5x10^{-6})	7	7x10^{+0}
DPP2C	OTS,(RT,120ºC)	4x10^{-5} (3x10^{-5})	-10	4x10^{+1}
DPP2C	HMDS,(RT)	6x10^{-6} (5x10^{-6})	30	5x10^{+0}
DPP2C	HMDS,(RT,120ºC)	2x10^{-5} (2x10^{-5})	-10	1x10^{+1}
DPP2C	ST,(RT)	NA	NA	NA
DPP2C	ST,(RT, 120ºC)	NA	NA	NA

Table 6.25. n-channel OFET derived electrical data for **DPP2C**. Both best and average (in parenthesis) mobility values are shown.

Compound	Subst. Treatment	μ_h (cm^2 V^{-1} s^{-1})	V_T(V)	I_{ON}/I_{OFF}
DPP4C	OTS,(RT)	3x10^{-3} (2x10^{-3})	4	1x10^{+4}
DPP4C	OTS,(RT,120ºC)	5x10^{-3} (3x10^{-3})	-15	3x10^{+3}
DPP4C	HMDS,(RT)	6x10^{-3} (4x10^{-3})	-28	2x10^{+5}
DPP4C	HMDS,(RT,120ºC)	6x10^{-3} (6x10^{-3})	-5	1x10^{+4}
DPP4C	ST,(RT)	2x10^{-4} (1x10^{-4})	-22	4x10^{+2}
DPP4C	ST,(RT, 120ºC)	7x10^{-4} (5x10^{-4})	-22	1x10^{+3}

Table 6.26. n-channel OFET derived electrical data for **DPP4C**. Both best and average (in parenthesis) mobility values are shown.

Compound	Subst. Treatment	μ_h (cm^2 V^{-1} s^{-1})	V_T(V)	I_{ON}/I_{OFF}
DPP6C	OTS,(RT)	NA	NA	NA
DPP6C	OTS,(RT,120ºC)	$2x10^{-2}$ ($2x10^{-2}$)	-12	$2x10^{+4}$
DPP6C	HMDS,(RT)	$6x10^{-3}$ ($5x10^{-3}$)	-11	$1x10^{+4}$
DPP6C	HMDS,(RT,120ºC)	$5x10^{-3}$ ($5x10^{-3}$)	-18	$5x10^{+3}$
DPP6C	ST,(RT)	$1x10^{-5}$ ($1x10^{-5}$)	-9	$2x10^{+1}$
DPP6C	ST,(RT, 120ºC)	$1x10^{-4}$ ($1x10^{-4}$)	-17	$1x10^{+2}$

Table 6.27. n-channel OFET derived electrical data for **DPP6C**. Both best and average (in parenthesis) mobility values are shown.

6.3 List of publications

The research work developed during my PhD has resulted in six publications, four of them directly linked to this Thesis and two additional papers related to parallel investigations.

- Publications directly linked to the present Thesis:

  1. **R. González-Núñez**, M. J. Alonso-Navarro, F. Suárez-Blas, E. Gala, M. M. Ramos, J. L. Segura and R. Ponce Ortiz, Tuning the charge stabilization and transport in naphthalimide-based semiconductors via a fused-ring and core-engineering strategy, *Volume 8, Issue 8, Pages 1981 - 1992*, 2024, **8**, 1981–1992. **doi.org/10.1039/D4QM00029C**

  2. **R. González-Núñez**, A. de la Peña, C. Valderrama-Callejón, J. L. Segura and R. Ponce Ortiz, Small asymmetric halogenated Phenylene–Naphthalimide molecules for organic field-effect transistors, *Dyes and Pigments*, 2025, **242**, 112984. **doi.org/10.1016/j.dyepig.2025.112984**

  3. M. J. Alonso-Navarro, A. Harbuzaru, **R. González-Núñez**, M. M. Ramos, J. L. Segura and R. Ponce Ortiz, Tunable electroactive oligothiophene-naphthalimide semiconductors via end-capped engineering: cumulative effects beyond the linker, *J Mater Chem C*, 2023, **11**, 10852–10863. **doi.org/10.1039/D3TC02099A**

  4. **R. González-Núñez**, G. Martinez, N. R. Avila-Rovelo, K. I. Hong, A. Ruiz-Carretero and R. Ponce Ortiz, The effect of hydrogen bond interactions on the electronic nature of DPP-based organic semiconductors: implications on charge transport, *J Mater Chem C*, 2024, **12**, 18264–18273. **doi.org/10.1039/D4TC02496F**

MATERIALS CHEMISTRY
FRONTIERS

CCS 中国化学会 CHINESE CHEMICAL SOCIETY
ICCAS
ROYAL SOCIETY OF CHEMISTRY

RESEARCH ARTICLE

View Article Online
View Journal

Cite this: DOI: 10.1039/d4qm00029c

Tuning the charge stabilization and transport in naphthalimide-based semiconductors *via* a fused-ring and core-engineering strategy†

Raúl González-Núñez,‡[a] Matías J. Alonso-Navarro, ‡[bc] Fátima Suárez-Blas,‡[bc] Elena Gala, [bc] M. Mar Ramos,[c] José L. Segura *[b] and Rocío Ponce Ortiz *[a]

Received 9th January 2024,
Accepted 6th March 2024

DOI: 10.1039/d4qm00029c

rsc.li/frontiers-materials

The synthesis and characterization of a family of rationally designed compounds based on naphthalimide units attached, through conjugated nitrogenated linkers (*i.e.* pyrazine and imidazoline units), to fused thiophene-based moieties is shown. This combination of different donor–acceptor moieties allows fine tuning of the HOMO and LUMO energy levels, and thus the modulation of their electronic properties. A comprehensive physical chemistry study is carried out, in which the nature of the neutral and charged species are analyzed and their electrical performance is understood in terms of molecular and supramolecular characteristics.

Introduction

The tunable electronic and structural properties of organic semiconductors together with their flexibility, low molecular weight, high solution processability and low cost in comparison with inorganic semiconductors are some of the key points for the current interest in the development of π-conjugated small molecules and polymers for a wide variety of applications. Among them, their use as active materials stands out in organic light-emitting diodes (OLEDs),[1,2] organic phototransistors (OPTs),[3–5] organic solar cells (OSCs),[6–9] organic field-effect transistors (OFETs)[10–13] and, more recently, in wearable electronics[14,15] or memory arrays.[16,17] However, despite the significant advances in organic electronics over the last few decades, the performances of the organic devices are often below that exhibited by the inorganic counterparts, mainly attributed to lower charge carrier mobilities.[18] For this reason, it is mandatory to design and synthesize novel organic semiconductors with enhanced processability and tunable properties to overcome current limitations.[19,20]

In this regard, different molecular building blocks have been used for the synthesis of π functional materials with tunable properties and high performances in organic electronic devices.[7,21–23] The design and synthesis of ambipolar materials are receiving a great deal of attention with the aim of obtaining materials with good charge transport abilities and tunable HOMO/LUMO energy levels.[24,25] On the one hand, imide units, and more specifically naphthalimide derivatives, are often used as strong electron-acceptor moieties to obtain processable organic materials with low-lying LUMO energy levels and good optical, electrochemical and electrical properties.[26–30] On the other hand, the covalent linkage of naphthalimide units with strong donor scaffolds such as oligothiophenes or triarylamines has shown to be a promising approach to obtain ambipolar materials.[31,32] Thus, in our research groups we have widely demonstrated that the combination of donor and acceptor units through different rigid and conjugated linkers can pave the way to functional materials with tunable and, sometimes unexpected, optical and electrochemical properties and good n-type or ambipolar characteristics in OFETs or OSCs.[33–40]

In the last 5 years, the fused-ring electron acceptor strategy (FREA) has become efficient in the modulation of the donor ability of organic materials without introducing strong donor moieties. This is the case of ITIC/IDIC or Y6 fused ring molecules with strong electron-acceptors in the terminal position in which it is possible to fine tune their donor abilities by controlling the length of the donor units.[41,42]

In this article, we have designed, synthesized and characterized a novel family of compounds based on the combination of electron-withdrawing naphthalimide units with strong thiophene-based donor moieties through different rigid and conjugated nitrogenated linkers. In order to fine-tune the HOMO energy levels, we have extended the length of the thiophenic unit and tested different isomers. As for the LUMO, the introduction of

---

[a] Department of Physical Chemistry, University of Málaga, Málaga, 29071, Spain. E-mail: rocioponce@uma.es
[b] Department of Organic Chemistry, Complutense University of Madrid, Faculty of Chemistry, Madrid 28040, Spain. E-mail: segura@ucm.es
[c] Chemical and Environmental Technology, Department. Univ. Rey Juan Carlos, Móstoles, 28933, Spain

† Electronic supplementary information (ESI) available. See DOI: https://doi.org/10.1039/d4qm00029c

‡ These authors contributed equally to this work.

Dyes and Pigments 242 (2025) 112984

Contents lists available at ScienceDirect

Dyes and Pigments

journal homepage: www.elsevier.com/locate/dyepig

Small asymmetric halogenated Phenylene–Naphthalimide molecules for organic field-effect transistors

Raúl González-Núñez [a,1], Alejandro de la Peña [b,c,1], Claudia Valderrama-Callejón [a],
José L. Segura [b,*], Rocío Ponce Ortiz [a,d,**]

[a] *Department of Physical Chemistry, University of Málaga, Málaga, 29071, Spain*
[b] *Department of Organic Chemistry, Complutense University of Madrid, Faculty of Chemistry, Madrid, 28040, Spain*
[c] *Chemical and Environmental Technology Department. Univ. Rey Juan Carlos, Móstoles, 28933, Spain*
[d] *Instituto Universitario de Materiales y Nanotecnología, IMANA, University of Málaga, Campus de Teatinos, 29071, Málaga, Spain*

ARTICLE INFO

Keywords:
Organic semiconductors
Naphthalimide
Halogenation
Field-effect transistors
Electron transport

ABSTRACT

A series of polycyclic aromatic hydrocarbons (PAH) based on phenylene-naphthalimide assemblies, in which both the phenylene unit and the electron-withdrawing moiety of naphthalimide are directly conjugated through rigid inverted amidine (NAI) bonds, are synthesized and characterized. Different halogen atoms (F and Cl) are introduced into the phenylene unit to modulate the electron-accepting and charge-transport properties of the new systems. A physicochemical study is performed in which the neutral and charged species are analyzed together with the electronic properties of the naphthalimide derivatives, switching from ambipolar mobility in phenylene-naphthalimide to n-type mobility in the halogenated derivatives. Maximum n-type field effect mobilities of 0.1 cm^{2}V^{-1}s^{-1} and 0.2 cm^{2}V^{-1}s^{-1} were measured for the halogenated compounds, **NAI-Ph-F** and **NAI-Ph-Cl**, respectively. It has been demonstrated that halogenation at the phenylene unit is a convenient strategy to facilitate charge injection, due to the lowering of the frontier energy levels and reduction potentials, without sacrificing molecular planarity, and thus maximizing charge stabilization and transport.

1. Introduction

Organic semiconductor materials are a viable alternative to inorganic-based semiconductors due to their low cost, processability, and tuneable structure and properties [1]. These materials are precious in various optoelectronic applications, including organic light-emitting diodes (OLEDs)[2–4], organic solar cells (OSCs) [5–9], organic photodetectors (OPDs) [10–12], and organic field-effect transistors (OFETs) [13–17]. A critical parameter for evaluating the suitability of organic semiconductors in optoelectronic applications is charge carrier mobility, which is typically measured in OFET devices[18–21]. This parameter is mainly influenced by molecular structure, orbital energy levels [22,23], and molecular packing [24–26]. Despite substantial advances in the production of new π-conjugated organic materials, the performance of organic devices is often inferior to that of their inorganic devices, mainly due to the lower mobility of charge carriers. However, a great effort has been devoted to the development of new materials with improved charge carrier mobility and to the optimization of the fabrication techniques, thus enabling the production of high-quality thin films with competitive performances [27]. In addition, the nature of organic semiconductors, being composed of carbon-based materials, offers advantages such as flexibility, lightweight, biocompatibility and lower production costs, being these characteristics essential for their use in emerging applications. [28,29]. Despite this, there is still the need to boost the performance and stability of organic semiconductors.

To address these challenges, researchers are focusing on the design and synthesis of organic semiconductors with enhanced processability and tuneable properties. Various molecular building blocks have been employed to create π-functional materials with high performance in organic electronic devices. Naphthalimide derivatives are commonly used as strong electron-accepting moieties, resulting in processable organic materials with low LUMO energy levels and favourable optical, electrochemical, and electrical properties [30]. Furthermore, the covalent linkage of naphthalimide units with strong donor structures has

---

* Corresponding author.
** Corresponding author. Department of Physical Chemistry, University of Málaga, Málaga, 29071, Spain.
E-mail address: rocioponce@uma.es (R. Ponce Ortiz).
[1] These authors contributed equally to this work.

https://doi.org/10.1016/j.dyepig.2025.112984
Received 11 May 2025; Received in revised form 18 June 2025; Accepted 19 June 2025

Journal of
Materials Chemistry C

ROYAL SOCIETY
OF CHEMISTRY

PAPER

View Article Online
View Journal | View Issue

Check for updates

Cite this: *J. Mater. Chem. C*, 2023, **11**, 10852

Tunable electroactive oligothiophene-naphthalimide semiconductors *via* end-capped engineering: cumulative effects beyond the linker†

Matías J. Alonso-Navarro, ‡[ab] Alexandra Harbuzaru, ‡[c] Raúl González-Núñez, [c] M. Mar Ramos,[b] José L. Segura *[a] and Rocío Ponce Ortiz *[c]

Received 16th June 2023,
Accepted 21st July 2023

DOI: 10.1039/d3tc02099a

rsc.li/materials-c

Aiming to obtain novel functional semiconducting materials for their use in organic electronics, the combination of strong donor moieties with electron-withdrawing units is one of the most useful strategies to obtain ambipolar semiconductors with tunable properties. Nowadays most of the efforts headed to efficient materials are based on small changes in the alkyl pendant chains or by replacing single atoms. However, a precise design of new functional materials is still challenging. For this reason, in this work we present a new synthetic approach for achieving redox amphoteric organic semiconductors by tuning their opto-electrochemical properties *via* rational chemical modifications. All these materials present low-lying LUMO levels, lower than −4.00 eV with broad absorption up to 800 nm in the UV-Vis-NIR spectra. In addition, they have been characterized by DFT, absorption and Raman vibrational spectroscopies, while their charge stabilization abilities are studied by means of spectroelectrochemical techniques. The results point out to a quite complex electronic scenario that goes beyond the expected cumulative effects of the independent molecular units constituting the final molecular assembly.

1. Introduction

Organic semiconducting materials have demonstrated to be a good alternative for metal-based semiconductors[1] due to their good performance, low-cost, good processability and their tunable structure and properties in optoelectronic[2,3] applications like organic light-emitting diodes (OLEDs),[4,5] organic solar cells (OSCs),[6,7] organic photodetectors (OPD)[8] and organic field-effect transistors (OFETs).[9–12] One of the key parameters to check the suitability for the application of organic semiconductors in optoelectronic applications is the charge carrier mobility, which is normally measured in an organic field-effect transistor device.[13,14] This parameter is affected by different factors such as molecular structure, orbital energy levels or molecular packing.[15–17] However, following the advances in the production of new organic π-conjugated hole-conducting (p-type) materials, there is still a need to develop novel n-type (electron-conducting) and ambipolar organic semiconductors.[18] For this reason, the design and development of ambient stable and high-performance n-type organic semiconductor materials is still challenging and desirable.[19]

In order to obtain these organic electron transporters, designing π-conjugated electron deficient systems with planar backbones functionalized with solubilizing alkyl chains is one of the best strategies nowadays.[10,20–22] This strategy has been used in the last years in order to obtain suitable acceptor–donor–acceptor (A–D–A) fullerene-free architectures with remarkable performances in OFETs[23,24] and OSCs.[24,25] In this regard, rylenimide derivatives have been described as one of the best choices for efficient n-type organic materials in OFETs, due to their good stability, easy functionalization and tunable optoelectronic properties.[26,27] Among them, naphthalimide-based assemblies have been employed as electron acceptors due to their electron-deficient backbone and optimal LUMO levels, tunable absorption range, supramolecular organization properties[28,29] and remarkable good transport properties for their single-crystal structures.[30]

With the aim of obtaining n-type or ambipolar semiconductor materials, Segura and coworkers have developed different series of donor–acceptor molecular assemblies based on oligothiophene-naphthalimide moieties (Fig. 1a) connected through

---

[a] *Department of Organic Chemistry, Complutense University of Madrid, Faculty of Chemistry, Madrid 28040, Spain. E-mail: segura@ucm.es*

[b] *Chemical and Environmental Technology Department, Univ. Rey Juan Carlos, Móstoles, 28933, Spain*

[c] *Department of Physical Chemistry, University of Málaga, Málaga, 29071, Spain. E-mail: rocioponce@uma.es*

† Electronic supplementary information (ESI) available. See DOI: **https://doi.org/10.1039/d3tc02099a**

‡ These authors contributed equally to this work.

Journal of
Materials Chemistry C

ROYAL SOCIETY
OF CHEMISTRY

PAPER

View Article Online
View Journal

Check for updates

Cite this: DOI: 10.1039/d4tc02496f

The effect of hydrogen bond interactions on the electronic nature of DPP-based organic semiconductors: implications on charge transport†

Raúl González-Núñez, ‡[a] Gabriel Martinez,‡[b] Nelson Ricardo Avila-Rovelo, §[b]
Kyeog-Im Hong, ¶[bc] Amparo Ruiz-Carretero *[bc] and Rocío Ponce Ortiz *[a]

Received 14th June 2024,
Accepted 4th October 2024

DOI: 10.1039/d4tc02496f

rsc.li/materials-c

In this work, we show that hydrogen bond interactions, in addition to directing supramolecular order, can have an intriguing effect on the molecular and electronic properties of DPP derivatives, facilitating redox processes in the solid state. As a result, charge carrier formation can be enhanced in devices, contributing to the improvement of electrical performances of two exceptionally small molecular semiconductors based on a thiophene-capped diketopyrrolopyrrole (DPP) as the electroactive component and amide groups as hydrogen-bonding units. Two different topologies of the amide groups were explored, C-centered and N-centered (**HDPPBA-C** and **HDPPBA-N**, respectively), and the results were compared to the **HDPPH** molecule with no amide groups. Spectroelectrochemical experiments, in conjunction with vibrational spectroscopies and DFT calculations, demonstrate that hydrogen bond formation promotes modifications on the effective conjugation length of the studied semiconductors, which may facilitate the generation of free charge carriers in organic field effect transistors (OFETs). These results open a new strategy towards the simple design of organic semiconductors and control over their morphological and electrical properties by simple hydrogen bond formation.

Introduction

Organic materials have appeared in the last few decades as great alternatives for the fabrication of electronic devices, such as organic field effect transistors (OFETs)[1] or organic solar cells.[2] The versatility of organic synthesis allows us to provide small molecules or polymers with the desired optoelectronic properties.[3] Interestingly, the final efficiency of a given device does not only depend on the molecular design but also, very importantly, on the way the materials assemble.[4] It is here that noncovalent interactions play a crucial role, since they guide the assembly process in solution and when depositing molecules on thin films. In the case of organic semiconductors, since they are based on conjugated segments and aromatic moieties, π stacking is the main non-covalent interaction guiding their molecular packing. Nevertheless, the interplay of π stacking with other non-covalent interactions, such as hydrogen-bonding, has been proven a promising strategy to improve the morphology of organic electronic devices by creating well-connected domains of semiconductors able to transport charges efficiently.[5–12]

Despite the exciting results, where the beneficial role of hydrogen bonding is highlighted, the incorporation of such moieties in organic semiconductors for the fabrication of different organic electronic devices is still underexplored. In addition, in the search of efficient organic semiconductors reaching the performance required for device commercialization, a great effort has been mostly devoted over the years to the optimization of structure–property relationships of pristine organic semiconducting materials, looking for a proper balance between molecular and intermolecular characteristics for efficient charge transport. However, in the last few years, enormous interest has emerged in the use of molecular dopants, which allows tuning the energy gap and the optical and electrical properties of semiconducting materials.[13] Thus, this

---

[a] *Department of Physical Chemistry, University of Málaga, Campus de Teatinos s/n, Málaga 29071, Spain. E-mail: rocioponce@uma.es*

[b] *University of Strasbourg, Institute Charles Sadron, CNRS, UPR22, 23 Rue du Loess, 67034, Strasbourg Cedex 2, France. E-mail: amparo.ruiz@ics-cnrs.unistra.fr*

[c] *Instituto de Ciencia de Materiales de Madrid, Consejo Superior de Investigaciones Científicas CSIC, Sor Juana Inés de la Cruz 3, 28049, Madrid, Spain*

† Electronic supplementary information (ESI) available: Experimental details, characterization data, and DFT calculation results. See DOI: **https://doi.org/10.1039/d4tc02496f**

‡ R.G.-N and G.M. contributed equally to the manuscript.

§ Current affiliation: Institute for Chemistry and Processes for Energy, Environment and Health, ICPEES, UMR 7515, 25 Rue Becquerel, 67087, Strasbourg Cedex 2, France

¶ Current affiliation: Instituto Madrileño de Estudios Avanzados, IMDEA Nanoscience, Calle Faraday 9, 28049, Madrid, Spain

- Other publications:

5. S. Mori, S. Moles Quintero, N. Tabaka, R. Kishi, **R. González Núñez**, A. Harbuzaru, R. Ponce Ortiz, J. Marín-Beloqui, S. Suzuki, C. Kitamura, C. J. Gómez-García, Y. Dai, F. Negri, M. Nakano, S. ichiro Kato and J. Casado, Medium Diradical Character, Small Hole and Electron Reorganization Energies and Ambipolar Transistors in Difluorenoheteroles, *Angewandte Chemie - International Edition*, 2022, **61**, e202206680. **doi.org/10.1002/anie.202206680**

6. S. Ma, J. Wang, K. Feng, H. Zhang, Z. Wu, Y. Wang, B. Liu, Y. Li, M. An, **R. Gonzalez-Nuñez**, R. Ponce Ortiz, H. Y. Woo and X. Guo, n-Type Polymer Semiconductors Based on Dithienylpyrazinediimide, *ACS Applied Materials and Interfaces* , 2023, **15**, 1639–1651. **doi.org/10.1021/acsami.2c17969**

7. **R. González-Núñez**, I. Badía-Domínguez, S. Gámez-Valenzuela, A. Yangb, J. Moore, F. Huang, M.C. Ruiz Delgado and R. Ponce Ortiz. The influence of linkers in the charge-transport properties of carbazole-based macrocyclic. *In preparation*.